Development of tissue-engineered three-dimensional infection models to study pathogenesis of *Campylobacter jejuni*

Entwicklung dreidimensionaler Infektionsmodelle
basierend auf Gewebezüchtung zur Erforschung
der Pathogenese von *Campylobacter jejuni*

Dissertation

for a doctoral degree (Dr. rer. nat.)
at the *Graduate School of Life Sciences*,
Julius-Maximilians-Universität Würzburg

Section: Infection and Immunity

submitted by

Mona Alzheimer

from Würzburg

Würzburg, 2019

Submitted on:

Members of the Thesis Committee:

Chair person:	Prof. Dr. Thomas Dandekar Lehrstuhl für Bioinformatik, Biozentrum, Julius-Maximilians-Universität Würzburg
Primary Supervisor:	Prof. Dr. Cynthia M. Sharma Institut für Molekulare Infektionsbiologie (IMIB), Molekulare Infektionsbiologie II Julius-Maximilians-Universität Würzburg
Supervisor (second):	Prof. Dr. Heike Walles Forschungszentrum Dynamische Systeme (CDS), Otto von Guericke Universität Magdeburg
Supervisor (third):	Prof. Dr. Jörg Vogel Institut für Molekulare Infektionsbiologie (IMIB), Julius-Maximilians-Universität Würzburg Helmholtz Institut für RNA-basierte Infektionsforschung (HIRI)

Date of Public Defense:

Date of Receipt of Certificate:

Affidavit/Eidesstattliche Erklärung

I hereby confirm that my thesis entitled "Development of tissue-engineered three-dimensional infection models to study pathogenesis of *Campylobacter jejuni*" is the result of my own work. I did not receive any help or support from commercial consultants. All sources and/or material applied are listed and specified in the thesis.

Furthermore, I confirm that this thesis has not yet been submitted as part of another examination process neither in identical nor in similar form.

Würzburg, _____

Mona Alzheimer

Ich erkläre hiermit an Eides statt, dass ich die vorliegende Dissertation „Entwicklung dreidimensionaler Infektionsmodelle basierend auf Gewebezüchtung zur Erforschung der Pathogenese von *Campylobacter jejuni*" eigenständig, d.h. insbesondere ohne die Hilfe oder Unterstützung von kommerziellen Promotionsberatern, angefertigt habe. Ergänzend bestätige ich, dass ich keine anderen als die von mir angegebenen Quellen oder Hilfsmittel verwendet habe.

Ich erkläre außerdem, dass diese Dissertation weder in gleicher noch in ähnlicher Form bereits in einem Prüfungsverfahren vorgelegen hat.

Würzburg, _____

Mona Alzheimer

Dedicated to my husband, Dominik Preisendörfer, and my parents, Bruno & Daniela Alzheimer

Summary

Infectious diseases caused by pathogenic microorganisms are one of the largest socioeconomic burdens today. Although infectious diseases have been studied for decades, in numerous cases, the precise mechanisms involved in the multifaceted interaction between pathogen and host continue to be elusive. Thus, it still remains a challenge for researchers worldwide to develop novel strategies to investigate the molecular context of infectious diseases in order to devise preventive or at least anti-infective measures. One of the major drawbacks in trying to obtain in-depth knowledge of how bacterial pathogens elicit disease is the lack of suitable infection models to authentically mimic the disease progression in humans. Numerous studies rely on animal models to emulate the complex temporal interactions between host and pathogen occurring in humans. While they have greatly contributed to shed light on these interactions, they require high maintenance costs, are afflicted with ethical drawbacks, and are not always predictive for the infection outcome in human patients. Alternatively, *in-vitro* two-dimensional (2D) cell culture systems have served for decades as representatives of human host environments to study infectious diseases. These cell line-based models have been essential in uncovering virulence-determining factors of diverse pathogens as well as host defense mechanisms upon infection. However, they lack the morphological and cellular complexity of intact human tissues, limiting the insights than can be gained from studying host-pathogen interactions in these systems.

The focus of this thesis was to establish and innovate intestinal human cell culture models to obtain *in-vitro* reconstructed three-dimensional (3D) tissue that can faithfully mimic pathogenesis-determining processes of the zoonotic bacterium *Campylobacter jejuni* (*C. jejuni*). Generally employed for reconstructive medicine, the field of tissue engineering provides excellent tools to generate organ-specific cell culture models *in vitro*, realistically recapitulating the distinctive architecture of human tissues. The models employed in this thesis are based on decellularized extracellular matrix (ECM) scaffolds of porcine intestinal origin. Reseeded with intestinal human cells, application of dynamic culture conditions promoted the formation of a highly polarized mucosal epithelium maintained by functional tight and adherens junctions. While most other *in-vitro* infection systems are limited to a flat monolayer, the tissue models developed in this thesis can display the characteristic 3D villi and crypt structure of human small intestine.

First, experimental conditions were established for infection of a previously developed, statically cultivated intestinal tissue model with *C. jejuni*. This included successful isolation of bacterial colony forming units (CFUs), measurement of epithelial

barrier function, as well as immunohistochemical and histological staining techniques. In this way, it became possible to follow the number of viable bacteria during the infection process as well as their translocation over the polarized epithelium of the tissue model. Upon infection with *C. jejuni*, disruption of tight and adherens junctions could be observed via confocal microscopy and permeability measurements of the epithelial barrier. Moreover, *C. jejuni* wildtype-specific colonization and barrier disruption became apparent in addition to niche-dependent bacterial localization within the 3D microarchitecture of the tissue model. Pathogenesis-related phenotypes of *C. jejuni* mutant strains in the 3D host environment deviated from those obtained with conventional *in-vitro* 2D monolayers but mimicked observations made *in vivo*. Furthermore, a genome-wide screen of a *C. jejuni* mutant library revealed significant differences for bacterial factors required or dispensable for interactions with unpolarized host cells or the highly prismatic epithelium provided by the intestinal tissue model. Elucidating the role of several previously uncharacterized factors specifically important for efficient colonization of a 3D human environment, promises to be an intriguing task for future research.

At the frontline of the defense against invading pathogens is the protective, viscoelastic mucus layer overlying mucosal surfaces along the human gastrointestinal tract (GIT). The development of a mucus-producing 3D tissue model in this thesis was a vital step towards gaining a deeper understanding of the interdependency between bacterial pathogens and host-site specific mucins. The presence of a mucus layer conferred *C. jejuni* wildtype-specific protection against epithelial barrier disruption by the pathogen and prevented a high bacterial burden during the course of infection. Moreover, results obtained in this thesis provide evidence *in vitro* that the characteristic corkscrew morphology of *C. jejuni* indeed grants a distinct advantage in colonizing mucous surfaces.

Overall, the results obtained within this thesis highlight the strength of the tissue models to combine crucial features of native human intestine into accessible *in-vitro* infection models. Translation of these systems into infection research demonstrated their ability to expose *in-vivo* like infection outcomes. While displaying complex organotypic architecture and highly prismatic cellular morphology, these tissue models still represent an imperfect reflection of human tissue. Future advancements towards inclusion of human primary and immune cells will strive for even more comprehensive model systems exhibiting intricate multicellular networks of *in-vivo* tissue. Nevertheless, the work presented in this thesis emphasizes the necessity to investigate host-pathogen interactions in infection models authentically mimicking the natural host environment, as they remain among the most vital parts in understanding and counteracting infectious diseases.

Zusammenfassung

In der heutigen Zeit tragen insbesondere durch pathogene Mikroorganismen ausgelöste Infektionskrankheiten zur sozioökonomischen Belastung bei. Obwohl bereits jahrzehntelang an der Entstehung von Infektionskrankheiten geforscht wird, bleiben in zahlreichen Fällen die genauen Mechanismen, welche an den vielfältigen Interaktionen zwischen Pathogen und Wirt beteiligt sind, unbeschrieben. Gerade deshalb bleibt es für Wissenschaftler weltweit eine Herausforderung, neue Strategien zur Untersuchung des molekularen Kontexts von Infektionskrankheiten zu entwickeln, um präventive oder zumindest anti-infektive Maßnahmen ergreifen zu können. In den meisten Fällen ist jedoch das Fehlen geeigneter Infektionsmodelle, mit denen der Krankheitsverlauf im Menschen authentisch nachgestellt werden kann, eines der größten Hindernisse um detailliertes Wissen darüber gewinnen zu können wie bakterielle Pathogene die Krankheit auslösen.

Zahlreiche Studien sind dabei auf Tiermodelle angewiesen, um die komplexen zeitlichen Abläufe zwischen Wirt und Pathogen im menschlichen Körper nachzuahmen. Während diese Modelle in hohem Maß dazu beigetragen haben, Aufschluss über diese Abläufe zu geben, sind sie doch sehr kostenintensiv, mit ethischen Bedenken behaftet und können nicht immer die Folgen einer Infektion im menschlichen Patienten vorhersagen. Seit Jahrzehnten werden daher alternativ *in-vitro* 2D Zellkultursysteme eingesetzt, um den Verlauf von Infektionskrankheiten zu erforschen, welche die Bedingungen im menschlichen Wirt wiederspiegeln sollen. Diese auf Zelllinien basierenden Modelle sind essentiell in der Entdeckung von Virulenzfaktoren diverser Pathogene, aber auch in der Aufklärung von wirtsspezifischen Abwehrmechanismen. Dennoch fehlt ihnen die morphologische und zelluläre Komplexität von intaktem menschlichen Gewebe. Dadurch sind die Erkenntnisse, die mit diesen Systemen über Infektionsverläufe gewonnen werden können, limitiert.

Die vorgelegte Arbeit konzentriert sich auf die Etablierung und Weiterentwicklung intestinaler, humaner Zellkulturmodelle, um dreidimensionales Gewebe *in vitro* zu rekonstruieren mit dem Ziel, Pathogenese-beeinflussende Prozesse des zoonotischen Bakteriums *C. jejuni* nachzustellen. Das Fachgebiet der Gewebezüchtung wird üblicherweise für rekonstruktive Medizin eingesetzt und bietet exzellente Mittel zur *in-vitro* Herstellung organspezifischer Zellkulturmodelle, welche die unverkennbare Mikroarchitektur humanen Gewebes realistisch nachempfinden können. Die in dieser Arbeit verwendeten Modelle basieren auf einem extrazellulären Matrixgerüst, das aus der Dezellularisierung von Schweinedarm gewonnen wurde. Durch die Wiederbesiedelung mit human Kolonzellen und der Kultivierung unter dynamischen Bedingungen entwickelte sich ein hochpolarisiertes mucosales Epithel, das durch funktionale Zell-Zell-Kontakte (tight und adherens junctions)

aufrechterhalten wird. Während andere *in-vitro* Infektionssysteme meist durch die Präsenz einer flachen Zellschicht limitiert werden, entwickelt das in dieser Arbeit eingeführte Gewebemodell die für den menschlichen Dünndarm charakteristische Architektur aus Villi und Krypten.

Zunächst wurden experimentelle Bedingungen für die Infektion eines zuvor entwickelten, statisch kultivierten Dünndarmmodells mit *C. jejuni* etabliert. Dies beinhaltete die erfolgreiche Isolierung koloniebildender Einheiten, die Messung der epithelialen Barrierefunktion, sowie immunhistochemische und histologische Färbetechniken. Dadurch konnte die Anzahl der Bakterien sowie deren Translokalisierung über das polarisierte Epithel während des Infektionsprozesses nachvollzogen werden. Außerdem konnte die Beeinträchtigung von Zell-Zell-Kontakten durch konfokale Mikroskopie und Permeabilitätsmessungen der epithelialen Barriere beobachtet werden. Neben der Bestimmung der Kolonisierungsrate von *C. jejuni* Isolaten und der dadurch hervorgerufenen spezifischen Zerstörung der epithelialen Barriere konnten die Bakterien auch innerhalb der 3D Mikroarchitektur des Gewebemodells lokalisiert werden. Außerdem konnte im Rahmen der 3D Gewebeumgebung beobachtet werden, dass Pathogenese-relevante Phänotypen von *C. jejuni* Mutantenstämmen im Vergleich zu konventionellen *in-vitro* 2D Zellschichten abwichen, diese aber dafür mit den *in-vivo* gemachten Beobachtungen übereinstimmten. Darüber hinaus wies die genomweite Suche einer *C. jejuni* Mutantenbibliothek signifikante Unterschiede zwischen bakteriellen Faktoren, die für die Interaktion mit nicht polarisierten Wirtszellen oder dem hochprismatischen Epithel des Gewebemodells bedeutsam oder entbehrlich waren, auf. Die Aufklärung der Funktion einiger bisher nicht charakterisierter Faktoren, die zu einer effizienten Kolonisierung menschlichen Gewebes beitragen, verspricht eine faszinierende Aufgabe für die zukünftige Forschung zu werden.

Die vorderste Verteidigungslinie gegen eindringende Pathogene bildet die schützende, viskoelastische Mukusschicht, die mukosale Oberflächen entlang des menschlichen Gastrointestinaltrakts überzieht. Mit der Entwicklung eines mukusproduzierenden Gewebemodells in der hier vorgelegten Arbeit gelang ein entscheidender Schritt zur Erforschung der Wechselbeziehungen zwischen bakteriellen Pathogenen und wirtsspezifischen Muzinen. Während des Infektionsverlaufs wurde das unterliegende Epithel durch die Anwesenheit der Mukusschicht vor der Zerstörung durch die Mikroben geschützt und eine erhöhte bakterielle Belastung verhindert. Darüber hinaus liefern die Resultate dieser Arbeit einen *in-vitro* Nachweis für den bakteriellen Vorteil einer spiralförmigen Morphologie, um muköse Oberflächen zu besiedeln.

Zusammenfassend unterstreicht diese Arbeit das Potential der hier entwickelten Gewebemodelle, entscheidende Eigenschaften des menschlichen Darms in einem leicht

zugänglichen *in-vitro* Infektionsmodell zu vereinigen. Der Einsatz dieser Modelle im Rahmen der Infektionsforschung bewies deren Fähigkeit *in-vivo* beobachtete Infektionsverläufe widerzuspiegeln. Während diese Infektionsmodelle bereits organotypische Architektur und hochprismatische Zellmorphologie aufweisen, ist ihre Darstellung von menschlichem Gewebe noch nicht perfekt. Durch den Einsatz von humanen Primär- und Immunzellen wird es in Zukunft möglich sein, noch umfassendere Modellsysteme zu entwickeln, die komplexe multizelluläre Netzwerke von *in-vivo* Geweben aufweisen. Nichtsdestotrotz verdeutlicht die hier vorgelegte Arbeit wie wichtig es ist, die Interaktionen zwischen Wirt und Pathogen innerhalb von Infektionsmodellen zu erforschen, welche die natürliche Wirtsumgebung wiedergeben. Dies spielt eine entscheidende Rolle, um die Entstehung von Infektionskrankheiten nachvollziehen und ihnen entgegenwirken zu können.

Table of contents

Abbreviation index

2D	two-dimensional
3D	three-dimensional
aa	amino acid
ADH	adherence
AJ/AJs	adherens junction(s)
approx.	approximately
APS	ammonium persulfate
BB	Brucella broth
BioVaSc	biological vascularised scaffold
BSA	bovine serum albumin
$C_6H_8O_7 \bullet H_2O$	citric acid monohydrate
$CaCl_2$	calcium chloride
CH_3CO_2K	potassium acetate
CCV	*Campylobacter*-containing vacuole
C. difficile	*Clostridium difficile*
CDS	coding sequence
CDT	cytolethal distending toxin
CFU/CFUs	colony forming unit(s)
CH_3COOH	acetic acid
$CHCl_3$	chloroform
Cia	*Campylobacter* invasion antigens
C. jejuni	*Campylobacter jejuni*
CLEM	correlative light-electron microscopy
Cm^R	chloramphenicol resistance
CO_2	carbon dioxide
co-IP	co-immunoprecipitation
C. perfringens	*Clostridium perfringens*
CPS	capsular polysaccharide
CRISPR	clustered regularly interspaced short palindromic repeats
DAPI	4',6-Diamidine-2'-phenylindole dihydrochloride
DAPT	*N*-[*N*-(3,5-Difluorophenacetyl)-l-alanyl]-*S*-phenylglycine *t*-butyl ester
Dlg	discs large
DMEM	Dulbecco's Modified Eagle Medium
DMSO	dimethyl sulfoxide
DNA	deoxyribonucleic acid
dNTPs	deoxynucleoside triphosphates
DPBS	Dulbecco's Phosphate-Buffered Saline
dRNA-seq	differential RNA sequencing
ECM	extracellular matrix
E. coli	*Escherichia coli*
EDTA	ethylenediaminetetraacetic acid
e.g.	exempli gratia (engl. for example)
EHEC	enterohemorrhagic *E. coli*
EPEC	attaching and effacing lesions-forming enteropathogenic *E. coli*
ESC	embryonic stem cell

EtOH	ethanol
FCS	fetal calf serum
FDPA	FITC-dextran permeability assay
Fed	flagella co-expressed determinant
Fe-S	iron-sulfur
FITC	fluorescein isothiocyanate
GalNAc	*N*-acetylgalactosamine
GBS	Guillain-Barré syndrome
gDNA	genomic DNA
GIT	gastrointestinal tract
H_2O	water (distilled)
H_3BO_3	boric acid
HCl	hydrochloric acid
H&E	hematoxylin and eosin
HIV-1	human immunodeficiency virus-1
H. pylori	*Helicobacter pylori*
HTH	helix-turn-helix
IBD	inflammatory bowel disease
IclR	isocitrate lyase-type regulator
i.e.	id est (engl. that is to say)
IGB	Integrated Genome Browser
IHC	immunohistochemical staining
IL-10	interleukin-10
IM	inner membrane
INT	internalization
iPSC	induced pluripotent stem cell
IscR	iron-sulfur cluster regulator
iTSS	internal transcriptional start site
$K_2S_2O_5$	potassium pyrosulfite
Kan^R	kanamycin resistance
KCl	potassium chloride
Kdo	ketodeoxyoctonic acid
KH_2PO_4	monopotassium phosphate
KRT18	cytokeratin-18
LB	Lennox broth
Leg	legionaminic acid
LGR5	leucine rich repeat containing G protein-coupled receptor 5
L. monocytogenes	*Listeria monocytogenes*
LOS	lipooligosaccharide
LPS	lipopolysaccharide
LSFM	light sheet fluorescent microscopy
MALT	mucosa-associated lymphoid tissue
MC	Methacarn
MCP	methyl-accepting chemotaxis protein
MDR1	multidrug resistance protein 1
MEM	Minimal Essential Medium
MeOH	methanol

MeOPN	*O*-methyl phosphoramidate
$MgCl_2$	magnesium chloride
MH	Mueller Hinton
$MnCl_2$	manganese chloride
MOI	multiplicity of infection
MUC	mucin
N_2	nitrogen
NaCl	sodium chloride
Na_2HPO_4	sodium phosphate
NaOH	sodium hydroxide
NASA	National Aeronautics and Space Administration
NEAA	non-essential amino acids
Neu5Ac	*N*-acetylneuraminic acid
N. gonorrhoeae	*Neisseria gonorrhoeae*
O_2	oxygen
OD_{600}	optical density at a wavelength of 600 nm
OM	outer membrane
O-Me	*O*-methyl
ORF/ORFs	open reading frame(s)
P	promoter
PAA	polyacrylamide
P. aeruginosa	*Pseudomonas aeruginosa*
PAS	periodic acid-Schiff
PBS	phosphate-buffered saline
PC	polycarbonate
PCR	polymerase chain reaction
PDMS	polydimethylsiloxane
PDZ	postsynaptic density-95, discs large, zonula occludens-1
PET	polyethylene terephthalate
PFA	paraformaldehyde
PG	peptidoglycan
p. i.	post infection
PSD-95	postsynaptic density-95
Pse	pseudaminic acid
pTSS	primary transcriptional start site
RBS	ribosome binding site
RNA	ribonucleic acid
RT	room temperature
RWV	rotating wall vessel
Salmonella	*Salmonella enterica* subsp. *enterica* serovar Typhimurium
S. aureus	*Staphylococcus aureus*
SD/SDs	standard deviation(s)
sfGFP	superfolder green fluorescent protein
S. flexneri	*Shigella flexneri*
SIGIRR	single IgG IL-1 related receptor
SISmuc	small intestinal submucosa
SPI-1	*Salmonella* pathogenicity island-1

SPIM	selective plane illumination microscopy
spp.	species
sRNA/sRNAs	small regulatory non-coding RNA(s)
SSR/SSRs	simple sequence repeat(s)
SUP	supernatant
T3SS	type 3 secretion system
T4SS	type 4 secretion system
T. brucei	*Trypanosoma brucei*
TEM	transmission electron microscopy
TEMED	tetramethylethylendiamin
TER	transepithelial electrical resistance
TJ/TJs	tight junction(s)
TLR5	toll-like receptor 5
T_m	melting temperature
Tn	transposon
Tn-seq	transposon sequencing
TR	transcriptional regulator
TSS	transcriptional start site
TW	Transwell
V. cholerae	*Vibrio cholerae*
vs.	versus
WHO	World's Health Organization
WT	wildtype
Y. pseudotuberculosis	*Yersinia pseudotuberculosis*
ZO-1	zonula occludens-1

Units

%	percent
°C	degree Celsius
bp	base pair(s)
cm	centimeter
Da	Dalton
dyn	dyne (centimeter-gram-second unit of force)
F	Farad
g	gram
h/hrs	hour(s)
l	liter
M	molar
m	meter
min	minute(s)
Mio	million
molar	gram molecule
nt	nucleotide(s)
pH	minus the decimal logarithm of the hygrogen concentration
rpm	rounds per minute
s/sec	second(s)
u	unit
V	volt
x *g*	g-force
Ω	ohm

Multiples

M	mega (10^6)
k	kilo (10^3)
m	milli (10^{-3})
µ	micro (10^{-6})
n	nano (10^{-9})
p	pico (10^{-12})

Aim of this thesis

As the largest mucosal surface of the human body, the gastrointestinal epithelium together with its viscous mucus layer forms an impressive defensive line against pathogenic microorganisms. Enteric pathogens have evolved numerous strategies to successfully colonize and persist in the human GIT. This includes the intestinal pathogen *C. jejuni*, which is currently the most common cause of bacterial foodborne gastroenteritis in humans and mainly resides in the mucus layer overlying the GIT epithelium (Schielke *et al.*, 2014; Kaakoush *et al.*, 2015). Infection research with *C. jejuni* – similar to many other enteric pathogens – mainly relies on small animal models or *in-vitro* 2D cell culture systems to study virulence mechanisms. In the case of *C. jejuni*, this has uncovered a so far limited range of dedicated virulence factors involved in the interaction with human host cells. By contrast, general biological features of *C. jejuni* such as adaptation to different environments, its shape, and its powerful flagellar system proofed to be crucial for a successful lifestyle (Young *et al.*, 2007; Burnham & Hendrixson, 2018). Current *in-vitro* and *in-vivo* infection models granted many insights into this complex interplay between *C. jejuni* and its host. Yet, 2D cell culture systems lack important characteristics of intact tissue, and animal models cannot always faithfully predict the disease development in humans. *In-vitro* bioengineered human tissue might complement and extend current infection models because it could provide an authentic representation of the host environment encountered by the pathogen. Tissue engineering represents an interdisciplinary scientific field focused on the generation of tissues from cells with the support of biomaterials and/or scaffolds. Utilizing this technology, a 3D intestinal *in-vitro* tissue model was developed based on the human Caco-2 cell line reseeded on an extracellular matrix scaffold (Pusch *et al.*, 2011).

This thesis aims to employ and advance *in-vitro* tissue-engineered 3D cell culture models for the application in infectious disease research. For *C. jejuni*, this includes the establishment of infection-relevant conditions and readouts as well as the exploration of bacterial factors involved in host-pathogen interactions. To study the intricate processes unwinding at the interface of host and pathogen, it is critical to advance the tissue-engineered infection models to approach the microenvironment of the human intestine. As the mucus layer along the GIT does not only serve as the first layer of defense against invading pathogens but also offers a natural habitat for many microbes including *C. jejuni*, this thesis aims to incorporate a mucus layer into the 3D tissue model. In concert with conventional infection models, the bioengineered *in-vitro* tissue developed in this thesis can support the simulation of the multifaceted pathogenesis-determining processes generally observed in a human body.

Contribution by others

The work described in this PhD thesis was conducted under supervision of Prof. Dr. Cynthia M. Sharma in her group "Deep Sequencing Approaches to Pathogenesis", Chair of Molecular Infection Biology II, Institute for Molecular Infection Biology (IMIB), Julius-Maximilians-University of Würzburg, Germany. Parts of the here described work that have been contributed by others and/or have been conducted in collaboration with others, are indicated below.

- Characterization of fluid dynamics to investigate fluidic shear forces induced by shaker movements was conducted by Ivo Schwedholm under supervision of PD Dr. Marco Metzger (Tissue Engineering and Regenerative Medicine, University Hospital Würzburg, Germany).
- Some *C. jejuni* mutant, complementation, and sfGFP-fusion strains were constructed by Dr. Gaurav Dugar or Dr. Sarah L. Svensson (Sharma lab).
- Design, construction, and sequencing of the Tn5-based transposon mutant library of *C. jejuni* strain NCTC11168 was performed by Dr. Sarah L. Svensson (Sharma lab).
- Processing of transposon sequencing data and bioinformatic analyses were performed by Dr. Thorsten Bischler (Sharma and Vogel lab, SysMed Core Unit of the Medical Faculty, University of Würzburg, Germany).

1. Biological background

The human GIT is a crucial platform for the interaction between microorganisms and their mammalian host. With its estimated surface area of approximately (approx.) 32 m^2 (Helander & Fändriks, 2014), it offers residence to trillions of bacteria, archea, viruses, and fungi. However, through its contact with the outside world, it is also vulnerable to invading pathogens of various species threatening the carefully maintained equilibrium between the microbiota and the host. This in turn can have dire consequences for the health of the human body. Currently, *C. jejuni* is the most prevalent foodborne bacterial pathogen with an incidence rate of more than 96 million cases per year worldwide (Schielke *et al.*, 2014; Havelaar *et al.*, 2015; Kaakoush *et al.*, 2015). In general, bacteria use a variety of virulence strategies such as toxins and secretion systems/effectors to interact with their host, survive, and cause disease. Very often, *e.g.* in the case of *C. jejuni*, the underlying molecular mechanisms remain largely unknown, not the least due to the lack of suitable infection models.

The following chapters are meant to provide a general overview of the anatomy and physiology of the human intestinal tract (primarily of the small intestine), bacterial strategies to establish residence in intestinal niches with a particular focus on the zoonotic bacterium *C. jejuni*, in consideration of current and novel infection models to study virulence mechanisms of gut pathogens.

1.1. Anatomical and physiological properties of the human gastrointestinal tract

As a multifunctional organ, the human GIT is mainly responsible for intake, digestion, and absorption of food, as well as excretion of bodily waste. The main organs of digestion include the stomach, the small, and the large intestine with their respective mucosal surfaces optimized to efficiently absorb nutrients, water, and electrolytes from food (Figure 1.1). At the same time, while the GIT is in constant contact with the external environment, it forms a major line of defense against invading pathogens. This is achieved by a particularly effective combination of a specialized viscoelastic mucus layer and an underlying tight epithelium maintained by cellular junction complexes. Together, they create a unique mucosal lining that still allows nutrient exchange while providing effective protection against harmful substances or microbes.

1.1.1. Morphological characteristics of the stomach and colon

The human stomach contains a complex, three-dimensional epithelium folded into gastric pits (Figure 1.1 A-I). These pits can reach deep into the underlying lamia propria and end up in branched tubular glands. While the fundus region is the major source for peptidases and

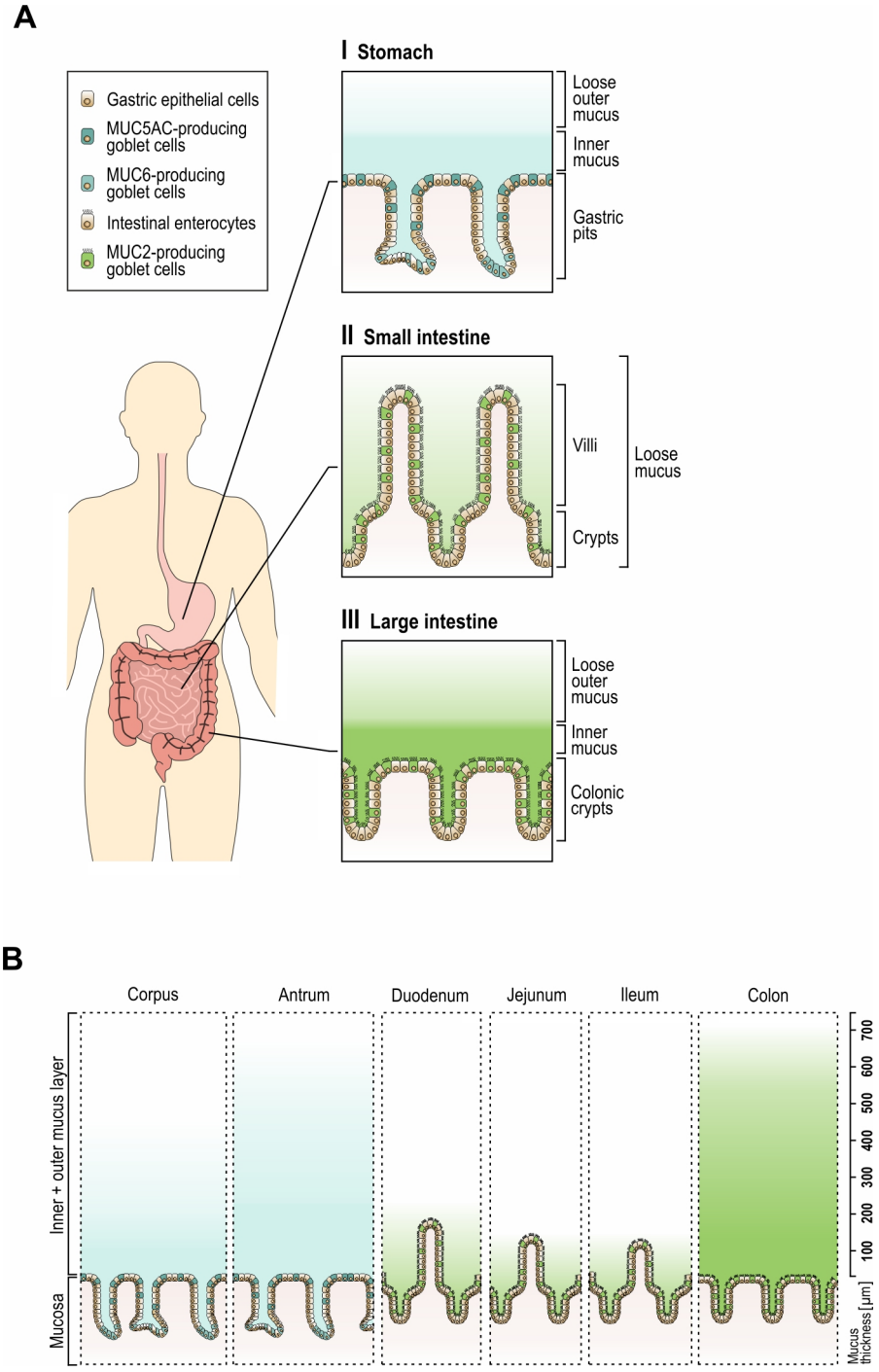

Figure legend on next page

Figure 1.1: Anatomical and mucin-specific properties of the human GIT. (A) Schematic representation of the mucosal morphology of the stomach **(I)**, small **(II)**, and large intestine **(III)**. Gastric pits and colonic crypts are covered by an inner membrane-bound and a loose outer mucus layer generated by goblet cells secreting MUC5AC/MUC6 and MUC2 in the stomach and colon, respectively. Distinguished by its characteristic villi and crypt architecture, the small intestinal mucosa is coated by just one loose mucus layer composed of the MUC2 mucin. **(B)** Comparison of mucus thickness along the human GIT ranging from 100 µm to > 700 µm from the gastric corpus to the proximal large intestine.

acid, mucus-secreting cells are most concentrated in the antral part of the stomach (Mills & Shivdasani, 2011; McCracken *et al.*, 2014). The single layer of columnar epithelial cells is coated by an inner attached mucus layer coupled to an outer unattached loose mucus layer, both comprised of the gastric MUC5AC mucin (Atuma *et al.*, 2001; Johansson *et al.*, 2013) in addition to the gel-forming MUC6 (Figure 1.1 A-I and B) (De Bolós *et al.*, 1995; Phillipson *et al.*, 2008).

The principle of a two-layered mucus system is also reflected in the large intestine. Similar to the gastric architecture, the single-layered mucosal epithelium of the colon is structured into intestinal glands also called colonic crypts, which are covered by a dense, inner mucus layer, and a loosely associated outer mucus layer (Figure 1.1 A-III and B). Both are formed by the intestinal mucin MUC2, creating a sterile barrier between the epithelial cells and the microbiota that can generally be found in the thicker outer mucus layer of the colon (Audie *et al.*, 1993; Johansson *et al.*, 2008).

1.1.2. Small intestinal topography and physiology

Contrary to stomach and colon, the small intestine harbors only one unattached mucus layer, which is also formed by MUC2. Due to its loose structure, it is more reminiscent of the outer mucus layer of the colon (Figure 1.1 A-II) (Johansson *et al.*, 2013; Johansson & Hansson, 2016). This protective viscoelastic barrier can be found throughout the whole GIT and its thickness ranges from 100 – 300 µm in the stomach and small intestine, to 700 µm in the large intestine (Figure 1.1 B) (Johansson *et al.*, 2011; Juge, 2012).

1.1.2.1. Small intestinal cell types and their protective mucus layer

The mucus layer is generally produced and secreted by goblet cells that can be found distributed throughout the intestinal mucosa or even as sentinel goblet cells at the entrances to crypts of Lieberkühn (Figure 1.2 A and B-I) (Martens *et al.*, 2018). Towards

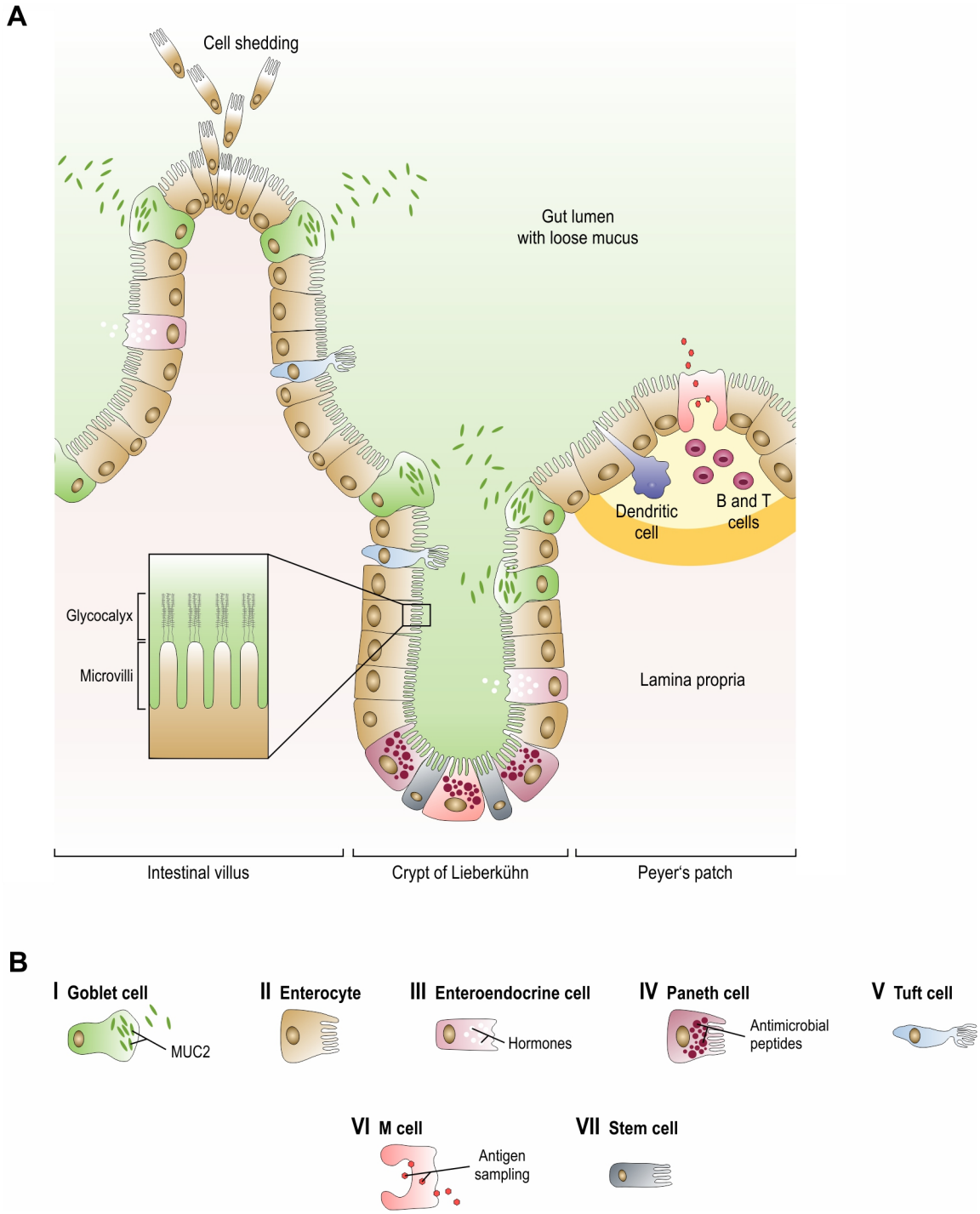

Figure 1.2: Microarchitecture of the small intestine with its cellular subtypes. (A, B) Overview of the architectural composition and cell types in the small intestine including the characteristic villus structures, crypts of Lieberkühn, and Peyer's patches. Goblet cells **(I)** continuously secret mucins into the gut lumen to replenish the loose mucus layer throughout the small intestine. Ion, nutrient, and water resorption is performed by enterocytes **(II)**, whose microvilli are additionally covered by the glycocalyx (inlet). Distributed throughout the mucosa are enteroendocrine **(III)** and tuft **(V)** cells, responsible for hormone production and chemosensoric, respectively. M cells **(VI)** are generally located in the part of the mucosa that covers underlying lymphoid aggregates called Peyer's patches. Antigens sampled by M cells are transmitted to antigen-presenting cells such as dendritic or B cells.

Stem cells **(VII)** are located at the crypt bottom intercalated with Paneth cells **(IV)** (production of antimicrobial peptides) continuously providing a fresh supply of new cells. At the villus tips, dying cells are shed off into the gut lumen. Figure inspired by (Martens *et al.*, 2018).

their apical membrane, goblet cells contain intracellular mucin-loaded vesicles that fuse with the cell membrane to release their content into the gut lumen, forming the different kinds of mucus layer in the GIT. As the MUC2 mucin is the main structural component of the intestinal mucus, goblet cells have a major task in production and assembly of this large and complex molecule (Karlsson *et al.*, 1996; McGuckin *et al.*, 2011). The most abundant cells in the intestine however are enterocytes with their columnar shape and a highly specialized apical membrane mediating the uptake of nutrients and ions (Figure 1.2 A and B-II). In order to properly fulfill their resorptive function, the surface of the enterocyte apical membrane is expanded by microvilli and protected by a carbohydrate-rich glycocalyx (Figure 1.2 A inlet) (Pelaseyed *et al.*, 2014). This glycocalyx reaches approx. one micrometer out from the brush border and is mostly composed of the transmembrane mucins MUC3, MUC12, and MUC17 (Linden *et al.*, 2008; Pelaseyed *et al.*, 2013). Apart from goblet cells and enterocytes, the intestinal mucosa is interspersed with additional differentiated cell types that serve defined functions (Figure 1.2 A and B-III to VI): hormone-releasing enteroendocrine cells (III), Paneth cells providing antimicrobial peptides (IV), tuft cells involved in taste-chemosensory responses (V), and microfold (M) cells responsible for antigen sampling (VI) (Gerbe *et al.*, 2012; Martens *et al.*, 2018). In addition, the intestinal epithelium is highly regenerative and its tissue-renewing proficiency is owed to the presence of stem and progenitor cells in the crypts of Lieberkühn surrounding the intestinal villi (Figure 1.2 A and B-VII) (Barker, 2014). At the villus tips, dying cells are shed off into the gut lumen to promote continual health of the mucosa (Watson & Hughes, 2012). As barrier integrity needs to be maintained throughout the intestinal tract, approx. 10^{11} new cells are generated every day to replace these cells within the intestine. This ensures a complete renewal of the small intestinal mucosa every 5 – 6 days (Messmann, 2011; Darwich *et al.*, 2014).

1.1.2.2. Cell-cell junctions in the intestinal mucosal barrier

Together, the above-described cell types form a tight mucosal barrier controlled by their connection via tight (TJs) and adherens junctions (AJs) (Turner, 2009). These intercellular junctions are crucial for the formation and maintenance of epithelial barriers. TJ protein complexes connect adjacent cells near their apical pole (Bischoff *et al.*, 2014) and are comprised of three possible transmembrane proteins namely occludin, claudins, or adhesion proteins such as the junctional adhesion molecules (Figure 1.3) (Matter & Balda,

2003). Intracellularly, they interact with the zonula occludens (ZO) proteins, which are in direct contact with the cytoskeleton. This way, TJs play a crucial role in regulation of the cellular polarity by restricting apical-basolateral diffusion of *e.g.* receptor proteins, thus ensuring responsiveness of cells to directional stimuli. Moreover, paracellular permeability is crucially dependent on fully functional TJ proteins as the intercellular space of TJs is almost completely abolished. This in turn selectively mediates the flow of ions or small molecules, in addition to preventing invading pathogens to reach deeper tissue regions via the submucosal space (König *et al.*, 2016).

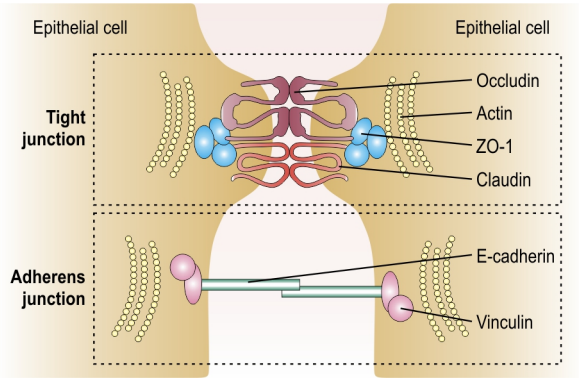

Figure 1.3: Composition of cellular junction complexes in the human small intestine. Epithelial barrier integrity is maintained by tight and adherens junction complexes. Tight junctions are composed of claudin and occludin and are anchored to the actin cytoskeleton by zonula occludens-1 (ZO-1) proteins. Vinculin and E-cadherin homodimers are key components of adherens junctions. The figure was modified according to (Neunlist *et al.*, 2013).

AJs are positioned immediately below the tight junctional complexes and are most often formed by cadherin-cadherin adhesive units connected to intracellular vinculin and subsequently to cytoplasmic actin filaments (Figure 1.3) (Takeichi, 1991; Niessen, 2007). Zonula adherens is the most prominent AJ and can be found in most epithelial cells. These complexes form a belt-like structure linking the cells together to a continuous sheet while in the process also separating the apical and basolateral membranes of the highly polarized enterocytes (Harris & Tepass, 2010). Consequently, the intestinal mucosal barrier poses an impressive host defense line against invading microorganisms.

1.1.2.3. Virulence strategies of bacterial pathogens to conquer the gastrointestinal mucosa

Pathogenic bacteria have evolved a wide range of specific strategies to gain entry into and even subvert mucosal barriers. For starters, they have to penetrate the mucus layer overlaying the epithelium to actually reach the surface of intestinal cells. This can, for example, be efficiently achieved by secretion of mucus-degrading enzymes. In the case of *Vibrio cholerae* (*V. cholerae*), the haemagglutinin protease (Hap) is secreted from the bacterium to promote mucin gel penetration through its mucinolytic activity (Figure 1.4 A) (Silva *et al.*, 2003). A different strategy to overcome the mucus layer is employed by the facultative intracellular bacterium *Shigella flexneri* (*S. flexneri*). This pathogen actively dampens mucin biosynthesis in addition to remodeling mucin glycosylation thereby reshaping mucin structures, and ultimately weakening the mucus barrier to its benefit (Sperandio *et al.*, 2013). Rather than actually having to penetrate the mucus layer, some enteric pathogens have developed a strategy to avoid it altogether while still being able to enter or traverse the mucosal barrier by targeting M cells. These specialized cells reside in the dome epithelium overlaying the Peyer's patches of the small intestine. As M cells are responsible for antigen sampling from the gut microbiota (Siebers & Finlay, 1996; Neutra *et al.*, 1999), it is sensible that they are located in the dome epithelium, which lacks goblet cells and thus, mucus coverage in this area is rather sparse. However, this renders M cells highly susceptible to invading pathogens such as *Salmonella enterica* subsp. *enterica* serovar Typhimurium (hereafter referred to as *Salmonella*). While it is also able to directly invade intestinal enterocytes or certain immune cells, it primarily uses M cells to gain access to the submucosal space (Figure 1.4 B) (Clark *et al.*, 1994). In addition, expression of β1-integrin receptors is higher on M cells compared to other epithelial cells. Consequently, this mode of access to the intestinal mucosa is preferably exploited by certain *Yersinia* or *Mycobacteria* species (Figure 1.4 C) (Clark *et al.*, 1998; Secott *et al.*, 2004). Pathogen-specific interactions with surface-exposed β1-integrin receptors permit the invading bacteria to cross the intestinal epithelial barrier via M cells while simultaneously avoiding the strenuous journey through the viscoelastic mucus barrier. In addition to targeting specific intestinal cell subtypes, many bacterial pathogens disrupt the epithelial barrier by targeting TJ proteins to gain access to the basolateral membrane of enterocytes. As the lateral side of the cells is not protected by mucus or a glycocalyx, it grants a seemingly easier entrance point for invading microorganisms. Most often, disruption of TJs leads to increased permeability and facilitates the translocation and systemic spread of pathogens into the body. For example, several

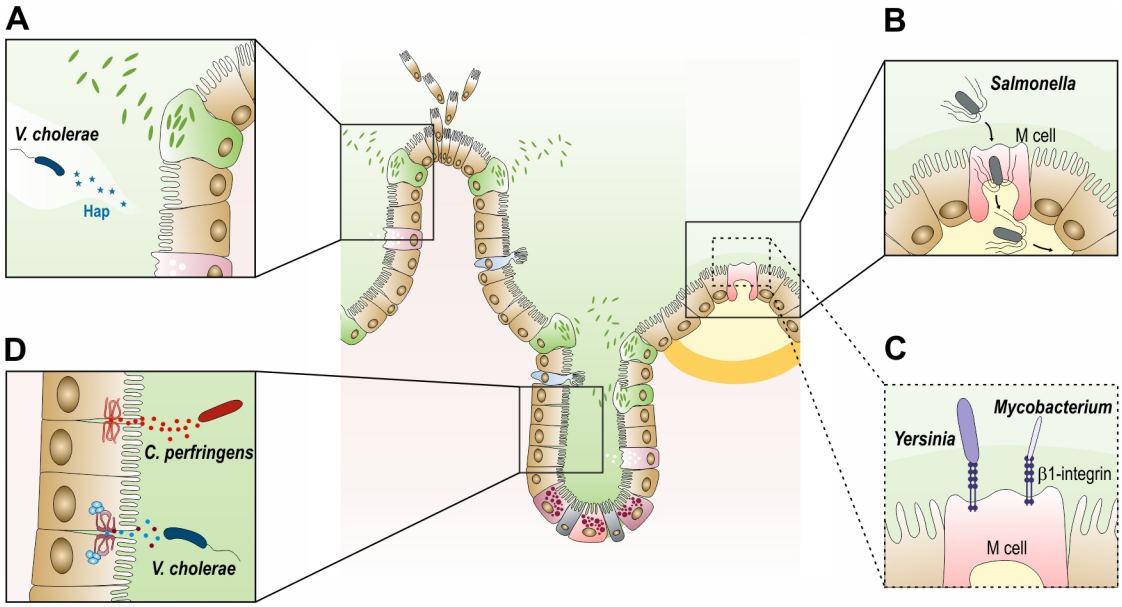

Figure 1.4: Strategies of bacterial pathogens to overcome the small intestinal barrier. **(A)** *V. cholerae* disrupts the mucus layer overlying the mucosa by secretion of the haemagglutinin protease (Hap), which possesses mucinolytic activity. **(B)** By targeting M cells, *Salmonella* avoids the thick mucus layer present in other regions of the small intestine and can thus cross the epithelium without additionally having to penetrate the viscoelastic protective barrier as well. **(C)** Similar to *Salmonella*, certain *Yersinia* and *Mycobacteria* species can invade the intestinal epithelium by targeting M cells. Through direct binding to β1-integrin receptors expressed on the M cell surface, these pathogenic bacteria can transit into the underlying Peyer's patch. **(D)** *C. perfringens* and *V. cholerae* can gain entrance to the submucosal space by targeting components of the tight junction complex via secretion of an enterotoxin and the zonula occludens toxin (ZOT), respectively. Figure inspired by (Martens *et al.*, 2018).

members of the claudin protein family are receptors for an enterotoxin produced by *Clostridium perfringens* (*C. perfringens*). Binding of the enterotoxin results in disintegration of TJs leading to an increase in paracellular permeability across the intestinal barrier (Figure 1.4 D) (Saitoh *et al.*, 2015). Along the same line, *V. cholerae* can disrupt mucosal integrity by targeting other TJ proteins such as occludin or ZO-1 via production of its zonula occludens toxin (Figure 1.4 D) (Fasano *et al.*, 1991; Wu *et al.*, 2000). Intriguingly, the gastric pathogen *Helicobacter pylori* (*H. pylori*) requires secretion of HtrA to traverse polarized epithelia (Hoy *et al.*, 2010; Tegtmeyer *et al.*, 2017). This serine protease is able to cleave the TJ proteins occludin and claudin-8 (Tegtmeyer *et al.*, 2017) as well as the AJ factor E-cadherin (Hoy *et al.*, 2010; Schmidt *et al.*, 2016) permitting paracellular access to integrin receptors localized on the basolateral site of enterocytes. This in turn enables binding of the *H. pylori* type 4 secretion system (T4SS) pili to basolateral β1-integrin receptors leading to host cell injection of the cytotoxin-associated gene A (CagA) oncoprotein (Kwok *et al.*, 2007; Kaplan-Türköz *et al.*, 2012; Bonsor *et al.*, 2015; Backert *et al.*, 2018).

Taken together, bacterial pathogens have evolved numerous strategies to overcome mucosal barriers in order to establish infection in the human GIT. Disruption or rearrangement of the mucus layer or the cell-cell junction complexes can easily dampen the resilience of the intestinal mucosa allowing invading microorganisms access to the submucosal space and thereby the rest of the body.

1.2. The foodborne pathogen *Campylobacter jejuni*

As described above, maintaining a healthy and resilient intestinal mucosa is vital in order to uphold the balance between nutrient and water resorption via the small intestinal epithelium while simultaneously providing a strong line of defense against harmful substances or invading microorganisms. One way for a pathogen to gain entrance to its human host is to tag along with ingested food or water. Currently, the most prevalent foodborne pathogen is the Gram-negative Epsilonproteobacterium *C. jejuni* (Schielke *et al.*, 2014; Kaakoush *et al.*, 2015). This motile, helical bacterium lives as a commensal in livestock (*e.g.* cattle, sheep, pigs, and poultry), where it mainly resides in the mucus layer of the intestinal epithelium (Ogden *et al.*, 2009; Burnham & Hendrixson, 2018). In addition, *C. jejuni* reservoirs in contaminated water sources or improperly pasteurized/raw milk products can equally elicit an outbreak of campylobacteriosis (Korlath *et al.*, 1985; Jones, 2001; Clark *et al.*, 2003). A minute dose of approx. 800 bacterial CFUs is sufficient to cause infection in healthy individuals (Teunis *et al.*, 2005). Disease development in humans can range from mild to severe gastroenteritis with watery to bloody diarrhea. Although in the majority of cases the infection is self-limiting and resolves completely, a significant number of cases that presented with a preceding campylobacteriosis were followed by post-infectious sequelae. This includes for example inflammatory bowel disease (IBD) (García Rodríguez *et al.*, 2006) or secondary neuropathies such as the Guillain-Barré (GBS) or the Miller-Fisher syndrome (Yuki, 1997; Yuki & Miyatake, 1998; Ang *et al.*, 2002; Yuki *et al.*, 2004). However, so far little is known about *C. jejuni* pathogenicity and its genome sequence lacks homologs of dedicated virulence factors known from other enteric bacteria (Parkhill *et al.*, 2000; Young *et al.*, 2007; Gilbreath *et al.*, 2011). The vast majority of *C. jejuni* genes identified as necessary for the interaction with host cells are *e.g.* related to its motility (Guerry, 2007; Young *et al.*, 2007; Gao *et al.*, 2014), shape (Frirdich *et al.*, 2012, 2014; Stahl *et al.*, 2016), modification of surface structures (Karlyshev *et al.*, 2005; Howard *et al.*, 2009; Hitchen *et al.*, 2010; Zebian *et al.*, 2016), and metabolic factors (Hofreuter *et al.*, 2008; Liu *et al.*, 2012; Hofreuter, 2014; Gao *et al.*, 2017).

Thus, the following chapters are dedicated to explore the various unique aspects of *C. jejuni* biology that contribute to its successful lifestyle as an enteric pathogen in the human host.

1.2.1. General biological features contributing to *C. jejuni* virulence

While *C. jejuni* is thought to live primarily as an extracellular pathogen in the mucus layer or close to the mucosal epithelium of the lower intestinal tract, colonic biopsies from campylobacteriosis patients indicate that bacteria can invade human enterocytes (van Spreeuwel *et al.*, 1985). Once inside the host cell, the bacterium can reside inside a compartment called the *Campylobacter*-containing vacuole (CCV). As this compartment does not fuse to lysosomes and *C. jejuni* does not appear to use it as a replicative niche (Watson & Galán, 2008; Burnham & Hendrixson, 2018), the significance of the CCV has yet to be determined. Nonetheless, a strong correlation with virulence could be drawn for strains able to adhere to and get internalized into host cells or traverse polarized epithelial cell monolayers *in vitro* (Konkel & Joens, 1989; Brás & Ketley, 1999).

1.2.1.1. Phase-variable surface structures and morphology

Transition from a commensal existence in livestock to establishing colonization in the human intestine requires *C. jejuni* to rapidly adapt to these changing environments. Phase variation represents one proficient way to contribute to phenotypic heterogeneity within bacterial populations via high-frequent and stochastic reversible genotype switching (van der Woude, 2011). Very often, variable simple sequence repeats (SSRs) are a major source of phase variation in these contingency loci enabling rapid bacterial adaptation during changing conditions (Moxon *et al.*, 2006; Zhou *et al.*, 2014). Intragenic SSRs can cause frame-shift mutations or result in premature translation termination, while length variation of intergenic SSRs can influence transcription by *e.g.* changing the spacing of promoter elements or transcription factor binding sites. In *C. jejuni*, hypervariable regions are most often associated with genes coding for cell-surface structures such as lipooligosaccharide (LOS) or capsular polysaccharides (CPS) (Parkhill *et al.*, 2000). *In vitro* and *in vivo*, these loci are able to phase vary in order to generate diverse structures within a *C. jejuni* population to *e.g.* evade immune responses or increase/decrease host cell adhesion or internalization (Karlyshev *et al.*, 2002; Bayliss *et al.*, 2012; Kim *et al.*, 2012b; Mohawk *et al.*, 2014).

Most other enteric bacteria produce the high molecular weight, smooth form of lipopolysaccharide (LPS), whereas the outer membrane of *C. jejuni* is decorated with low molecular weight smooth LPS lacking *O*-polysaccharide chains termed LOS (Figure 1.5 A). The pathogenesis of some *C. jejuni* strains inducing GBS is thought to be based on the highly variable bacterial surface structures such as sialic acid-containing LOS (Moran, 1997; Szymanski *et al.*, 2003). Via a mechanism of molecular mimicry, those structures resemble ganglioside epitopes on human peripheral nerves leading to an autoimmune-driven destruction of nerves (Yuki, 1997; Ang *et al.*, 2002; Yuki *et al.*, 2004). In addition, swapping of LOS epitopes via a phase-variable ON/OFF switch of the LOS galactosyltransferase *cgtA* has been reported to confer increased serum resistance and invasion (Guerry *et al.*, 2002).

In addition to its phase-variable LOS surface structures, *C. jejuni* produces extracellular CPS (Karlyshev *et al.*, 2000) that can undergo ON/OFF phase variation (Holst Sørensen *et al.*, 2012). Via a lipid anchor, the polysaccharide backbone of the CPS is secured to the outer membrane. One hallmark of backbone modifications in the *C. jejuni* capsule is the expression of *O*-methyl phosphoramidate (MeOPN) (Figure 1.5 B) (Guerry *et al.*, 2012). While the CPS backbone, but not the MeOPN modifications, is necessary for commensal colonization (McNally *et al.*, 2007; van Alphen *et al.*, 2014), loss of MeOPN reduces serum resistance while simultaneously increasing bacterial invasion capacity (Maue *et al.*, 2013; van Alphen *et al.*, 2014; Pequegnat *et al.*, 2017).

As *C. jejuni* generally resides in the mucus layer overlaying the intestinal epithelium, its corkscrew-like shape is suggested to contribute to its successful enteric lifestyle and colonization of this particular niche (Burnham & Hendrixson, 2018). In addition, spiral morphology is postulated to contribute to a very fast motility especially in viscous environments (Ferrero & Lee, 1988; Shigematsu *et al.*, 1998). The helical shape is retained at least in part by the peptidoglycan (PG) layer in the periplasmic space. This is evidenced by studies showing that mutations of PG-modifying enzymes such as Pgp1 and Pgp2 lead to a rod-shaped morphology. While the change in morphology does not seem to impact *C. jejuni* interaction with host cells *in vitro*, it has been demonstrated that the straight cell body hinders the colonization potential of *C. jejuni in vivo* (Frirdich *et al.*, 2012, 2014; Stahl *et al.*, 2016).

1.2.1.2. The extraordinary multifunctional flagella apparatus

The seeming absence of virulence factors dedicated to penetrate the intestinal mucus layer in order to reach the underlying mucosal epithelium demands a very sophisticated motility system. In *C. jejuni*, this is mediated by its amphitrichous flagella that promote a very fast

darting motility by moving continuously back and forth, thereby increasing the probability of contact with host cells (Szymanski *et al.*, 1995; Shigematsu *et al.*, 1998). An extremely high level of torque for the flagellar rotation is provided by a perfectly evolved motor system, allowing the bacterial cells to reach velocities higher than 40 µm/s (Ferrero & Lee, 1988; Karim *et al.*, 1998). This in turn enables *C. jejuni* to be propelled through highly viscous environments such as the intestinal mucus, where other less powerful bacterial motility systems would simply fail. Such an extraordinary torque and velocity is owed to the incorporation of a relatively high number of stator complexes granting increasing power and force to the motor (Beeby *et al.*, 2016). The *C. jejuni* flagella filament is composed of the

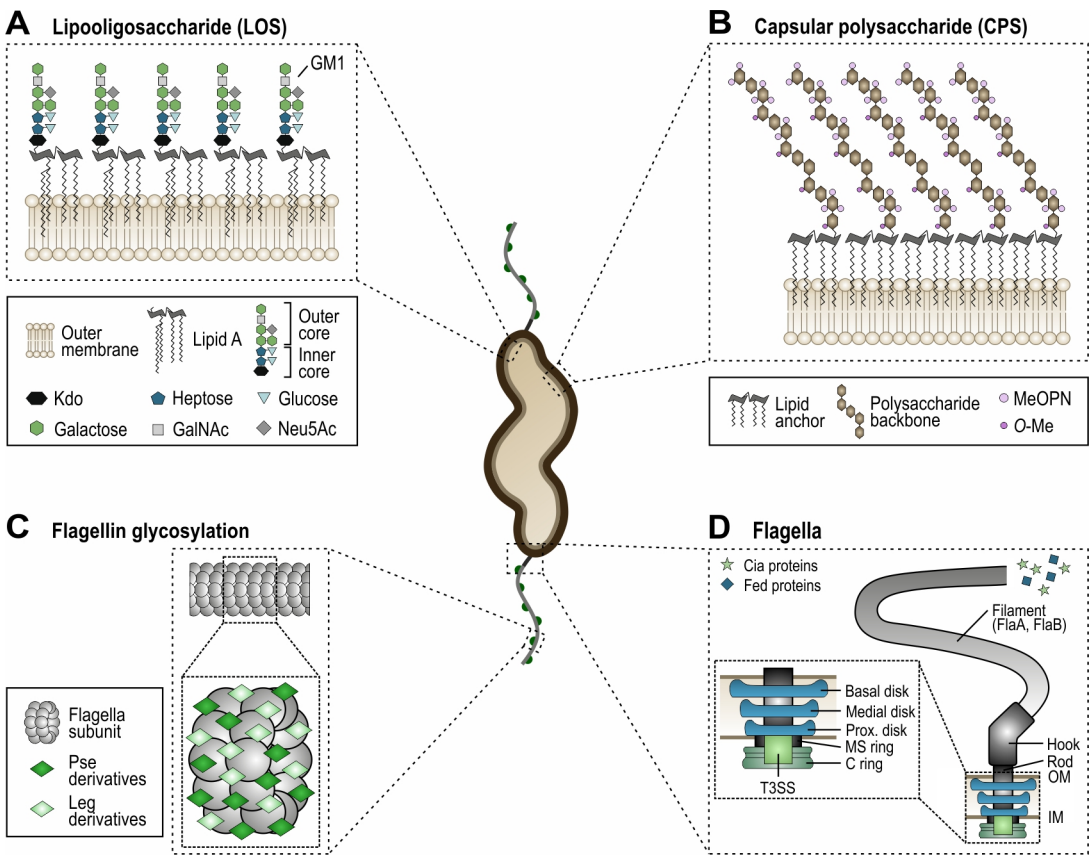

Figure 1.5: General biological aspects influencing *C. jejuni* pathogenesis. The center depicts the *C. jejuni* cell body with its characteristic helical shape and amphitrichous flagella. **(A)** In contrast to other enteric bacteria, *C. jejuni* produces lipooligosaccharide (LOS) structures. These structures mimic human ganglioside epitopes found on peripheral nerves and present associations of differently linked ketodeoxyoctonic acid (Kdo), Heptose, Glucose, Galactose, *N*-acetylgalactosamine (GalNAc), and *N*-acetylneuraminic acid (Neu5Ac). Depending on their linkage, they mimic a range of gangliosides with the here-presented GM1 as an example. **(B)** Attached via a lipid anchor to the outer membrane is the extracellular CPS of *C. jejuni*. The polysaccharide backbone is decorated with *e.g. O*-methyl phosphoramidate (MeOPN) or *O*-methyl (*O*-Me) groups. **(C)** Flagella subunits can be modified with pseudaminic acid (Pse) and its derivatives, as well as in some strains legionaminic acid (Leg) and its derivatives via *O*-linked flagellin glycosylation. **(D)** The multifunctional flagellum of *C. jejuni* is

equipped with a T3SS located in the inner membrane (IM), which is surrounded by an MS and a C ring structure (inlet). Cia and Fed effector proteins are secreted via this T3SS. The flagellum itself is composed of an extracellular filament (consisting of the major flagellin FlaA and the minor flagellin FlaB), anchored by a rod and a hook structure that cross the periplasm and outer membrane (OM). The flagellar rod in the periplasm is surrounded by three disk structures (basal, medial, and proximal), which incorporate a relatively high number of stator complexes into the motor granting an extremely high torque to the *C. jejuni* flagellum.

major flagellin FlaA and the minor flagellin FlaB (Guerry *et al.*, 1991). Whereas deletion of *flaA* leads to an almost complete loss of motility owing to a truncated flagella filament, deletion of the minor flagellin does not seem to greatly impact flagella structure or motility itself (Guerry *et al.*, 1991; Wassenaar *et al.*, 1991). Many studies have quite unanimously demonstrated that mutations of genes required for *C. jejuni* motility result in defective interactions with host cells *in vitro* and *in vivo* (Yao *et al.*, 1994; Hendrixson & DiRita, 2004; Guerry, 2007; Young *et al.*, 2007; Gao *et al.*, 2014; de Vries *et al.*, 2017a, 2017b; Burnham & Hendrixson, 2018). In addition to its role in motility, the extracellular flagella filament is also thought to mediate a direct adhesion to host cells (Guerry, 2007) as *C. jejuni* does not produce pili structures (Gaynor *et al.*, 2001), which are generally responsible for facilitating an initial contact between bacterium and host cell. A role for a flagella-mediated adhesion process is supported by an *O*-linked protein glycosylation system that specifically modifies flagellins (Figure 1.5 C) (Thibault *et al.*, 2001; McNally *et al.*, 2006). Whereas these modifications with pseudaminic or legionaminic acid derivatives are essential for correct filament polymerization and thus motility, in the absence of a toll-like receptor 5 (TLR5) subdomain (Andersen-Nissen *et al.*, 2005), they seem to be directly contributing to host-pathogen interactions (Goon *et al.*, 2003; Howard *et al.*, 2009; Ulasi *et al.*, 2015; Zebian *et al.*, 2016).

The extracellular flagella filament is anchored through the hook and rod structure that cross the outer membrane and periplasm. Located in the inner membrane is a flagellar type III secretion system (T3SS) surrounded by the MS and C ring rotor complex, composed of the motor switch proteins FliF and FliG, respectively (Figure 1.5 D) (Boll & Hendrixson, 2013). The *C. jejuni* T3SS is not only tasked with secretion of flagellar components but seems to moonlight as a secretion apparatus of other bacterial peptides such as the *Campylobacter* invasion antigen (Cia) proteins (Konkel *et al.*, 1999, 2004) or the flagella co-expressed determinant (Fed) proteins (Barrero-Tobon & Hendrixson, 2012). Even tough it has been reported that both the Cia and Fed proteins are involved in mammalian and commensal colonization, respectively, the precise mechanism by which they exert their function remains unknown (Konkel *et al.*, 1999; Christensen *et al.*, 2009; Buelow *et al.*, 2011; Barrero-Tobon & Hendrixson, 2012, 2014).

In addition to its role in motility and secretory activity, the *C. jejuni* flagellum is also equipped with a chemotaxis system to navigate the bacterial cell towards the most beneficial niche in the lower intestinal tract of the host (Hugdahl *et al.*, 1988; Lertsethtakarn *et al.*, 2011). The chemotaxis machinery, including the methyl-accepting chemotaxis proteins (MCP), allows directional movement towards chemoattractants such as galactose (Day *et al.*, 2016), fucose (Dwivedi *et al.*, 2016), pyruvate and fumarate (Hendrixson *et al.*, 2001), aspartate (Hartley-Tassell *et al.*, 2010), formate (Tareen *et al.*, 2010), lactate, and chicken mucus (Vegge *et al.*, 2009). In addition, *C. jejuni* exhibits energy taxis mediated by a bipartite energy system, which possesses structural similarities to the *Escherichia coli* (*E. coli*) energy taxis receptor Aer (Elliott & Dirita, 2008).

With its multitasking flagella, *C. jejuni* gains a powerful tool, whose contribution to colonization and pathogenesis goes far beyond simple motility or chemotaxis.

1.2.1.3. Unique metabolic adaptations to an enteric lifestyle

In lieu of the variable environments *C. jejuni* is comfortable colonizing, it has evolved well-adapted metabolic pathways. As a commensal in the intestinal tract of avian species, a temperature of 42 °C exerts no thermal stress on this zoonotic bacterium. Contrary to other enteric facultative anaerobic pathogens, *C. jejuni* is obligate microaerophilic requiring a certain amount of oxygen (O_2) mainly for its oxygen-dependent ribonucleotide reductase (Sellars *et al.*, 2002). As O_2 conditions in the gut lumen are detrimental for its growth, residence in the mucus layer or relatively close to the mucosal epithelium provides optimal oxygen conditions for the bacterium to thrive (Krieg & Hoffman, 1986; Lee *et al.*, 1986; Beery *et al.*, 1988). *C. jejuni* has a very narrow range of carbon sources and is incapable of catabolizing glucose, setting it apart from many other gastrointestinal pathogens (Dandekar *et al.*, 2012; Fuchs *et al.*, 2012). While only a few isolates are able to utilize fucose (Stahl *et al.*, 2011), its preferred niche in the host provides amino acids essential for *in-vivo* growth such as serine, aspartate, asparagine, glutamine, glutamate, and proline (Ahlman *et al.*, 1993; Velayudhan *et al.*, 2004). Many more metabolic aspects of the *C. jejuni* lifestyle, including but not limited to its restricted carbohydrate catabolism and the remarkable respiratory reprogramming when residing inside host cells, have been proposed to enhance bacterial viability *in vitro* and *in vivo* (Hofreuter, 2014; Gao *et al.*, 2017).

1.2.2. Dedicated pathogenicity-determining factors of *C. jejuni*

The *C. jejuni* chromosome (1.6 Mbp) seems to be largely devoid of pathogenicity islands or dedicated secretion systems known from other enteric pathogens (Parkhill *et al.*, 2000). However, many studies have suggested various factors to directly mediate pathogenesis-promoting processes such as adhesion, internalization, transmigration, or immune evasion. Surface-exposed proteins such as CadF and FlpA are implicated in facilitating adhesion through putative interaction with fibronectin (Figure 1.6 I) (Monteville *et al.*, 2003; Flanagan *et al.*, 2009; Konkel *et al.*, 2010). The JlpA lipoprotein is similarly connected to directly convey association with the host cell surface *in vitro* and *in vivo* (Figure 1.6 I) (Jin *et al.*, 2001). However, no specific host receptor could thus far be identified for these putative *C. jejuni* adhesins. Many conflicting studies exist regarding the internalization process of

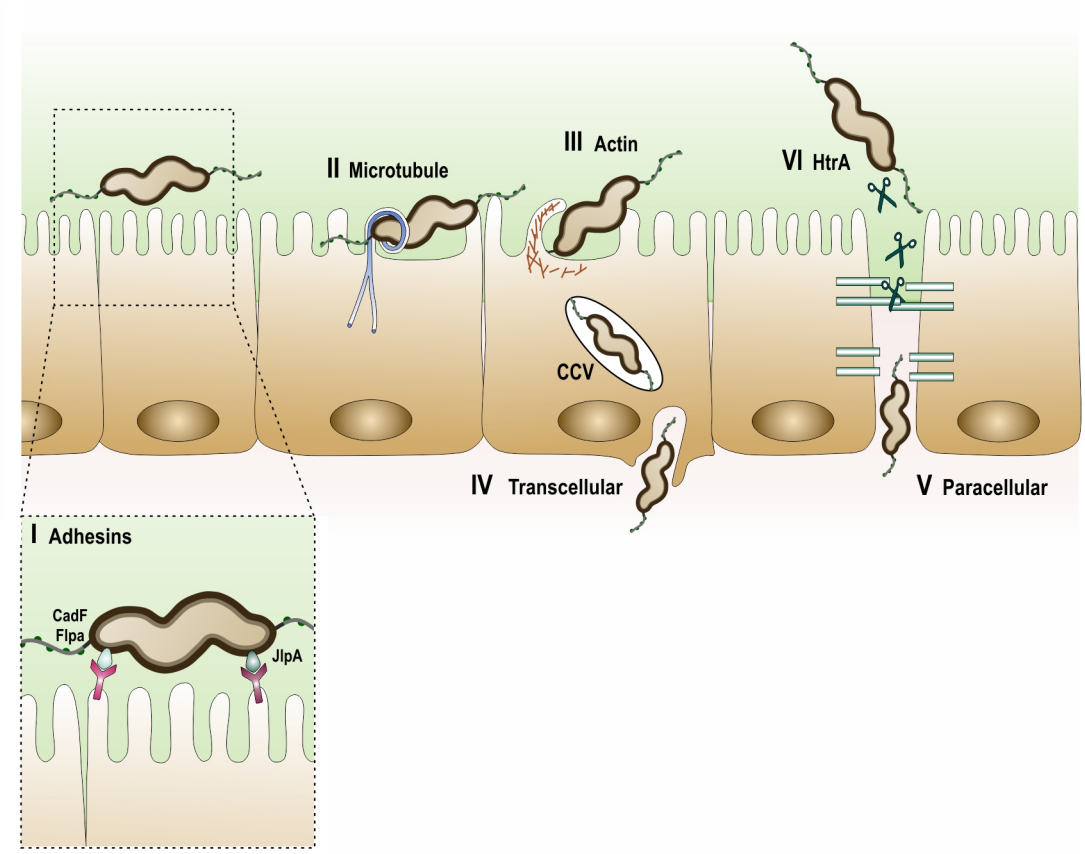

Figure 1.6: Dedicated putative virulence factors of *C. jejuni*. Putative adhesins such as CadF, FlpA, or JlpA have been proposed to influence adherence of *C. jejuni* to host cells **(I)**. Once attached to the eukaryotic cell, the bacterial invasion process can potentially involve host cell protrusions formed by microtubules **(II)** or actin filaments **(III)**. In order to reach the submucosal space, *C. jejuni* needs to traverse the intestinal epithelial barrier. Migrating transcellularly **(IV)** involves bacterial internalization on the apical cell surface, intracellular survival in the *Campylobacter* containing vacuole (CCV), and exiting the host cell on the basolateral side. Paracellular migration **(V)** across the

mucosa requires the disruption of epithelial cell-cell junctions. The serine protease HtrA **(VI)** has been previously implicated in this process by cleaving the AJ protein homodimer E-cadherin (Backert *et al.*, 2013) and the TJ protein occludin (Harrer *et al.*, 2019).

C. jejuni. So far, evidence for both microtubule-/actin-dependent and -independent uptake mechanisms into host cells was presented (Figure 1.6 II and III) (Oelschlaeger *et al.*, 1993; Hu & Kopecko, 1999; Biswas *et al.*, 2003; Watson & Galán, 2008). Similarly undetermined, the route of transmigration across the intestinal barrier has been proposed to be paracellular, transcellular, or both (Figure 1.6 IV and V) with several factors *e.g.* the serine protease HtrA (Figure 1.6 VI) directly or indirectly involved in the process (Backert *et al.*, 2013; Harrer *et al.*, 2019). One common denominator to other enteric pathogens is the production of an enterotoxin among *Campylobacter* species. The *C. jejuni* genome codes for the cytolethal distending toxin (CDT), an AB2 type toxin causing DNA damage and subsequently cell cycle arrest (Whitehouse *et al.*, 1998; Lara-Tejero & Galán, 2000, 2001). While CDT has been proposed to contribute to colonization, systemic spread, inflammation, or even promotion of colorectal tumorigenesis (Purdy *et al.*, 2000; Fox *et al.*, 2004; He *et al.*, 2019), the presence of the toxin-encoding genes does not solely determine the severity of the clinical outcome (Abuoun *et al.*, 2005; Mortensen *et al.*, 2011).

Taken together, in the absence of dedicated virulence factors, *C. jejuni* has evolved into a very unique enteric pathogen. Among few committed adhesins and the enterotoxin CDT, its specific arsenal of colonization- and disease-contributing factors includes highly variable LOS and CPS surface structures, an amino acid-based metabolism, and most importantly a powerful multitasking flagellum.

1.3. Current and novel gastrointestinal infection models to study virulence strategies of gut pathogens

The controversies and divergences in the above-described infection studies stem in large part from the immense genomic heterogeneity in *C. jejuni* strains and isolates used in different laboratories. Acquiring an expanded understanding of bacterial factors involved in *C. jejuni* disease-promoting mechanisms and thus ultimately advancing the development of antibiotics, therapeutics, or vaccines is partially hampered by the large intra-strain diversity. Additionally, the choice of model system to study host-pathogen interactions can influence the pathogenic phenotypes observed during infection. Both *in-vitro* cell culture and *in-vivo* animal models have been fundamental in deciphering the molecular mechanisms

underlying pathogenesis and immune response elicited by gastrointestinal pathogens. Yet, results obtained from animal studies are not easily transferable to human patients. Furthermore, 2D cell culture models lack *in-vivo* tissue complexity limiting the discernible interactions between pathogen and host.

1.3.1. *In-vivo* animal models

To follow virulence strategies of intestinal pathogens as close to the human host as possible, small animal models such as mice are most often the infection system of choice. They offer an all-encompassing environment starting from the natural route of infection to the exceptional anatomy and physiology of the GIT including the host's innate immune system. While animal models remain essential to the understanding of fundamental host cell changes elicited by the pathogen, they also present certain limitations. Notably, these models are very costly, not easily established in every lab, and afflicted with ethical drawbacks. In addition, many human enteric pathogens exhibit a limited host-range including *e.g. Salmonella* Typhi and Paratyphi A, *Shigella*, or attaching and effacing lesions-forming enteropathogenic *E. coli* (EPEC) and enterohemorrhagic *E. coli* (EHEC) (McClelland *et al.*, 2004; Kang *et al.*, 2018). For example, the only known natural host of *Shigella* spp. is the intestinal tract of primates and humans. So far, there is no ideal small animal model to mimic symptoms of shigellosis (Kang *et al.*, 2018). Furthermore, infection studies with the human-specific gastric pathogen *H. pylori* are most commonly conducted in mice or Mongolian gerbils. In humans, chronic infection with this bacterium can cause gastric ulcers and even gastric cancer (Wroblewski *et al.*, 2010; Salama *et al.*, 2013). However, the clinical outcome of *H. pylori* infection in mice is usually a mild gastritis that does not further progress to ulceration or cancer (O'Rourke & Lee, 2003; Solnick *et al.*, 2016a). In Mongolian gerbils, some *H. pylori* strains are able to elicit cancerous lesions and tumor formation. Unfortunately, these animals are outbred and reagents and tools for genetic manipulation are severely limited (O'Rourke & Lee, 2003; Solnick *et al.*, 2016b).

Along the same line, *in-vivo* analysis of campylobacteriosis is hampered by the fact that *C. jejuni* only readily colonizes avian species as a commensal. Even though colonization levels are high in the chicken intestine, there is no inflammatory response or disease progression and thus, examining human clinical symptoms elicited by this pathogen is simply not possible (Young *et al.*, 2007). The use of mouse models to study *C. jejuni* pathogenesis has lagged behind, since most mouse strains are not susceptible to efficient *Campylobacter* colonization (Bereswill *et al.*, 2011). This colonization resistance is thought to result from competition between *C. jejuni* and the mouse intestinal microbiota (Bereswill

et al., 2011; Stahl *et al.*, 2017). Thus, scientists have focused on the development of novel mouse models, where the murine microbiota was depleted or otherwise modified (Figure 1.7 A). In this case, microbial depletion by antibiotics confers an increased susceptibility to enteric pathogens allowing them to replicate to high numbers in the GIT (Kampmann *et al.*, 2016). For example, *C. jejuni* readily colonizes germ-free mice (Chang & Miller, 2006), adult mice with an eradicated (Bereswill *et al.*, 2011) or antibiotic-depleted microbiota (Stahl *et al.*, 2014), gnotobiotic mice reassociated with a human intestinal microbiota (Bereswill *et al.*, 2011), or conventional infant mice (Haag *et al.*, 2012a; Heimesaat *et al.*, 2013, 2014). Yet, even if the murine intestine is effectively colonized by *C. jejuni*, it rarely shows significant indications of disease. To overcome this obstacle, genetic manipulation in addition to depletion of the murine microbiota is necessary to elicit signs of inflammation and colitis. Earlier models focused on interleukin-10 (IL-10) deficient mice, which developed a non self-limiting acute ulcerative colitis with bloody diarrhea upon *C. jejuni* infection, mimicking key features of campylobacteriosis in immunocompromised patients (Mansfield *et al.*, 2007; Haag *et al.*, 2012b). More recently, it was shown that microbiota-depleted mice deficient for the Single IgG IL-1 Related Receptor (SIGIRR), an inhibitor of MyD88-dependent signaling, exhibited severe gastroenteritis upon infection with *C. jejuni* (Stahl *et al.*, 2014; Stahl & Vallance, 2015). All of the above-described criteria are inherently critical to consider when translating the obtained findings into the human host, as animal models may not always faithfully recapitulate pathogen-induced disease progression in humans.

1.3.2. *Ex-vivo* organ cultures

The GIT is a highly organized and inherently complex organ making it tremendously demanding to model all its properties *in vitro*. *Ex-vivo* organ cultures of freshly excised tissue (Figure 1.7 B) can provide the opportunity to study host-pathogen interactions in a physiologically relevant *in-vivo* environment due to the preserved multicellular microarchitecture (Frost *et al.*, 1997; Haque *et al.*, 2004; Grant *et al.*, 2006; Tsilingiri *et al.*, 2012). These tissue explants can then simply be placed in multi-well plates, mounted with culture medium, and subsequently infected with bacterial pathogens (Figure 1.7 B-I). Inoculation with bacterial cells on top of the tissue sample allows contact to the mucosal cell surface but also grants access to the submucosal space as no strict separation of apical and basolateral side occurs by way of this culture system (Hicks *et al.*, 1996).

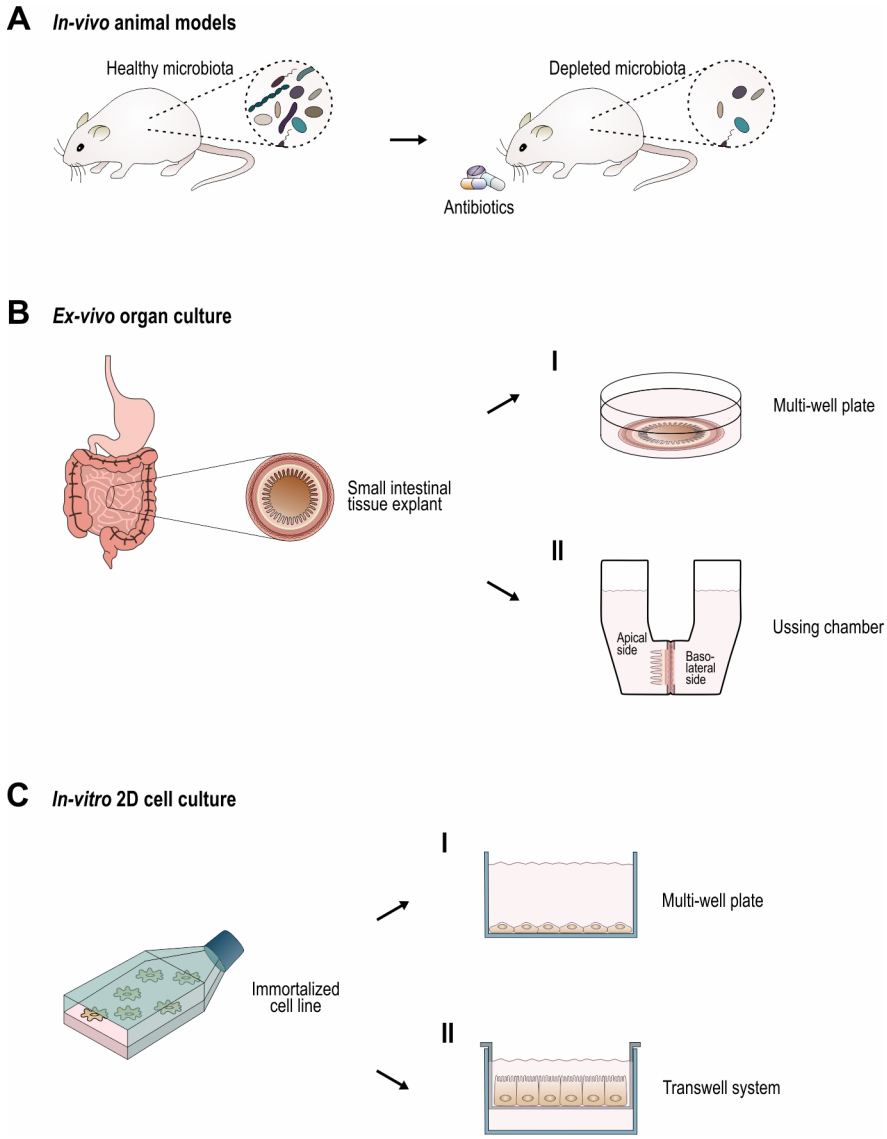

Figure 1.7: Current infection models to study virulence of gastrointestinal pathogens. (A) *In-vivo* animal models such as laboratory mice represent a comprehensive infection system to study many aspects of host-pathogen interactions. Due to the different composition of the intestinal microbiota in human and mice, most often antibiotic treatment is required to deplete the microbiome load or certain species to allow colonization of the GIT by the pathogen to be studied. **(B)** A very inclusive human alternative to animal models is *ex-vivo* organ cultures. Freshly excised tissue includes the characteristic architecture of the small intestinal mucosa composed of the various cell types present in the epithelium. For convenience, the tissue explants can be placed in multi-well plates **(I)** to allow infection with the pathogen of choice from the apical site. Fixing the tissue explant inside an Ussing chamber **(II)** separates the apical from the basolateral mucosal surface. Post infection, this allows for quantitative analysis of host characteristics such as barrier integrity via transepithelial electrical resistance (TER) measurements or transport studies in addition to quantification of adhered, internalized, or transmigrated bacteria. **(C)** *In-vitro* 2D cell culture allows for simple propagation of immortalized cell lines with subsequent seeding into multi-well plates **(I)**. While this grants easy access for infecting bacteria, cells in multi-well plates lack many important characteristics of *in-vivo* tissue such as an apical-basolateral polarization, extracellular matrix components, or a basolateral compartment to name just a few. Cultivation and differentiation in

Transwell systems **(II)** can produce a certain degree of epithelial polarization in a small subset of cell lines as well as mucus production in an even smaller subset of cells.

The Ussing chamber is a promising tool to utilize tissue explants for functional studies (Figure 1.7 B-II). In this technical device, originally developed by Hans Ussing (Ussing, 1949), intestinal mucosa and submucosa are separated via two temperature-controlled chambers, filled with physiological buffer or media. This way, the apical and basolateral side of the tissue explant each contain their own compartments. Bacterial cells can then be introduced into the apical chamber, albeit for a limited amount of time, to study adherence and/or invasion (Worton *et al.*, 1989), transmigration across (Albanese *et al.*, 1994; Kurkchubasche *et al.*, 1998), or immune response by the intestinal epithelium (Grotz *et al.*, 1999). Moreover, this set-up enables transport studies and monitoring of intestinal barrier integrity via installed electrodes (Grotz *et al.*, 1999). An enormous challenge of *ex-vivo* models however remains the extremely short lifespan of these complex tissues due to an inability to revascularize the tissue post excision, prohibiting a sufficient nutrient supply. In the Ussing chamber, human intestinal mucosal biopsies might be viable for up to 24 hours (Browning & Trier, 1969). While *ex-vivo* organ cultures offer an *in-vitro* system holding *in-vivo* multicellular complexity and architecture, human tissue samples are not at all readily available, limiting the study of host-pathogen interactions with these model systems to explants of laboratory animals.

1.3.3. *In-vitro* cell culture models

Alternatively, studies of host-pathogen interactions are most often facilitated by *in-vitro* 2D cell culture assays, in which immortalized cell lines are grown as monolayers on solid, impermeable surfaces and infected with the pathogen of interest. In comparison to animal models, *in-vitro* cell culture models are cost effective, readily accessible and allow experimental flexibility. These infection systems have greatly contributed and continue to contribute to our understanding of basic host-pathogen interactions. Whereas animal models provide a holistic approach to study the onset and progression of infectious diseases, bottom-up development of *in-vitro* infection systems allows the experimental analysis of pathogenicity-determining process with increasing complexity. These *in-vitro* models can range from simple cell line-based monolayer cultures on impermeable surface structures, to a whole continuum of 3D cell culture systems covering a collection of progressively complex experimental models.

1.3.3.1. 2D monolayer systems

Most often, virulence strategies of pathogenic bacteria are studied in cell line-based *in-vitro* 2D monolayer cultures (Figure 1.7 C-I). Immortalized gastrointestinal cell lines can simply be seeded into multi-well plates and subsequently infected with pathogenic bacteria, allowing easily achievable readouts on both the host and the pathogen side. These include for example assessment of adherence, invasion, survival, and replication capabilities of the bacteria in addition to determining host cell components involved in these processes as well as immune responses elicited by the microbes (Bergmann & Steinert, 2015). Compared to animal models, 2D *in-vitro* cell culture experiments are cost effective, allow experimental flexibility, and can be used in high throughput. Together with the continuing advancement in microscopic imaging techniques, genetic manipulation, as well as biochemical and immunologic tools, these model systems have greatly advanced the discovery and understanding of principle mechanisms of host-pathogen interactions (Barrila *et al.*, 2018). However, 2D cell culture models lack key properties of *in-vivo* 3D human tissue making it difficult to correlate *in-vitro* and *in-vivo* host responses or pathogenic processes. For instance, cells cultured in 2D monolayers generally do not achieve the 3D architecture of parental tissue in part owing to the lacking interaction with ECM proteins (Abbott, 2003; Schmeichel & Bissell, 2003; Zhang, 2004; Nickerson *et al.*, 2007). As a result of this, they do not display biochemically distinct polarity and therefore lack the potential to respond to chemical and molecular gradients in three dimensions (apical, basal, and lateral) (Zhang, 2004). As described in chapter 1.1, most often the first line of defense against invading microorganisms is the thick mucus layer protecting the underlying epithelium by trapping bacterial pathogens in the viscous gel and clearing them during mucus turnover and gut movement. Thus, it should ideally be possible for an *in-vitro* infection model to also include a mucus layer in order to mimic the route of bacteria towards mucosal epithelial surfaces. It has become increasingly evident that this “flat biology” approach lacks key phenotypic and functional characteristics of native organ-specific tissue and is thus poorly predictive of *in-vivo* host responses to invading pathogens (Abbott, 2003; Nickerson *et al.*, 2004, 2007).

The general lack of cell polarization and mucus production in 2D systems can partially be overcome in Transwell-based cell culture models, in which the cells are cultivated on a porous membrane, effectively allowing the cells to develop apical-basolateral polarity, to form cell-cell junctions, and to produce varying degrees of mucus (Figure 1.7 C-II) (Birkness *et al.*, 1995; Navabi *et al.*, 2013). These systems have been successfully used to study for example paracellular and transcellular migration of pathogens over an epithelial barrier (Konkel *et al.*, 1992; Boehm *et al.*, 2012, 2015; Louwen *et al.*, 2012; Backert *et al.*,

2013), loss of barrier function during infection (MacCallum *et al.*, 2005; Chen *et al.*, 2006; Wine *et al.*, 2008; Boehm *et al.*, 2012, 2015), and interaction of pathogens with mucins (Alemka *et al.*, 2010). The use of such Transwell-based cell culture models has been remarkably demonstrated in *H. pylori* research. Using these systems, it could be shown that injection of its major virulence factor CagA leads to disruption of cell-cell junctions (Amieva *et al.*, 2003) and ultimately assists the bacteria in forming microcolonies by altering host cell polarity and facilitating iron acquisition from host cells (Tan *et al.*, 2009, 2011). Nevertheless, *in-vitro* cell culture models based on the Transwell system still lack the three-dimensionality of intact tissue as well as cell-ECM interactions.

1.3.3.2. 3D intestinal tissue models

In order to counteract human disease elicited by gastrointestinal pathogens such as *Shigella* spp. or *C. jejuni*, for which no physiologically relevant small animal model is available, it is vital to study their interactions with and the response of the host in an environment reflective of their natural intestinal niche. Furthermore, as *C. jejuni* lives mostly extracellular in the mucus layer close the mucosal cell surface, its human host environment cannot be easily recapitulated *in vitro* without the presence of extracellular matrix, polarized cell-surface molecules, a 3D tissue architecture, and a mucosa-covering mucus layer. Advanced *in-vitro* cell culture models mimicking complex phenotypic characteristics of *in-vivo* tissue seem ideal to examine cellular interactions of the mucosal epithelium with these pathogenic bacteria. In fact, several studies could already show that 3D cell culture models compared to the same cells grown in a 2D system were more reminiscent of their respective native tissue. Moreover, these tissue models when infected with different microbial pathogens, elicited a response reflecting the *in-vivo* infection process (Nickerson *et al.*, 2001, 2004; Carterson *et al.*, 2005; Höner zu Bentrup *et al.*, 2006; Smith *et al.*, 2006; Straub *et al.*, 2007).

1.3.3.2.1. Gastrointestinal organoid culture

In the last decades, a wide variety of techniques such as 3D culture, organotypic culture, and organoid culture has been developed using a range of culture systems to recapitulate the multicellular organization and the 3D architecture of native tissue. One approach combining lineage-specific differentiated cell types with tissue-of-origin-determined morphology is organoid culture (Figure 1.8 A) (Dutta & Clevers, 2017). These can be expanded from primary cells freshly isolated from mammalian tissues, from embryonic stem cells (ESC), or

from induced pluripotent stem cells (iPSC) (D'Amour *et al.*, 2005; Sato *et al.*, 2009, 2011; Clevers, 2016). For example, Sato and colleagues showed that intestinal LGR5-positive stem cells properly stimulated by external cues recreate the villus-crypt architecture of the small intestine when cultivated in a structural 3D environment. These organoids displayed a highly polarized, multicellular epithelium consisting of key intestinal cell types such as enterocytes, goblet cells, Paneth cells, and enteroendocrine cells (Sato *et al.*, 2009). This is a key advantage of organoid cultures regarding infection research, as they can account for potential host cell tropisms of pathogens. Thus, gastrointestinal 3D organoids have been employed to study a wide variety of bacterial and viral pathogens including for example *C. difficile* (Engevik *et al.*, 2015; Tao *et al.*, 2016), *Salmonella* (Zhang *et al.*, 2014; Forbester *et al.*, 2015; Nickerson *et al.*, 2018), norovirus (Ettayebi *et al.*, 2016; Zhang *et al.*, 2017), or enteroviruses (Drummond *et al.*, 2017).

Gastric organoids grown from surgical samples of human corpus tissue have already been successfully applied for microarray studies of the global epithelial response to infection with the gastric pathogen *H. pylori* (Bartfeld *et al.*, 2015). However, this infection study like many others (Zhang *et al.*, 2014; Engevik *et al.*, 2015; Sigal *et al.*, 2015) mainly focused on the host side of the infection process and did not address quantitative assessment of bacterial adherence, invasion, transmigration, or pathogen-induced disruption of epithelial barrier function. This might be a result of the "basal-out" manner, in which organoids generally grow when suspended in Matrigel (Figure 1.8 A-I). When considering the GIT as the source of cells, these multicellular structures grow as closed, spherical complexes with their apical surface facing the inside of the sphere. This in turn causes intestinal crypts or gastric pits to protrude outwards allowing access to the crypt lumen only from inside of the sphere. The organization as such poses a challenge to deliver the infecting bacteria into the lumen from outside the organoid. Infection studies with gastrointestinal pathogens have thus employed microinjection of bacterial cells into the lumen in order to take the normal infection route into consideration. This way, interactions of the pathogen with the apical host cell surface or the overlying mucus layer can be observed (Figure 1.8 A-I) (Forbester *et al.*, 2015; Wilson *et al.*, 2015; Barrila *et al.*, 2018). While this has been demonstrated to be mechanistically feasible without causing extensive damage to the organoid itself (Bartfeld & Clevers, 2015; Dutta & Clevers, 2017), it still remains a laborious task and it is impractical to infect every single organoid in one drop of Matrigel. Moreover, this technique is not at all easily achievable for every lab (Schlaermann *et al.*, 2016).

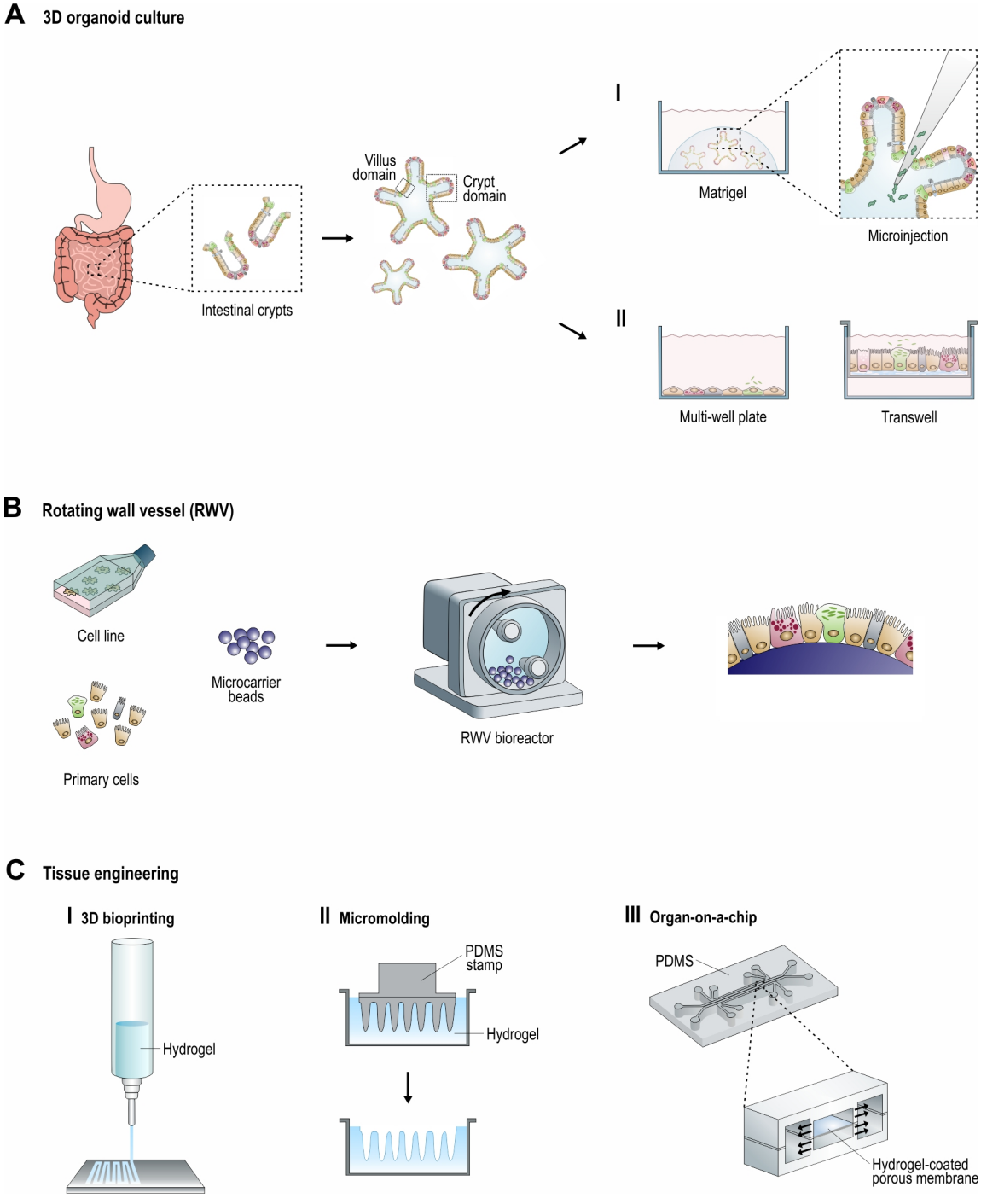

Figure 1.8: Approaches to generate 3D *in-vitro* tissue models. (A) Organoid cultures can be generated from adult tissue biopsies from specific compartments such as intestinal crypts. As these crypts harbor LGR5-positive stem cells, they will expand into organoid cultures with intestinal architecture and fully differentiated cell types, given the proper environment of growth factors and extracellular matrix substitutes such as Matrigel. These closed, sphere-like structures generate protrusions into the outside medium representing intestinal crypt structures with the connecting regions resembling villi areas of the small intestine. Thus, the gut lumen would be represented by the enclosed space of these organoids. In order to utilize organoid cultures for infection purposes, pathogenic microorganisms can be introduced via microinjection **(I)**, a laborious and technically challenging procedure. By disrupting the organoid structures, single cells can be seeded into multi-

well or collagen-coated Transwell systems **(II)**, granting easy access for subsequent infection studies. While maintaining a mixture of cellular intestinal subtypes, this technique leads to the loss of the characteristic 3D architecture. **(B)** The rotating wall vessel technology enables the growth of immortalized cell lines or human primary cells on porous microcarrier beads in a specially designed bioreactor system. Cultivation during rotation affects differentiation of cells due to spacial orientation and subsequent infection can either be performed directly in the bioreactor or more conveniently in multi-well plates after cellular differentiation. **(C)** Tissue engineering approaches most often include the reseeding of primary cells or cell lines on three-dimensional scaffolds. 3D bioprinting **(I)** or micromolding **(II)** of various hydrogel compositions can either result in random 3D mesh networks or pre-designed architectural scaffolds. One limitation of these processes is the resolution by which scaffolding structures can be designed, which is not always sufficient for recreating *in-vivo* architecture. Organ-on-a-chip technologies **(III)** represent micromodels of the smallest organ unit possible. The creation of microfluidic channels by flexible and porous polydimethylsiloxane (PDMS) membranes enables the establishment of tissue barriers when reseeded with human cell lines or even primary cells. Both the medium perfusion of the channels and the application of cyclic strain (indicated by the outward facing black arrows) can strengthen the differentiation of the growing tissue layers.

To circumvent the challenges associated with microinjection, organoid cultures can be dissociated into single cells and grown as monolayers either in conventional multi-well plates or on Matrigel-/collagen-coated Transwells (Figure 1.8 A-II) (Ettayebi *et al.*, 2016; In *et al.*, 2016; Schlaermann *et al.*, 2016; Noel *et al.*, 2017; Boccellato *et al.*, 2018). This methodology facilitates access to the apical host cell surface for infecting pathogens, and by use of the Transwell system enables assessment of the epithelial barrier as well as easy sampling of cytokines or signaling molecules released into the apical supernatant. However, it comes at the price of losing the definitive organ-specific 3D microarchitecture. Moreover, organoids are generally grown in a static environment, which does not provide biomechanical stimuli such as shear stress, which is thought to induce essential developmental cues for the cells *in vivo* (Basson, 2003).

1.3.3.2.2. 3D organotypic tissue grown in the rotating wall vessel bioreactor

The rotating wall vessel (RWV) technology incorporates low fluid shear into its suspension culture conditions resulting in 3D organotypic models that regain many key features of *in-vivo* tissue (Figure 1.8 B) (Barrila *et al.*, 2010). Initially designed by the National Aeronautics and Space Administration (NASA), the RWV bioreactor is an optimized form of suspension culture enabling the observation of host cells and pathogen in a 3D environment (Unsworth & Lelkes, 1998; Lin *et al.*, 2008). First grown as conventional monolayers, host cells of choice are then co-incubated with porous ECM-coated microcarrier beads. Subsequently, these cell-bead complexes are introduced into the rotating bioreactor, where they develop

into polarized epithelial structures (Figure 1.8 B). Complexity and developmental time of the bead cultures is dependent on the initial type of host cells and can take up to 32 days after co-incubation of host cells and beads (Nickerson *et al.*, 2001; Carterson *et al.*, 2005; Barrila *et al.*, 2010). Afterwards, these RWV models can be infected by directly adding the bacterial or viral pathogen into the rotating bioreactor or alternatively, by harvesting the tissue-beads into multi-well plates and subsequent infection in this more convenient format. Due to the porous nature of the beads, the attached cells can respond to chemical and molecular gradients in three dimensions. This enables a high degree of cellular polarization visualized by highly localized junctional and brush border proteins (Nickerson *et al.*, 2001; Carvalho *et al.*, 2005; Höner zu Bentrup *et al.*, 2006).

Supporting the usefulness of 3D tissue models in bacterial infection research was impressively demonstrated for the application of the RWV technology to investigate pathogenesis of *Salmonella*. Previous research has indicated that invasion of the intestinal epithelium is vital for *Salmonella* virulence and that this process is dependent on a functional pathogenicity island-1 (SPI-1) (Zhou & Galán, 2001). However, animal infection studies revealed that *Salmonella* is still able to invade and elicit gastrointestinal symptoms even in the absence of SPI-1 (Murray & Lee, 2000; Hurley & McCormick, 2003) and a human outbreak of *Salmonella enterica* subsp. *enterica* serovar Senftenberg lacking SPI-1 supported these observations (Hu *et al.*, 2008). Using the RWV technology, it could be demonstrated *in vitro* that a *Salmonella* strain deficient for a functional SPI-1 could easily invade the 3D reconstructed colonic epithelium (Höner zu Bentrup *et al.*, 2006). This was the first time that an *in-vitro* intestinal tissue model was able to demonstrate a bacterial virulence phenotype generally only observed *in vivo*, stressing the importance for three-dimensionality of tissues to study host-pathogen interactions.

1.3.3.2.3. Tissue engineering technologies

Among many 3D cell culture approaches, tissue engineering represents a biology-driven approach to *in-vitro* engineer complex 3D tissue models harboring the microenvironment of human organs (Figure 1.8 C). As an interdisciplinary combination of engineering, material sciences, medical, chemical, and biological skills, tissue engineering offers the chance to mimic human physiology by creating complex *in-vitro* tissue substitutes harboring essential morphological, chemical, and mechanical properties (Griffith & Swartz, 2006). Similar to other 3D cell culture systems, the technique is driven by the concept that tissue proliferation and homeostasis rely on precisely controlled signals in a distinct spatial and temporal organization. Employed for a variety of applications, including infection biology

(Höner zu Bentrup *et al.*, 2006; Crabbé *et al.*, 2014; Kim *et al.*, 2014; Barrila *et al.*, 2017; DeCicco RePass *et al.*, 2017; Tezera *et al.*, 2017), tissue engineering most often combines the structure of a supporting scaffold with a variety of mammalian cells in order to mimic the 3D environment of the respective native organ. An important factor to promote and support this cellular differentiation into mature tissue is by mechanical stimulation typically experienced by the cells in their native upbringing. Individual cells integrate many external cues including mechanical forces to generate their differentiated phenotype and react to perturbations in their immediate and distant environment (Griffith & Swartz, 2006).

Anatomic complexity can be provided with engineered biomaterial microenvironments as supporting constructs for later-on seeded cells. Such auxiliary structures can for example be produced by 3D bioprinting (Figure 1.8 C-I), which is a relatively recent manufacturing technique in order to build scaffolds or whole tissues layer by layer utilizing bioinks (Schacht *et al.*, 2015; Torras *et al.*, 2018). Hydrogels are among the most commonly used bioinks as they have high printing resolution and easily modifiable chemical structures (Jakus *et al.*, 2016; Gopinathan & Noh, 2018). Thus, these biomaterials are also most often used for micromolding techniques (Figure 1.8 C-II), where the scaffold of choice is produced in a series of molding and de-molding steps (Wang *et al.*, 2017; Torras *et al.*, 2018). However, in the field of tissue engineering and regenerative medicine, silk-based scaffolds are more frequently used due to their exceptional mechanical properties, biocompatibility, and mild inflammatory responses *in vivo* (Kundu *et al.*, 2013; Floren *et al.*, 2015). For example, a model system for human large and small intestine was established using 3D porous silk protein scaffolds coupled with a geometrically engineered hollow lumen that supported growth and polarization of human cell lines (Chen *et al.*, 2015) as well as primary cells (Chen *et al.*, 2017). Besides bioprinting and micromolding, organ-on-a-chip technologies combine tissue-engineering methodologies with microfabrication techniques. Here, tissue barriers can for example be modelled by incorporating flexible and porous polydimethylsiloxane (PDMS) membranes into microfluidic channels (Figure 1.8 C-III). Appling cyclic strain in addition to continuously perfusing the epithelial chamber supports the development of polarized columnar epithelia (Zhang *et al.*, 2018). While all three techniques are fairly young and still have technical and/or experimental drawbacks, they have impressively set the stage for the development of human intestinal tissue models *in vitro* (Kim *et al.*, 2012a, 2016; Chen *et al.*, 2015; Madden *et al.*, 2018; Zhou *et al.*, 2018).

Another intriguing approach to generate extracellular matrix scaffolds is the decellularization of tissue (Mertsching *et al.*, 2005; Finkbeiner *et al.*, 2015). For instance, Schanz and colleagues introduced a vascularized human tissue model based on the so-called BioVaSc (Biological Vascularised Scaffold), a decellularized segment of the porcine jejunum

(Figure 1.9 A) (Mertsching *et al.*, 2005; Schanz *et al.*, 2010). Using a chemical decellularization process with sodium deoxycholate, porcine intestinal cells are removed from the tissue leaving behind a structured ECM scaffold with its native microarchitecture. Subsequently, the scaffold is digested with DNase and sterilized using gamma-radiation and can be stored at 4 °C submerged in PBS for several months. Previous work has shown that the decellularization process does not affect the composition of extracellular matrix components or the characteristic villi and crypt architecture of the small intestine (Mertsching *et al.*, 2005; Schweinlin *et al.*, 2016). This vascularized ECM scaffold was subsequently reseeded with human Caco-2 epithelial cells and primary human microvascular endothelial cells. The human, colorectal adenocarcinoma Caco-2 cell line is the most widely used immortalized human cell line for gastrointestinal *in-vitro* test systems. Their morphology and physiology closely resembles those of small intestinal human enterocytes in that they form brush borders with microvilli and maintain tight junctions (Delie & Rubas, 1997; Artursson *et al.*, 2001; Sarmento *et al.*, 2012). Cultivation in a sophisticated perfusion bioreactor system provided mechanical shear stress on the cells resulting in the reorganization of the intestinal villi morphology (Schanz *et al.*, 2010). However, these vascularized tissue models require very high maintenance and are not easily applicable to high throughput assays required for *e.g.* drug screening or infection research.

Thus, Pusch and colleagues introduced a 3D intestinal *in-vitro* tissue model based on the techniques obtained for the BioVaSc scaffold (Pusch *et al.*, 2011). Here, the porcine tissue is harvested without vasculature but decellularized in the same manner as described for the vascularized scaffold. This resulting ECM scaffold was termed SISmuc (small intestinal submucosa with mucosa) and is subsequently fixed in a so-called cell crown (composed of an outer and inner metal ring) providing an apical compartment with the former mucosal side of the intestine and a basolateral site with the former serosa (Figure 1.9 B). Reconstitution of the intestinal mucosa is achieved by apically reseeding with polarizing Caco-2 cells. Cultivation conditions included static settings in a 24- or 12-well plate format in a conventional cell culture incubator (Figure 1.9 C, *left panel*) allowing simultaneous cultivation of a greater number of tissue models compared to the vascularized system (Schanz *et al.*, 2010). Developing tissue models based on SISmuc scaffolds can additionally be cultivated in a perfusion bioreactor (Figure 1.9 C, *right panel*), where a continuous flow of cell culture medium provides mechanical stimuli to aid tissue differentiation (Pusch *et al.*, 2011). Whereas Caco-2 cells cultured under static conditions grow into a tight epithelial monolayer on the SISmuc, tissue models in the bioreactor environment display multilayer formation composed of highly prismatic cells (Figure 1.9 D) (Pusch *et al.*, 2011). Both model systems express important intestinal mucosal cell markers

such as occludins (TJs), E-cadherin (AJs), and villin (brush border). In addition, the applied biomechanical and physiological cues provided by bioreactor cultivation and adhesion to ECM proteins, respectively, increased the expression of cellular transporters such as

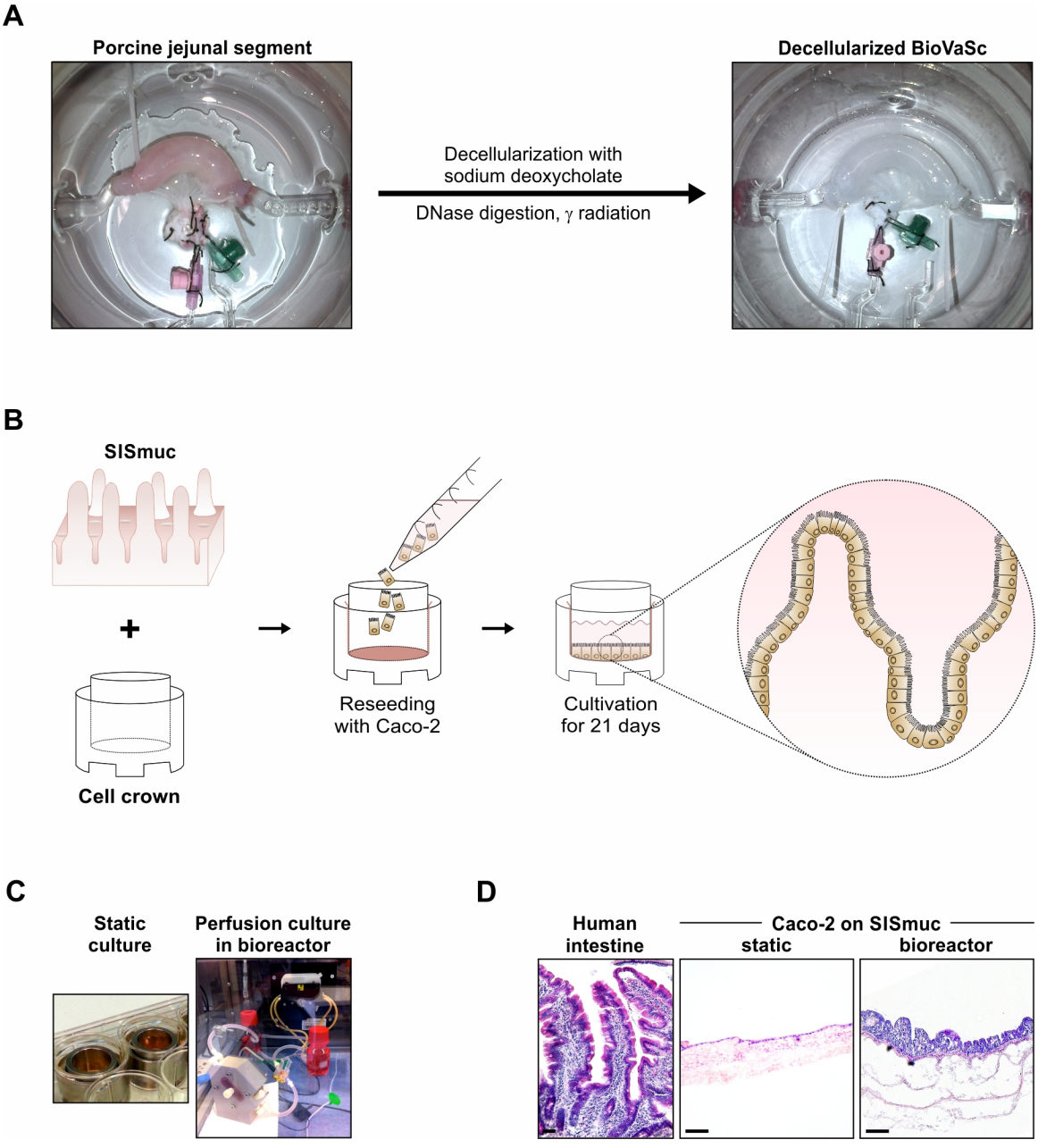

Figure 1.9: Generation of extracellular matrix scaffolds and set-up of the Caco-2 cell line-based intestinal tissue model. (A) Chemical decellularization of a vascularized porcine jejunal segment with sodium deoxycholate leads to a biological vascularized extracellular matrix scaffold (BioVaSc). Subsequent DNase digestion and gamma-radiation preserves the scaffold for several months. **(B)** The extracellular matrix scaffold SISmuc is fixed in between two metal rings (cell crown). The former mucosal side faces the apical compartment and is subsequently reseeded with Caco-2 epithelial cells and statically cultivated for up to 21 days. **(C)** Images of the static (*left panel*) and perfusion bioreactor (*right panel*) cultivation conditions for the establishment of 3D tissue models. Under static

conditions, metal cell crowns containing the reconstructed tissue are cultured in conventional 12-well plates without additional mechanical stimulation. The perfusion bioreactor enables the cultivation of tissue models under a continuous medium flow over the cell surface leading to stimulating shear stress on the cells. **(D)** Hematoxylin and eosin (H&E) staining of human small intestinal tissue (*left panel*) or Caco-2 cells on SISmuc after 21 days in static (*middle panel*) or perfusion bioreactor culture (*right panel*). Tissue samples were fixed with 2 % PFA, processed for paraffin embedding and sectioned with 5 µm thickness using a Leica RM2255 microtome (Leica Biosystems). Scale bar 200 µm.

the MDR1 (multidrug resistance protein 1) efflux transporter (Pusch *et al.*, 2011). This suggests that the integration of cellular cues such as shear stress and a supporting ECM is crucial to establish a reliable 3D tissue model *in vitro*. This model has been suggested as a suitable tool to study the physiology of the human intestine in addition to pharmacological applications for drug screening.

This 3D tissue model also presents an exceptional opportunity to study virulence of human gastrointestinal pathogens. It combines the complex 3D architecture of the small intestine with epithelial cells grown in biochemically relevant contact to extracellular matrix proteins. Moreover, the intestinal tissue model can be established relatively inexpensively in every scientific laboratory, scaled up to at least medium throughput, and – in particular relevant to infection studies – it provides easy access to both the apical and basolateral epithelial side enabling easy readouts for both the pathogen and the host. Once the initial culture system is set up, it is completely conceivable that there are many more potential future developments advancing the *in-vitro* tissue model with each step towards the native environment of the human intestinal tract.

2. Adaptation and enhancement of an intestinal 3D tissue model to study pathogenesis of *C. jejuni*

Research on infectious diseases depends on the recreation of virulence-determining processes elicited by bacterial or viral pathogens using suitable model systems. Drawbacks of current infection models limit the ability to understand such intricate mechanisms. This includes the study of the foodborne pathogen *C. jejuni*. Numerous bacterial factors contributing to the symptoms of campylobacteriosis in humans have been identified utilizing *in-vitro* and *in-vivo* infection models (Young *et al.*, 2007; Butcher & Stintzi, 2017; Burnham & Hendrixson, 2018). However, these are either limited by their lack of native 3D tissue architecture or – in the case of animal models – confront *C. jejuni* with a non-human environment. The intestinal tissue model introduced in the previous chapter would overcome some of the limitations present in current infection models. Thus, the aim was to ascertain whether this *in-vitro* engineered tissue would be suitable to explore *C. jejuni* pathogenesis and bacterial factors involved in interactions with host cells.

2.1. Set-up of infection parameters for *C. jejuni* in the statically cultivated intestinal 3D tissue model

Upon ingestion by a susceptible host, *C. jejuni* survives the gastric environment and colonizes the lower intestinal tract including the ileum, jejunum, and colon (Dasti *et al.*, 2010). Most *C. jejuni* strains have a characteristic spiral morphology (Garrity, 2005) that has been proposed to influence motility and colonization of viscous environments such as the intestinal mucosal surface (Lertsethtakarn *et al.*, 2011; Frirdich *et al.*, 2014). In general, interaction of bacterial pathogens such as *C. jejuni* with human gastrointestinal epithelia involves adherence to tissues, replication, disruption of barrier function, and invasion into epithelial cells (Backert & Hofreuter, 2013; Butcher & Stintzi, 2017). Accordingly, readouts for these processes needed to be established to follow *C. jejuni* infection in the statically cultivated intestinal tissue model (Figure 2.1 A). The assessment of both pathogen and host parameters included (I) the isolation of CFUs for bacterial adherence (adherence + internalization), internalization only, and transmigration, (II) measurement of potential disruption of the epithelial barrier function during infection, as well as (III) immunohistochemical staining (IHC) for tissue and host cell characteristics (Figure 2.1 A).

To set up infection conditions in the tissue model, two frequently employed *C. jejuni* wild-type strains, 81-176 and NCTC11168, were tested for their ability to interact with the 3D architecture provided by the tissue model. Both of these *C. jejuni* isolates are highly

motile. In general, strain 81-176 is a spiral-shaped isolate and accepted to be highly pathogenic as well as a very efficient colonizer in animal and 2D *in-vitro* cell culture models (Backert & Hofreuter, 2013). By comparison, many isolates of NCTC11168, including the wild-type strain used here as well as the original genome-sequenced strain (Parkhill *et al.*, 2000), show rod-shaped morphology, although some other isolates of this strain can also be spiral (Revez *et al.*, 2012). According to previous studies with these wildtypes, a multiplicity of infection (MOI) of 20 using *C. jejuni* grown to mid-log phase ($OD_{600} \sim 0.4$) in rich media was chosen for subsequent infection experiments (Backert & Hofreuter, 2013). To be able to calculate the MOI, the mean number of epithelial cells on tissue crowns after cultivation needed to be determined. Two independent methods (Appendix Table 2.1 for cell counting; Table 2.2 for Pico-Green assay) showed that following reseeding and static cultivation for 21 days, approx. 675,000 Caco-2 cells are present on each crown. To monitor bacterial CFUs during the infection of the 3D tissue model in a reproducible manner, a reisolation process for the bacteria was developed. Utilizing a tissue punch, equal sized areas of the infected tissue are cut out, from which the bacteria are isolated and plated in serial dilutions. For this thesis, numbers presented for adhered bacterial cells are always comprised of both adhered and internalized CFUs, while internalized CFUs solely represent intracellular bacteria. The isolation of intracellular bacteria was achieved by use of the gentamicin protection assay. Here, cell culture models are treated with gentamicin for two additional hours in order to eliminate extracellular bacterial cells. Bacteria inside host cells are thereby protected from the antibiotic treatment and can be subsequently isolated. Two previously used detergents (Boehm *et al.*, 2011; Louwen *et al.*, 2012), namely saponin (Figure 2.1 B) and Triton X-100 (Figure 2.1 C), were applied to disrupt epithelial cells and recover bacteria. Both detergents worked equally well in isolating bacterial CFUs from the Caco-2 cell-based tissue model. Whereas the number of CFUs for both *C. jejuni* wild-type strains still increased with a 10-fold higher concentration of either detergent (compared to 0.01 %), 0.1 % of both saponin or Triton X-100 proofed to be sufficient to recover *C. jejuni* CFUs from the cell crowns as no further increase in bacterial load could be observed with a detergent concentration of 1.0 %.

C. jejuni has been reported to disrupt epithelial barrier function during infection of 2D *in-vitro* cell culture systems (MacCallum *et al.*, 2005; Chen *et al.*, 2006; Boehm *et al.*, 2015). Most often, this is determined by measuring the transepithelial electrical resistance (TER) facilitated by the epithelium. However, the metallic nature of the cell crowns used to set up the tissue model in this thesis eliminated this possibility. Moreover, hand-held electrode measurement devices such as the Millicell® ERS-2 Voltohmmeter (Millipore) are restricted by a fairly small interspace between the electrodes and thus would not be suitable

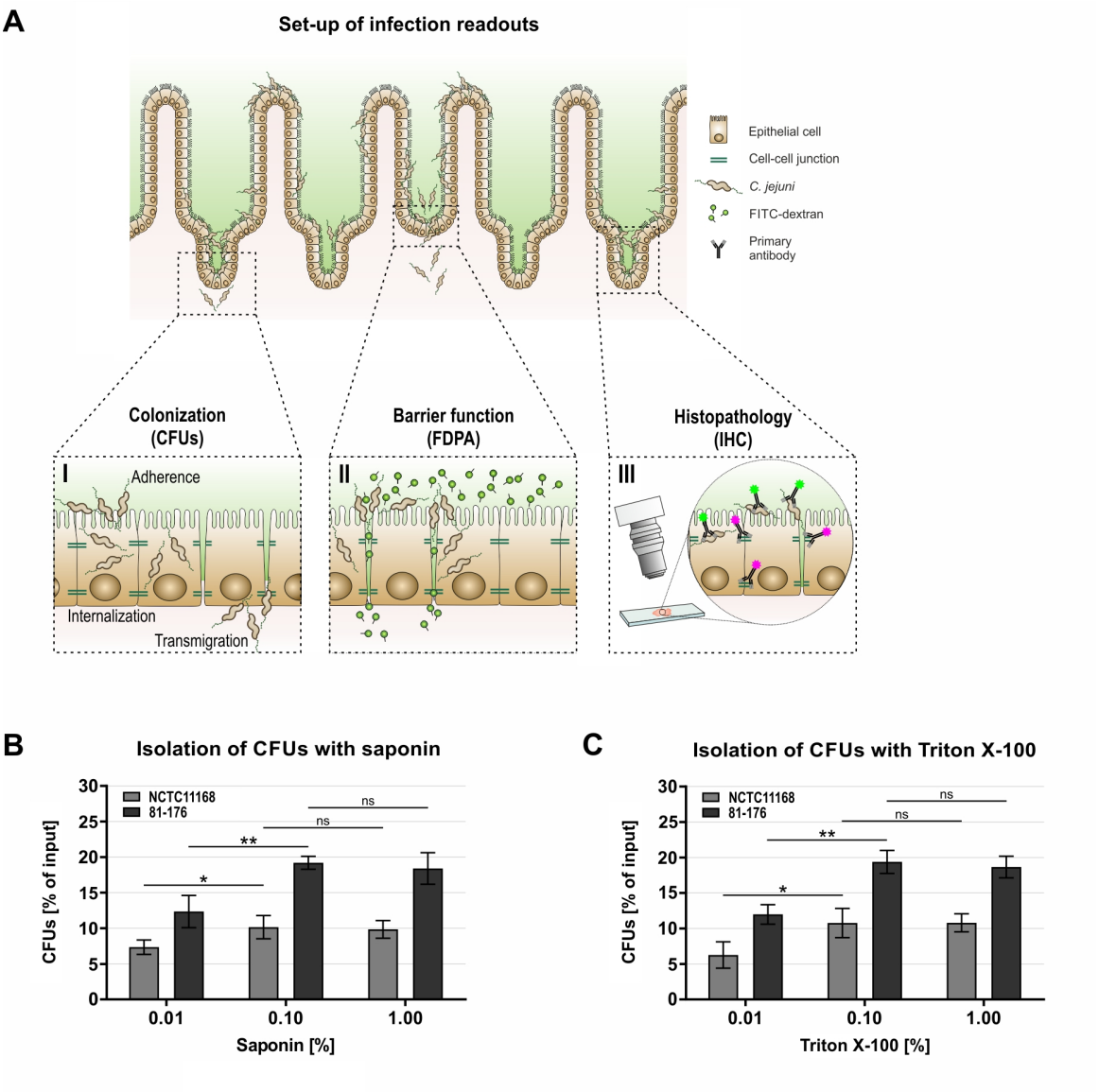

Figure 2.1: Set-up of infection readouts and isolation of bacterial CFUs from the intestinal 3D tissue model. (A) After infection of the 3D tissue model with *C. jejuni* (MOI 20), cell crowns are investigated for bacterial burden by isolation of CFUs using a tissue punch (5 mm diameter) and enumeration by serial dilution on agar plates **(I)**, for disruption of epithelial barrier function by FDPA **(II)**, or for phenotypic characteristics by confocal microscopy analyses after immunohistochemical staining (IHC) **(III)**. **(B, C)** Detergent test for isolation of CFUs from the tissue model. Recovery of CFUs (adherent and/or internalized) from the static Caco-2 cell-based tissue model 24 hrs post infection (p. i.) with *C. jejuni* wild-type strains NCTC11168 and 81-176. Different concentrations (0.01 %, 0.1 %, and 1.0%) of saponin **(B)** and Triton X-100 **(C)** were tested for their potential to isolate bacteria from infected tissue. **: $p < 0.01$, *: $p < 0.05$, ns: not significant. The Student's *t*-test was employed for statistical analysis.

for the thicker walls of the cell crowns. Consequently, the fluorescein isothiocyanate- (FITC) dextran permeability assay (FDPA) was employed to ascertain the paracellular flux of FITC-coupled dextran (Hubatsch *et al.*, 2007). Compared to electrical resistance determining

voltage measurements, where an increase in resistance signifies the onset of a confluent monolayer and later on the development of cell-cell junctions, permeability measurements rely on the decreasing penetrablity of a cell monolayer. Accordingly, a decrease in permeability is comparable to an increase in resistance. FITC-dextran with an average molecular weight of 4 kDa was used. Due to its size, this molecule cannot pass through cells and thus, can only diffuse from the apical to the basolateral compartment if cell-cell junctions are not yet fully formed or destroyed by extraneous causes. In order to measure permeability during the cultivation period of the tissue models and upon infection with *C. jejuni*, 0.25 mg/ml of FITC-dextran was applied apically in 500 µl of cell culture medium and incubated for 30 minutes at 37 °C. Afterwards, 100 µl samples were taken out of the basolateral compartment in triplicates and measured for their fluorescence at a TECAN infinite M200 fluorometer (excitation at 492 nm, emission at 520 nm). FDPA values are presented as percentages of their respective input FITC-dextran concentration. Throughout this thesis, this set-up of the FITC-dextran permeability measurements was utilized to indicate the differentiation of the cells into an epithelial barrier and its potential disruption during infection with *C. jejuni*.

The intestinal epithelial barrier mediates the transport of molecules through trans- and paracellular pathways. In particular, a single layer of enterocytes connected via tight and adherens junctions controls the paracellular flux of molecules. A leaky intestinal barrier is unable to prevent the permeation of luminal endotoxins or bacteria into deeper tissue regions and ultimately the blood stream. In order to visualize the cell-cell junction barrier und potential disruptions thereof elicited by *C. jejuni*, histological and immunohistochemical (IHC) staining protocols needed to be established. While top view microscopic images are easily achievable for conventional 2D cell culture (including the Transwell system), the 3D models have to undergo the same treatment as real tissue. This included paraffin embedding, subsequent microtome sectioning, and an antigen retrieval step in the case of IHC. Typical retrieval after paraffin embedding includes either boiling in citrate buffer or an enzymatic treatment. However, antibody labeling of eukaryotic cell components such as tight and adherens junction proteins in conjunction with *C. jejuni* bacterial cells proofed challenging. In the end, a combination of both retrieval steps was necessary to achieve specific fluorescence signals for both host cell proteins and bacteria at the same time. Similar to the permeability analysis, the established tissue processing, sectioning, and staining techniques were applied throughout this thesis and results will be discussed in more detail where appropriate.

2.2. Cultivation with mechanical stimulation influences barrier function in the Caco-2 cell-based 3D tissue model

So far, the format of the intestinal tissue model requires static culture in 12-well plates in a conventional cell culture incubator. While this type of cultivation is easily achievable, it lacks physiological tissue conditions resulting in restricted tissue morphology and cellular differentiation. Contrary to that, a perfusion bioreactor, where the reconstructed tissue is cultivated under a continuous flow of cell culture medium, provides specific mechanical stimuli to aid tissue differentiation (Pusch *et al.*, 2011). This in turn can guide the Caco-2 cells towards a differentiation phenotype reminiscent of human intestinal enterocytes and help to improve mucosal folding. However, such devices are not widely available and decrease the throughput capacity of these models. More precisely, for a typical infection experiment conducted throughout this thesis with the aim to test the impact of a bacterial virulence factor on the adherence and/or internalization capacity of the pathogen or on the host response, at least eight tissue models would be required. Per condition (*i.e.* adherence or internalization), this includes a non-infected control (mock) and three cell culture models infected with the wildtype, a deletion mutant, and a complementation. Adding different time points or technical replicates would increase the number of required tissue models to 16 or even 24. This kind of parallel cultivation is so far not manageable within a bioreactor. Thus, the aim would be to provide an environment that mimics microfluidic shear on the cells while retaining a higher throughput for tissue culture.

It has previously been reported that various gastrointestinal cell lines showed improved cell morphology when grown on Transwell inserts while being mechanically stimulated by a rocking board (Navabi *et al.*, 2013). Consequently, it was tested whether cultivation on an orbital shaker while inside a cell culture incubator would provide adequate stimulation for the 3D model to enhance tissue and cell morphology towards native enterocyte-like conditions. To accurately emulate mechanical impulses experienced by intestinal cells *in vivo*, shear forces induced by movement of the medium over the cell surface were simulated tailored to the specifications of the shaker by a dynamic computer modulation (provided by Ivo Schwedholm, Tissue Engineering and Regenerative Medicine, University Hospital Würzburg, Germany) (Figure 2.2 A). Consequently, rotatory frequency was adjusted to 65 rounds per minute (rpm), where computational modeling predicted an average shear distribution of $1.6 \times 10^{-2} \pm 4.7 \times 10^{-3}$ dyne/cm^2 across the scaffold surface, mimicking mechanical stimulation found along the GIT *in vivo* (Kim *et al.*, 2012).

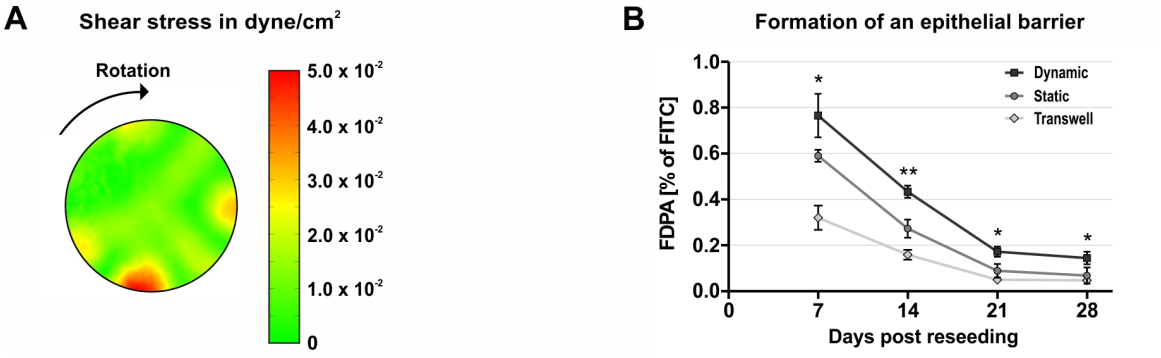

Figure 2.2: Mechanical stimulation during cultivation positively influences barrier function of the 3D tissue model. (A) Simulation of fluid dynamics over the surface of a cell crown during orbital shaking with 65 rpm (clockwise rotation) revealed a consistent mechanical shear stress distribution. Average shear was measured at $1.6 \times 10^{-2} \pm 4.7 \times 10^{-3}$ dyne/cm^2. **(B)** FITC-dextran permeability assays (FDPA) of Caco-2 cells reseeded on either Transwell inserts (permeable polycarbonate membrane, 0.4 µm pore size, static cultivation) or on SISmuc within 28 days of cultivation under both static and dynamic conditions. FDPA values represent the percentage of input FITC-dextran that has diffused to the basolateral compartment. Error bars signify standard deviations (SDs) of three independent biological replicates. Statistical analysis is indicated for permeability differences between the statically and dynamically cultivated tissue models. Asterisks indicate significance of differences observed in the dynamic model in comparison to the static tissue model as well as from Caco-2 cells grown on Transwell inserts. **: $p < 0.01$, *: $p < 0.05$. Statistical analyses were performed with the Student's *t*-test.

Distribution of shear stress across the surface of a cell crown proved to be fairly homogenous with hotspots of stronger shear around the periphery caused by the start and stop rotary movements of the shaker.

To check the impact of this dynamic cultivation on the development of an epithelial barrier in the Caco-2 cell-based tissue model, paracellular flux of FITC-dextran was assessed during a cultivation period of 28 days. Caco-2 cells grown statically on Transwell inserts were used as a control to consider the influence of the ECM scaffold and fluidic shear. In comparison to Caco-2 cells on Transwells, both statically and dynamically cultivated tissue models showed a delayed onset of epithelial barrier formation indicated by the higher values of permeability at day 7 and 14 post reseeding (Figure 2.2 B). This delay was even more pronounced for tissue models cultivated under shear stress. Moreover, at later time points (21 and 28 days), permeability in the dynamically cultivated tissue model continued to be significantly different from Caco-2 cells on Transwell inserts and from tissue models under static cultivation. This is in line with previous observations reporting rather high TER values for Caco-2 cells on Transwells, which do not reflect barrier strength of native human small intestine (Sjöberg *et al.*, 2013). In addition, it has also been previously shown that tight junction formation between Caco-2 cells can lead to unnaturally tight epithelial

barriers (van Breemen & Li, 2005). These results show that the epithelial barrier formed by the tissue model under shear stress is less tight compared to either static cultivation or Caco-2 cells on Transwell inserts, and thus might be more reflective of resistance measurements of native tissue. Nevertheless, all cell culture models showed no significant further decrease of permeability after 21 days in culture and FDPA values remained stably low at 28 days post reseeding. Thus, all further downstream analyses of tissue models based on Caco-2 cells were performed after 21 days in culture.

2.3. Fluidic shear stress enhances tissue morphology and cellular differentiation into a columnar epithelium

FDPA measurements of Caco-2 cells grown on different scaffolds (Transwell insert and SISmuc) as well as during different cultivation conditions indicated the formation of an epithelial barrier under shear stress that might be more reminiscent of physiological tissue properties. Paracellular permeability along the GIT is tightly regulated via cellular junctions, which are tasked with the exclusion of harmful substances while permitting a steady influx of nutrients. Thus, unnaturally low FDPA values would not reflect a physiologically relevant intestinal barrier that rather requires a certain degree of permeability. To correlate the observations of the previous chapter with the formation of barrier-specific cell-cell junctions, microscopic analyses of all cell culture models were conducted. To observe overall tissue morphology, cell culture models were fixed with 2 % paraformaldehyde (PFA), processed for paraffin sectioning, and stained with histological H&E (Figure 2.3), thereby marking cell nuclei in blue followed by a counterstaining of eosinophilic structures in shades of red and pink. As a control, samples of human intestine were processed the same

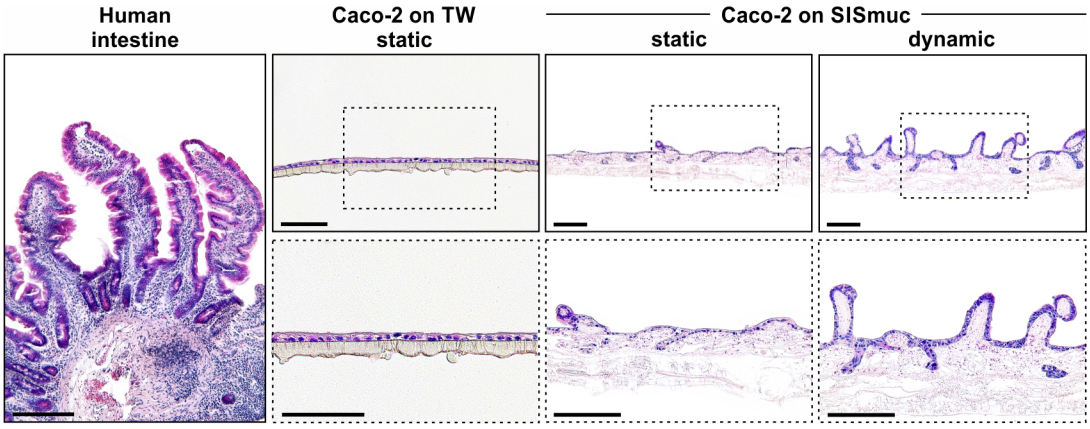

Figure legend on next page

Figure 2.3: Dynamic cultivation of the Caco-2 cell-based tissue model enhances architectural topographies reminiscent of human small intestine. Tissue samples were fixed with PFA, embedded in paraffin and sectioned into 0.5 µm thick slices for subsequent H&E staining. Images depict human small intestinal tissue (*left panel*) or Caco-2 cells either on Transwell inserts (TW; 0.4 µm pore size) (*middle panel*) or on SISmuc after 21 days in static or dynamic culture (*right panels*). Images below are higher magnifications of the above micrographs. Scale bar 200 µm.

way to account for effects on native tissue during embedding, sectioning, and staining. Biopsy samples were obtained from obese adults during routine stomach bypass surgery in collaboration with the surgical unit at the University Hospital Würzburg (PD Dr. med. Christian Jurowich, PD Dr. med. Florian Seyfried; study approval number 182/10). All cell culture models showed a confluent monolayer atop their respective support scaffolds (Transwell or SISmuc) independent of their cultivation status. Whereas Caco-2 cells on the Transwell exhibited a flat and unstructured organization, the same cells on SISmuc demonstrated a clear differentiation into crypts and villi resembling structures. However, while this effect was only scarcely visible under static cultivation, fluidic shear conditions seemed to improve tissue morphology towards being more reminiscent of the native human small intestine.

In addition, immunofluorescence labeling of the adherens junction protein E-cadherin (Figure 2.4 A) and the tight junction protein occludin (Figure 2.4 B) showed the formation of more fully developed cell-cell junctions in the dynamically cultivated tissue model compared to Caco-2 cells on Transwell inserts or on SISmuc under static cultivation. Localization of tight junctions is more common near the apical region of epithelial cells, which can be distinctly detected in the dynamically cultivated Caco-2 cell-based tissue model. Moreover, cells on Transwell inserts as well as in the static tissue model exhibited a more flattened, squamous cellular shape, whereas cells cultivated under fluidic shear conditions displayed an elongated shape more reminiscent of columnar epithelia. As a quantitative readout for this observation, the height of cells cultivated on the different scaffolds and during static and dynamic cultivation was determined (Figure 2.4 C). Approximately 300 cells for each condition were measured from basal to apical side using the program ImageJ. This quantification revealed that with increasing complexity of cell culture models (static Transwell to static tissue model to dynamic tissue model) up to native biopsies, epithelial cells grew in height and reached columnar dimensions. Cells grown on SISmuc – even under static conditions – were already almost two-fold taller than those grown on Transwell inserts. In comparison, fluidic shear dynamics increased cell height about two- to three-fold when compared to Caco-2 cells on either SISmuc (static) or Transwell, respectively. Even tough the cells in the dynamic tissue model were still

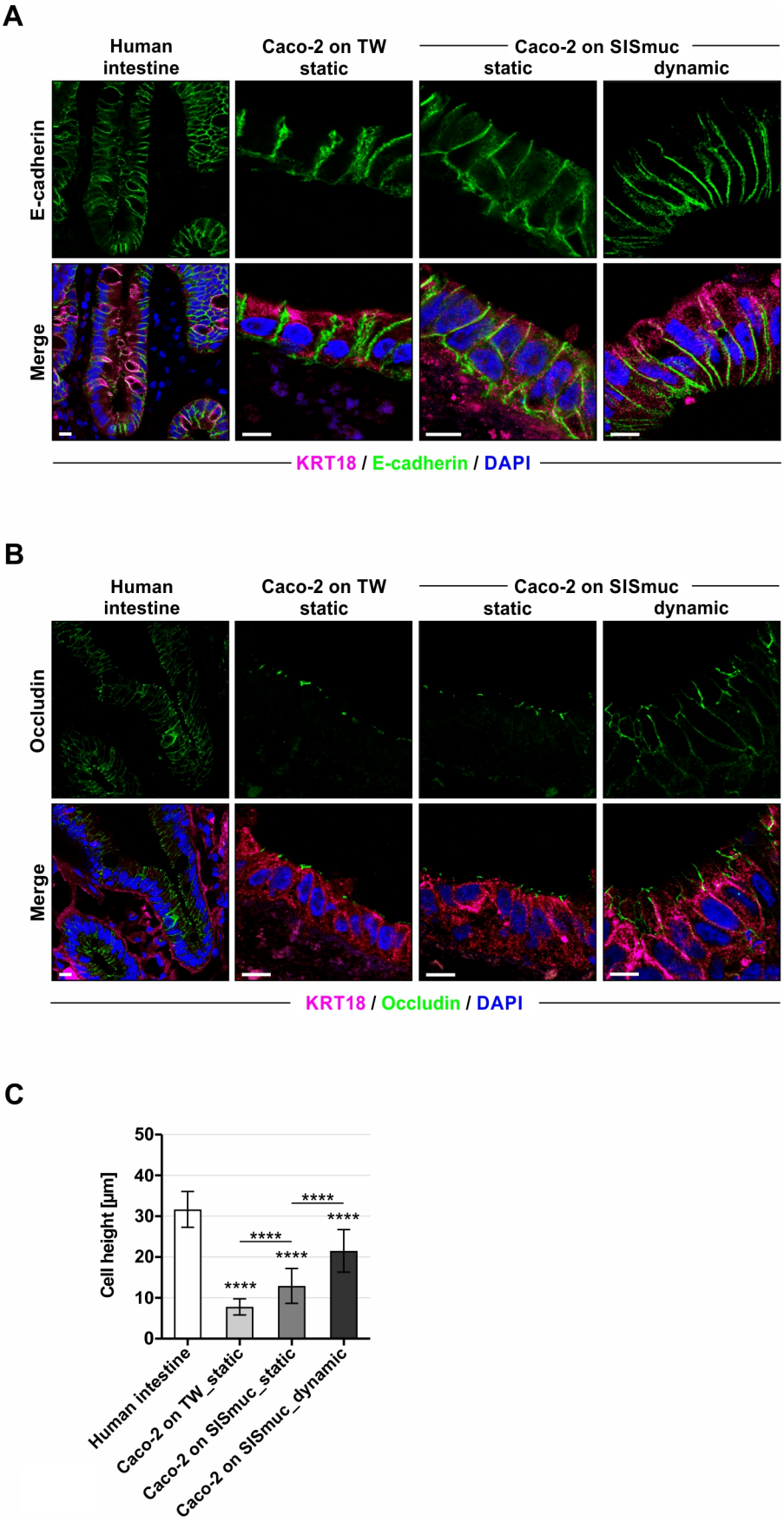

Figure legend on next page

Figure 2.4: Mechanical stimulation during cultivation of the tissue models enhances localization of cell-cell junction proteins and promotes cell height. Tissue samples were fixed with 2 % PFA, processed for paraffin embedding, and sectioned with 5 µm thickness using a Leica RM2255 microtome (Leica Biosystems). **(A, B)** Confocal microscopy images of paraffin sections of human small intestine (*left panel*), Caco-2 cells on Transwell inserts (*middle panel*), statically, or dynamically cultivated Caco-2-based tissue models (*right panels*). Tissues were stained with DAPI (nuclei, blue) and antibodies for cytokeratin-18 (KRT18, magenta), adherens junction protein E-cadherin (green) **(A)** and tight junction protein occludin (green) **(B)**. Scale bar 10 µm. **(C)** Determination of the average cell height for Caco-2 cells on Transwells (static cultivation), SISmuc (static and dynamic conditions), and native human intestine. Ten confocal microscopy images each of five different Transwell or tissue models based on Caco-2 cells (static and dynamic conditions) and five different patient samples were used to measure the cell height of every second cell in the pictures using ImageJ. Asterisks above each column indicate the significant difference of the respective cell height when compared to native human intestine. Asterisks above lines drawn between columns specify the significance of the hell height compared between the different cell culture models, *i.e.* between Caco-2 cells grown on Transwell compared to statically cultivated Caco-2 on SISmuc, and between the static tissue models compared to cells grown under shear stress on the ECM scaffold. ****: $p < 0.0001$ (using the Student's *t*-test).

significantly smaller compared to native enterocytes, with an average height of 21.52 ± 0.3125 µm, Caco-2 cells dynamically cultivated on the SISmuc scaffold reached nearly similar dimensions as measured for native human intestine and as previously reported (Bullen *et al.*, 2006; Kim *et al.*, 2012).

Overall, these results demonstrate that simulation of shear stress reminiscent of mechanical stimulation experienced *in vivo* resulted in a more pronounced microarchitecture reminiscent of the native human intestine as well as in a stronger differentiation of the reseeded Caco-2 epithelial cells into a columnar mucosal barrier.

2.4. *C. jejuni* colonizes the 3D tissue model and disrupts the epithelial barrier in a strain-specific manner

Initially, both Caco-2 cell-based models (static and dynamic) were infected with two different *C. jejuni* wild-type strains (NCTC11168 and 81-176). Although tissue models were cultivated either with or without shear stress induced by an orbital shaker, subsequent infection experiments were always conducted without additional mechanical stimulation in both the statically and the dynamically cultivated tissue model. The *C. jejuni* infection experiments were carried out strictly under static conditions. Following the fate of the bacteria over the time course of infection, the observation could be made that, independent of the cultivation status of the tissue model, at 24 hrs p. i., approx. 12 % and 20 % of adhered and internalized bacteria were recovered for NCTC11168 and 81-176 infected crowns, respectively (Figures 2.5 A and B). This indicates that cultivation conditions of the tissue

model might not affect initial adherence and/or internalization of *C. jejuni*. The decreased colonization potential of NCTC11168 might reflect strain-specific differences in adherence to/colonization of epithelial cells as has been previously observed (Harvey *et al.*, 1999; Hu *et al.*, 2008; Wine *et al.*, 2008). Starting at 24 hrs p. i., a constantly increasing number of CFUs could be recovered in both cell culture models for both strains, suggesting that *C. jejuni* is able to survive and replicate on the tissue model. At 72 hrs p. i., the bacterial load even surpassed the initial input. While the slightly lower colonization of the tissue model by NCTC11168 compared to 81-176 observed at 24 hrs p. i. continued up to later infection stages (120 hrs p. i.) in the dynamically cultivated tissue model, no significant difference in colonization among the two strains could be observed in the static system from 72 – 120 hrs p. i. (Figure 2.5 A). In the dynamic Caco-2 model, colonization remained significantly

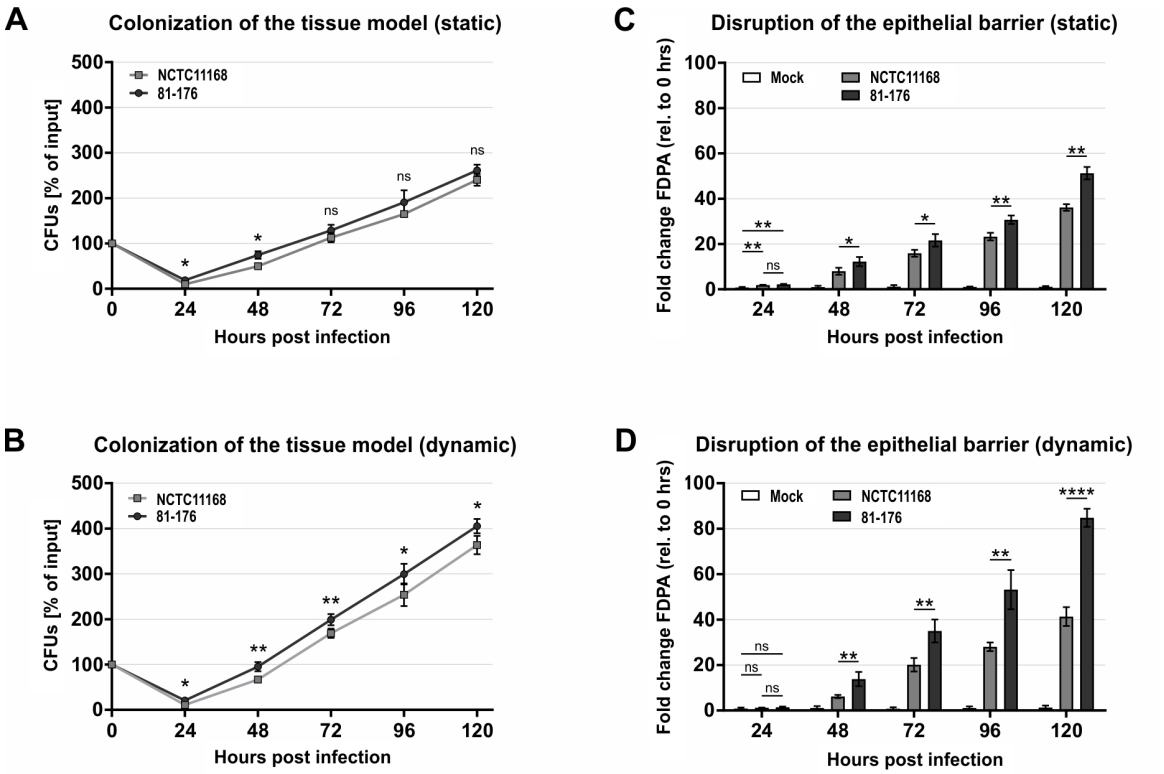

Figure 2.5: The tissue models are colonized by *C. jejuni* and epithelial barrier disruption occurs in an isolate-specific manner. (A, B) CFU quantifications of bacterial burden during infection with *C. jejuni* strains NCTC11168 and 81-176 from 24 – 120 hrs p. i. in the static **(A)** and the dynamic **(B)** tissue model. CFUs are displayed as the percentage of input CFUs. Error bars are calculated from four biological replicates with indicated SDs. **(C, D)** Corresponding disruption of epithelial barrier function by *C. jejuni* wild-type strains was determined by FDPA in tissue models cultivated without **(C)** or with fluidic shear stress **(D)**. Depicted is the mean of four independent experiments with corresponding SDs. Mock indicates non-infected controls. FDPA values are depicted as fold changes relative to the value at time point zero. ****: $p < 0.0001$, **: $p < 0.01$, *: $p < 0.05$, ns: not significant. Statistical analyses were performed with the Student's *t*-test.

attenuated for strain NCTC11168 compared to 81-176 (Figure 2.5 B), suggesting that the microenvironment of the dynamic tissue model might be able to uncover more subtle phenotypes of colonization even during later stages of the infection process. Moreover, CFUs of both wild-type strains at various time points post infection appeared to be higher in the dynamically cultivated tissue model compared to its static counterpart indicating a more stimulating environment for *C. jejuni* growth, replication, or survival in the dynamic setting.

FDPA measurements during the time course of infection revealed that the presence of either wildtype results in an increasing loss of barrier integrity for both the static and the dynamic tissue model (Figures 2.5 C and D). While permeability of the dynamically cultivated tissue model infected with either wild-type strain (Figure 2.5 D) did not significantly increase after 24 hrs, models cultivated under static conditions already showed a slight increase in permeability of two- to three-fold after 24 hrs of infection with both strains (Figure 2.5 C). This supports the premise that the model can mimic and allow for quantification of barrier disruption by *C. jejuni* as reported previously for 2D *in-vitro* culture systems (MacCallum *et al.*, 2005; Chen *et al.*, 2006; Boehm *et al.*, 2015). Moreover, a delayed onset of increasing permeability in the dynamically cultivated tissue model even with comparable bacterial load hints towards an ability of greater resistance towards pathogen-induced leakage of the epithelium. Yet, loss of barrier function increased in both tissue models during later stages of the infection process (up to 120 hrs p. i.) albeit to a greater extent in the dynamic system compared to the static Caco-2 model. This might be a result of the stronger increase in bacterial load on the tissue model cultivated with fluidic shear. This could indicate that the dynamic model might provide initial protection against *C. jejuni*-induced disruption of barrier function but does not, at large, prevent opening of epithelial cell-cell junctions. Epithelial barrier function decreased even further over time in both tissue culture models and revealed a higher disruption of the epithelial barrier by strain 81-176 compared to NCTC11168 (Figures 2.5 C and D). This strain-specific opening of the barrier was even more pronounced in the dynamically cultivated Caco-2 model (Figure 2.5 D) and again might reflect the greater potential of strain 81-176 to colonize this particular tissue model. As the tissue model cultured under dynamic shear fluid conditions seemed to be more resistant against initial *C. jejuni*-induced barrier disruption in addition to showing greater sensitivity in distinguishing strain-specific colonization patterns, all further downstream infection experiments were performed with the dynamically cultivated model.

The observed increase in paracellular permeability, in particular upon colonization by 81-176, indicated the opening of cell-cell junctions. Thus, distribution of the adherens junction protein E-cadherin (Figure 2.6 A) and the tight junction protein occludin (Figure 2.6 B) was examined during the time course of infection with *C. jejuni* strain 81-176

compared to non-infected controls. Similar to other studies (MacCallum *et al.*, 2005; Chen *et al.*, 2006; Harrer *et al.*, 2019), redistribution of cell-cell junction proteins from the lateral membranes to an intracellular localization could be observed. This was mostly visible during later stages of the infection (72 – 120 hrs). For visualization of E-cadherin at early

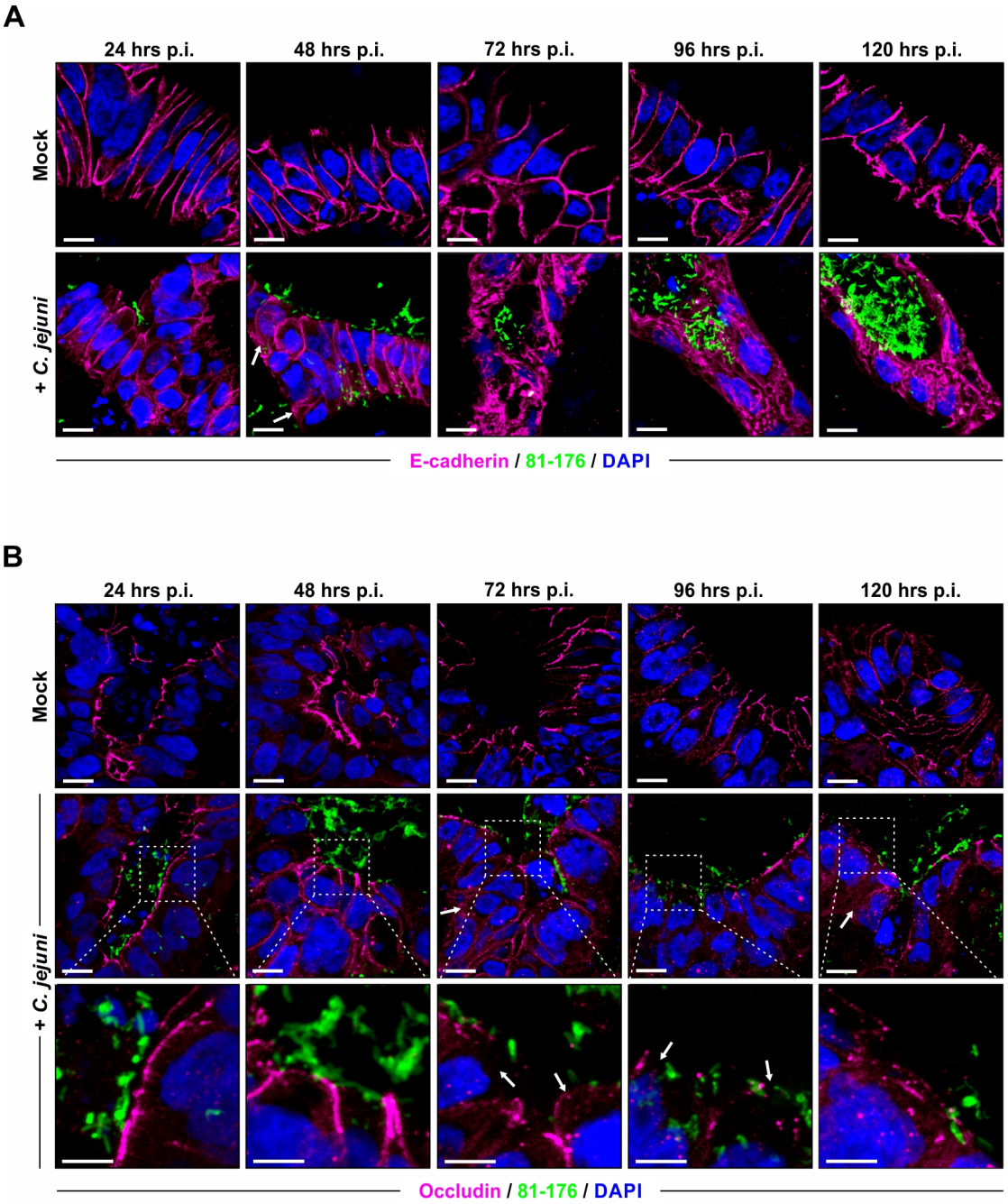

Figure 2.6: Infection of the Caco-2 cell-based tissue model with *C. jejuni* disturbs the localization of tight and adherens junction proteins. (A, B) Confocal microscopy images of paraffin sections of the Caco-2 tissue model cultivated dynamically during infection with *C. jejuni* strain 81-176 (24 – 120 hrs p. i.) or non-infected controls. Bacteria were visualized with an anti-*C. jejuni* antibody (green), nuclei were stained with DAPI (blue), and cell-cell junctions were imaged

using an anti-E-cadherin antibody (adherens junctions, magenta) **(A)**, or an anti-occludin antibody (tight junctions, magenta) **(B)**. White arrows indicate regions of redistribution of tight and adherens junction staining from the periphery of the cell to intracellular regions as well as loss of apical staining for occludin. Inlets in **(B)** are 2-fold magnifications of the indicated regions in the respective confocal image. Scale bar 10 µm (inlets 5 µm).

stages of the infection process (24 and 48 hrs p. i.), only a small part of the adherens junction protein was diffusely localized (Figure 2.6 A, indicated by white arrows), while the larger part was confined to the periphery of the cells. A pronounced apical localization of tight junction protein occludin could be observed in non-infected control crowns throughout the cultivation period (24 – 120 hrs p. i.). These apically distinct patterns were visible to a lesser extent upon infection with *C. jejuni* strain 81-176 and also resulted in an intracellular redistribution (Figure 2.6 B, indicated by white arrows and magnified inlets). This has also recently been observed in human intestinal biopsy samples from campylobacteriosis patients, where ZO-1 and occludin were redistributed from apical sites to intracellular locations (Harrer *et al.*, 2019). However, this phenomenon did not seem to be restricted to areas of direct contact between epithelial cells and bacteria indicating a non-localized disruption of cell-cell junctions. Throughout the infection process, bacterial cells seemed to accumulate in the crypts of the tissue model (Figure 2.6 A, 72 – 120 hrs p. i.). This observation has previously been reported for *in-vivo* animal infection studies (Young *et al.*, 2007; Van Deun *et al.*, 2008; Stahl *et al.*, 2014) but could so far not be observed *in vitro*.

In conclusion, the bacterial infection of the Caco-2 cell-based tissue models shows that both *C. jejuni* wild-type strains adhere to the epithelial surface and can use it as a replicative niche. While barrier destruction increased along with bacterial burden, the model is still able to display strain-specific differences in disruption of epithelial cell-cell junctions as well as niche-specific localization of the bacteria in the tissue model.

2.5. Adherence, internalization, and transmigration by *C. jejuni* is delayed in the 3D tissue model compared to 2D cell culture systems

The proof-of-principle infections with the Caco-2 tissue model showed that both bacterial colonization and host epithelial barrier function could be observed during infection. All experiments from this point forward were conducted with the dynamically cultivated Caco-2 model. While *C. jejuni* is primarily considered to be an extracellular pathogen, it can also be found inside cells in human colonic biopsies (van Spreeuwel *et al.*, 1985) and internalized into epithelial cells *in vitro* (Backert & Hofreuter, 2013). Thus, infection assays in the 3D tissue model with *C. jejuni* strains 81-176 and NCTC11168 were compared to

infection of a 2D non-polarized but confluent Caco-2 monolayer, the current *in-vitro* standard for assessing bacterial adherence and internalization (Figure 2.7 A).

At 4 hrs p. i. during 2D infection, *C. jejuni* strain 81-176 (Figure 2.7 B) reached higher adherence and internalization rates than those compared to strain NCTC11168 (Figure 2.7 C). In contrast, little or almost no bacteria could be isolated from the 3D tissue model for either wild-type strain at that relatively early time point (Figures 2.7 B and C). However, after 24 hrs in the tissue model, adherence and internalization rates equaled those observed during 2D infections at 4 hrs p. i., irrespective of the *C. jejuni* strain background. Thus, the onset of infection seems to be delayed in the 3D tissue environment compared to a 2D monolayer. Moreover, the tissue model enables the assessment of infection over a longer time course, whereas infection in a conventional 2D culture system could not exceed 12 hrs due to increasing death of host cells (data not shown).

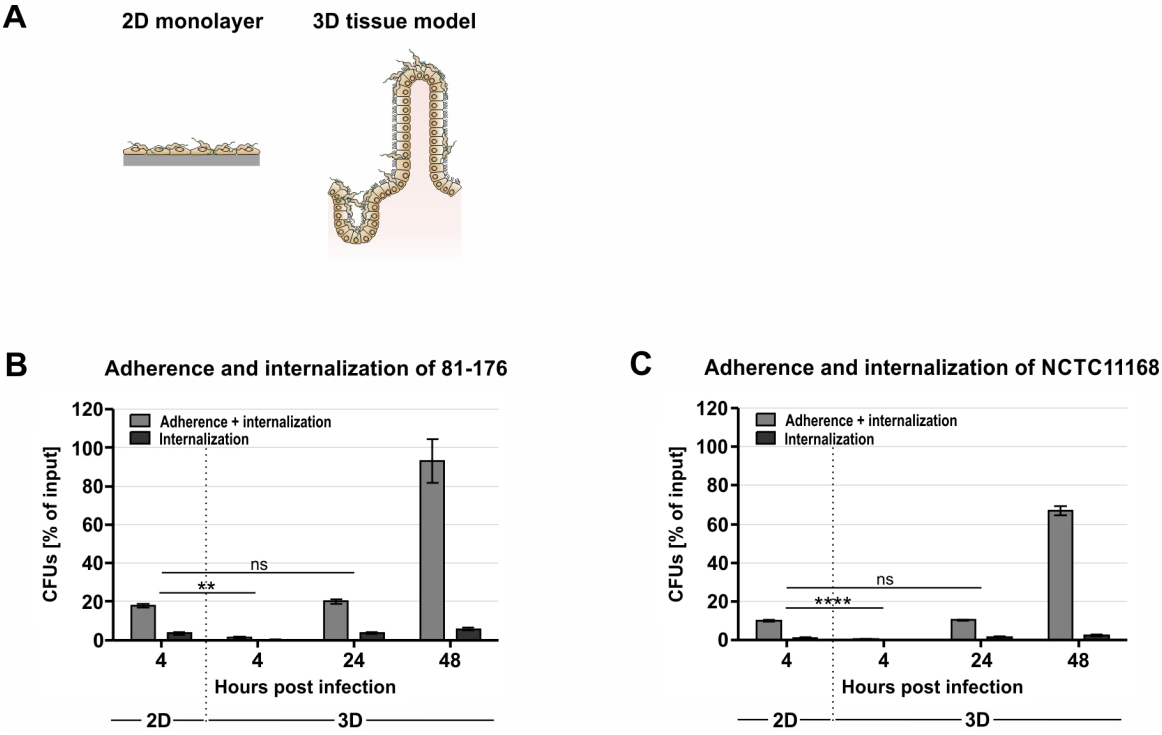

Figure 2.7: Adherence and internalization of *C. jejuni* isolates is impeded in the 3D tissue environment. (A) For comparative infections, 2D cell monolayers (Caco-2 cells in multi-well plates) as well as dynamically cultivated 3D tissue models were infected with *C. jejuni* strains 81-176 and NCTC11168 and quantified for bacteria adherent to and internalized into both cell culture systems. **(B, C)** Adherence and internalization of *C. jejuni* strains 81-176 **(B)** and NCTC11168 **(C)** were examined at 4 hrs p. i. in 2D Caco-2 monolayers and 4 – 48 hrs p. i. in Caco-2 cell-based 3D tissue models. Bar graphs represent the mean of four independent experiments with respective SDs. Statistical analysis represents the difference between adherence and internalization only between different time points. ****: $p < 0.0001$, **: $p < 0.01$, ns: not significant. For statistical analysis, the Student's *t*-test was employed.

To reach deeper tissue regions or underlying organ systems and establish potential reservoirs for long-term, chronic, or recurring infection, various intestinal pathogens have to cross the epithelial barrier (Kazmierczak *et al.*, 2001; Backert & Hofreuter, 2013). The transmigration of *C. jejuni* across the intestinal epithelium during the infection process is also a major contributor to tissue damage (Young *et al.*, 2007), and 2D Transwell systems have been used to assess its transmigration potential (Boehm *et al.*, 2012, 2015; Backert *et al.*, 2013). For this, epithelial cells are seeded onto porous polycarbonate (PC) or polyethylene terephthalate (PET) inserts and are statically grown in order to reach a polarized differentiation status. In order to investigate how the 3D tissue model performs regarding transmigration compared to conventional 2D Transwell inserts (Figure 2.8 A), the

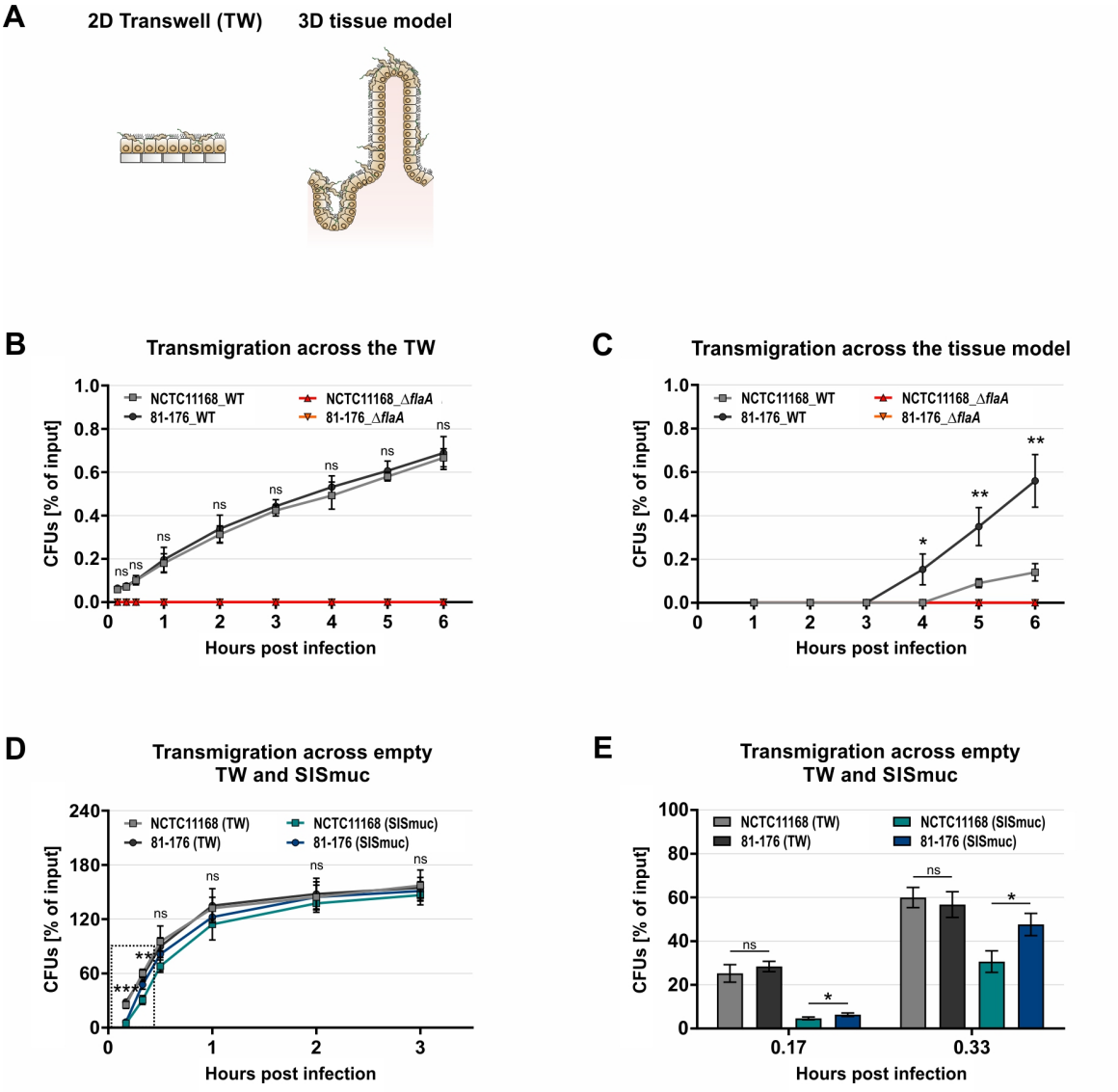

Figure legend on next page

Figure 2.8: *C. jejuni* translocation across the 3D tissue model is delayed. (A) The conventional 2D Transwell-based cell culture model was used to assess crossing of *C. jejuni* to the basolateral compartment in comparison to the 3D tissue model (Caco-2 cells on SISmuc). **(B, C)** Caco-2 cells were grown either on porous PC inserts (Transwell, pore size 3 µm) for 21 days under static conditions or on SISmuc scaffolds for 21 days under dynamic conditions. Transmigration of *C. jejuni* wild-type strains 81-176 and NCTC11168 and their respective *flaA* deletion strains (Δ*flaA*) was determined by isolating CFUs up to 6 hrs p. i. from the basolateral compartment of the Transwell-based infection model **(B)** or the 3D tissue model **(C)**. Experiments were conducted four times and CFUs are depicted as the percentage of input CFUs. Graphs represent the mean value with corresponding SDs. While transmigration across the Transwell and tissue model of both wild-type strains was significantly different from their respective Δ*flaA* mutant strains throughout the experiment, only the significance between strain 81-176 and NCTC11168 is indicated above the respective time points. **(D, E)** Isolation of CFUs from the basolateral compartment of non-reseeded Transwell (TW) and SISmuc from 0.17 – 3 hrs p. i. **(D)** with *C. jejuni* wild-type strains NCTC11168 and 81-176. Asterisks at early time points (0.17 and 0.33 hrs p. i.) indicate a significant difference of both *C. jejuni* wild-type strains between their transmigration through the different scaffolds. Early time points (0.17 and 0.33 hrs p. i.) are depicted separately as a bar graph in **(E)** to demonstrate an additionally strain-specific transmigration behavior across scaffolds. Experiments were conducted four times and graphs represent the mean value with corresponding SDs. ***: $p < 0.001$, **: $p < 0.01$, *: $p < 0.05$, ns: not significant. The Student's *t*-test was employed for statistical data analysis.

number of transmigrated bacteria of *C. jejuni* strains 81-176 and NCTC11168 in Transwells (Figure 2.8 B) and the tissue model (Figure 2.8 C) was quantified. Motility is absolutely required for *C. jejuni* interactions with host cells and its transmigration through the epithelium. Thus as a control, isogenic non-motile Δ*flaA* mutant strains were also examined for each strain background. Increasing numbers of bacteria were detected in the basolateral compartment of the Transwell system and the 3D tissue model for both WT strains following inoculation (Figures 2.8 B and C). Consistent with previous reports, it could be observed that motility was indeed required for transmigration, as no CFUs could be recovered from the basolateral compartment for the Δ*flaA* mutant strains (Grant *et al.*, 1993; Boehm *et al.*, 2012). Interestingly, *C. jejuni* strains needed approximately eight times longer to cross the epithelial barrier provided by the 3D tissue model (Figure 2.8 B) than in the Transwell system (Figure 2.8 C). Although FDPA measurements suggested the epithelial barrier on the Transwell insert to be even less permeable (Figure 2.2 B), the bacteria were able to cross this barrier in less than 30 min (Figure 2.8 B), whereas it took them almost three to four hours to transmigrate across the epithelial barrier in the tissue model (Figure 2.8 C). As the supporting scaffold in these two systems differs (ECM scaffold for the tissue model and polycarbonate membrane for the Transwell), the migration behavior of both *C. jejuni* wild-type strains through a non-reseeded SISmuc and Transwell insert was also tested (Figures 2.8 D and E) in order to exclude secondary effects of the supporting scaffolds. As expected, the number of transmigrating bacteria was significantly higher when

an epithelial barrier was missing. Moreover, transmigration across the SISmuc scaffold could now already be observed after 10 min p. i.. Whereas at these early time points (10 – 20 min p. i.), transmigration of both strains was significantly lower across the ECM scaffold compared to the Transwell, this difference was abrogated at later time points (30 min – 3 hrs p. i.) (Figure 2.8 D). This suggests that while the SISmuc scaffold poses a slightly greater obstacle for bacterial transmigration, it does not account for the observed time difference when an epithelial barrier is present This difference seems to be largely due to the tissue morphology of the 3D cell culture model as well as its tight and adherens junctions. In addition, in the Caco-2 cell-based tissue model a strain-dependent transmigration behavior could be observed (Figure 2.8 C). For the Transwell, both 81-176 and NCTC11168 crossed the epithelial barrier at comparable times and to a similar extent (Figure 2.8 B). However, in the 3D tissue model, NCTC11168 reached the basolateral side almost one hour later than 81-176 (Figure 2.8 C). This could in part be due to a potential strain-specific interaction with extracellular matrix proteins, as NCTC11168 showed a significantly reduced number of transmigrated CFUs through an empty SISmuc scaffold when compared to 81-176 at early time points (Figure 2.8 E).

Taken together, these data suggest that the 3D tissue model poses a greater obstacle for *C. jejuni* to overcome than 2D cell culture systems in regards to adherence and internalization as well as transmigration. Moreover, strain-dependent behavior such as traversing an ECM-maintained epithelium was only observable in the tissue model supporting its potential for infection research.

2.6. The Caco-2 cell-based 3D tissue model reveals infection phenotypes of *C. jejuni* mutant strains that differ from 2D monolayer assays

Virulence properties of *C. jejuni* such as adherence to and invasion into epithelial cells are most commonly studied using 2D *in-vitro* monolayer cultures of various gastrointestinal cell lines. So far, this thesis has provided evidence that the presence of the microarchitecture of the intestine in the 3D tissue model greatly influences host-pathogen interactions in terms of *C. jejuni* adherence, colonization/replication, internalization, transmigration, as well as bacterial-induced barrier disruption. Moreover, the *in-vitro* experiments regarding the wildtype-specific colonization patterns of *C. jejuni*, which are not always apparent in conventional 2D cell culture models, offer the opportunity to study *C. jejuni* colonization factors, whose relevance could so far only be observed *in vivo*. As the tissue model facilitated the ability of *C. jejuni* to infect intestinal epithelial cells, the question remained whether the resulting phenotypes would depend on its pathogenicity-determining factors. *C. jejuni* lacks

many of the classical virulence factors utilized by other gastrointestinal bacterial pathogens (Dasti *et al.*, 2010). In addition to morphology, its flagella, and thereby also its motility, its capsule, and its global regulators have been recognized as major contributors to *C. jejuni* pathogenicity (Backert & Hofreuter, 2013; Burnham & Hendrixson, 2018). To test these areas of *C. jejuni* biology and their respective implications for bacterial behavior during infection of the newly developed tissue model, the effect of various deletion mutant strains (Figure 2.9 A) on their respective colonization ability was evaluated. Deletion of the major flagellin protein FlaA (Δ*flaA*) results even in the presence of the minor flagellin FlaB in a truncated flagellum and thus, renders *C. jejuni* mutant strains non motile (Figures 2.9 A-I and C). This has been previously associated with an inability to invade epithelial cells *in vitro* (Wassenaar *et al.*, 1991) as well as with a lack of colonization *in vivo* (Wassenaar *et al.*, 1991; Stahl *et al.*, 2014). Another key aspect participating in *C. jejuni* pathogenesis is its polysaccharide capsule, which is thought to be a key virulence-associated cellular structure (Bacon *et al.*, 2001; Karlyshev *et al.*, 2001). The *kpsMT* genes are encoded in the capsule polysaccharide locus of *C. jejuni* and code for the associated ABC transporter permease (*kpsM*) and ATP-binding protein (*kpsT*), respectively. Consequently, deletion of this transporter (Δ*kpsMT*) results in the loss of the whole capsule surrounding the bacterium while having no effect on bacterial swimming behavior (Figure 2.9 A-II and C). This has previously been reported to affect the pathogen's interaction with intestinal epithelial cells *in vitro* (Wong *et al.*, 2015) as well as attenuate colonization *in vivo* (Jones *et al.*, 2004; Stahl *et al.*, 2014; Wong *et al.*, 2015).

Many *C. jejuni* isolates, including NCTC11168, possess a type II-C CRISPR/Cas system (Dugar *et al.*, 2013; Louwen *et al.*, 2014). Previously identified as a prokaryotic adaptive immunity system (Makarova *et al.*, 2015; Mohanraju *et al.*, 2016; Koonin *et al.*, 2017), CRISPR/Cas elements of many pathogenic bacteria have also been suggested to play a potential role in virulence (Jerome *et al.*, 2011; Sampson & Weiss, 2013; Sampson *et al.*, 2014; Westra *et al.*, 2014; Li *et al.*, 2016; Müller-Esparza & Randau, 2017). In particular, the *cas9* gene – a hallmark gene of all species harboring a type II CRISPR/Cas system (Makarova *et al.*, 2011) – showed differential expression after passage through a mouse intestine (Jerome *et al.*, 2011). Moreover, deletion of *cas9* in GBS-inducing *C. jejuni* isolates resulted in decreased adherence to and internalization into non-polarized host cells via a potential CRISPR/Cas-mediated regulation of bacterial surface structures (Louwen *et al.*, 2013) while not influencing bacterial motility (Figure 2.9 A-III and C).

Another interesting candidate for governing *C. jejuni* biology is the pleiotropic regulator CsrA, which has previously been implicated in *C. jejuni* biofilm formation, oxidative stress response, infection, and motility (Figure 2.9 A-IV) (Fields & Thompson,

2008; Lucchetti-Miganeh *et al.*, 2008). Specifically, CsrA has recently been identified to mainly bind the major flagellin *flaA* mRNA in *C. jejuni* (Dugar *et al.*, 2016). While *flaA* is repressed by CsrA, it can also act as a sponge to titrate CsrA activity (Figure 2.9 B, *left panel*). Thus, it was not surprising to find a deletion mutant of *csrA* slightly attenuated in its ability to swim in soft agar when compared to wildtype (Figure 2.9 C).

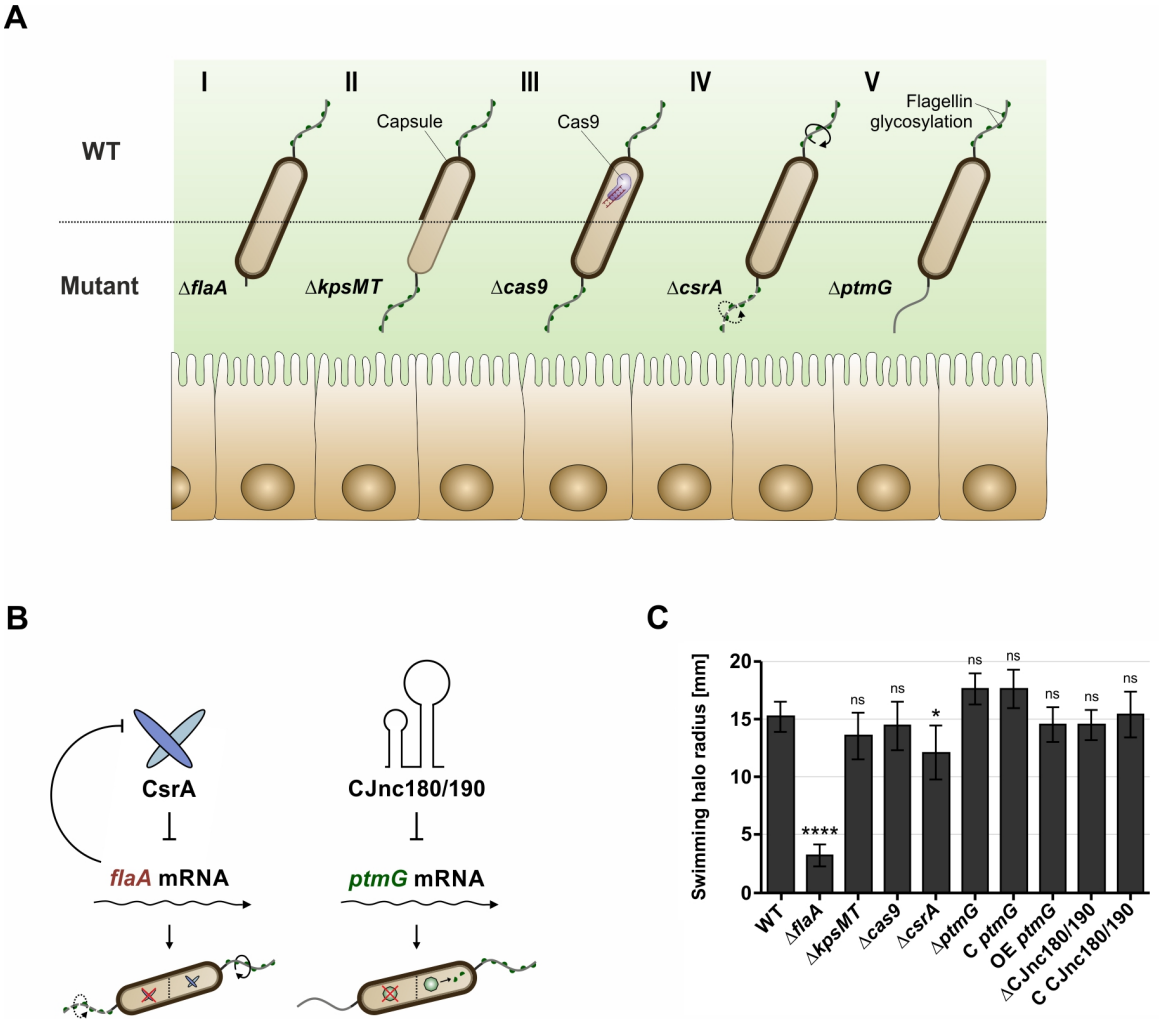

Figure 2.9: Illustration and motility assay of *C. jejuni* deletion mutant strains. (A) Comparison between NCTC11168 wild-type phenotype (*upper panel*) and respective phenotypic manifestation by deletion (*lower panel*) of *flaA* **(I)**, *kpsMT* **(II)**, *cas9* **(III)**, *csrA* **(IV)**, and *ptmG* **(V)**. **(B)** Schematic representation of regulation by *csrA* (*left panel*) and the sRNA pair CJnc180/190 (*right panel*). The pleiotropic regulator CsrA is involved in repression of the *flaA* mRNA. In turn, *flaA* can act as a sponge and titrate CsrA away from other regulatory partners involved in this complex network (*left panel*). The sRNA pair CJnc180/190 has been shown to repress *ptmG* mRNA (Svensson and Sharma, unpublished), which in turn is involved in the legionaminic acid flagellin glycosylation pathway in *C. jejuni*. **(C)** Motility assay of the *C. jejuni* NCTC11168 wildtype (WT), respective deletion mutants (Δ*flaA*, Δ*kpsMT*, Δ*cas9*, Δ*csrA*, Δ*ptmG*, ΔCJnc180/190), complementations (C *ptmG*, C CJnc180/190), and overexpression (OE *ptmG*). Strains were grown overnight in BB liquid culture to mid-log phase (OD_{600} 0.4) and subsequently stabbed into 0.4 % soft agar Mueller-Hinton (MH) plates. After

incubation at 37 °C in a microaerobic environment, motility was measured by determining the swimming halo radius in comparison to wild-type behavior. Bar graphs and corresponding SDs represent the mean of three biological replicates. ****: $p < 0.0001$, *: $p < 0.05$, ns: not significant. The Student's *t*-test was used for statistical analysis.

As the relatively small *C. jejuni* genome (1.6 Mbp) codes for very few putative regulators and only three sigma factors (Parkhill *et al.*, 2000), it was intriguing to discover a strain-specific repertoire of small regulatory non-coding RNAs (sRNAs) using a differential RNA-seq approach (Dugar *et al.*, 2013). Regulatory non-coding RNAs in pathogenic bacteria have previously been found to contribute to diverse virulence-determining mechanisms (Gripenland *et al.*, 2010; Papenfort & Vogel, 2010; Svensson & Sharma, 2016; Heroven *et al.*, 2017; Quereda & Cossart, 2017). Therefore it is plausible to argue that especially *C. jejuni* might depend on its regulatory sRNA repertoire to successfully adapt to different niches in the host ensuring long-term colonization. Of particular interest was the conserved and abundant CJnc180/190 sRNA pair first identified in (Dugar *et al.*, 2013), as it regulates the expression of Cj1324 (*ptmG*) encoded in the *O*-linked flagellin glycosylation island in *C. jejuni* strain NCTC11168 (Svensson and Sharma, unpublished) (Figure 2.9 B, *right panel*).

Glycosylation of flagella in a number of Gram-negative bacteria, including the related Epsilonproteobacterium *H. pylori*, has been reported to play a role in the interaction with eukaryotic cells as well as host cell specificity (Arora *et al.*, 2001; Josenhans *et al.*, 2002; Logan, 2006). The bipolar flagella of *C. jejuni* are decorated with *O*-linked glycans, most of which are derivatives of pseudaminic acid or an acetamidino form of legionaminic acid (Logan *et al.*, 2009). The product of the *ptmG* gene is required for biosynthesis of a legionaminic acid precursor, which is added to NCTC11168 flagellin, whilst having no impact on bacterial motility (Figure 2.9 A-V and C). In line with these observations, PtmG was shown to play a significant role in the colonization of chickens, while being dispensable for *in-vitro* human host-cell interactions (Howard *et al.*, 2009). Consequently, it seemed intriguing to analyze the impact of *ptmG* and its regulatory sRNA pair CJnc180/190 on the *C. jejuni* infection process in the 3D environment of the human intestinal tissue model.

As selected representatives of their respective areas of *C. jejuni* biology, deletion mutants of the above-described genes were tested for their potential to adhere to and get internalized into polarized intestinal epithelial cells in comparison to their ability to interact with a non-polarized 2D monolayer of Caco-2 cells (Figure 2.10 A – D). In chapter 2.5 of this thesis, it was demonstrated that two *C. jejuni* wild-type strains reached similar levels of adherence and internalization into Caco-2 cells after 4 hrs in 2D and 24 hrs in the 3D tissue model (Figure 2.7 B and C). Thus, the same time points were used to test the deletion mutants in the strain background of the motile, rod-shaped isolate NCTC11168. As expected,

a Δ*flaA* mutant showed almost no adherence to the colonic epithelial cells, neither in 2D nor in 3D (Figure 2.10 A). In addition, deletion of the major flagellin also prevented *C. jejuni* from being internalized into polarized (3D) and non-polarized (2D) Caco-2 cells (Figure 2.10 B). This phenotype had been perceived previously in many 2D cell lines as well as in various animal models (Wassenaar *et al.*, 1993; Stahl *et al.*, 2014), suggesting that *C. jejuni* motility is equally important for host cell interaction in the 3D tissue model. An intriguing phenotype could be observed for the *C. jejuni* strain lacking the capsule surrounding the bacterial cell. While deletion of KpsMT led to an increase in bacterial adherence and internalization in conventional 2D monolayer infections, the opposite phenotype was detected in the 3D tissue model (Figure 2.10 A and B). Interaction of *kpsMT*-deficient bacteria with the reconstructed polarized intestinal epithelium yielded a significantly lower percentage of bacterial cells attached to or internalized into host cells when compared to its parental wildtype. These observations in 2D are in line with previously published studies, where deletion of *kpsM* resulted in increased levels of host cell interacting bacteria (Wong *et al.*, 2015). More importantly, *in-vivo* animal infections with a Δ*kpsM* mutant revealed a diminished capacity of this strain to colonize the intestinal tract of chicks (Jones *et al.*, 2004; Wong *et al.*, 2015) as well as the SIGIRR mouse model (Stahl *et al.*, 2014). Thus, the results so far indicate that the intestinal *in-vitro* 3D tissue model can recapitulate *C. jejuni* host cell interactions that can normally only be observed *in vivo*, suggesting a potentially similar colonization strategy of this bacterial pathogen in living tissue and our recreated intestinal microenvironment. As demonstrated for *C. jejuni* strains lacking capsular polysaccharides, bacterial surface structures are important pathogenicity-determining factors. Specifically, ganglioside-like LOS structures on the cell envelope of certain *C. jejuni* isolates have been shown to contribute to immunogenicity and increased virulence (Guerry *et al.*, 2000; Louwen *et al.*, 2008). In GBS-inducing *C. jejuni* strains, a previous study indicated a potential functional link between sialylated LOS and the Type II-C CRISPR/Cas system (Louwen *et al.*, 2013). However, no effect on adherence and/or internalization could be observed in either infection model for a *cas9* deletion mutant in strain NCTC11168 (Figure 2.10 A and B). Although a slight reduction in its adhesion capabilities could be observed for the Δ*cas9* mutant when faced with the polarized surface of the tissue model (Figure 2.10 A), this adherence rate was not significantly different when compared to WT. Additionally, deletion of *cas9* did not abrogate or reduce *C. jejuni* internalization into the 3D tissue model (Figure 2.10 B). As the here used NCTC11168 strain is not a GBS-inducing isolate, Cas9 might not affect colonization of this strain in a similar manner as it does for example *C. jejuni* strain GB11 (Louwen *et al.*, 2013).

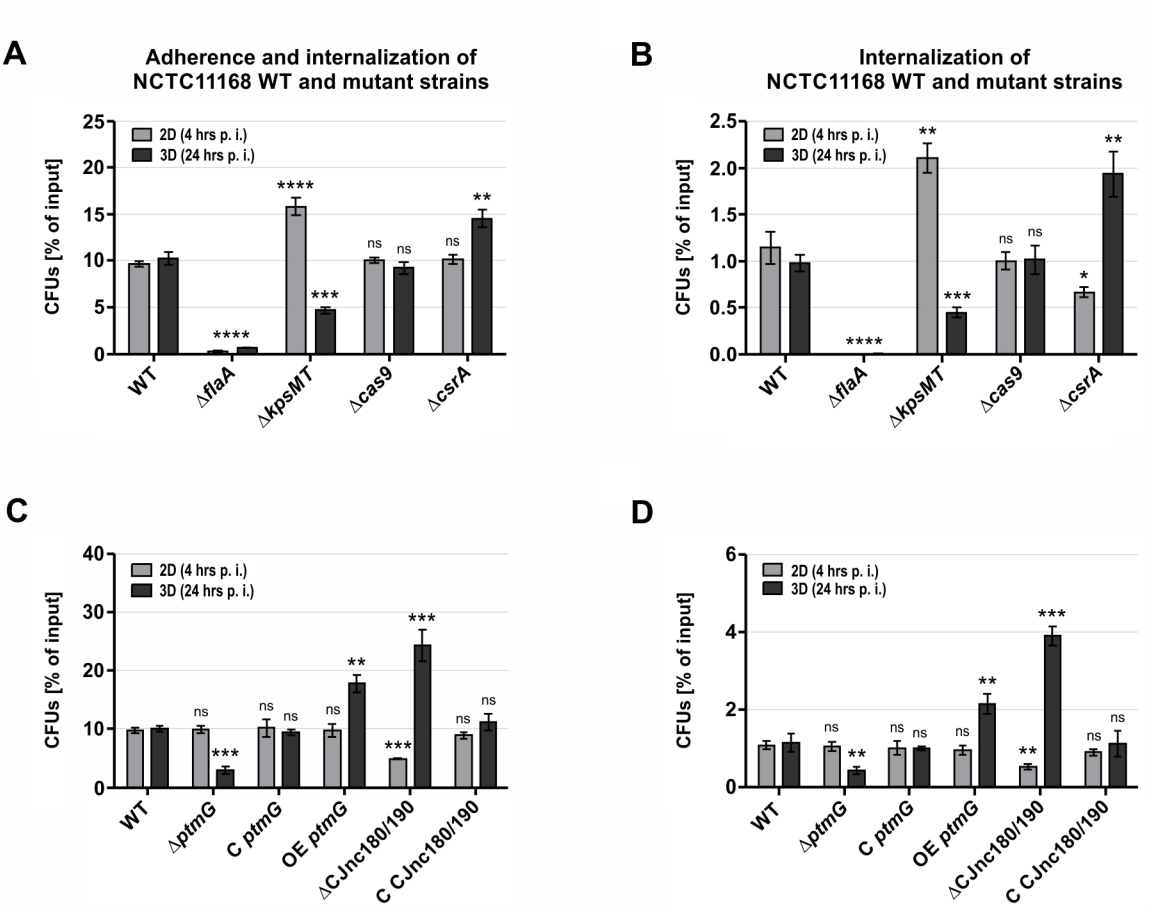

Figure 2.10: Infection outcome of various *C. jejuni* deletion mutants differs between 2D monolayer and 3D tissue model. (A – D) Isolation of CFUs from either 2D Caco-2 monolayers (4 hrs p. i.) or Caco-2 cell-based 3D tissue models (24 hrs p. i.) for *C. jejuni* NCTC11168 wildtype (WT), respective deletion mutants (Δ*flaA*, Δ*kpsMT*, Δ*cas9*, Δ*csrA*, Δ*ptmG*, ΔCJnc180/190), complementations (C *ptmG*, C CJnc180/190), and overexpression (OE *ptmG*). Bacteria that were both adhered to and internalized into the respective infection models are depicted in **(A, C)**, whereas gentamicin-treated models were utilized to isolate internalized bacteria only **(B, D)**. CFUs are depicted as the percentage of their respective input CFUs and represent the mean of three biological replicates with corresponding SDs. Asterisks or ns above each column indicates the significance of the tested mutant strain compared to the wildtype in 2D or 3D. ****: $p < 0.0001$, ***: $p < 0.001$, **: $p < 0.01$, *: $p < 0.05$, ns: not significant. Statistical analyses were performed with the Student's *t*-test.

During colonization of the gastrointestinal tract, *C. jejuni* is faced with different host milieus and defensive barriers. In order to successfully navigate these changing environments and finally establish residence in the human lower intestine, it has to adjust its gene expression according to its surroundings. *In-vitro* 2D infection studies with the *C. jejuni* NCTC11168 Δ*csrA* mutant strain showed no significant reduction in adherence when compared to the wildtype (Figure 2.10 A). However, internalization into non-polarized Caco-2 cells was significantly diminished indicating a dispensability of CsrA for the initial adhesion to the host cells surface but an integer role during the internalization

process and/or intracellular survival (Figure 2.10 B). When faced with the villi and crypt microarchitecture and the polarized epithelium of the tissue model, *csrA*-deficient bacteria were able to increase their adherence to and internalization into host cells (Figure 2.10 A and B). This seemingly opposite phenotype of a Δ*csrA* strain in 2D and 3D infection experiments might suggest a distinctive function of the regulator during colonization and survival in these very contrasting environments. This in turn could indicate a differential regulation by CsrA depending on the surrounding milieu *C. jejuni* is subjected to. Moreover, previous *in-vivo* infection experiments in mice demonstrated that a *csrA*-deficient strain was significantly attenuated to compete against its wildtype (Fields *et al.*, 2016), suggesting an even more diverse role of this regulator depending on whether *C. jejuni* is colonizing a murine or human lower intestine.

To assess whether *ptmG* and/or the sRNA pair CJnc180/190, which regulates expression of *ptmG* (Svensson and Sharma, unpublished), contribute to *C. jejuni* virulence depending on the provided host environment, deletion, complementation, and in the case of *ptmG* an overexpression strain were tested for their adherence (Figure 2.10 C) and internalization (Figure 2.10 D) capabilities. Infection assays with a Δ*ptmG* strain using a confluent, but non-polarized monolayer of Caco-2 cells (2D) confirmed wild-type adherence (Figure 2.10 C) and internalization (Figure 2.10 D) levels (Howard *et al.*, 2009). Remarkably, in the 3D environment of the tissue model, the *ptmG*-deficient mutant displayed a two- to three-fold decrease in both adherence (Figure 2.10 C) as well as internalization (Figure 2.10 D) when compared to the wildtype. This colonization defect could be complemented by expression of the *ptmG* gene in the unrelated *rdxA* (Cj1066) locus, which is frequently used for complementation in *C. jejuni* (Ribardo *et al.*, 2010). Furthermore, approx. 2-fold overexpression of *ptmG* by addition of a second gene copy into the parental wild-type strain led to increased adherence and internalization in the 3D tissue model while having no effect on colonization of non-polarized Caco-2 cells (Figure 2.10 C and D). This indicates a diverging role of flagellar glycosylation, which is seemingly dispensable for host-pathogen interactions with flat host cells but appears to play an integral role when *C. jejuni* comes into contact with polarized epithelial cells. This premise is supported by the observation that a *ptmG*-deficient strain is also impeded in its colonization potential of the chicken intestinal tract (Howard *et al.*, 2009). It was thus very exciting to consider what role the regulation of *ptmG* by the sRNA pair CJnc180/190 would play during these infection experiments. While deletion of sRNAs in bacterial pathogens rarely leads to a macroscopic fitness defect during infection experiments, many non-coding RNAs are in fact differentially regulated during infection suggesting their involvement in host-pathogen interactions (Barquist *et al.*, 2016; Westermann *et al.*, 2016; Westermann, 2018). Likewise, simulation of infection-relevant

conditions also revealed differential expression of a number of *C. jejuni* non-coding RNAs (Taveirne *et al.*, 2013; Kreuder *et al.*, 2017). *C. jejuni* mutants lacking the sRNA pair showed an increased ability to adhere to polarized 3D Caco-2 cells (Figure 2.10 C). This was in addition to the observation of an increased number of intracellular bacteria recovered for ΔCJnc180/190 in the tissue model (Figure 2.10 D). This seemingly hypervirulent phenotype of the sRNA pair deletion mutant exhibits the same trend of increased colonization as an overexpression strain of *ptmG*, albeit to a much higher extent. However, deletion of CJnc180/190 significantly reduced *C. jejuni* adherence (Figure 2.10 C) and internalization (Figure 2.10 D) in conventional 2D monolayer infections. This fitness defect was restored to wild-type levels when the sRNA was expressed in *trans* suggesting that CJnc180/190 is indeed required for proper colonization of non-polarized intestinal host cells. As sRNAs can regulate multiple targets (Svensson & Sharma, 2016), it is perceivable that CJnc180/190 does not only influence expression of *ptmG*. This is supported by (I) the stronger colonization of the tissue model by ΔCJnc180/190 compared to OE *ptmG* and (II) the decreased adherence and internalization in 2D by ΔCJnc180/190 compared to wildtype-like colonization of Δ*ptmG*. It might be interesting to consider that this particular sRNA pair could initiate differential regulation of a variety of target genes depending on the nature of its interacting host cells in addition to the regulatory contribution of the single non-coding RNAs CJnc180 and CJnc190.

Taken together, the above-demonstrated results show that the intestinal 3D tissue model is able to recapitulate previously observed phenotypes of known *C. jejuni* colonization-determining factors such as the major flagellin FlaA. In addition, the tissue model provides the opportunity to compare and/or distinguish requirements of *C. jejuni* biology necessary during colonization of the human intestine and various animal models. This in turn can help to uncover pathogen-specific prerequisites that are uniquely necessary in order to colonize the 3D environment of the human intestinal tract. Moreover, it seems to be sensitive enough to detect the importance of factors such as *ptmG*, which seem to be dispensable for host-pathogen interactions with conventionally used non-polarized cells but might play a role in a three-dimensional host environment (*in vitro* and *in vivo*).

3. Tn-seq analysis of *C. jejuni* 2D and 3D infections identifies novel bacterial factors that contribute to host-pathogen interactions

In the previous chapter of this thesis, an intestinal tissue model was established for infection studies with *C. jejuni* wild-type and mutant strains. This model combines important characteristics of the human intestinal tract such as the three-dimensional villus and crypt architecture of the small intestine, a columnar epithelial cell morphology, and an extracellular matrix component. The model is readily colonized by two commonly used *C. jejuni* wild-type strains for up to five days with strain-specific behavior. Moreover, investigation of mutant strains validated previously known phenotypes upon deletion of recognized *C. jejuni* colonization-determining factors (Figure 2.10). Perhaps most importantly, the 3D environment of the tissue model revealed infection phenotypes for genes (*e.g. ptmG*) that have so far been undetected in standard assays with non-polarized epithelial cells but seem to be indispensable for host-pathogen interactions in an *in-vivo* model (Howard *et al.*, 2009). Consequently, this infection model offers the opportunity to discover additional potential virulence factors using global approaches.

3.1. Construction and characterization of a Tn5 mutant library in *C. jejuni* strain NCTC11168

Recently, deep sequencing has been adapted for global genetic fitness screens of high-density transposon (Tn) mutant libraries in several bacteria (so-called Tn-seq) (Barquist *et al.*, 2013; Chao *et al.*, 2016), including screens for colonization- and virulence-determining factors in pathogenic species. In this approach, the transposon-chromosome junctions in a pool of mutants are sequenced to identify insertion sites before and after a fitness selection. The ratio of insertions in a gene in the output to input libraries can provide information regarding the fitness contributions of that particular gene under the selective conditions. In *C. jejuni*, transposon mutagenesis screens have previously been used to identify potentially essential genes, as well as bacterial factors required for efficient colonization of *in-vitro* cell lines or *in-vivo* animal models including chicken, mouse, and piglets (Hendrixson & DiRita, 2004; Javed *et al.*, 2010; Gao *et al.*, 2014, 2017; Johnson *et al.*, 2014; de Vries *et al.*, 2017a, 2017b). Most of these Tn-seq approaches, including those performed with 2D intestinal epithelial cells, primarily identified flagellar genes as major contributors to a successful colonization. In addition, *C. jejuni* genes that are required for fitness during colonization of the avian or porcine gastrointestinal tract, or 2D human epithelial cell monolayers, might not equally affect disease progression in humans. Thus, one could reason that a global

screen of a high-density Tn mutant library in the 3D Caco-2 cell-based tissue model could reveal additional factors that might be required for *C. jejuni* fitness during colonization of and survival in the native human intestinal tract. To this end, a genome-wide insertion library was established in *C. jejuni* strain NCTC11168 with a modified Tn5 transposon (Svensson, Bischler, and Sharma, unpublished) (Figure 3.1 A).

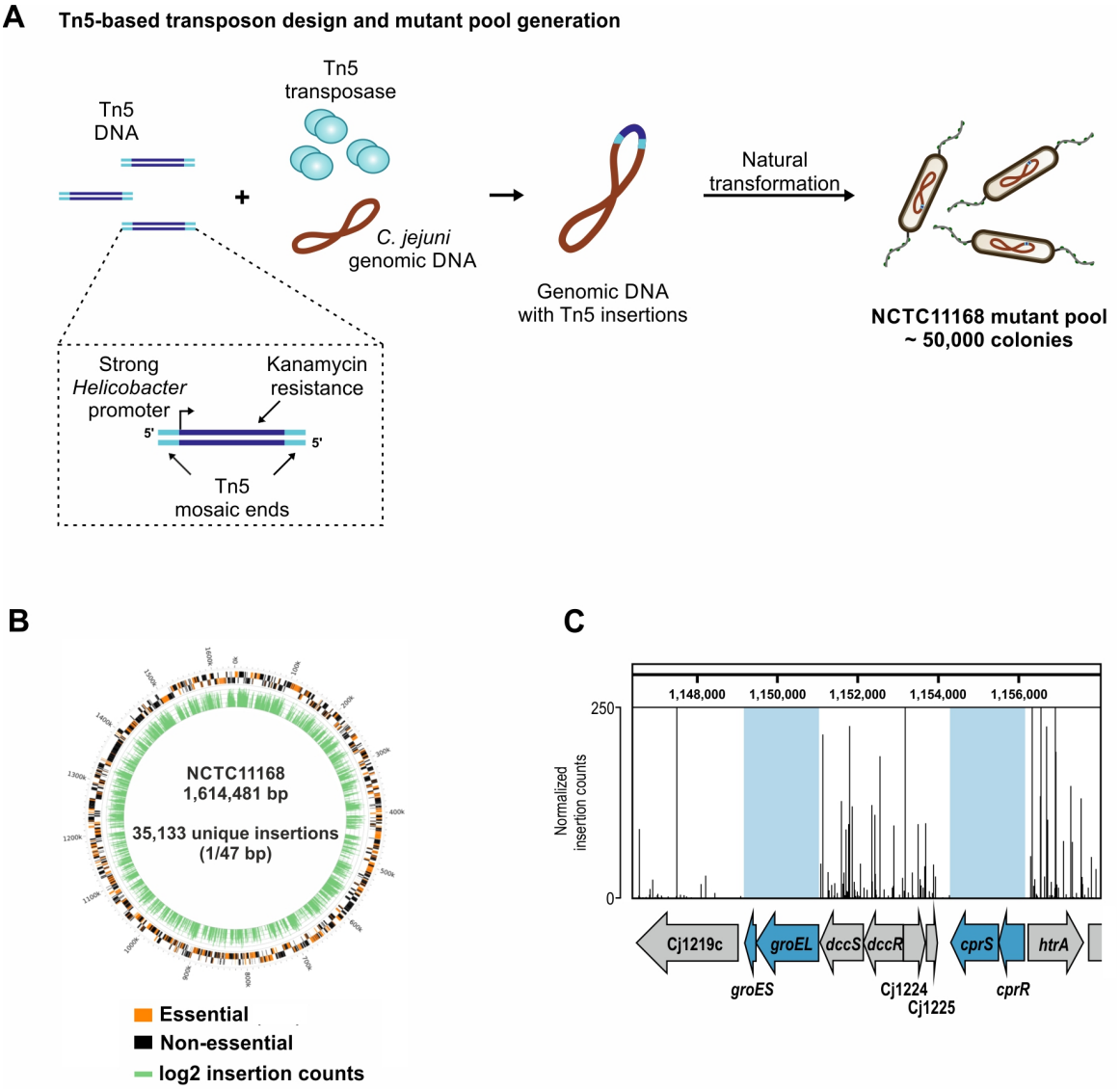

Figure 3.1: Generation and sequencing of a transposon mutant library in *C. jejuni* NCTC11168. **(A)** A Tn5-based transposon mutant library was generated by *in-vitro* transposition into genomic DNA (gDNA) from the *C. jejuni* wild-type strain NCTC11168. First, a *Campylobacter*-specific transposon was constructed with the Tn5 mosaic ends flanking a kanamycin resistance cassette (*aphA-3*) under control of the strong *repG* promoter from the related Epsilonproteobacterium *H. pylori* (Pernitzsch *et al.*, 2014). Mutagenized gDNA was naturally transformed into *C. jejuni* NCTC11168 and approx. 50,000 kanamycin-resistant colonies were collected. **(B)** After isolation of gDNA from the mutant pool, a library was prepared for Illumina sequencing with a Tn5-specific primer and sequenced on an Illumina NextSeq 500 platform. Reads were mapped to the NCTC11168

reference genome (NC_002163) and analyzed via a modified version of the Bio-TraDIS pipeline (Barquist *et al.*, 2016). The plot was generated using Circos (Krzywinski *et al.*, 2009) and depicts insertion site counts per gene (green) in the *C. jejuni* chromosome as well as genes identified as essential (orange) or non-essential (black). **(C)** IGB screenshot for selected loci harboring potentially essential genes, representing insertion counts from the Tn-seq analysis of the mutant library mapped to its reference genome. Blue arrows represent the putative essential genes *groES*, *groEL*, *cprS*, and *cprR* as indicated by the lack of insertions in the light blue areas.

Tn5-based transposons have been successfully used as a basis in other studies for various *C. jejuni* isolates including NCTC11168 (Reid *et al.*, 2008; Stahl & Stintzi, 2011; Mandal *et al.*, 2017). For the mutant library generated in this thesis, a modified transposable element was constructed that contains a kanamycin resistance cassette (*aphA-3*) under the control of a strong *Helicobacter* promoter (P_{repG}) (Pernitzsch *et al.*, 2014) flanked by the Tn5 mosaic ends. After *in-vitro* transposition, the mutagenized genomic DNA was naturally transformed into NCTC11168 wildtype and approx. 50,000 kanamycin-resistant colonies were collected. Characterization of the mutant library was conducted by sequencing of the transposon insertion sites and bioinformatic analysis using a modified protocol of the Bio-TraDIS pipeline (Barquist *et al.*, 2016). This investigation indicated that the library consisted of approx. 30,000 unique insertion mutants well distributed across the *C. jejuni* genome, with an average density of one insertion per 47 bp (Figure 3.1 B). For 439 protein-coding genes, no insertions (that passed our data processing cutoffs) were identified in the original NCTC11168 mutant pool. This suggests that they might be essential under the growth conditions applied to recover the transposon library after natural transformation (MH agar plates for ~ 36 – 48 hrs at 37 °C in a microaerobic environment). This gene set showed approx. 75 % overlap with a compilation of putative essential annotated protein coding genes identified in other studies (Metris *et al.*, 2011; Stahl & Stintzi, 2011; Gao *et al.*, 2014; de Vries *et al.*, 2017a; Mandal *et al.*, 2017). The greatest overlap (72 %) was observed with the table of potentially essential genes provided by (de Vries *et al.*, 2017a). However, only a limited set of the putative essential genes identified in this thesis overlapped with each of the other studies individually (15 – 30 %). Likely explanations for these observations could include a limited number of transposon mutants in previous studies (*e.g.* ~ 7,000 – 10,000 mutants in (Metris *et al.*, 2011) and (Stahl & Stintzi, 2011), respectively), varying growth conditions (*e.g.* 37 °C vs. 42 °C or MH agar vs. blood agar), or the use of different *C. jejuni* strains (*e.g.* NCTC11168 vs. 81-176). In addition, the use of different transposons (*e.g.* Tn5 or Mariner), the applied Tn-seq library preparation protocol, and downstream bioinformatics analyses can markedly influence the outcome of an experiment. All of these factors might have also contributed to a relatively limited overlap of predicted essential genes common to all of these other genome-wide screens. Among genes identified

in all screens, including this thesis, were for example *cprR* (Cj1227c; two-component regulator) and *groES* (Cj1220; co-chaperonin). No insertions could be detected for these potentially essential candidates, which is displayed in a screenshot from the Integrated Genome Browser (IGB; http://genoviz.sourceforge.net/) representing the number of normalized mapped reads per insertion site in the *C. jejuni* NCTC11168 genome (Figure 3.1 C). The essentiality of *cprR* is supported by studies reporting the inability to delete this particular gene (Raphael *et al.*, 2005; Svensson *et al.*, 2009). The lack of transposon insertions in the gene encoding its cognate sensor histidine kinase *cprS* (Cj1226c) indicates that it might also be indispensable for *C. jejuni* viability. However, a previous study showed that while it can be deleted, the resulting mutant has a strong growth defect in broth culture (Svensson *et al.*, 2009). This suggests that the list of putative essential genes identified in this thesis might also include genes whose inactivation results in severely compromised growth and/or survival and are thus not per se essential, but nonetheless lost from or underrepresented in the mutant pool. In addition to *groES*, there were also no insertions found in the chaperone gene *groEL* (Cj1221), which was observed in only one other genome-wide mutagenesis screen in *C. jejuni* (de Vries *et al.*, 2017a). As *groEL* has been reported to be essential for growth of *Salmonella* (Langridge *et al.*, 2009) and *E. coli* (Gerdes *et al.*, 2003; Baba *et al.*, 2006) under many environmental conditions, it might also be required for *C. jejuni* survival and/or growth. On the other hand, genes such as *htrA* (Cj1228c) displayed many transposon insertion sites in the Tn5 based mutant library created here. While it has been shown that *htrA* seems to be essential in the closely related pathogen *H. pylori* (Salama *et al.*, 2004; Hoy *et al.*, 2010), previous studies were able to delete the respective genome locus in *C. jejuni* (Brøndsted *et al.*, 2005; Boehm *et al.*, 2012; Heimesaat *et al.*, 2014), and no other genome-wide screen found *htrA* to be essential for *C. jejuni* survival. All of these observations support the validity of the insertion library constructed here to identify genes potentially involved during host-pathogen interactions. They also illustrate some of the features of Tn-seq screens that could contribute to different candidate gene sets in different experiments or even replicates.

3.2. Genome-wide analysis of *C. jejuni* determinants for interaction with host cells in 2D and 3D

To identify fitness factors required for colonization, the transposon insertion library was screened for mutants exhibiting increased/decreased adherence to or internalization into Caco-2 cells grown as 2D monolayers or as a 3D tissue model (Figure 3.2).

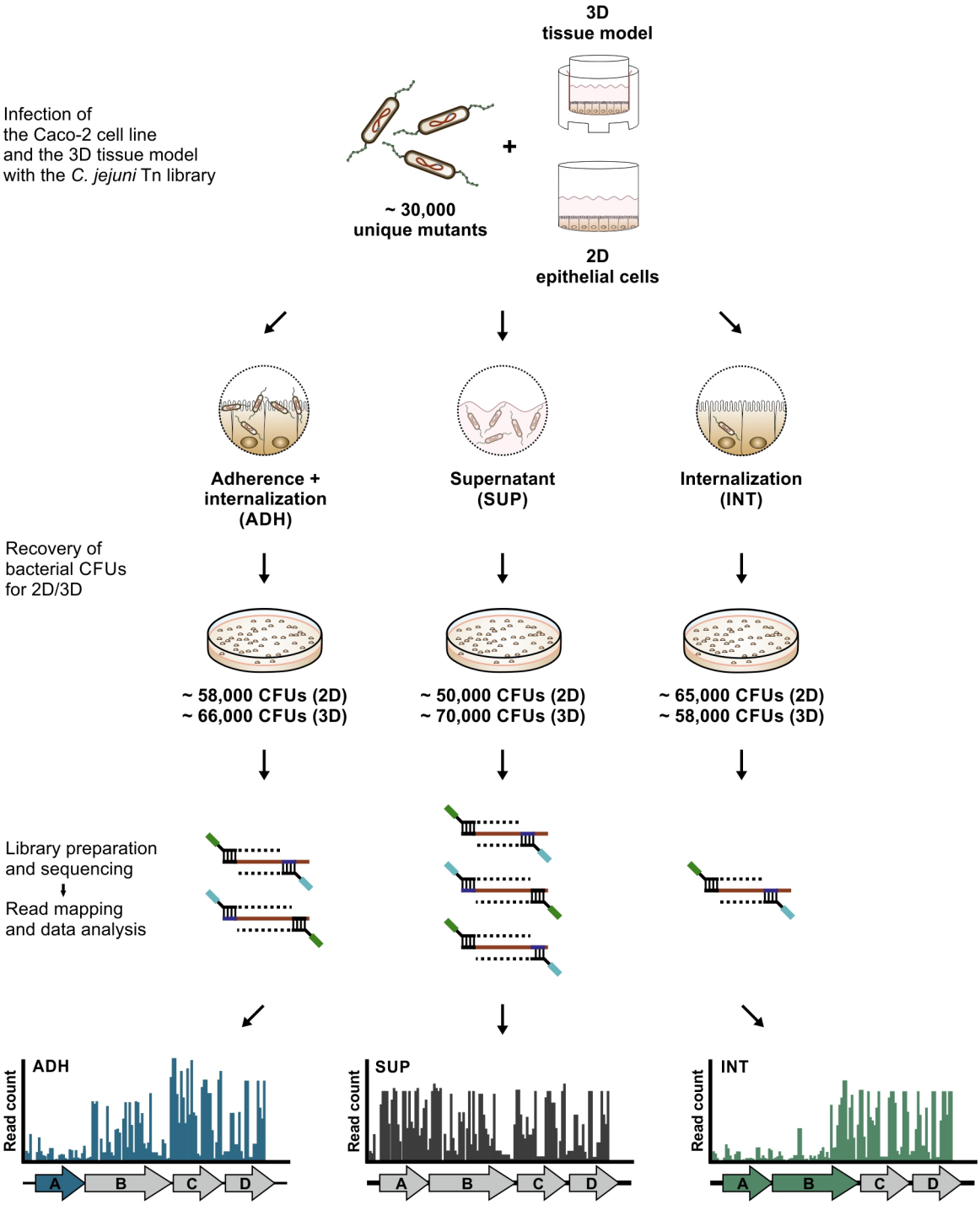

Figure 3.2: Tn-seq infection strategy. The high-density transposon mutant library in *C. jejuni* strain NCTC11168 was grown in an overnight liquid culture to mid-log phase (OD_{600} 0.4). With MOI 20, this liquid culture was used to infect 12 Caco-2 tissue models (six each for ADH and INT) and 12 x 6-well plates with 2D Caco-2 monolayers. After 24 hrs in 3D and 4 hrs in 2D, CFUs were isolated on MH agar plates containing vancomycin and kanamycin for adherent + internalized bacteria (ADH) and non cell-associated bacteria from the supernatant (SUP). After additional 2 hrs treatment with gentamicin to kill extracellular bacteria, CFUs for internalized bacteria only (INT) were plated as well. Bacterial CFUs were recovered on 15 MH agar plates (Ø 140 mm) for each condition with an average colony density of approx. 4,000 CFUs per plate. Subsequently, gDNA was isolated from the colonies pooled from each condition (ADH, INT, and SUP), libraries were prepared and sequenced on an Illumina

NextSeq 500 platform followed by bioinformatic analysis to identify genes with decreased or increased fitness. Comparison of the representation of insertion mutants in the bacterial supernatant (SUP) with that in the bacteria obtained after the infection experiment (ADH or INT) allowed the detection of genes potentially involved in host-pathogen interactions (indicated by the blue and green arrows). The Tn-seq screen was conducted in two independent biological replicates for both 2D and 3D.

As previously shown, the four-hour time point post infection in 2D monolayers resembles a 24-hour time point in the tissue model regarding bacterial load (Figure 2.7). Therefore, these time points were chosen for comparison of the outcomes of a Tn screen between the two models. After 4/24 hours of infection with MOI 20 in the 2D/3D model, bacteria were isolated that were both adherent to and internalized into host cells (ADH). In addition, culture supernatant of all 2D/3D models were pooled into separate samples representing the fraction of non cell-associated bacteria (SUP). Intracellular bacteria (INT) were discerned by an additional treatment of gentamicin for two hours, effectively eliminating all extracellular bacteria. In general, CFUs were determined by plating serial dilutions on MH plates containing vancomycin as well as kanamycin to select for the Tn5 transposon. At least 50,000 colonies each were recovered for SUP, ADH, and INT (both 2D and 3D), from which genomic DNA was extracted and libraries for Illumina sequencing comprised of Tn5-chromosome junctions were prepared. Following read mapping and quality control, insertion counts between non cell-associated bacteria in the supernatant (SUP) and those adherent to (ADH) or internalized into (INT) host cells were compared. Bacteria in the supernatant presumably experience the same cell culture environment as bacteria interacting with the Caco-2 monolayer, without actually being in contact with the host cell. They thus represent the closest comparison possible to screen for transposon mutants directly involved in host-pathogen interactions. Attenuating transposon insertions due to effects of different culture media could therefore most likely be excluded. Moreover, this approach also takes into account that mutants with increased fitness over the 4-/24-hour time course (*e.g.* non-motile mutants) (Wösten *et al.*, 2004; Radomska *et al.*, 2016) may end up being overrepresented in the data, despite having a known infection defect. A cutoff requiring both a $\log_2$ fold change $\geq |1|$ (two-fold change in the ratio of Tn insertion reads in libraries prepared from adherent and/or internalized samples versus those from the supernatant bacteria) and a p-value of ≤ 0.05 were used to identify genes with transposon insertions that displayed altered fitness during the infection experiment.

3.2.1. Tn-seq analysis reveals attenuating transposon insertion mutants

The Tn-seq screen performed in this thesis identified genes previously found in other genome-wide studies to be important for *C. jejuni* host interactions (Hendrixson & DiRita, 2004; Novik *et al.*, 2010; Gao *et al.*, 2014, 2017; Johnson *et al.*, 2014; de Vries *et al.*, 2017a, 2017b). Table 3.1 displays the full list of 135 genes with attenuating transposon insertions.

Table 3.1: Tn-seq analysis for attenuating transposon insertion mutants during NCTC11168 infection in a 2D and 3D environment. Values represent log_2 fold changes of insertion reads obtained from libraries prepared from adherent and internalized samples (ADH) or internalized samples only (INT) versus those from the supernatant bacteria (SUP). Genes that showed a log_2 fold change ≤ 1 in the ratio of Tn insertion reads with a significant p-value ≤ 0.05 are listed in this table in bold numbers. Fold changes depicted in grey represent those that did not pass the set cut-offs, *i.e.* with log_2 fold changes < |1| and/or p-values > 0.05. Genes with less than 10 read counts per condition were excluded from the analysis and their values are not shown (–). References indicate other studies, where a similar search for *C. jejuni* pathogenicity-related fitness factors was conducted, or studies that have previously characterized the role of the respective gene during *C. jejuni* host-pathogen interactions. Genes that have not been identified in previous *in-vitro* or *in-vivo* genome-wide screens for *C. jejuni* factors involved in host-pathogen interactions are highlighted in grey. *****: phase variable gene. **OP**: genes that are expressed as part of an operon structure, in which more genes showed a significant log_2 fold change ≤ 1. Operon structures have been determined according to primary TSS annotations from (Dugar *et al.*, 2013). Detailed description about the present operon structures can be found in Appendix Table 3.1.

ID	Name	Description	2D Tn-seq ADH/INT	3D Tn-seq ADH/INT	References
Motility and chemotaxis					
Cj0549^{OP}	*fliS*	flagellar protein FliS	**-11.63/-11.79**	-0.77/**-3.34**	(Johnson *et al.*, 2014)
Cj1465	*flgN*	hypothetical protein	+2.19/**-9.46**	+0.25/-1.52	(Johnson *et al.*, 2014) (de Vries *et al.*, 2017a)
Cj0040^{OP}		hypothetical protein	+1.77/–	-1.74/**-9.32**	(de Vries *et al.*, 2017a) (Gao *et al.*, 2017)
Cj0163c^{OP}		hypothetical protein	+0.21/-0.94	**-1.88/-7.26**	(Gao *et al.*, 2014)
Cj1026c^{OP}	*flgP*	lipoprotein	+0.82/-0.94	**-2.88/-6.08**	(Sommerlad & Hendrixson, 2007) (Gao *et al.*, 2014) (de Vries *et al.*, 2017a, 2017b)
Cj0454c^{OP}		membrane protein	+0.18/-0.67	**-2.83/-5.88**	(Hendrixson & DiRita, 2004) (Novik *et al.*, 2010) (de Vries *et al.*, 2017a, 2017b) (Gao *et al.*, 2014, 2017)
Cj0336c^{OP}	*motB*	flagellar motor protein MotB	+0.25/-0.76	**-2.85/-5.85**	(Mertins *et al.*, 2013) (de Vries *et al.*, 2017a) (Gao *et al.*, 2014, 2017)
Cj0390	*pflB*	transmembrane protein	+0.19/-0.74	**-2.72/-5.85**	(de Vries *et al.*, 2017a, 2017b) (Gao *et al.*, 2014, 2017)
Cj0455c^{OP}		hypothetical protein/pseudogene	+0.19/-0.79	**-2.80/-5.81**	(de Vries *et al.*, 2017a) (Gao *et al.*, 2017)
Cj1565c	*pflA*	paralysed flagellum protein	-0.22/-0.99	**-2.65/-5.79**	(Novik *et al.*, 2010) (Johnson *et al.*, 2014) (de Vries *et al.*, 2017a, 2017b) (Gao *et al.*, 2014, 2017)

continued on next page

ID	Name	Description	2D Tn-seq ADH/INT	3D Tn-seq ADH/INT	References
Cj1025c^{OP}	*flgQ*	hypothetical protein	-0.14/-0.45	**-2.50/-5.47**	(Sommerlad & Hendrixson, 2007) (Gao *et al.*, 2014) (de Vries *et al.*, 2017a, 2017b)
Cj0337c^{OP}	*motA*	flagellar motor protein MotA	+0.45/**-1.22**	**-2.61/-5.42**	(Johnson *et al.*, 2014) (de Vries *et al.*, 2017a, 2017b) (Gao *et al.*, 2014, 2017)
Cj0060c^{OP}	*fliM*	flagellar motor switch protein FliM	+0.07/-1.06	**-2.22/-5.20**	(Johnson *et al.*, 2014) (de Vries *et al.*, 2017a) (de Vries *et al.*, 2017b) (Gao *et al.*, 2014, 2017)
Cj0061c^{OP}	*fliA*	flagellar biosynthesis RNA polymerase sigma factor	-0.91/**-1.15**	**-2.44/-5.15**	(de Vries *et al.*, 2017a, 2017b) (Gao *et al.*, 2014, 2017)
Cj1024c*	*flgR*	sigma-54 associated transcriptional activator	-0.30/-1.40	-1.02/**-3.96**	(Gao *et al.*, 2014, 2017)
Cj1339c	*flaA*	flagellin A	-1.04/-0.74	**-1.85/-3.91**	(de Vries *et al.*, 2017a) (de Vries *et al.*, 2017b)
Cj0351^{OP}	*fliN*	flagellar motor switch protein FliN	+3.00/+3.33	-1.59/**-3.82**	(de Vries *et al.*, 2017a, 2017b)
Cj0059c	*fliY*	flagellar motor switch protein FliY	-0.25/-0.55	**-2.00/-3.72**	(de Vries *et al.*, 2017a) (de Vries *et al.*, 2017b) (Gao *et al.*, 2014, 2017)
Cj1075	*fliW*	flagellar assembly protein	+1.17/–	**-1.56/-3.61**	(de Vries *et al.*, 2017a)
Cj0319^{OP}	*fliG*	flagellar motor switch protein FliG	-0.29/**-1.44**	**-1.07/-3.24**	
Cj0062c^{OP}		integral membrane protein	+2.00/+2.10	**-1.47/-3.20**	(de Vries *et al.*, 2017a) (Gao *et al.*, 2014, 2017)
Cj0670	*rpoN*	RNA polymerase factor sigma-54	-0.67/**-1.27**	-0.83/**-3.19**	(de Vries *et al.*, 2017a) (de Vries *et al.*, 2017b) (Gao *et al.*, 2014, 2017)
Cj0793	*flgS*	signal transduction histidine kinase	-0.43/-0.78	-0.84/**-3.11**	(de Vries *et al.*, 2017a) (Gao *et al.*, 2014, 2017)
Cj0320^{OP}	*fliH*	flagellar assembly protein FliH	+1.92/+0.81	-0.93/**-3.10**	
Cj1179c	*fliR*	flagellar biosynthesis protein FliR	-0.69/**-1.46**	**-1.03/-3.09**	(Novik *et al.*, 2010) (de Vries *et al.*, 2017a) (de Vries *et al.*, 2017b) (Gao *et al.*, 2014, 2017)
Cj0882c^{OP}	*flhA*	flagellar biosynthesis protein FlhA	-0.69/**-1.36**	-0.96/**-3.99**	(de Vries *et al.*, 2017a, 2017b) (Gao *et al.*, 2014, 2017)
Cj0456c^{OP}		hypothetical protein	+0.52/+0.45	**-2.11/-3.96**	(Hendrixson & DiRita, 2004) (Novik *et al.*, 2010) (de Vries *et al.*, 2017a) (Gao *et al.*, 2014, 2017)
Cj0318^{OP}	*fliF*	flagellar MS-ring protein	-0.19/-0.45	**-1.08/-3.94**	
Cj0041^{OP}	*fliK*	flagellar hook-length control protein	+0.35/-0.90	-0.66/**-3.92**	(Johnson *et al.*, 2014) (de Vries *et al.*, 2017a) (de Vries *et al.*, 2017b)
Cj1675	*fliQ*	flagellar biosynthesis protein FliQ	-0.21/-0.72	-0.93/**-3.91**	(Gao *et al.*, 2014)
Cj0195	*fliI*	flagellum-specific ATP synthase	+0.03/-0.69	-0.77/**-3.83**	(Novik *et al.*, 2010) (de Vries *et al.*, 2017a) (Gao *et al.*, 2014, 2017)
Cj0820c	*fliP*	flagellar biosynthesis protein FliP	-0.59/-0.57	**-1.07/-3.65**	(de Vries *et al.*, 2017a, 2017b) (Gao *et al.*, 2014, 2017)
Cj1462	*flgI*	flagellar basal body P-ring protein	-0.14/+0.84	+0.04/**-3.63**	(Johnson *et al.*, 2014) (de Vries *et al.*, 2017a)↑
Cj0064c	*flhF*	flagellar biosynthesis regulator FlhF	-0.79/-1.01	**-1.03/-3.59**	(Novik *et al.*, 2010) (Gao *et al.*, 2014, 2017)
Cj0769c	*flgA*	flagellar basal body P-ring biosynthesis protein FlgA	-0.41/+0.37	-0.70/**-3.57**	
Cj0335	*flhB*	flagellar biosynthesis protein FlhB	-0.38/-0.46	-0.88/**-3.55**	(Johnson *et al.*, 2014) (de Vries *et al.*, 2017a, 2017b) (Gao *et al.*, 2014, 2017)
Cj1497c	*fliJ*	hypothetical protein	+0.37/-0.03	-0.60/**-3.53**	(Gao *et al.*, 2014)
Cj0687c	*flgH*	flagellar basal body L-ring protein	-0.71/-0.59	-0.67/**-3.47**	(Novik *et al.*, 2010) (de Vries *et al.*, 2017a)

continued on next page

ID	Name	Description	2D Tn-seq ADH/INT	3D Tn-seq ADH/INT	References
Cj0977		hypothetical protein	+0.05/+0.54	**-2.20/-3.26**	(Goon *et al.*, 2006) (Novik *et al.*, 2010) (de Vries *et al.*, 2017a, 2017b) (Gao *et al.*, 2014, 2017)
Cj0697	*flgG2*	flagellar basal-body rod protein	–/–	+0.30/**-3.25**	
Cj1334	*maf3*	hypothetical protein	-0.53/-0.74	**-1.19/-3.09**	(Johnson *et al.*, 2014) (de Vries *et al.*, 2017a)
Cj1729c	*flgE2*	flagellar hook protein FlgE2	–/-0.07	-0.36/**-2.96**	(Novik *et al.*, 2010) (Johnson *et al.*, 2014) (de Vries *et al.*, 2017a) (de Vries *et al.*, 2017b)
Cj0548^{OP}	*fliD*	flagellar hook-associated protein 2	-0.48/-2.14	-0.84/**-2.75**	(Johnson *et al.*, 2014) (de Vries *et al.*, 2017a) (de Vries *et al.*, 2017b)
Cj1466	*flgK*	flagellar hook-associated protein FlgK	-0.90/-4.32	-0.39/**-2.62**	(Johnson *et al.*, 2014) (de Vries *et al.*, 2017a) (de Vries *et al.*, 2017b) (Gao *et al.*, 2014, 2017)
Cj0887c		flagellin	-0.76/-2.57	-0.36/**-2.26**	(de Vries *et al.*, 2017a, 2017b)
Cj1338c	*flaB*	flagellin B	**-2.03**/-0.22	-0.07/-0.85	(de Vries *et al.*, 2017a, 2017b)
Cj0162c^{OP}	*flgW*	periplasmic protein	**+1.76**/+1.04	-0.14/**-1.95**	(Gao *et al.*, 2014)
Cj1340c^{OP}		motility protein	-0.38/-0.07	-0.92/**-1.94**	(Golden & Acheson, 2002) (Novik *et al.*, 2010)
Cj1110c	*cetZ*	MCP-type signal transduction protein	**-1.81/-1.89**	-0.29/-0.74	(de Vries *et al.*, 2017a, 2017b)
Cj0042^{OP}	*flgD*	flagellar hook assembly protein	+0.72/+1.35	+0.06/**-1.56**	(Johnson *et al.*, 2014) (Gao *et al.*, 2017)
Cj0043^{OP}	*flgE*	flagellar hook protein FlgE	**-1.40**/-0.70	+0.02/+0.51	(de Vries *et al.*, 2017a)
Cj0019c		MCP-domain signal transduction protein	-0.64/**-1.10**	+0.23/+0.23	(Vegge *et al.*, 2009) (de Vries *et al.*, 2017a, 2017b)
Flagella modifications					
Cj1316c	*pseA*	pseudaminic acid biosynthesis protein PseA	+0.28/-0.55	**-1.40/-3.29**	(Naikare *et al.*, 2013) (Gao *et al.*, 2014) (de Vries *et al.*, 2017a, 2017b)
Cj1317	*pseI*	pseudaminic acid synthase	–/–	-0.57/**-3.26**	
Cj1333^{OP}	*pseD*	protein PseD	-0.77/-0.56	**-1.67/-3.17**	(Johnson *et al.*, 2014)
Cj1337	*pseE*	protein PseE	+0.19/-1.88	-0.36/**-2.64**	(de Vries *et al.*, 2017a) (de Vries *et al.*, 2017b)
Cj1293	*pseB*	UDP-N-acetylglucosamine 3.6-dehydratase	-0.58/-1.88	-0.46/**-2.47**	(Gao *et al.*, 2014) (de Vries *et al.*, 2017b)
Cj1329	*ptmE*	sugar-phosphate nucleotide transferase	**+2.48/+3.00**	**-1.39/-1.64**	
Cj1331^{OP}	*ptmB*	CMP-N.N'-diacetyllegionaminic acid synthase	**-1.61**/-0.07	+0.08/-0.47	
Cj1332^{OP}	*ptmA*	flagellin modification protein A	-0.33/-0.71	-0.75/**-1.48**	
Cj1324	*ptmG*	hypothetical protein	**-1.14**/-0.69	-0.24/-0.06	
Previously reported virulence factors					
Cj0788	*ciaD*	hypothetical protein	-0.05/-0.42	-0.55/**-3.12**	(Novik *et al.*, 2010) (Samuelson *et al.*, 2013)
Cj1029c	*mapA*	outer membrane lipoprotein MapA	**-2.08/-1.88**	-0.03/-0.71	(Johnson *et al.*, 2014) (de Vries *et al.*, 2017a) (Gao *et al.*, 2017)
Cj0268c		transmembrane protein	**-1.25/-1.03**	+0.19/**-1.06**	(Novik *et al.*, 2010) (Tareen *et al.*, 2013) (Heimesaat *et al.*, 2014) (Johnson *et al.*, 2014) (de Vries *et al.*, 2017a) (Gao *et al.*, 2014, 2017)

continued on next page

ID	Name	Description	2D Tn-seq ADH/INT	3D Tn-seq ADH/INT	References
Broad regulatory function					
Cj0883c^{OP}		transcriptional regulator	-0.35/-0.11	+0.28/**-2.49**	(de Vries *et al.*, 2017a) (de Vries *et al.*, 2017b) (Gao *et al.*, 2014, 2017)
Stress-response and DNA-related processes					
Cj1473c	*ctsP*	ATP/GTP-binding protein	**-13.49**/+0.04	+0.42/+1.04	
Cj0635		Holliday junction resolvase-like protein	**-8.75**/-1.73	–/–	
Cj0011c		non-specific DNA binding protein	-4.14/**-6.10**	**+2.65/+2.67**	
Cj1586	*cgb*	single domain hemoglobin	-0.77/**-1.67**	-0.22/-0.51	
Cj1516		oxidoreductase	-0.58/**-1.14**	0.00/+0.32	
Cj0170*		hypothetical protein	-0.45/**-1.05**	+0.19/-0.23	
Iron uptake and metabolism					
Cj1398	*feoB*	ferrous iron transport protein	**-1.34**/-0.86	-0.10/-0.52	
Cj0173c	*cfbpC*	iron-uptake ABC transporter ATP-binding protein	**-1.02/-1.31**	+0.02/-0.14	
Cj1224	*herB*	iron-binding protein / hemerythrin	-0.85/-0.26	-0.22/**-1.01**	(Johnson *et al.*, 2014) (de Vries *et al.*, 2017a)
General cell processes and metabolism					
Cj0332c	*ndk*	nucleoside diphosphate kinase	**-13.12**/+1.17	-0.02/+0.66	
Cj0193c	*tig*	trigger factor	**-10.92**/-1.95	-0.17/+0.85	
Cj0997		rRNA small subunit methyltransferase G	**-9.01**/-0.57	-0.89/+0.45	(de Vries *et al.*, 2017b)
Cj1379	*selB*	selenocysteine-specific elongation factor	**-5.50**/-0.78	-0.21/+1.04	
Cj1268c	*mnmC*	bifunctional tRNA (mnm(5)s(2)U34)-methyltransferase/FAD-dependent cmnm(5)s(2)U34 oxidoreductase	-0.55/-0.52	**-2.13/-2.72**	
Cj0846		metallophosphoesterase	-0.26/+0.41	-0.11/**-1.93**	
Cj0965c		acyl-CoA thioester hydrolase	**-1.65**/-0.44	+0.13/-0.04	
Amino acid transport and metabolism					
Cj0762c	*aspB*	aspartate aminotransferase	**-13.78**/-0.68	+0.53/+1.04	(Novik *et al.*, 2010) (Gao *et al.*, 2017)
Antibiotic resistance and bile tolerance					
Cj0367c	*cmeA*	multidrug efflux pump protein	-0.27/-0.52	-0.28/**-1.51**	(Novik *et al.*, 2010)
Cj0560		MATE family transport protein	**-1.20**/-0.91	+0.03/+0.31	(Johnson *et al.*, 2014)
Cj1687		efflux protein	-0.98/**-1.14**	+0.07/+0.18	(Johnson *et al.*, 2014)
Energy production and respiration					
Cj0688	*pta*	phosphate acetyltransferase	+0.82/+1.64	**-2.76**/-1.26	(de Vries *et al.*, 2017a, 2017b) (Gao *et al.*, 2017)
Cj1020c		cytochrome C	–/–	-0.94/**-2.24**	(de Vries *et al.*, 2017a) (Gao *et al.*, 2017)
Cj0580c		coproporphyrinogen III oxidase	**-1.64**/-0.83	+0.08/+0.17	
Cj1192	*dctA*	C4-dicarboxylate transport protein	**-1.23**/-0.37	-0.10/-0.64	
Cj0623	*hypB*	hydrogenase isoenzymes formation protein	**-1.09**/-0.48	+0.20/-0.05	

continued on next page

ID	Name	Description	2D Tn-seq ADH/INT	3D Tn-seq ADH/INT	References
Cell wall, membrane, and envelope biogenesis					
Cj1060c		membrane protein	**-13.12/-13.27**	-0.75/+0.18	
Cj0520		membrane protein	**-13.10**/-0.14	+0.19/-0.44	
Cj1115c		phosphatidylserine decarboxylase	**-13.48**/-1.85	-0.26/+0.38	(Gao *et al.*, 2017)
Cj0844c		integral membrane protein	-0.85/**-13.90**	+0.35/+0.17	(de Vries *et al.*, 2017a) (Gao *et al.*, 2017)
Cj0906c	*pgp2*	peptidoglycan hydrolase	–/–	-1.40/**-8.26**	(Frirdich *et al.*, 2014)
Cj1626c		membrane protein	**-2.06/-1.27**	-0.38/-0.80	
Cj0423		integral membrane protein	**-1.92**/-1.71	-0.49/-0.61	
Cj0183		integral membrane protein	**-1.69/-1.31**	-0.02/-0.60	(Salamasznska-Guz *et al.*, 2013) (de Vries *et al.*, 2017a)
Cj0236c		integral membrane protein	-0.16/-0.52	+0.16/**-1.40**	
Cj1670c	*cgpA*	Glycoprotein CgpA	-0.23/-0.49	-0.08/**-1.38**	(de Vries *et al.*, 2017b) (Gao *et al.*, 2017)
Cj1424c	*gmhA2*	phosphoheptose isomerase	-0.20/-0.43	+0.02/**-1.09**	
Cj0753c	*tonB3*	TonB transport protein	-0.66/**-1.37**	-0.29/+0.41	(Naikare *et al.*, 2013)
Cj0352		transmembrane protein	-0.44/**-1.30**	-0.18/-0.54	
Housekeeping and non-coding RNAs					
CJnc170		small non-coding RNA	**-12.44**/+0.98	-0.35/-1.82	
Cj0458c	*miaB*	tRNA-2-methylthio-N(6)-dimethylallyladenosine synthase	+0.18/**-11.72**	–/+0.47	(Johnson *et al.*, 2014)
Cjp25	*tRNASer*	tRNA-Ser	**-11.51**/-0.72	+0.39/–	
Cjr09		5S ribosomal RNA	**-7.33**/+0.66	**-2.14**/-0.49	
CJnc20		small non-coding RNA	**-1.78**/-0.32	+0.04/-0.42	
Unknown function					
Cj0959c*		membrane protein insertion efficiency factor	-1.68/**-14.00**	+0.69/-1.24	
Cj1084c		ATP/GTP-binding protein	**-13.39**/-0.74	+0.29/0.00	
Cj0496		hypothetical protein	-1.04/**-13.27**	–/–	
Cj0396c		lipoprotein	**-12.73**/-1.76	–/–	
Cj1079^{OP}		periplasmic protein	-0.89/**-11.25**	-0.74/+0.63	
Cj0892c		periplasmic protein	+0.12/**-1.11**	**-2.64/-5.52**	(Gao *et al.*, 2017)
Cj0978c		lipoprotein	-1.77/+0.07	**-2.52/-5.09**	(de Vries *et al.*, 2017a)
Cj1643*		periplasmic protein	+0.92/–	**-2.27/-3.75**	
Cj0808c^{OP}		hypothetical protein	–/–	-1.54/**-3.27**	
Cj0984		hypothetical protein	**-2.57**/-0.86	+0.08/+0.17	
Cj0733		HAD-superfamily hydrolase	-1.68/**-2.54**	+0.46/+0.22	
Cj0809c^{OP}		hydrolase	**-1.43/-1.72**	**-1.07/-2.46**	
Cj0350^{OP}		hypothetical protein	**-2.31/-2.21**	+0.20/**-1.06**	
Cj1240c		periplasmic protein	-0.76/**-2.07**	+0.36/+0.90	
Cj0118		hypothetical protein	-0.74/**-1.91**	-0.19/+0.01	
Cj0377		AAA ATPase	**-1.45/-1.14**	-0.12/-0.49	
Cj0719c		hypothetical protein	**-1.39**/-0.34	+0.03/-0.39	(Song *et al.*, 2004)
Cj0199c		periplasmic protein	-0.60/**-1.33**	+0.11/-0.28	
Cj0730		ABC transporter permease	**-1.27/-1.04**	-0.36/+0.01	(de Vries *et al.*, 2017a)
Cj1343c^{OP}		periplasmic protein	**-1.26**/-0.74	-0.39/-0.72	(de Vries *et al.*, 2017a)
Cj0168c		periplasmic protein	-1.04/**-1.21**	+0.32/+0.17	
Cj0998c		periplasmic protein	-0.64/**-1.21**	-0.05/-0.30	

continued on next page

ID	Name	Description	2D Tn-seq ADH/INT	3D Tn-seq ADH/INT	References
Cj0761		hypothetical protein	+0.08/-0.22	-0.24/**-1.09**	
Cj1532		periplasmic protein	**-1.01**/**-1.06**	-0.02/-0.22	(de Vries *et al.*, 2017b)
Cj1078^{OP}		periplasmic protein	-0.69/**-1.06**	+0.02/+0.40	
Cj1552c	*mloB*	hypothetical protein	**-1.06**/-0.90	+0.17/-0.02	
Cj0849c		hypothetical protein	-0.56/-0.23	-0.49/**-1.02**	

First, the list of factors required for 2D Caco-2 infection was analyzed. Infection of monolayers with the Tn library revealed 43 genes with lower representation in the ADH library and 42 genes with underrepresentation in the INT library, compared to the library constructed from the non cell-associated bacteria in the supernatant (Figure 3.3 A and Table 3.1). Shared between ADH and INT (14 genes in total) were mostly genes encoding for hypothetical proteins, but also motility- and chemotaxis-related genes, as well as genes involved in the cell envelope (*Cell wall, membrane, and envelope biogenesis*) (Figure 3.3 B). Moreover, two previously identified virulence factors of *C. jejuni* (Cj0268c and *mapA*) (Tareen *et al.*, 2013; Johnson *et al.*, 2014) were also among the genes with a decreased insertion ratio compared to the supernatant bacteria for ADH and INT. 29 Tn insertion mutants were impaired solely for adherence to the Caco-2 monolayer and spanned all functional categories including for example many genes involved in *General cell processes and metabolism* (*e.g. ndk*, *tig*, *selB*) or *Cell wall, membrane, and envelope biogenesis* (*e.g.* Cj0520 and Cj1115c) (Figure 3.3 A and B). Among the 28 insertion mutants unique to 2D INT were mainly genes with so far unknown function and those with a role in *Motility and chemotaxis* (Figure 3.3 B). In addition, disruption of *cgb* (single domain hemoglobin) and Cj1516 (putative oxidoreductase) also resulted in a specific fitness disadvantage during internalization of 2D Caco-2 cells. Cj1516 has been implicated in maintaining copper homeostasis (Hall *et al.*, 2008) and *cgb* is known to play a role in tolerance of nitrosative stress (Smith *et al.*, 2011). It is important to mention that Tn insertions identified in the INT library could not just point towards bacterial genes involved in host cell invasion or uptake, but also those contributing to successful intracellular survival including metabolic adjustments or adaptation to *e.g.* oxidative stress. Thus, Cj1516 and/or *cgb* could also contribute to optimal intracellular survival. Together, this suggests that the here-performed Tn-seq infection experiment in 2D could detect previously identified *C. jejuni* host interaction factors.

Next, genes required for fitness in the 3D tissue model were evaluated. This analysis identified 33 genes showing decreased insertion counts for the ADH library and 74 genes with underrepresented insertion counts for internalization (Figure 3.3 C and Table 3.1).

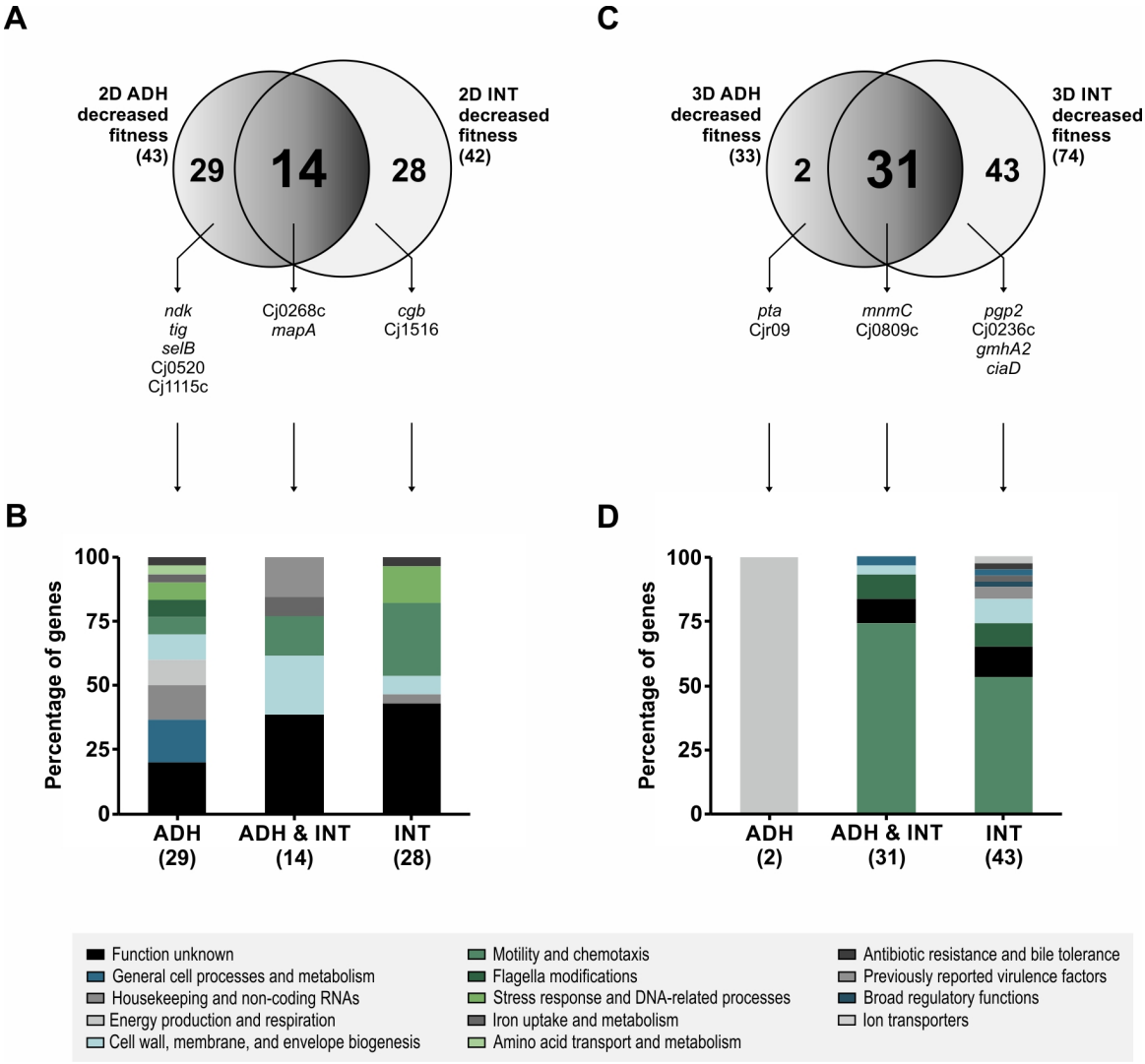

Figure 3.3: Decreased fitness genes identified by Tn-seq. (A, C) Venn diagrams showing the overlap between genes with decreased fitness during adherence to and internalization into 2D Caco-2 cells **(A)** or the 3D tissue model **(C)**. The total number of genes detected in each condition is indicated in brackets. For an overview of all detected genes with decreased fitness see also Table 3.1. **(B, D)** The total number of genes for 2D/3D adherence only (ADH), internalization only (INT), or shared between 2D/3D adherence and internalization (ADH & INT) was manually assessed, and the percentage of genes belonging to self-assigned functional categories was calculated. Each bar graph is composed of the proportional share of genes in the respective cellular processes.

Not surprisingly, the 31 identified gene insertions equally affecting adherence to and internalization into host cells were almost exclusively involved in *Motility and chemotaxis* and *Flagella modifications* (Figure 3.3 D). Exceptions were, for example, Tn insertion counts in *mnmC* (putative bifunctional tRNA methyltransferase/FAD-dependent oxidoreductase) and Cj0809c (putative hydrolase). There were only two Tn insertion mutants (Cjr09, *pta*) uniquely attenuated for adherence to the tissue model (Figure 3.3 C and D). This included the phosphate acetyltransferase Pta, which is required for the so-called “acetate switch” in

C. jejuni stationary growth phase, where the bacteria change from acetate excretion to acetate uptake (Wright *et al.*, 2009). Previous studies indicated that inactivation of *pta* seems to exclusively affect colonization of the mouse (Gao *et al.*, 2017) and pig intestinal tract, but not the GIT of chicken (de Vries *et al.*, 2017a, 2017b), where *C. jejuni* lives as a commensal. The observation that this particular Tn mutant is also attenuated in colonizing the intestinal tissue model coupled with the fact that Pta does not seem to be required for interaction with non-polarized intestinal Caco-2 cells (this thesis; (de Vries *et al.*, 2017a), supports the conclusion that the *in-vitro* 3D microarchitecture could be a suitable environment to study factors required for pathogenesis of *C. jejuni* reflective of host-pathogen interactions *in vivo*. Genes with decreased insertion counts specific for internalization in 3D (43 candidates) predominantly reflected those related to *Motility and chemotaxis* (Figure 3.3 D). In line with many previous studies, this stresses once again the absolute requirement of motility-related factors for *C. jejuni* host-cell interactions *in vitro* and *in vivo* (Yao *et al.*, 1994; Hendrixson & DiRita, 2004; Guerry, 2007; Young *et al.*, 2007; Gao *et al.*, 2014; de Vries *et al.*, 2017a). Among other Tn insertion mutants specifically attenuated for internalization in the 3D tissue model were those involved in *Cell wall, membrane, and envelope biogenesis* (Figure 3.3 D) such as *pgp2* (LD-carboxypeptidase), Cj0236c (putative integral membrane protein), or *gmhA2* (putative phosphoheptose isomerase). In addition to these candidates, a Tn insertion mutant of *ciaD* (*Campylobacter* invasion antigen D) showed decreased fitness during internalization as well, supporting a previous observation that CiaD is required for host cell invasion (Samuelson *et al.*, 2013).

In summary, infection of the novel 3D tissue model with a Tn5-based *C. jejuni* mutant library was able to identify many of the genes previously reported to be required for efficient bacterial colonization *in vitro*. More importantly, the Tn-seq study in the reconstructed intestinal mucosa additionally revealed many factors so far only uncovered *in vivo*, and many that were specific for the human 3D tissue environment.

The set-up of this genome-wide screen for *C. jejuni* fitness factors allowed for a direct comparison between genes required for efficient colonization of a non-polarized intestinal monolayer versus the 3D microenvironment presented by the tissue model. Consequently, genes that solely showed decreased fitness in the 3D tissue model were identified. Interestingly, there was very little overlap between the 2D and 3D datasets (Figure 3.4 A), with only 12 Tn insertion mutants exhibiting a decreased fitness in both infection models, namely *fliS*, *fliA*, *fliG*, *fliR*, *flhA*, *motA*, *rpoN*, Cjr09, Cj0268c, Cj0350, Cj0809c, and Cj0892c. More than half of the genes common between the two infection models encoded for motility-related proteins, which is not surprising, as the value of mobility for *C. jejuni* has undoubtedly been proven. This is supported by a functional enrichment

analysis using an existing functional classification (Gundogdu *et al.*, 2007) of genes from strain NCTC11168 (Figure 3.4 B – D). For genes common between the infection models, the only significantly enriched functional category was *Surface structures* and included genes involved in flagella biogenesis or the flagella motor (corresponding to the self-assigned category *Motility and chemotaxis* in Table 3.1) (Figure 3.4 C). Beyond flagellar genes, Tn insertions in the previously identified virulence factor Cj0268c and in three genes encoding proteins with unknown function (Cj0350, hypothetical protein; Cj0809c, putative hydrolase; Cj0892c, periplasmic protein) resulted in decreased fitness in both infection models (Figure 3.4 A). Remarkably, attenuating Tn insertions in genes related to *General cell process and metabolism*, *Iron uptake and metabolism*, *Amino acid transport and metabolism*, and *Cell wall, membrane, and envelope biogenesis* affected adherence or internalization in only one of the infection models, with no overlap between genes appearing in both datasets (Table 3.1). This indicates a very specific involvement of genes required for colonization of either a non-polarized cell monolayer or the environment presented by the intestinal tissue model.

Significantly enriched genes unique to the 2D dataset belonged to *Periplasmic proteins* and *Membranes, lipoproteins, and porins* (Figure 3.4 B). All of the gene products found in the here-performed screen that are assigned to the periplasmic space by their annotations are still uncharacterized and remain without a known function. This included for example the Cj1079 transcript, which has previously been described to be up-regulated in the presence of bile salts (Malik-Kale *et al.*, 2008). However, as the precise role in these processes remains to be elucidated, it is still unclear how disruption of these genes might impact the adherence to and/or internalization into unpolarized intestinal cells by *C. jejuni*. The second highest enriched group consisted of genes related to integral membrane proteins and lipoproteins (Figure 3.4 B). Among those were known pathogenicity-contributing factors, such as *mapA* (Johnson *et al.*, 2014), but also many genes with so far unknown function such as Cj0183. A putative ortholog of a TlyC-like hemolysin, Cj0183 has previously been implicated to play an additive role in *C. jejuni* internalization into Caco-2 cells together with Cj0588 (Sałamaszyńska-Guz & Klimuszko, 2008). Disruption of Cj1060c resulted in the overall highest fitness defect ($\log_2$ fold change ≈ -14) for adherence and internalization to unpolarized Caco-2 cells (Table 3.1). With a predicted length of only 36 amino acids, Cj1060c is considered a small protein, which are polypeptides encoded by small open reading frames (< 50 codons) (Storz *et al.*, 2014). As only a handful of small proteins have been characterized in bacterial pathogens, it is intriguing to consider that Cj1060c might play such a pivotal role during *C. jejuni* interaction with host cells, in particular due to the absence of many other bacterial virulence factors in this zoonotic pathogen. Along the same line, the two sRNAs CJnc170 and CJnc20 were among the

candidates uniquely required for bacterial interaction with host cells in a 2D environment (Figure 3.4 A). None of the sRNAs so far identified in *C. jejuni* (Dugar *et al.*, 2013; Porcelli *et al.*, 2013) has previously been implicated in *C. jejuni* pathogenesis. However, one study has reported a potential regulation of flagellar genes by CJnc170, which in turn could theoretically influence the infection process even though they found that deletion of CJnc170 did not affect host cell internalization (Le *et al.*, 2015).

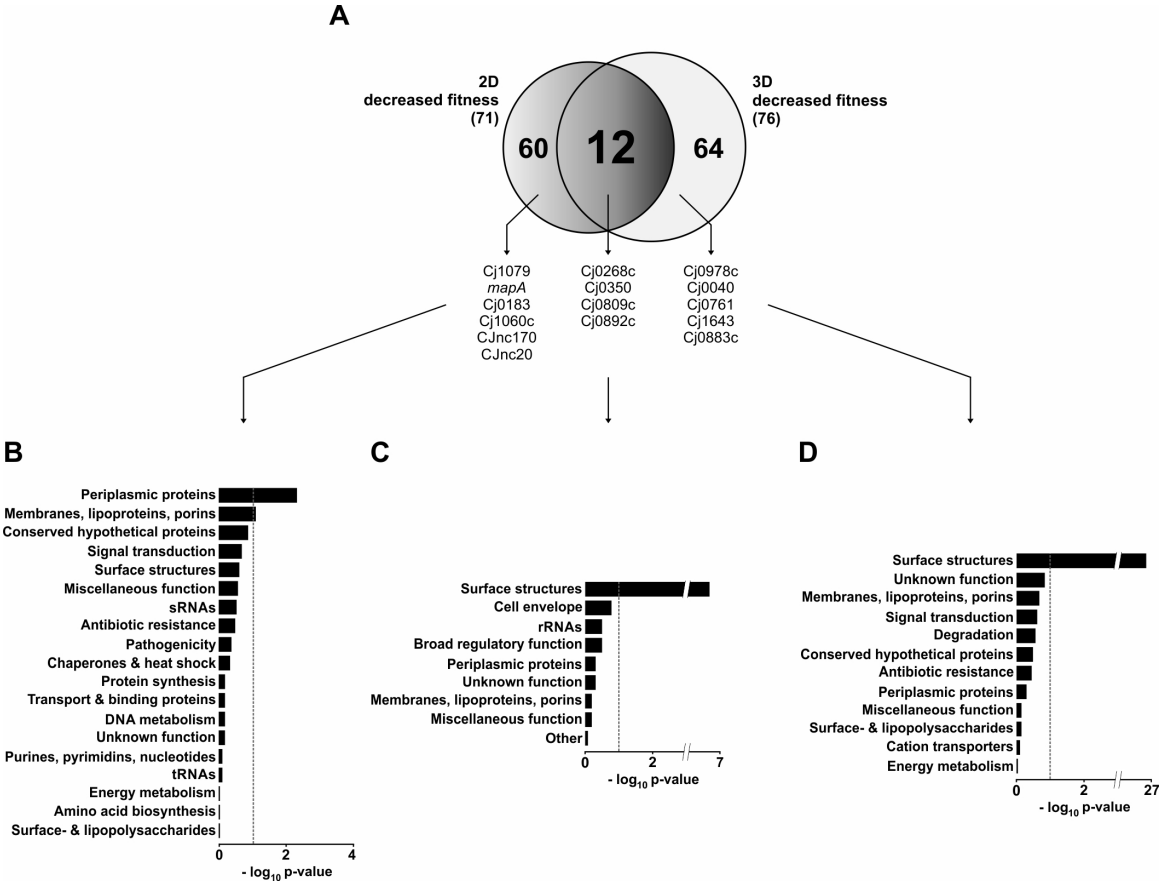

Figure 3.4: Tn insertion mutants with decreased fitness common and unique to the 2D and 3D infection model. (A) Venn diagram depicting the number of genes, whose disruption resulted in decreased adherence and internalization unique to either the 2D Caco-2 monolayer, to the 3D tissue model, or those shared between the two infection systems. **(B – D)** Functional enrichment analysis was performed on all genes with a decreased insertion count greater than 2-fold unique to the 2D dataset **(B)** or the 3D dataset **(D)** as well as for those shared between both infection models **(C)**. Functional categories are shown with $-\log_{10}$ p-value ≠ 0 and are based on the re-annotation of the *C. jejuni* NCTC11168 genome (Gundogdu *et al.*, 2007). Functional categories with a p-value ≤ 0.1 (represented by the dotted line) are considered significantly enriched.

Functional enrichment analysis for Tn-seq candidates unique to the interaction of *C. jejuni* with the 3D tissue model revealed the single most significantly enriched category to be *Surface structures* (Figure 3.4 D). Interestingly, taking a closer look at the genes assigned

to this functional class, not all of them are necessarily involved in motility and/or chemotaxis, but also directly or indirectly contribute for example to the modification of flagellins with legionaminic or pseudaminic acid. The second and third highest enriched functional categories – albeit not significantly – were comprised mostly of genes with so far unknown function or those belonging to *Membranes, lipoproteins, and porins* (Figure 3.4 D). This included for example Cj0978c (putative lipoprotein) or the hypothetical proteins Cj0040 and Cj0761, none of which has previously been reported to be required for *C. jejuni* host cell interaction. However, Cj0978c and Cj0040 have also been identified in two other Tn screens for *C. jejuni* factors important for host-pathogen interaction (de Vries *et al.*, 2017a; Gao *et al.*, 2017) (Table 3.1). Moreover, together with *fliK*, *flgD*, and *flgE*, Cj0040 is encoded in a flagellar hook operon, indicating a potential relevance for this hypothetical protein in *C. jejuni* motility or even polar effects of the Tn insertion. Even though the precise functional role of Cj0761 has so far not been described, it has been reported to be activated by iron restriction (Xu *et al.*, 2015) and its disruption could thus contribute to a decreased fitness phenotype inside polarized intestinal epithelial cells where iron availability is limited. Other than that, Cj1643 (putative periplasmic protein) was among the top five genes with the highest fitness defect in the 3D dataset that was not described to have a role in motility. This particular candidate has never been identified to be required for *C. jejuni* colonization, transmigration, intracellular survival, or other pathogenesis-related processes (Figure 3.4 A and Table 3.1) and is thus unique to this screen. In addition, disruption of the transcriptional regulator Cj0883c was associated in our screen specifically with a decreased internalization phenotype in the tissue model only. This regulator has been identified in many other genome-wide screens for *C. jejuni* fitness factors (Gao *et al.*, 2014, 2017, de Vries *et al.*, 2017a, 2017b). However, this was most often attributed to a polar effect on the downstream gene *flhA*, disruption of which renders the bacterium non motile (Hendrixson & DiRita, 2004). Nevertheless, it might be intriguing to consider a very specific role of Cj0883c and its regulon other than motility during internalization or intracellular survival of *C. jejuni*.

In summary, Tn-seq has been successfully applied to identify fitness factors in *C. jejuni* strain NCTC11168 during infection of non-polarized intestinal epithelial cells and the Caco-2 cell-based 3D tissue model. These analyses suggest that the common denominators required for colonization of both infection models are motility and chemotaxis. Nonetheless, there are many more genes involved in diverse cell processes or with unknown function that could specifically determine the interaction of the pathogen with flat and non-polarized or columnar cells harboring an apical basolateral polarity.

3.2.2. Genome-wide screen identifies transposon insertion mutants with enhanced fitness

In addition to genes whose disruption by transposon insertion led to decreased fitness during *C. jejuni* infection, the screen performed in this thesis also detected genes for which insertion resulted in enhanced adherence and/or internalization in both infection models. Contrary to the attenuating candidates, this analysis showed very little overlap to other studies that also considered insertion mutants with an enriched phenotype *in vitro* or *in vivo* (Johnson *et al.*, 2014; de Vries *et al.*, 2017a, 2017b). As the goal of most other studies is to identify new genes that are essential during *C. jejuni* colonization of epithelial cells or the mammalian/avian intestinal tract, Tn insertion mutants resulting in a "hypervirulent" phenotype are most often excluded from their analysis (Novik *et al.*, 2010; Gao *et al.*, 2014, 2017). Nonetheless, they could reveal interesting insights into *C. jejuni* pathogenesis. Table 3.2 depicts a summary of all 128 genes whose disruption resulted in increased adherence/internalization in both infection models, in addition to a reference to previous studies describing the respective candidate genes.

Table 3.2: Tn insertion mutants with an increase in bacterial adhesion and internalization during infection of the 2D and 3D cell culture model. This table contains a list of genes, disruption of which led to an overrepresentation of Tn insertion reads obtained from libraries prepared from adherent and internalized samples (ADH) or internalized samples only (INT) versus those from the supernatant bacteria. Selection criteria were a $\log_2$ fold change ≥ 1 with a p-value ≤ 0.05. Fold changes depicted in grey represent those that did not pass the set cut offs, *i.e.* with $\log_2$ fold changes < |1| and/or p-values > 0.05. Genes with less than 10 read counts per condition were excluded from the analysis and their values are not shown (–). References refer to other genome-wide studies of *C. jejuni* strains or to studies in which the gene of interest was previously characterized/described. Genes unique to this study are highlighted in grey. *****: phase variable gene. **OP**: genes that are expressed as part of an operon structure, in which more genes showed a significant $\log_2$ fold change ≥ 1. Operon structures have been determined according to primary TSS annotations from (Dugar *et al.*, 2013). Detailed description about the present operon structures can be found in Appendix Table 3.2.

ID	Name	Description	2D Tn-seq ADH/INT	3D Tn-seq ADH/INT	Reference
Motility and chemotaxis					
Cj0698	*flgG*	flagellar basal body rod protein	–/–	**+7.66**/–	
Cj1118c	*cheY*	chemotaxis protein CheY	**+3.83**/**+3.86**	**+1.04**/+0.83	(Yao *et al.*, 1997) (Hendrixson & DiRita, 2004) (Raphael *et al.*, 2005) (Johnson *et al.*, 2014)
Cj0923c	*cheR*	MCP protein methyltransferase	**+3.75**/**+5.37**	-0.84/+0.34	(Kanungpean *et al.*, 2011) (de Vries *et al.*, 2017a, 2017b) (Gao *et al.*, 2017)
Cj0547	*flaG*	flagellar protein FlaG	**+6.49**/–	-0.84/-0.98	(Johnson *et al.*, 2014) (de Vries *et al.*, 2017a)

continued on next page

ID	Name	Description	2D Tn-seq ADH/INT	3D Tn-seq ADH/INT	Reference
Cj0284c^{OP}	*cheA*	chemotaxis histidine kinase	**+3.18/+3.65**	+0.70/**+1.49**	(Johnson *et al.*, 2014) (Gao *et al.*, 2017)
Cj0249^{OP}	*cheQ*	chemotaxis regulator Q	**+1.46/+2.35**	+0.86/**+1.27**	(de Vries *et al.*, 2017a, 2017b) (Gao *et al.*, 2017)
Cj1190c	*cetA*	bipartate energy taxis response protein CetA	-0.80/-0.99	**+1.65/+2.31**	(Hendrixson *et al.*, 2001)
Cj0144	*tlp2*	methyl-accepting chemotaxis signal transduction protein	**+1.62/+1.99**	+0.07/-0.27	
Cj0262c	*tlp4*	methyl-accepting chemotaxis signal transduction protein	**+1.59/+1.91**	-0.38/+0.06	(de Vries *et al.*, 2017a)
Cj0248^{OP}	*cheP*	chemotaxis regulator P	**+1.09/+1.75**	+0.48/+0.25	(de Vries *et al.*, 2017a, 2017b) (Gao *et al.*, 2017)
Cj0285c^{OP}	*cheV*	chemotaxis protein	+0.86/**+1.52**	+0.46/+0.74	(Johnson *et al.*, 2014) (de Vries *et al.*, 2017a) (Gao *et al.*, 2017)
Flagella modifications					
Cj1329	*ptmE*	sugar-phosphate nucleotide transferase	**+2.48/+3.00**	**-1.39/+1.64**	
Cj1321*		putative transferase/pseudogene	**+1.36/+2.66**	-0.11/+0.60	(Howard *et al.*, 2009)
Previously reported virulence factors					
Cj0039c	*typA*	GTP-binding protein TypA	−/−	−/**+3.15**	(Novik *et al.*, 2010) (de Vries *et al.*, 2017a) (Gao *et al.*, 2017)
Cj0983	*jlpA*	lipoprotein	**+1.71/+1.77**	-0.20/-0.50	(Jin *et al.*, 2001) (de Vries *et al.*, 2017a)
Broad regulatory function					
Cj1261^{OP}	*racR*	two-component regulator	−/+3.80	**+9.02**/−	(Brás *et al.*, 1999)
Cj1209		ribonuclease Y	−/−	**+7.72**/−	(Novik *et al.*, 2010)
Cj0258	*arsR*	ArsR family transcriptional regulator	−/−	**+7.14**/−	
Cj1262^{OP}	*racS*	two-component sensor histidine kinase	**+2.13/+2.58**	+0.52/+0.73	(Apel *et al.*, 2012) (de Vries *et al.*, 2017a)
Cj0571		transcriptional regulator	**+1.50/+2.16**	+0.28/+0.13	
Cj1546	*rrpA*	transcriptional regulator	**+1.36**/+0.62	+0.23/+0.18	(Gundogdu *et al.*, 2016) (de Vries *et al.*, 2017b)
Cj0480c		transcriptional regulator	**+1.01**/+0.25	+0.23/-0.18	
Stress-response and DNA-related processes					
Cj0011c		non-specific DNA binding protein	-4.14/**-6.1**	**+2.56/+2.67**	
Cj1157	*dnaX*	DNA polymerase III subunits gamma and tau	−/−	−/**+3.80**	
Cj1636c	*rnhA*	ribonuclease H	−/−	**+3.26**/+2.31	
Cj0518	*htpG*	chaperone protein HtpG	**+2.21/+1.48**	-0.07/+0.18	(de Vries *et al.*, 2017a)
Cj1664		thioredoxin	**+1.14/+1.90**	-0.10/+0.41	(Johnson *et al.*, 2014)
Cj0757	*hrcA*	heat-inducible transcription repressor	**+1.56/+1.76**	+0.19/+0.36	
Cj1077	*ctsT*	periplasmic protein	-0.21/+0.29	+0.19/**+1.53**	
Cj1034c		adenylosuccinate lyase	**+1.26/+1.51**	-0.01/+0.31	(de Vries *et al.*, 2017a, 2017b) (Gao *et al.*, 2017)
Cj1159c		hypothetical protein	-0.56/-0.74	**+1.51**/+1.18	
Cj0509c	*clpB*	chaperone protein ClpB	+0.32/+0.44	**+1.35**/+0.42	(de Vries *et al.*, 2017a, 2017b)
Cj1052c	*mutS*	endonuclease MutS2	+0.81/**+1.21**	-0.05/+0.23	

continued on next page

ID	Name	Description	2D Tn-seq ADH/INT	3D Tn-seq ADH/INT	Reference
Cj1073c	*lon*	ATP-dependent protease La	+0.54/**+1.17**	+0.27/0.00	(Cohn *et al.*, 2007) (de Vries *et al.*, 2017b)
Iron uptake and metabolism					
Cj1614	*chuA*	hemin uptake system outer membrane receptor	**+1.32**/**+1.87**	+0.22/+0.84	
Cj1615	*chuB*	hemin uptake ABC transporter permease	**+1.11**/+0.90	+0.07/+0.79	(Johnson *et al.*, 2014)
Ion transporters					
Cj0948c		cation efflux family protein	+1.07/+0.74	**+2.70**/**+2.77**	
Cj0935c		sodium:amino-acid symporter family protein	**+1.91**/**+2.00**	+0.02/-0.11	(de Vries *et al.*, 2017b) (Gao *et al.*, 2017)
Cj1163c[OP]		cation transport protein	+0.26/**+1.53**	+1.18/**+1.40**	
Cj0832c		Na+/H+ antiporter family protein	**+1.10**/**+1.45**	-0.64/+0.02	
General cell processes and metabolism					
Cj0228c	*pcm*	protein-L-isoaspartate O-methyltransferase	–/–	**+7.41**/–	
Cj0979c		nuclease	**+3.90**/**+3.09**	-0.87/+0.32	
Cj0123c		tRNA-dihydrouridine synthase	**+3.36**/**+3.01**	+0.49/+0.67	
Cj1028c		purine/pyrimidine phosphoribosyltransferase	**+1.85**/**+2.35**	-0.06/+0.05	
Cj1280c		pseudouridine synthase	+0.51/-1.36	-0.28/**+2.10**	(Chang & Miller, 2006)
Cj1644	*ispA*	geranyltranstransferase	+0.88/**+1.78**	+0.70/-0.41	
Cj1050c	*npdA*	NAD-dependent protein deacetylase	+1.12/**+1.74**	+0.12/-0.50	
Cj1581c	*sapD*	peptide ABC transporter ATP-binding protein	-1.14/-1.85	**+1.67**/+0.42	
Cj1109	*aat*	leucyl/phenylalanyl-tRNA-protein transferase	+0.79/**+1.20**	+0.44/+0.46	(de Vries *et al.*, 2017a)
Cj1369		permease	**+1.18**/+0.69	-0.75/-0.49	(de Vries *et al.*, 2017b)
Cj1628	*exbB2*	ExbB/TolQ family transport protein	+0.44/+0.25	-0.03/**+1.14**	
Amino acid transport and metabolism					
Cj0929	*pepA*	cytosol aminopeptidase	**+2.94**/**+3.80**	+0.25/**+1.68**	(de Vries *et al.*, 2017b)
Cj1015c	*livG*	ABC transporter ATP-binding protein	**+2.98**/**+3.65**	-0.56/+0.26	(de Vries *et al.*, 2017a)
Cj1097	*sstT*	serine/threonine transporter SstT	**+1.29**/**+1.51**	-0.28/-0.15	(Novik *et al.*, 2010)
Cj1392	*metC*	hypothetical protein	**+1.10**/**+1.48**	-0.05/-0.25	
Cj0903c		amino acid transport protein	+0.97/**+1.37**	-0.10/+0.66	(Hendrixson & DiRita, 2004) (de Vries *et al.*, 2017b)
Cj1604	*hisI*	bifunctional phosphoribosyl-AMP cyclohydrolase/phosphoribosyl-ATP pyrophosphatase	+0.40/-0.07	+0.30/**+1.15**	
Cj1314c	*hisF*	imidazole glycerol phosphate synthase subunit HisF	**+1.08**/+0.81	+0.13/-0.39	
Cj0009	*gltD*	glutamate synthase subunit beta	**+1.05**/+0.99	-0.27/-0.05	
Energy production and respiration					
Cj0252	*moaC*	cyclic pyranopterin monophosphate synthase accessory protein	–/**+10.82**	-1.75/+0.09	
Cj0025c		sodium:dicarboxylate symporter	–/+4.26	–/**+9.47**	

continued on next page

ID	Name	Description	2D Tn-seq ADH/INT	3D Tn-seq ADH/INT	Reference
Cj1509c	*fdhC*	formate dehydrogenase cytochrome B subunit	–/**+9.42**	-0.76/+2.13	
Cj1411c^{OP}		cytochrome P450	**+3.22/+5.28**	-0.01/+0.64	(Alvarez *et al.*, 2013)
Cj0559		pyridine nucleotide-disulfide oxidoreductase	+0.60/+0.73	**+2.58/+2.87**	(de Vries *et al.*, 2017a)
Cj0689	*ackA*	acetate kinase	**+2.21/+2.85**	-0.31/-1.19	(de Vries *et al.*, 2017b) (Gao *et al.*, 2017) (Luethy *et al.*, 2017)
Cj0783	*napB*	nitrate reductase small subunit	**+2.21/+2.33**	-0.30/-0.17	
Cj0555		dicarboxylate carrier protein MatC	**+1.52/+1.97**	-0.08/+0.38	
Cj1002c		phosphoglycerate/bisphospho glycerate mutase	**+1.05**/-0.04	0.00/+0.70	
Cell wall, membrane, and envelope biogenesis					
Cj1438c^{OP}		sugar transferase	**+12.40/+15.35**	–/–	
Cj1414c	*kpsC*	capsule polysaccharide modification protein	**+13.13/+13.74**	+1.25/+2.26	(Novik *et al.*, 2010) (Johnson *et al.*, 2014)
Cj1444c^{OP}	*kpsD*	capsule polysaccharide ABC transporter substrate-binding protein	**+13.65/+13.23**	+2.19/+2.20	(Johnson *et al.*, 2014)
Cj1432c^{OP}		sugar transferase	**+12.72/+13.89**	-0.81/+1.50	
Cj1441c^{OP}	*kfiD*	UDP-glucose 6-dehydrogenase	**+13.14/+13.59**	–/–	
Cj1448c^{OP}	*kpsM*	capsule polysaccharide ABC transporter permease	–/**+13.15**	–/–	(Bacon *et al.*, 2001) (Jones *et al.*, 2004) (Stahl *et al.*, 2014) (Wong *et al.*, 2015)
Cj1440c^{OP}		sugar transferase	**+12.57**/–	**+3.36/+3.71**	(Johnson *et al.*, 2014)
Cj1413c	*kpsS*	capsule polysaccharide modification protein	–/**+11.99**	+1.28/+2.50	(Gao *et al.*, 2017)
Cj1434c^{OP}		sugar transferase	**+11.60**/–	–/–	
Cj1148	*waaF*	heptosyltransferase II	**+10.93**/–	–/–	(Kanipes *et al.*, 2004) (Perera *et al.*, 2007) (Johnson *et al.*, 2014)
Cj1447c^{OP}	*kpsT*	capsule polysaccharide ABC transporter ATP-binding protein	**+7.30/+7.77**	+1.80/+2.58	
Cj1439c^{OP}	*glf*	UDP-galactopyranose mutase	**+5.2/+6.31**	+2.01/**+2.88**	
Cj1412c		integral membrane protein	**+3.27/+5.49**	+1.81/+1.13	(Johnson *et al.*, 2014)
Cj1410c^{OP}		membrane protein	+3.61/**+5.18**	+0.68/+0.50	
Cj1135^{OP}		glucosyltransferase	**+3.33/+3.89**	+0.13/+0.03	(de Vries *et al.*, 2017a) (Gao *et al.*, 2017)
Cj1183c	*cfa*	cyclopropane-fatty-acyl-phospholipid synthase	**+3.02/+3.62**	-0.12/+0.48	
Cj1138		glycosyltransferase	**+2.64/+2.73**	+0.14/-0.02	
Cj1137c		glucosyltransferase	**+2.07/+2.52**	+0.19/+0.28	
Cj0564		integral membrane protein	**+2.42**/+1.84	-0.09/+0.04	(Johnson *et al.*, 2014)
Cj1136^{OP}		glycosyltransferase	**+2.20/+2.36**	+0.14/-0.15	(Javed *et al.*, 2010)
Cj1427c		sugar-nucleotide epimerase/dehydratase	**+2.33/+1.76**	-0.07/+0.16	
Cj1142^{OP}	*neuC1*	UDP-*N*-acetylglucosamine 2-epimerase	**+2.29/+2.06**	-0.17/+0.13	
Cj1140^{OP}	*cstIII*	alpha-2,3 sialyltransferase	**+2.19/+2.13**	-0.24/-0.11	
Cj1445c^{OP}	*kpsE*	capsule polysaccharide ABC transporter permease	+3.49/**+3.90**	+1.19/+0.55	(Bachtiar *et al.*, 2007)

continued on next page

ID	Name	Description	2D Tn-seq ADH/INT	3D Tn-seq ADH/INT	Reference
Cj1141^{OP}	*neuB1*	sialic acid synthase	**+2.02/+2.14**	-0.23/-0.59	
Cj1143^{OP}	*neuA1*	bifunctional beta-1,4-*N*-acetylgalactosaminyltransferase/ CMP-Neu5Ac synthase	**+1.92/+1.92**	-0.02/+0.70	(Johnson *et al.*, 2014)
Cj1425c	*hddA*	D-glycero-D-manno-heptose 7-phosphate kinase	**+1.64/+1.78**	+0.10/-0.13	(Novik *et al.*, 2010) (Gao *et al.*, 2017)
Cj1120c	*pglF*	UDP-N-acetyl-alpha-D-glucosamine C6 dehydratase	**+1.15/+1.40**	+0.25/-0.47	(Novik *et al.*, 2010) (de Vries *et al.*, 2017a, 2017b) (Gao *et al.*, 2017)
Cj1012c		membrane protein	**+1.40**/+0.79	+0.05/-0.41	(Gao *et al.*, 2017)
Cj1436c^{OP}		aminotransferase	**+1.21**/+0.92	+0.25/-0.17	
Cj0937		integral membrane protein	+0.53/-0.21	+0.13/**+1.07**	
Cj0505c	*gnnB*	DegT family aminotransferase	**+1.01**/+0.68	-0.08/-0.65	
Cj0986c		pseudogene	+0.68/**+1.01**	-0.14/+0.49	
Housekeeping and non-coding RNAs					
CJnc30		small non-coding RNA	–/**+12.75**	–/+1.11	
CJnc22		small non-coding RNA	**+2.13/+2.41**	+0.02/+0.01	
Function unknown					
Cj0878		hypothetical protein	**+13.02**/–	+1.44/-0.28	
Cj0711		hypothetical protein	–/–	**+7.64/+8.90**	
Cj1004		periplasmic protein	+1.03/-1.64	**+8.83**/–	
Cj1486c		periplasmic protein	–/–	–/**+5.55**	
Cj0962		acetyltransferase	–/–	–/**+3.42**	
Cj1640		hypothetical protein	–/–	**+3.23**/–	
Cj1145c*		hypothetical protein	**+2.54/+3.14**	-0.30/+0.70	
Cj0395c		hypothetical protein	–/–	**+2.84**/–	
Cj1164c^{OP}		hypothetical protein	**+1.97/+2.68**	-0.99/+0.56	
Cj1720		hypothetical protein	**+2.59/+2.09**	+0.03/-0.51	
Cj0162c		periplasmic protein	**+1.76**/+1.04	-0.14/**-1.95**	(Gao *et al.*, 2014)
Cj0592c		periplasmic protein	**+1.88/+1.74**	+0.14/+0.31	
Cj0488		hypothetical protein	**+1.46/+1.86**	+0.39/+1.16	
Cj0747		hypothetical protein	**+1.78/+2.62**	-0.03/+0.30	
Cj0565*		hypothetical protein	+0.81/**+1.71**	+0.17/+0.25	
Cj1089c		hypothetical protein	+0.89/+1.29	+0.65/**+1.63**	
Cj1254		hypothetical protein	+1.08/**+1.41**	+0.06/-0.62	(Johnson *et al.*, 2014)
Cj0182		transmembrane transport protein	+0.92/+0.73	+0.26/**+1.28**	
Cj0561c		periplasmic protein	+0.92/**+1.25**	+0.02/-0.20	(Guo *et al.*, 2008)
Cj1367c		nucleotidyltransferase	**+1.18/+1.04**	+0.03/-0.15	(de Vries *et al.*, 2017a)
Cj1371		periplasmic protein	+0.35/**+1.16**	+0.16/+0.34	
Cj0272		hypothetical protein	**+1.12**/+0.77	0.00/+0.32	(Johnson *et al.*, 2014)
Cj0970		hypothetical protein	-0.46/-0.15	-0.10/**+1.04**	
Cj1468		integral membrane protein	+0.52/**+1.04**	+0.14/-0.19	(Johnson *et al.*, 2014) (de Vries *et al.*, 2017b)
Cj1041c		ATP/GTP-binding protein	**+1.01**/+0.97	-0.18/+0.54	(Johnson *et al.*, 2014)

Similar to the analysis of decreased fitness genes, in a first step genes dispensable for infection of a 2D Caco-2 monolayer were analyzed. When compared to non cell-associated bacteria in the supernatant of the 2D infection model, our analysis discovered 78 genes with an increased number of reads in the ADH, and 78 genes with an

overrepresentation in the INT library (Figure 3.5 A). Disruption of 58 genes resulted in both higher adherence and internalization rates. In particular, disruption of many genes involved in *Cell wall, membrane, and envelope biogenesis* led to some of the highest observed fold changes for both adherence and internalization (Figure 3.5 B). This included many genes encoded in the CPS locus, such as Cj1438c, *kpsC*, or *kpsD*. The latter has been shown to be down-regulated when *C. jejuni* is grown in the presence of human intestinal epithelial cells (Corcionivoschi *et al.*, 2009) suggesting that the ability to turn CPS expression off might be advantageous during colonization of non-polarized epithelial cells. Likewise, among the candidates with an overrepresentation of reads in the 2D adherence library only (20 genes) were many CPS-related genes, but also those coding for transcriptional regulators such as *rrpA* or Cj0480c (Figure 3.5 A and B). Deletion of *rrpA* results in increased biofilm formation (Gundogdu *et al.*, 2016), which has previously been assessed to be a potential contributor to the pathogenic potential of extra-intestinal pathogenic *E. coli* (Fakruddin *et al.*, 2014). Cj0480c is an isocitrate lyase-type (IclR-type) transcriptional regulator, which are widespread in both Gram-positive and -negative bacteria and are for example involved in carbon metabolism, quorum-sensing, and virulence (Molina-Henares *et al.*, 2006). Tn insertion mutants unique to increased internalization into unpolarized epithelial cells (20 genes) were mainly represented by those with so far unknown function or with a role in *General cell processes and metabolism* such as *ispA*, a putative geranyltranstransferase (Figure 3.5 A and B). These enzymes are involved in prenylation of target proteins and, among other phenotypes, deletion of *ispA* has been linked to an increased resistance against antimicrobial peptides in *Staphylococcus aureus* (Krute *et al.*, 2014), potentially explaining an increased intracellular representation of such an insertion mutant.

In summary, screening of the *C. jejuni* mutant library revealed predominantly CPS-related genes to be expendable for both adherence to and internalization into a non-polarized epithelial cell monolayer.

In a second step, genes potentially impeding efficient host-pathogen interactions in the intestinal tissue model were examined. However, contrary to increased representation of reads in the 2D libraries, only a reduced number of genes showed enhanced adherence and/or internalization upon disruption by transposon insertion in the 3D tissue model. Infection with the Tn library revealed 20 genes with an increased insertion ratio in adherence and 25 genes in internalization libraries (Figure 3.5 C). Seven of those were shared and favored no particular functional category (Figure 3.5 C and D). Among these Tn insertion mutants was the bipartite energy taxis response protein CetA (Tlp9), which is potentially involved in aerotaxis by either directly sensing molecular oxygen or indirectly

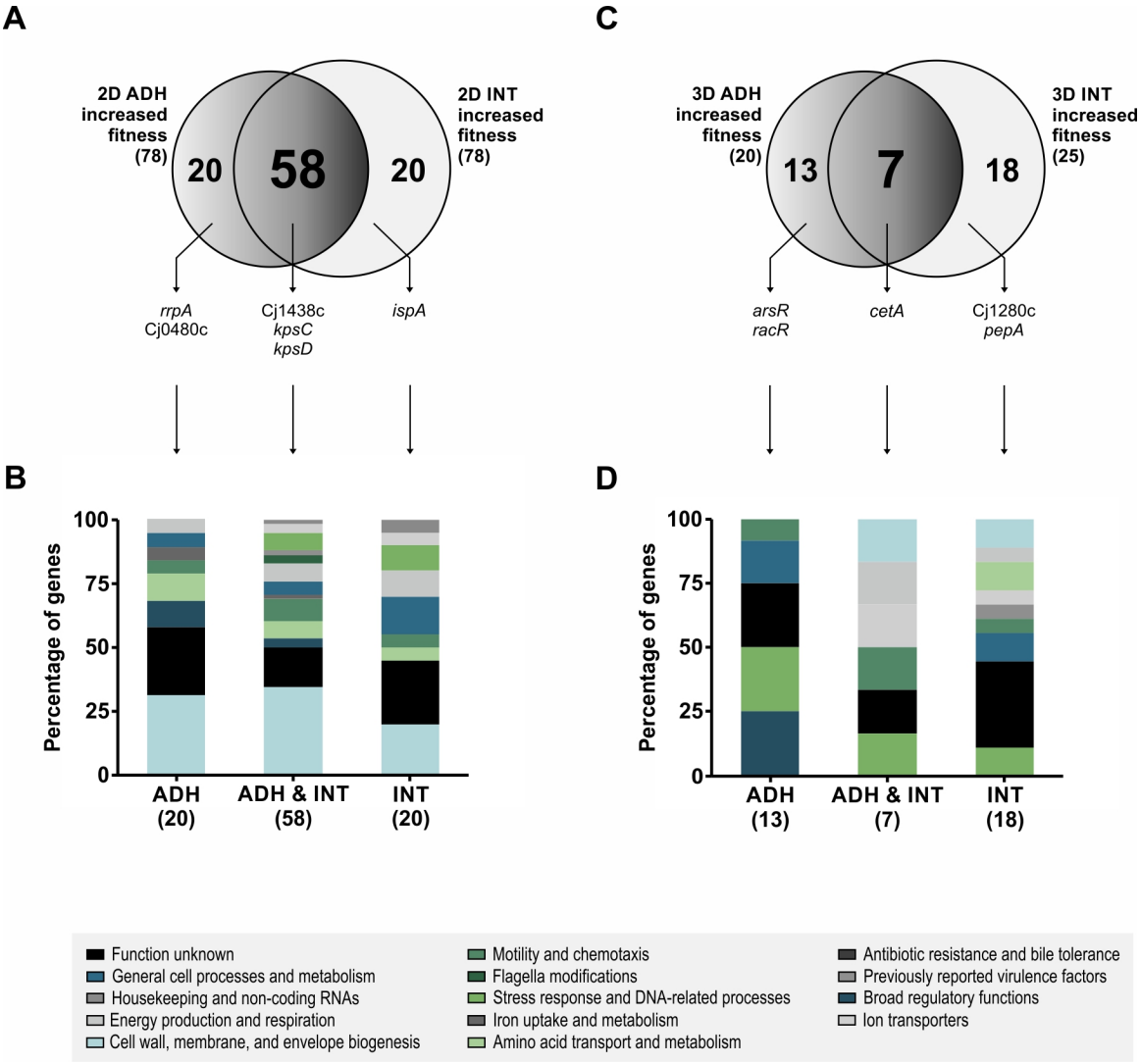

Figure 3.5: Increased fitness genes identified by Tn-seq. (A, C) Overlap of the number of Tn insertion mutants resulting in increased bacterial adherence and internalization in the 2D Caco-2 monolayer **(A)** or the 3D tissue model **(C)** depicted by Venn diagrams. The total number of genes detected in each condition is indicated in brackets. For an overview of all detected genes with increased fitness see also Table 3.2. **(B, D)** The total number of genes for 2D/3D adherence only (ADH), internalization only (INT), or shared between 2D/3D adherence and internalization (ADH & INT) was manually assessed, and the percentage of genes belonging to self-assigned functional categories was calculated. Each bar graph is composed of the proportional share of genes in the various cellular processes.

sensing redox conditions (Reuter & van Vliet, 2013). Disruption of 13 genes showed a tendency to be specifically beneficial for adherence in the tissue model, most of which belonged to the categories *Stress-response and DNA-related processes* and *Broad regulatory function* (Figure 3.5 C and D) such as the transcriptional repressor ArsR involved in arsenic resistance in *C. jejuni* (Wang *et al.*, 2009), or the two-component response regulator RacR. During colonization of the gut, where oxygen is limited, *C. jejuni* uses less efficient electron

acceptors such as nitrate or fumarate (Sellars *et al.*, 2002). As RacR together with its sensor kinase RacS in their inactive form allow the utilization of fumarate for respiration (van der Stel *et al.*, 2014), disruption of the response regulator seems to be beneficial for colonization of the 3D tissue model.

Most of the Tn insertions specifically beneficial for internalization (18 candidates) in the tissue model were located in genes coding for hypothetical or periplasmic proteins with so far no annotated function (Figure 3.5 C and D). Other affected genes mainly split into four functional categories: *Cell wall, membrane, and envelope biogenesis*; *General cell processes and metabolism* (*e.g.* Cj1280c, pseudouridine synthase); *Amino acid transport and metabolism* (*e.g. pepA*, cytosol aminopeptidase)*;* and *Stress-response and DNA-related processes*. Thus, it might be plausible to speculate that Tn insertion mutants affecting these processes might rather impact intracellular survival than the actual internalization into host cells.

A direct comparison between genes with enriched representation during interaction with either non-polarized Caco-2 cells or the 3D tissue model showed a very limited overlap of only eight genes (Figure 3.6 A), two of which – Cj1439c and Cj1440c – are encoded in the CPS locus (Parkhill *et al.*, 2000). The polysaccharide capsule of *C. jejuni* has been implicated in many pathogenesis-related processes, disruption or phase-variation of which can either be detrimental (Bacon *et al.*, 2001; Jones *et al.*, 2004; Bachtiar *et al.*, 2007) or beneficial for colonization (Stahl *et al.*, 2014; van Alphen *et al.*, 2014; Wong *et al.*, 2015) both *in vitro* and *in vivo*. The other genes common for 2D and 3D included *pepA*, Cj0249, Cj0929, Cj1118c, Cj1163c, Cj1329, as well as the two chemotaxis-related genes *cheA* and *cheY*. No particular functional category was enriched above all others for Tn insertion mutants shared between the infection models (Figure 3.6 C). However, a statistically significant enrichment for *Surface- and lipopolysaccharides* could be observed for the set of Tn insertion mutants unique for host-pathogen interactions in 2D (89 genes) (Figure 3.6 A and B). Likewise, genes coding for chemotaxis-related behavior were also significantly enriched among Tn insertion mutants specific for the 2D dataset (Figure 3.6 B). This included for example the two methyl-accepting chemotaxis signal transduction proteins Tlp2 and Tlp4. Whereas Tlp2 has been loosely associated with mediating chemotactic behavior towards iron and inorganic phosphate (Chandrashekhar *et al.*, 2017), Tlp4 along with other Tlp proteins has been shown to be essential for mediating chemotaxis toward sodium deoxycholate (Li *et al.*, 2014). In addition, two sRNAs (CJnc30 and CJnc22) were also among the candidates whose disruption seemed to be specifically beneficial for interaction with non-polarized Caco-2 cells. While the role of CJnc30 seemed to be restricted to the processes of internalization

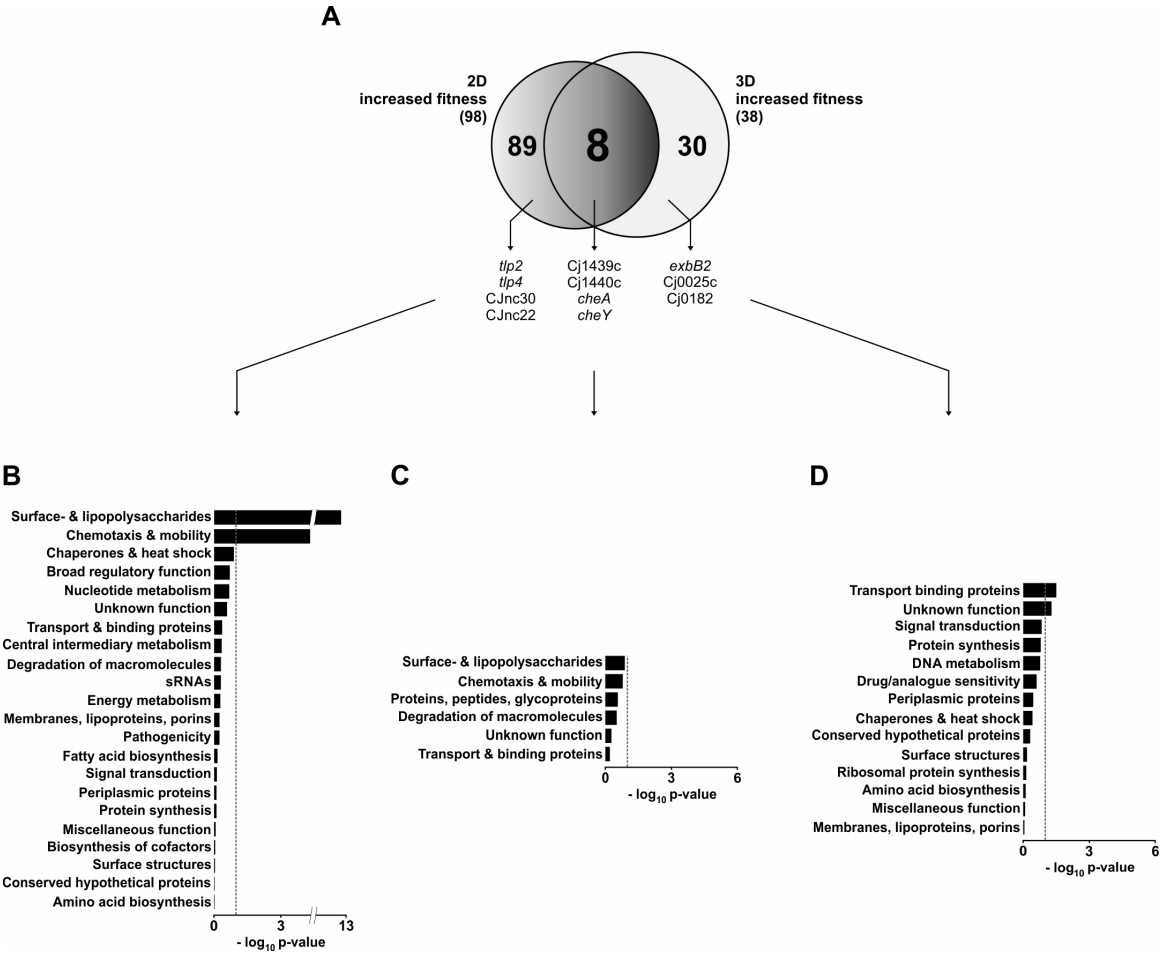

Figure 3.6: Tn insertion mutants with increased fitness common and unique to the 2D and 3D infection model. (A) Comparison between the number of Tn insertion mutants unique to the 2D or 3D cell culture model and those shared between the two systems represented in a Venn diagram. **(B – D)** Functional enrichment analysis was performed on all genes with a decreased insertion count greater than 2-fold unique to the 2D dataset **(B)** or the 3D dataset **(D)** as well as for those shared between both infection models **(C)**. Functional categories are shown with $-\log_{10}$ p-value ≠ 0 and are based on the re-annotation of the *C. jejuni* NCTC11168 genome (Gundogdu *et al.*, 2007). Functional categories with a p-value ≤ 0.1 are considered significantly enriched.

or survival inside host cells, interference with CJnc22 had an impact on both bacterial adhesion and internalization. However, how precisely these two regulatory RNAs affect the interaction between host and pathogen remains to be elucidated.

Tn insertion mutants unique to the 3D dataset (30 genes) were enriched for *Transport binding proteins* and genes with *Unknown function* (Figure 3.6 A and D). Among the transport binding proteins were for example ExbB2, an ExbB/TolQ family transport protein. ExbB2 is a putative inner membrane-embedded part of the TonB-ExbB-ExbD energy transduction system in *C. jejuni* powering the translocation of iron sources across the outer membrane (Palyada *et al.*, 2004). Research on other transport proteins such as the

putative sodium:dicarboxylate family transmembrane symporter Cj0025c or the putative peptide/bleomycin uptake transporter Cj0182 has been scarce. Thus, their potential role during host-pathogen interactions has yet to be determined. As most of the other genes, whose disruption resulted in a hypervirulent phenotype, encode mainly hypothetical proteins or are annotated simply as periplasmic proteins (Figure 3.6 D), one can only speculate about their involvement during *C. jejuni* infection.

In summary, the Tn-seq screen performed in this thesis was also able to detect Tn insertion mutants with a seemingly beneficial effect on bacterial colonization both during interaction with non-polarized Caco-2 cells as well as with the 3D intestinal tissue model. In particular, many genes encoded in the *C. jejuni* LOS or CPS locus seemed to be specifically dispensable or even hindering during adherence or internalization to conventional Caco-2 monolayers. Comparing the surface structures of these cells with the columnar enterocyte-like cells present in the tissue model might reveal clues to potential receptors or surface structures required for initial *C. jejuni* adhesion.

3.3. Validation of gene candidates selected from the genome-wide screen of *C. jejuni* in two different cell culture models

So far, the genome-wide screen for putative *C. jejuni* virulence factors is based on data analysis of two biological replicates. While this gives potential insights into gene processes important or extraneous for successful colonization, experimental validation of insertion mutants is essential to grant the necessary credibility to the data acquired by the Tn-seq screen. As it would be favorable to characterize a factor that is required for *C. jejuni* during colonization, the list of Tn-insertion mutants with a decreased insertion count ratio was screened for such candidates. Focus was placed on so far uncharacterized genes, whose disruption resulted in decreased fitness predominantly in the 3D tissue model. The top three candidates (according to their fold changes) with so far unknown function, disruption of which led primarily to a significant attenuation in adherence and internalization in the intestinal 3D tissue model, were Cj0892c, Cj0978c, and Cj1643. Both lists for transposon insertion mutants with decreased and increased adherence and/or internalization hold many more interesting genes, whose potential involvement during *C. jejuni* pathogenesis remains to be uncovered. Nonetheless, initial focus was placed on the top three candidates, which were chosen for further experimental assessment.

In the Tn-seq screen, disruption of Cj0892c – encoding a putative periplasmic protein – lead to a decreased insertion count (Figure 3.7 A) in libraries constructed from

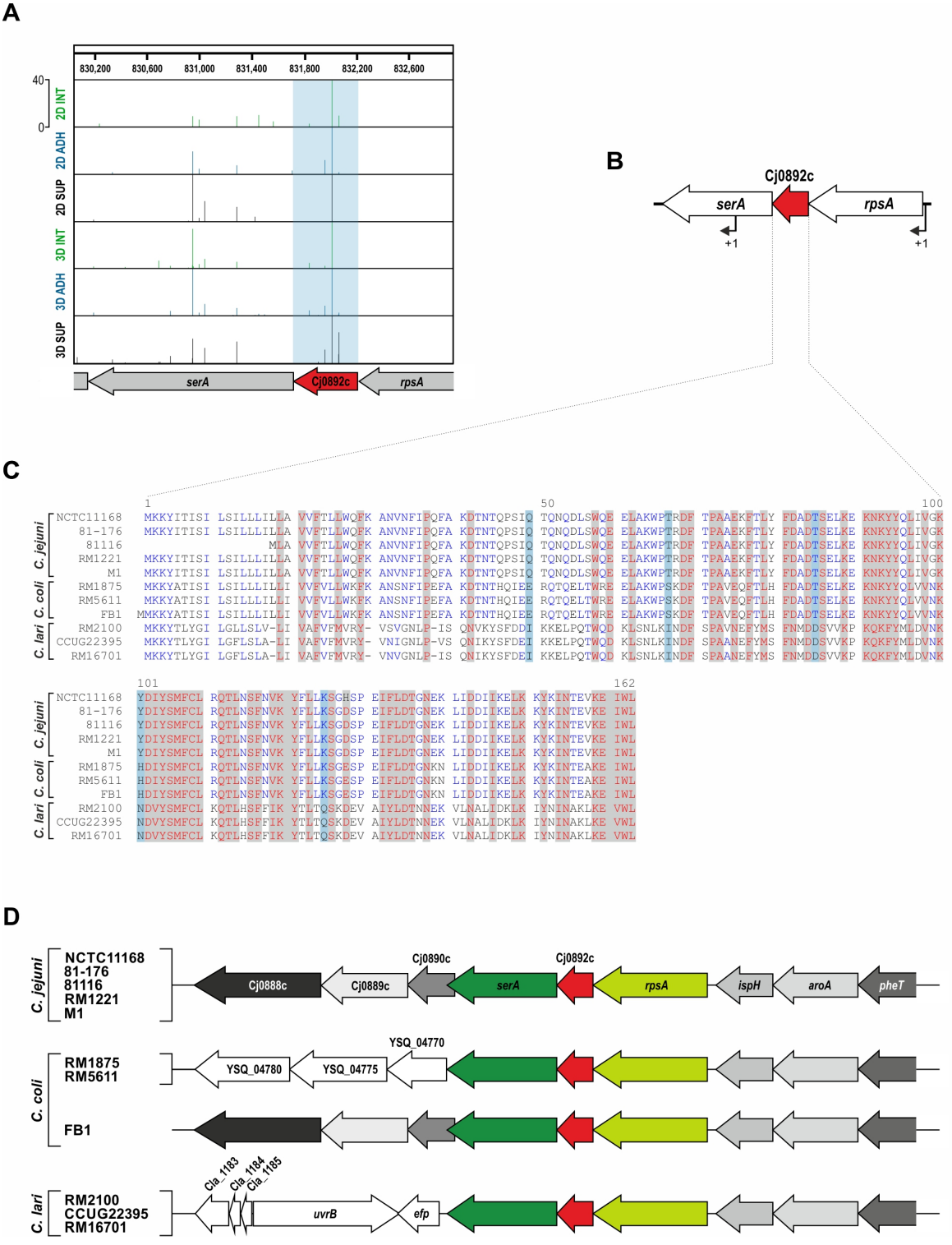

Figure 3.7: Tn insertion sites, genomic context, and protein sequence alignment of Cj0892c in different *C. jejuni*, *C. coli*, and *C. lari* strains. (A) Screenshot from the IGB showing the genomic region of Cj0892c and its surrounding genes with the read distribution for the respective genomic Tn insertion sites. Shown are libraries prepared from non cell-associated bacteria in the supernatant of the tissue model or the Caco-2 monolayer (3D/2D SUP, black), as well as those adherent to (3D/2D ADH, blue) or internalized into (3D/2D INT, green) host cells from the respective infection model. Arrows represent the annotated open reading frames (ORFs) with Cj0892c highlighted in red (arrow)

and in the light blue box (reads). **(B)** The 489-nt long Cj0892c gene is encoded between the upstream 30S ribosomal protein S1 (*rpsA*) and the dehydrogenase *serA* with primary transcriptional start sites (pTSS, +1; (Dugar *et al.*, 2013)) indicated by arrows. **(C)** Protein sequence alignment of Cj0892c from diverse *C. jejuni* strains and its orthologs from *C. coli* and *C. lari* isolates. Conserved residues are boxed in grey and Tn insertion sites are marked in light blue. Numbers indicate positions in the amino acid sequence respective to the annotated first amino acid from strain NCTC11168. **(D)** Cj0892c is located in the same genomic region in different *Campylobacter* species and its flanking genes are identical to the ones found in *C. jejuni* NCTC11168. Orthologous genes are marked with the same color and unrelated genes are illustrated in white. For simplicity, only one representative is shown for each species (NCTC11168 for *C. jejuni*; RM1875 for *C. coli*; RM2100 for *C. lari*) if the genomic context is identical to the other isolates in the same species.

bacteria internalized into 2D Caco-2 cells (2D INT), as well as those adherent to (3D ADH) and internalized into the 3D tissue model (3D INT), when compared to those constructed from their respective non cell-associated bacteria in the supernatant (2D SUP and 3D SUP). An IGB screenshot of the six Tn-seq libraries shows reduced insertion counts primarily for 3D ADH and 3D INT when compared to the respective supernatant (Figure 3.7 A) indicating a reduced presence of the transposon insertion mutant in the ADH and INT library (see also Table 3.1). This in turn is indicative for the requirement of Cj0892c for proper adherence and/or internalization of *C. jejuni* in the 3D tissue model. Cj0892c seems to be transcribed from a primary transcriptional start site (pTSS) of its upstream gene *rpsA* as determined in the *C. jejuni* comparative transcriptome analysis based on differential RNA-seq (dRNA-seq) from (Dugar *et al.*, 2013) (Figure 3.7 B). Its protein sequence is almost 100 % conserved in *C. jejuni* isolates, fairly similar to the homologs found in *Campylobacter coli* (*C. coli*) strains, and to a lesser extent to the *Campylobacter lari* (*C. lari*) orthologs (Figure 3.7 C, grey boxes indicate conserved residues). These three species are almost exclusively responsible for human gastrointestinal-related *Campylobacter* infections worldwide (Moore *et al.*, 2005). Tn insertions in the coding sequence (CDS) of Cj0892c were mostly found in residues that were conserved among *C. jejuni* and *C. coli* isolates but rarely among all three species (Figure 3.7 C, Tn insertion sites are marked in light blue boxes). In the genomes of all three *Campylobacter* species, Cj0892c is always encoded downstream of *rpsA* (30S ribosomal protein S1) and upstream of *serA* (D-3-phosphoglycerate dehydrogenase) (Figure 3.7 D). Whereas genes downstream of *serA* vary in different *Campylobacter* strains, the open reading frames (ORFs) upstream of *rpsA* are conserved in all three species. The conservation of Cj0892c among *Campylobacter* strains, together with the criteria described previously, marks it as a potentially interesting candidate to follow up on. In addition, it has recently been identified in a genome-wide screen for fitness determinants of *C. jejuni* strain 81-176 in a mouse model of infection (Gao *et al.*, 2017), undermining its potential relevance during infection.

The ratio of Tn insertion counts for Cj0978c demonstrated similar fold changes as for Cj0892c in the 3D tissue model, but no measurable change during infection of the 2D Caco-2 monolayer (Figure 3.8 A). The putative lipoprotein encoded by Cj0978c could

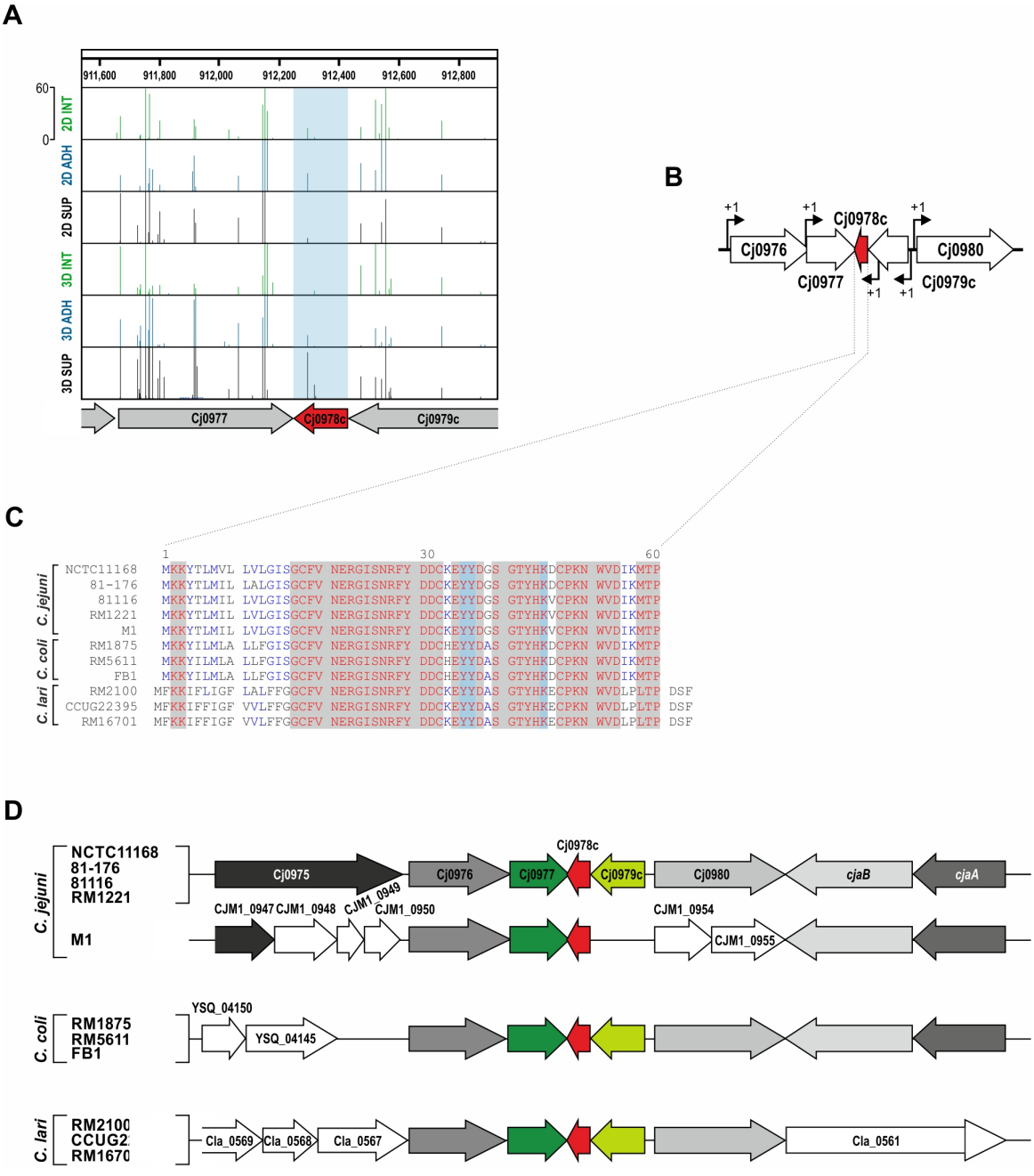

Figure 3.8: Tn insertion sites, genomic context, and protein sequence alignment of Cj0978c in different *C. jejuni*, *C. coli*, and *C. lari* strains. (A) Read coverage of genomic Tn insertion sites for Cj0978c (red arrow, reads highlighted in the light blue box) and its flanking genes (grey arrows) in an IGB screenshot including 3D/2D SUP (black), 3D/2D ADH (blue), and 3D/2D INT (green) libraries. **(B)** Cj0978c spans 174 nt and is flanked by a putative micrococcal nuclease (Cj0979c) and a hypothetical protein (Cj0977). pTSS are designated by +1 above their respective arrows and were previously identified in (Dugar *et al.*, 2013). **(C)** Alignment of the amino acid sequence encoded by

Cj0978c in five *C. jejuni* strains compared to the orthologous sequences from three *C. coli* and three *C. lari* isolates. Conserved residues are boxed in grey and Tn insertion sites are marked in light blue. Numbers indicate positions in the protein sequence respective to the annotated starting amino acid from strain NCTC11168. **(D)** Genomic context for Cj0978c and its surrounding genes. Orthologs in different *Campylobacter* strains are illustrated by the same color, whereas unrelated genes are indicated in white. For simplicity, only one representative is shown for each species (NCTC11168 for *C. jejuni*; RM1875 for *C. coli*; RM2100 for *C. lari*) if the genomic context is identical to the other isolates in the same species.

practically be considered a small protein as its coding sequence spans only 57 amino acids. It is transcribed from its own pTSS located internally in the upstream gene Cj0979c (Dugar *et al.*, 2013), which codes for a putative micrococcal nuclease (Figure 3.8 B). Except for eight amino acids, all other residues are identical in *C. jejuni* and *C. coli* isolates, and conservation among *C. lari* strains can likewise be considered fairly high (Figure 3.8 C, grey boxes mark conserved residues). Contrary to Cj0892c, all Tn insertion sites in Cj0978c (highlighted in light blue boxes) are limited to residues of complete conservation among all *Campylobacter* species analyzed. Location of Cj0978c downstream of the gene coding for a micrococcal nuclease seems to be conserved among *Campylobacter* species. The exception is *C. jejuni* isolate M1, which is missing an ortholog for this particular nuclease altogether (Figure 3.8 D). Similarly conserved across all species is a gene encoding a putative hypothetical protein downstream of Cj0978c, namely Cj0977, which has already been recognized in many studies – including this one – to be important for *C. jejuni* fitness *in vivo* and *in vitro* (Goon *et al.*, 2006; Yokoyama *et al.*, 2008; Novik *et al.*, 2010; Gao *et al.*, 2014). In contrast, Cj0978c has only been detected in one chicken infection Tn-seq screen of *C. jejuni* isolate M1 (de Vries *et al.*, 2017a). The M1 isolate is a rare case of direct transmission from chicken to human (Friis *et al.*, 2010). Taken all these properties together, Cj0978c equally qualifies as an intriguing candidate for further pursuit.

The next candidate was not just unique to this screen but also unique to the 3D tissue model, setting an intriguing premise for a potential novel factor contributing to the interaction of *C. jejuni* specifically with polarized intestinal human cells. Cj1643 is a putative periplasmic protein, disruption of which resulted in a decreased Tn insertion count for 3D ADH and 3D INT (Figure 3.9 A). It is located upstream of *ispA*, a geranyltranstransferase, and downstream of Cj1642, a putative nucleoid-associated protein (Figure 3.9 B). Transcription of Cj1643 could potentially be driven from a pTSS located internally in *murE* upstream of Cj1642 (Dugar *et al.*, 2013). In addition, it is also conceivable that Cj1643 might be transcribed as part of an operon spanning Cj1639 - Cj1650. In general, the polypeptide encoded by Cj1643, as well as its genomic location, is up to 99 % conserved among *C. jejuni*

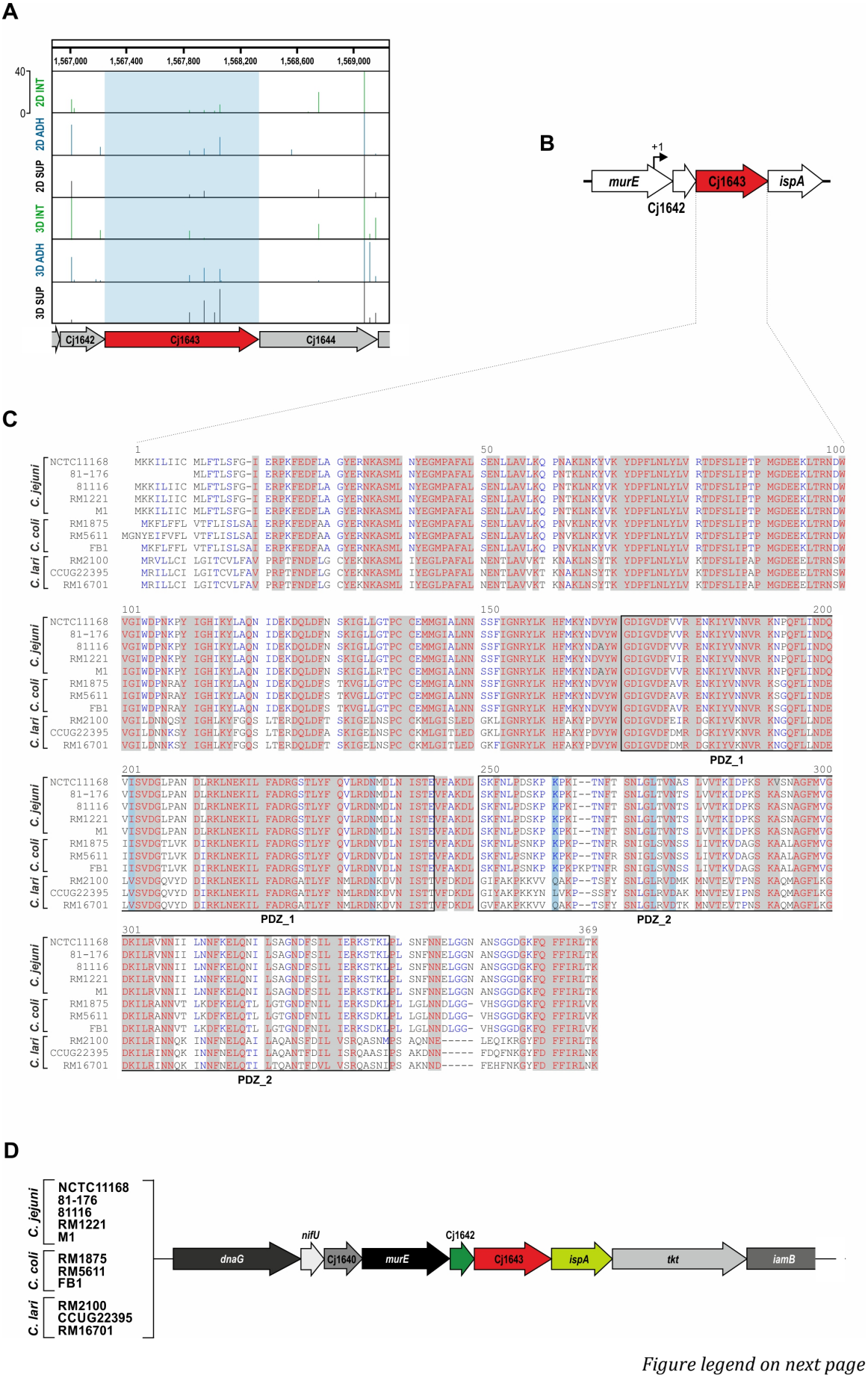

Figure legend on next page

Figure 3.9: Tn insertion sites, genomic context, and protein sequence alignment of Cj1643 in different *C. jejuni*, *C. coli*, and *C. lari* strains. (A) IGB screenshot for the Tn insertion sites in the genomic region coding for Cj1643 and its up- and downstream genes. Libraries were generated from 3D/2D SUP (black), 3D/2D ADH (blue), and 3D/2D INT (green). The red arrow represents the annotated ORF for Cj1643 (Tn insertion sites are highlighted in the light blue box) and the grey arrows signify the flanking genes. **(B)** In *C. jejuni* NCTC11168, the 1095-nt long Cj1643 is flanked upstream by Cj1642 (coding for a putative nucleoid-associated protein) and downstream by *ispA* (encoding a geranyltranstransferase). The pTSS potentially driving transcription for Cj1643 is marked by an arrow (+1) and was identified in (Dugar *et al.*, 2013). **(C)** Protein sequence alignment of Cj1643 for *C. jejuni*, *C. coli*, and *C. lari* isolates. Among the orthologous sequences, conserved residues are boxed in grey and Tn insertion sites are indicated in light blue. Areas framed in black mark the locations of the PDZ protein domains (PDZ_1, PDZ_2) predicted for strain NCTC11168, and the numbers specify positions in the amino acid sequence respective to the annotated first amino acid from strain NCTC11168. **(D)** Location of Cj1643 is preserved among *Campylobacter* species in between *ispA* and orthologs of Cj1642. Only one representative is shown (*C. jejuni* NCTC11168) as the genomic context is identical to the other species.

isolates (Figure 3.9 C and D). While its position in the genome is also very similar in *C. coli* and *C. lari* and the protein sequence is up to 80 % identical to the one found in *C. coli* isolates, *C. lari* strains show only partial overlap to the amino acid sequence of Cj1643 in NCTC11168 (Figure 3.9 C, conserved residues are marked in grey). Two PDZ (postsynaptic density 95, PSD-95; discs large, Dlg; zonula occludens-1, ZO-1) domains are predicted for the protein encoded by Cj1643 in strain NCTC11168 (Figure 3.9 C, indicated by black frames). Most notably, all of the Tn insertion hits are located in the PDZ domain-containing regions of the protein (Figure 3.9 C, Tn insertions are highlighted in light blue). These domains belong to the most commonly found protein-protein interaction domains from bacteria to mammals (Nourry *et al.*, 2003). Most often, proteins containing these domains participate in larger complexes to facilitate intracellular signaling (Ponting *et al.*, 1997). This might be an intriguing consideration for its putative role during *C. jejuni* infection in the human host.

Even though these above described candidates (Cj0892c, Cj0978c, Cj1643) were the top three candidates of unknown function, whose insertion mutants showed an attenuating phenotype primarily in the tissue model, the putative transcriptional regulator Cj0883c was considered as a fourth candidate. In the screen performed in this thesis, disruption of Cj0883c lead to a five-fold decrease of insertion counts in the library created from internalized bacteria from the tissue model only when compared to those that were not associated with cells (Figure 3.10 A, Table 3.1). As mentioned previously, disruption of this particular gene led to a decreased fitness phenotype in many other studies prior to this one (Hendrixson & DiRita, 2004; Gao *et al.*, 2014, 2017, de Vries *et al.*, 2017a, 2017b).

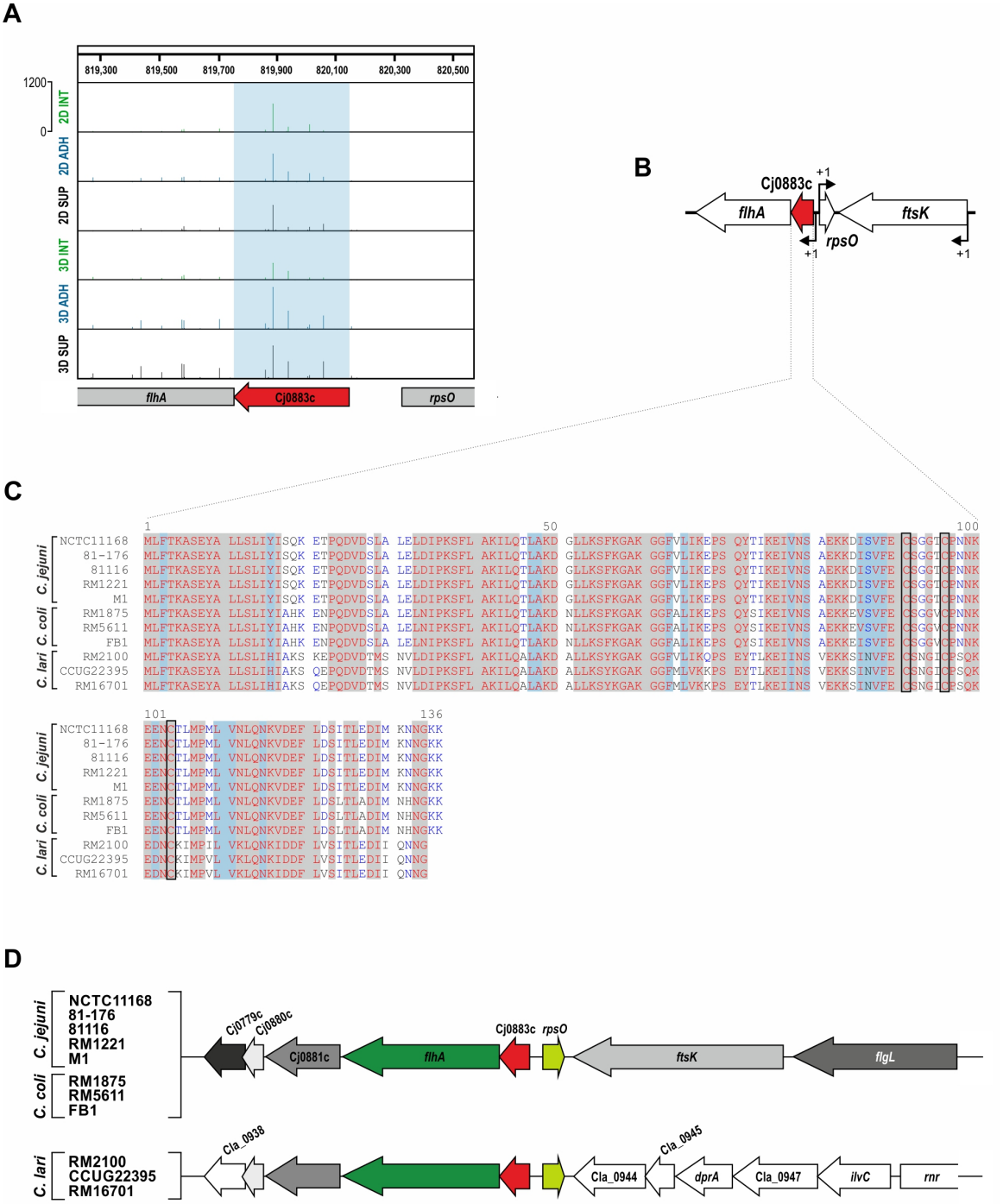

Figure 3.10: Tn insertion sites, genomic context, and protein sequence alignment of Cj0883c in different *C. jejuni*, *C. coli*, and *C. lari* strains. (A) Screenshot for the read distribution of Tn insertion sites in the genomic region of Cj0883c (red arrow, highlighted in the light blue box) and its flanking genes (grey arrows) taken from the IGB. Displayed are read counts for 3D/2D SUP (black), 3D/2D ADH (blue), and 3D/2D INT (green) libraries. **(B)** The 411-nt spanning putative transcriptional regulator Cj0883c is located upstream of *flhA* and its pTSS seems to be driving expression of both genes (pTSS, +1; (Dugar *et al.*, 2013)). Located upstream on the sense strand is the gene coding for the 30S ribosomal protein S15 (*rpsO*). **(C)** Alignment of the amino acid sequence encoded by Cj0883c in *C. jejuni* to the orthologs present in *C. coli* and *C. lari* isolates. Conserved residues are boxed in grey and Tn insertion sites are marked in light blue. The positions in the protein sequence relative to the

annotated first amino acid from strain NCTC11168 are indicated by numbers above the sequence. Black frames highlight three cysteine residues, which could potentially be involved in Fe-S cluster coordination. **(D)** Location of Cj0883c in the genome relative to its flanking genes in *C. jejuni* strains, as well in *C. coli* and *C. lari*. Orthologs in different *Campylobacter* strains are illustrated with the same color, whereas unrelated genes are indicated in white. As a representative for the genomic organization found in all *C. jejuni* strains and *C. coli* strains, only the genomic context for NCTC11168 is shown. Strain RM2100 represents the genomic arrangement for *C. lari* strains.

However, hits in Cj0883c were suggested to lead to potential polar effects on the downstream gene *flhA* (Figure 3.10 B) (Gao *et al.*, 2014), which upon deletion renders *C. jejuni* non motile (Hendrixson & DiRita, 2003). Thus, isogenic deletion mutants of the transcriptional regulator were often accompanied by a decreased or complete loss of motility (Hendrixson *et al.*, 2001; Gao *et al.*, 2014). This is a plausible scenario since Cj0883c is potentially transcribed from its own pTSS (Figure 3.10 B) that possibly also drives transcription of *flhA* (Dugar *et al.*, 2013). The amino acid sequence of this putative regulator is highly conserved among *Campylobacter* species and almost identical among *C. jejuni* and *C. coli* isolates (Figure 3.10 C, grey boxes highlight conserved residues and Tn insertions are marked in light blue). In the genome of all three *Campylobacter* species, Cj0883c is always encoded upstream of *flhA* and downstream of *rpsO* (Figure 3.10 D). Utilizing the InterPro database (Database of protein families, domains, and functional sites; (Finn *et al.*, 2017)), a very conserved winged helix-turn-helix (HTH) domain was predicted in Cj0883c as part of the large Rrf2 family of transcriptional regulators just like IscR in *E. coli* or *Salmonella*. IscR is widely conserved among bacteria (Rodionov *et al.*, 2006), and appears to be important for full virulence of many other pathogens such as *Pseudomonas aeruginosa* (Kim *et al.*, 2009), enterotoxic *E. coli* (Haines *et al.*, 2015), or *Yersinia pseudotuberculosis* (Miller *et al.*, 2014). Reminiscent of *E. coli* or *Salmonella* IscR, Cj0883c contains three cysteine residues towards its C-terminus (Figure 3.10 C, marked with black boxes) that could potentially be involved in the coordination of iron-sulfur (Fe-S) clusters. As disruption of Cj0883c shows such a specific fitness defect in our screen, which might be independent of a possible loss of motility due to *flhA*, further characterization of its role during *C. jejuni* infection could provide insights into how *C. jejuni* regulates its metabolism and maintains iron homeostasis within cells.

In order to confirm the results received from the Tn-seq experiments and further evaluate the role of the chosen candidate genes during the *C. jejuni* infection process, non-polar deletion mutants were constructed by replacement of most of their coding sequences with a non-polar kanamycin resistance cassette (*aphA-3*) (Figure 3.11 A, *left panel*). The use of a non-polar resistance cassette was particularly important for deletion of the transcriptional regulator Cj0883c. As its coding sequence partially overlaps with the downstream gene *flhA*,

potential polar effects had to be avoided in order to prevent impairment of bacterial motility. Therefore, the swimming behavior of the isogenic deletion mutants was first tested on motility agar plates and quantified measuring the radius of the swimming halo for each strain in three biological replicates (Figure 3.11 B). Disruption of Cj0883c by insertion of a kanamycin resistance cassette had no effect on bacterial motility when compared to the parental NCTC11168 wildtype excluding potential polar effects on the downstream-encoded *flhA*. The complementation strain expressing a wild-type copy of Cj0883c including its own pTSS and promoter region in the *rdxA* locus (Figure 3.11 A, *right panel*) was as motile as the deletion and the wild-type strain. While deletion of Cj0883c had no effect on *C. jejuni* motility, the assay revealed that deletion of the other three Tn-seq candidates (Cj0892c, Cj0978c, Cj1643) rendered the bacteria non motile leading to similar-sized swimming halos as the negative control Δ*flaA*. Expression of a wild-type copy of the respective genes under the control of the constitutive *metK* promoter in the *rdxA* locus complemented the non-motile phenotypes of ΔCj0892c, ΔCj0978c, and ΔCj1643 (Figure 3.11 A, *right panel* and B). This suggests that these are *bona-fide C. jejuni* motility factors that have not been previously identified as such.

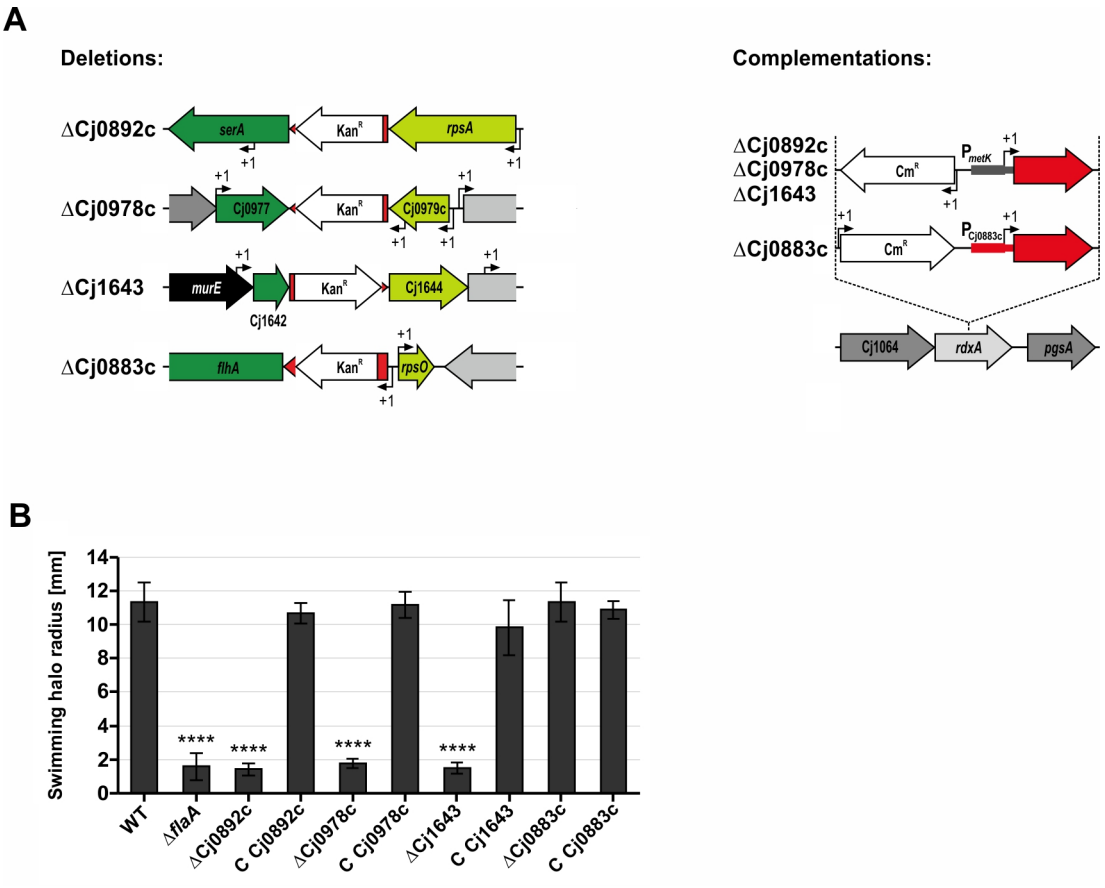

Figure legend on next page

Figure 3.11: Construction of deletion and complementation strains for Tn-seq candidate genes and motility assays. (A) (*Left panel*) Schematic representation of the cloning strategy used for the construction of *C. jejuni* NCTC11168 deletions, which have been identified in the Tn-seq screen for the 3D tissue model. The non-polar kanamycin cassette (*aphA-3*; Kan^R) was used to avoid polar effects. pTSS are denoted with +1. **(A)** (*Right panel*) Deletion mutant strains were complemented in *trans* at the unrelated *rdxA* locus. Wild-type copies of Cj0892c, Cj0978c, and Cj1643 were expressed under the control of the constitutive *metK* promoter, while a chloramphenicol resistance cassette (*C. coli cat*; Cm^R) was included for clone selection. In order to complement the deletion of Cj0883c, a wild-type copy of the coding sequence including its native promoter and 5' UTR was expressed in *trans*. Red arrows indicate the respective gene of interest; pTSS are depicted as arrows with +1; the respective promoter regions are shown in either grey (P_{metK}) or in red ($P_{Cj0883c}$). **(B)** Motility of *C. jejuni* strains was assessed by measuring the radius of the swimming halo on motility plates (BB with 0.4 % Difco agar). Bacteria were grown in an overnight BB liquid culture until mid-exponential phase (OD_{600} 0.4) and 1 µl of bacterial suspension was stabbed into the agar plate. Following microaerobic growth at 37 °C for approximately 18 hrs, the radius of the swimming halo was measured for all deletion (Δ) and complementation (C) strains, in addition to the NCTC11168 parental wildtype (WT) and a non-motile control deletion mutant of *flaA* (Δ*flaA*). Asterisks indicate the significant difference to WT. ****: $p < 0.0001$. For statistical data analyses, the Student's *t*-test was employed.

Subsequent infection experiments confirmed that disruption of Cj0892c, Cj0978c, and Cj1643 resulted in reduced adherence (Figure 3.12 A) and almost non-existent internalization (Figure 3.12 B) in the 3D tissue model. This phenotype was fully complemented by expression of the wild-type copy of the gene in *trans*. Similar to other non-motile *C. jejuni* strains such as a Δ*flaA* mutant (observed in Figure 2.10 and *e.g.* (Wassenaar *et al.*, 1991, 1993; Stahl *et al.*, 2014)), the same deletion mutants were equally reduced in their ability to interact with 2D Caco-2 cells (Figure 3.12 A and B). However, except for Cj0892c, Tn insertion mutants of Cj0978c and Cj1643 did not result in a reduced insertion count ratio in the previously performed Tn-seq screen with non-polarized Caco-2 cells. This is surprising as non-motile mutant strains generally demonstrate a very strong reduction in their ability to interact with host cells. However, none of the other genome-wide screens for *C. jejuni* fitness factors during infection of 2D intestinal epithelial cells were able to identify these genes either (Novik *et al.*, 2010; Gao *et al.*, 2014; de Vries *et al.*, 2017a). Only screens performed in animal models were able to pick up on the phenotype connected to the disruption of Cj0892c (Gao *et al.*, 2017) and Cj0978c (de Vries *et al.*, 2017a) emphasizing the power of the 3D tissue model employed in this thesis and suggesting a possibly more intricate participation of these genes during *C. jejuni* motility.

Outcomes of infection experiments with the deletion mutant of the transcriptional regulator Cj0883c matched the phenotype suggested by our Tn-seq screen. While the adhesion potential of ΔCj0883c did not seem to be compromised compared to its parental

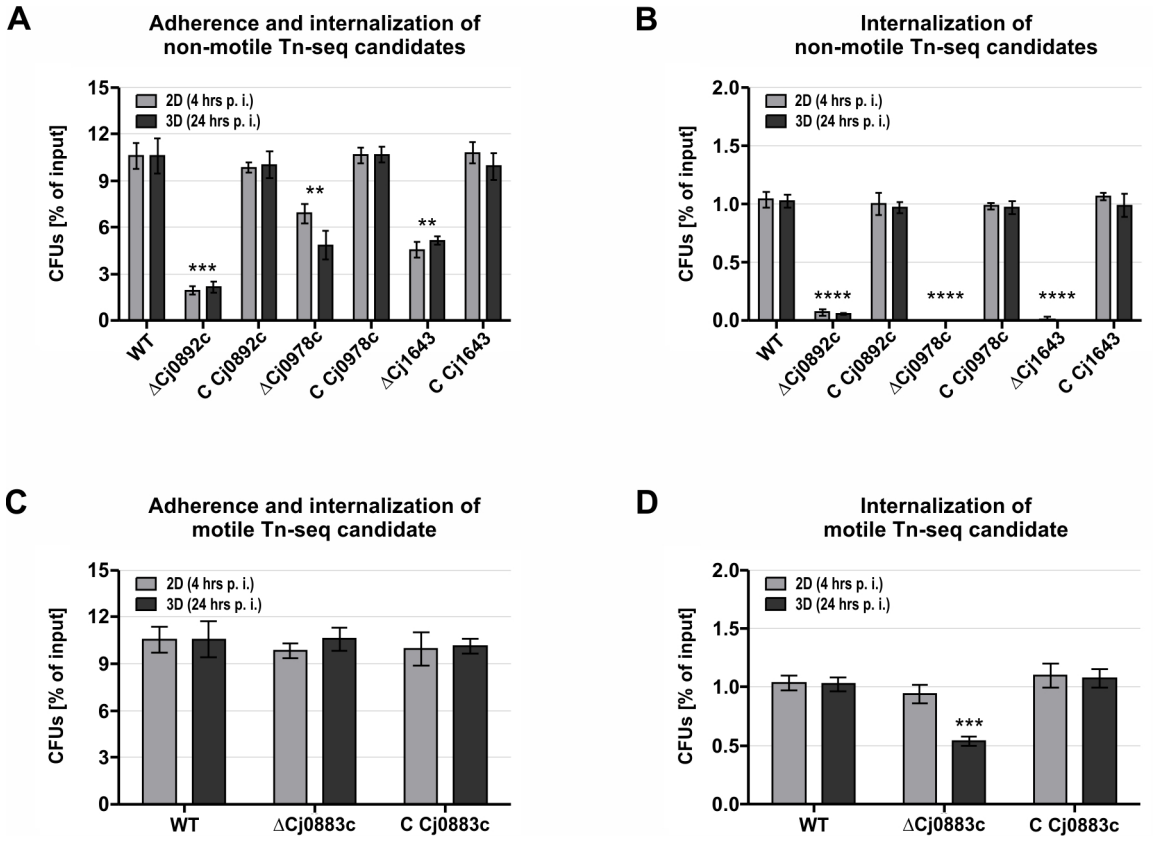

Figure 3.12: Infection experiments with Tn-seq candidate mutant strains. (A – D) CFUs were isolated for adherent and internalized bacteria **(A, C)** or internalized bacteria only **(B, D)** of NCTC11168 wildtype (WT), deletion (Δ), and complementation (C) of the respective non-motile candidates Cj0892c, Cj0978c, and Cj1643 **(A, B)**, or the motile transcriptional regulator Cj0883c **(C, D)** in 2D monolayer infections (4 hrs p. i.) and the Caco-2 cell-based 3D tissue model (24 hrs p. i.). CFUs are depicted as a percentage of input bacteria and represent the mean of three biological replicates with corresponding SDs. Significance is given in respect to the parental WT. ****: $p < 0.0001$, ***: $p < 0.001$, **: $p < 0.01$. The Student's *t*-test was used to determine statistical significance.

wild-type strain (Figure 3.12 C), this particular deletion mutant exhibited reduced fitness only during internalization of polarized 3D host cells (Figure 3.12 D). Neither adherence to nor internalization into unpolarized Caco-2 cells was affected by disruption of the transcriptional regulator (Figure 3.12 C and D). This could potentially suggest a unique role for this transcriptional regulator during *C. jejuni* infection of *in-vivo* like reconstituted tissue and thus, potentially *in vivo* itself, while not being required during infection of 2D intestinal epithelial cells. Nonetheless, Cj0883c was among the genes identified by an *in-vitro* INseq screen that exhibited a strong defect for host cell invasion (Gao *et al.*, 2014). Consistent with their cell invasion phenotype, they found a deletion mutant of the transcriptional regulator in *C. jejuni* strain 81-176 to be not motile. However, their complementation experiments suggested that the phenotype might be due to polar effects on the downstream gene *flhA*. In fact, introduction of a wild-type copy of *flhA* into their Cj0883c deletion strain was able to

fully restore motility and host cell invasion, indicating that also the phenotype elicited by the original insertion mutant might have more likely been due to disruption of *flhA*. As the deletion mutant strain of Cj0883c generated in this thesis was motile (Figure 3.11 B) and its internalization decrease into 3D host cells could be fully complemented (Figure 3.12 D), future research could be dedicated to uncovering the regulon of this putative transcriptional regulator. In support of the observation that Cj0883c indeed seems to play no role in motility, deletion of Cj0883c in the strain 81-176 likewise did not affect motility (data not shown). However, whether the reduced internalization CFU count of ΔCj0883c in the 3D tissue model is due to an actual deficiency in internalization/invasion or rather the result of a diminished intracellular survival capacity remains to be determined.

Deletion of either of three hypothetical genes (Cj0892c, Cj0978c, Cj1643) led to a loss in motility, which could potentially result from defects in flagellar assembly or impairment of the motor that propels flagella movement. In order to distinguish between these two possibilities, transmission electron microscopy (TEM) was applied to examine potential loss of one or both flagella or other structural deficiency in the flagellar filament (Figure 3.13 A). As a visual negative control, deletion of *flaA* exhibited extremely short flagella as expected when compared to the wildtype. Contrary to Δ*flaA*, deletion mutant strains of Cj0892c, Cj0978c, and Cj1643 as well as their respective complementation strains displayed apparently normal flagella at both cell poles. Similar to the wild-type strain, neither filament presence nor length seemed to be compromised upon disruption of the three Tn-seq candidates, suggesting that these mutations may rather affect motor function than flagella assembly. In order to further narrow down a direct involvement in *C. jejuni* motility, subcellular localization of these putative flagellar proteins might hint towards a potential function. As *C. jejuni* expresses one flagellum at each cell pole, a corresponding polar localization of Cj0892c, Cj0978c, and Cj1643 could point towards a direct involvement of their gene products in flagellar biogenesis or function. To this end, fusion constructs of the respective Tn-seq candidate gene to superfolder green fluorescent protein (sfGFP), a variant of GFP that robustly folds when fused to polypeptides (Pédelacq *et al.*, 2006), were generated (Figure 3.13 B). Together with a chloramphenicol resistance cassette, these fusion constructs were introduced into the *rdxA* locus of their respective deletion strains. The sfGFP fusions were able to fully restore motility of the deletion mutants, supporting the functionality of the respective sfGFP-tagged versions of the putative motility proteins (data not shown). Confocal microscopy revealed localization of the Cj0892c::sfGFP fusion to be almost equally distributed between bipolar, unipolar, or non-polar localization (Figure 3.13 C and D) with 33 % of bacteria showing localization at both poles and 35 % at one pole only.

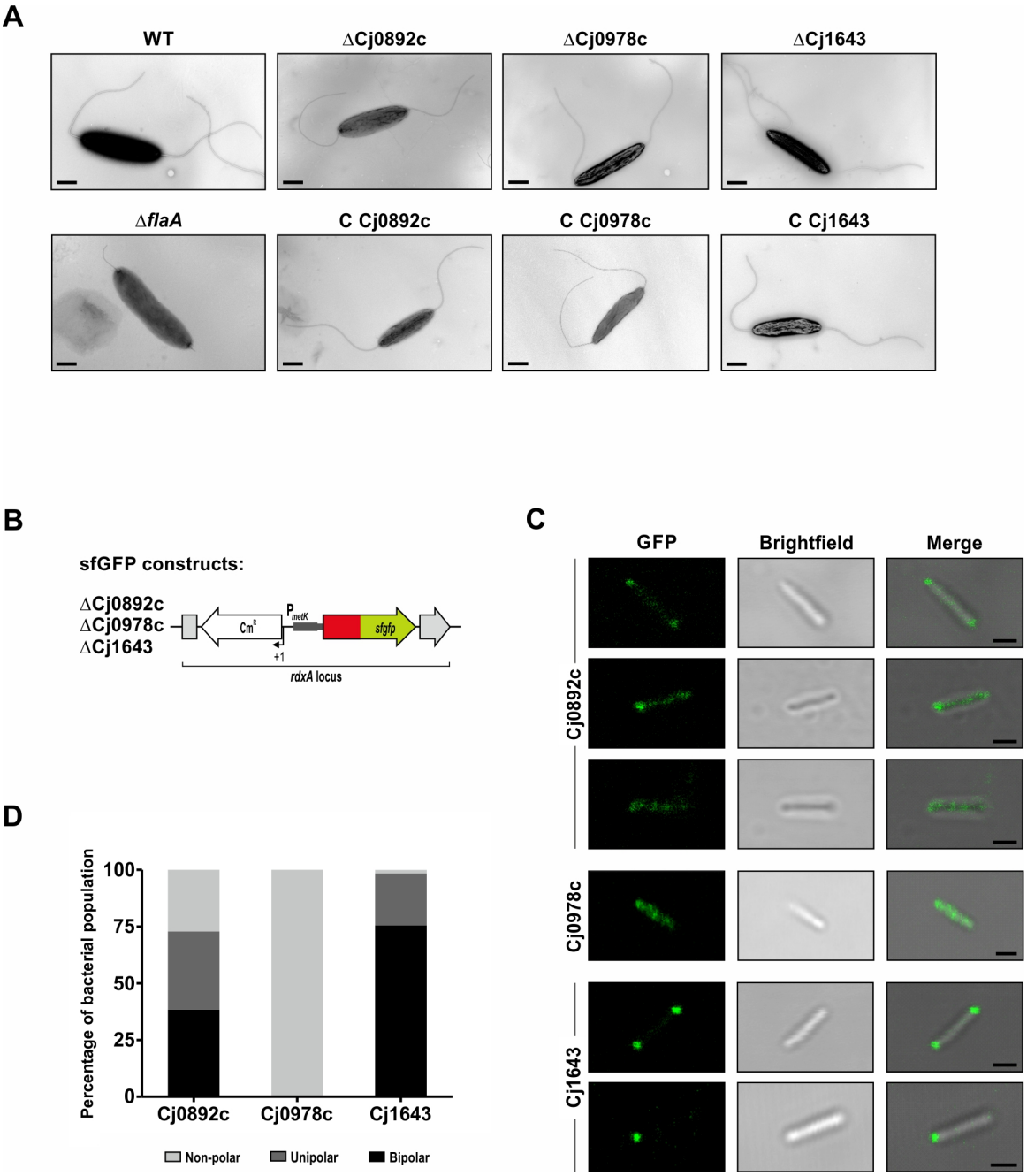

Figure 3.13: Transmission electron microscopy and subcellular localization of non-motile Tn-seq candidates. (A) TEM micrographs of wildtype (WT), Δ*flaA*, ΔCj0892c, ΔCj0978c, and ΔCj1643, as well as complementation strains of the deletion mutants (C Cj0892c, C Cj0978c, C Cj1643). Samples of the indicated strains were harvested from MH agar plates, carefully resuspended in PBS, and fixed overnight at 4 °C in 2 % glutaraldehyde in 0.1 M cacodylate buffer. After staining with 2 % uranyl acetate, bacterial cells were inspected using a Zeiss EM10 transmission electron microscope. Scale bar 0.5 µm. **(B)** Superfolder GFP (*sfgfp*) was fused to the second-to-last codon of Cj0892c, Cj0978c, and Cj1643 and expressed as a fusion gene product under control of the constitutive *metK* promoter (P_{metK}). Together with a chloramphenicol resistance cassette (*C. coli cat*; Cm^R), the fusion construct was inserted into the unrelated *rdxA* locus of the respective deletion mutant strains. A red arrow indicates the respective gene of interest. **(C)** Confocal microscopy images of the sfGFP-tagged proteins depicting the GFP channel only (488 nm), brightfield, and the merged images. For

Cj0892c::*sfgfp*, examples are shown for bipolar, unipolar, and non-polar localization. Cj0978c::*sfgfp* depicted no specific subcellular localization. Images for Cj1643::*sfgfp* portray bipolar or unipolar localization. Scale bar 1 µm. **(D)** Quantification of subcellular localization of the sfGFP-fusion proteins is depicted as the percentage of the bacterial population showing bipolar (black), unipolar (dark grey), or non-polar (light grey) localization. Cells counted for the respective strains: Cj0892c::*sfgfp* n = 218; Cj0978c::*sfgfp* n = 202; Cj1643::*sfgfp* n = 289.

In 32 % of the population, Cj0892c::sfGFP was diffusely distributed over the whole cell. In contrast, no polar localization could be detected for Cj0978c::sfGFP (Figure 3.13 C and D). Cj1643::sfGFP was observed predominantly at both cellular poles, while only a small percentage showed unipolar localization, and non-polar distribution could only be found in a negligible fraction of bacterial cells (Figure 3.13 C and D). These observations could potentially support the indication of a direct role for Cj0892c and Cj1643 in flagellar function, assembly, and/or biogenesis. Regarding the precise role for both of these putative motility genes as well as the motility involvement of Cj0978c, identification of interacting proteins via co-immunoprecipitation (co-IP) in the future might lead to a better functional understanding of these putative novel components of the *C. jejuni* flagellar system.

In summary, characterization of three candidate genes found in the genome-wide screen for *C. jejuni* fitness factors during infection of the Caco-2 cell-based 3D tissue model identified three novel *bona-fide* motility genes, which are highly conserved among *Campylobacter* species. Deletion of these genes did not result in loss of flagella pointing towards a role in flagella function rather than assembly. Co-IP experiments could uncover potential interacting protein partners for the motility genes hinting towards their precise role during *C. jejuni* motility. In addition, deletion of the transcriptional regulator Cj0883c revealed an internalization/intracellular survival phenotype unique to the tissue model, which could be uncoupled from the downstream gene *flhA*. Future research will focus on uncovering the regulon of the transcriptional regulator and thus, its precise role during *C. jejuni* infection of polarized intestinal epithelial cells.

4. Development and characterization of a mucus-containing intestinal tissue model and the impact of a protective mucus layer on *C. jejuni* pathogenesis

In addition to the 3D microenvironment of the GIT, it would be desirable to add an adherent mucus layer to an *in-vitro* infection model, as mucosal surfaces often use this viscoelastic coating as a first line of defense against invading pathogens. Hence, the mucous lining of the lower intestine is also the first site of interaction between *C. jejuni* and its niche in the human gut (Young *et al.*, 2007). Although this protective barrier can be found throughout the whole GIT, its thickness ranges from 200 – 300 µm in the stomach and small intestine, to 700 µm in the large intestine (Johansson *et al.*, 2011; Juge, 2012). Various gastrointestinal cell lines have been previously shown to produce different types of mucins adding up to mucus layers of diverse thickness, firmness, and confluence (Lindén *et al.*, 2007; Navabi *et al.*, 2013). In particular, HT29 and its daughter cell lines are often used to explore this viscoelastic gastrointestinal barrier. The HT29 cell line is a polarizing human colorectal adenocarcinoma cells, of which the HT29-MTX line originated from by treatment with the chemical compound methotrexate. This organic agent was previously used to act synergistically with 5-fluorouracil for chemotherapeutic treatment of colorectal cancer (Longley *et al.*, 2003). By treating the parental HT29 cell line with methotrexate, a resistant subclonal cell line (HT29-MTX) was separated that formed a homogenous monolayer of polarized goblet cells secreting mucins on their cell surface (Lesuffleur *et al.*, 1990, 1993). The development of a strong mucus-producing cell line was further refined by isolation of the HT29-MTX-E12 subclonal line, which was shown to form a tight confluent monolayer with a thick mucus layer on the apical cell surface (Behrens *et al.*, 2001; Alemka *et al.*, 2010; Navabi *et al.*, 2013). However, it is noteworthy that these HT29-derived cell lines only produce an adherent mucus layer upon polarization and differentiation of the cells, *e.g.* when grown on Transwell inserts. The same cells grown in flat 2D monolayer cultures are devoid of mucus and only sparsely produce mucins (data not shown; (Horstmann *et al.*, 2017; Li *et al.*, 2019). In order to test, whether these cells would support the development of a 3D intestinal tissue model comprised of a tight epithelial barrier and an adherent mucus layer, they were reseeded on the extracellular matrix scaffold SISmuc. First, they were investigated for their potential to form cell-cell junctions and in a second step for their ability to produce gastrointestinal mucins. From here on, these cell lines will be referred to as HT29, MTX (HT29-MTX), and E12 (HT29-MTX-E12) cells.

4.1. HT29-derived MTX and E12 cells establish an epithelial barrier on the SISmuc with similar permeability as human small intestine

HT29, MTX, and E12 cells were seeded onto the SISmuc scaffold and grown both under static and dynamic cultivation condition. As previously shown, permeability measurements using FITC-dextran (4 kDa) during cultivation of the tissue models were utilized to follow the formation of an epithelial barrier. Similar to the Caco-2 cell-based tissue model (Figure 2.2 B), permeability of the developing barrier of the HT29, MTX, and E12 cell lines on the SISmuc scaffold was measured during cultivation until FDPA values remained relatively constant (28 – 35 days). As described in chapter 2.2 of this thesis, dynamic cultivation on an orbital shaker employing a rotational speed of 65 rpm is able to simulate shear stress on the cells that is similar to what they experience in their native environment. For the Caco-2 tissue model, this led to an overall morphology that is reminiscent of small intestinal tissue, to a significantly increased cell height, and to a more precise location of tight junction proteins. As all of these factors are important for the development of an *in-vivo* like intestinal tissue model, static cultivation (Figure 4.1 A) in comparison to dynamic conditions (Figure 4.1 B) was tested for the mucus-producing cell lines as well.

Under static cultivation, permeability decreased in the first 21 days for all cell lines on the SISmuc. FDPA values of HT29 cells seemed to fluctuate at later time points, but permeability measurements of both MTX and E12 cells displayed a further decline on day 28 and remained constant until day 35 (Figure 4.1 A). However, permeability of all cell lines when grown statically on the SISmuc scaffold were closer to 2 % of the total FITC-dextran input than below 1 %. When compared to an FDPA value of approx. 0.07 % of the static Caco-2 based tissue model (see also Figure 2.2), this indicates that the HT29 cell line and its derivatives are not able to form a comparably tight epithelial barrier on the extracellular matrix scaffold. Thus, this method of cultivation might be less suitable for the combination of these cell lines with the SISmuc in order to set up an intestinal tissue model. However, permeability measurements during dynamic conditions (Figure 4.1 B) showed a gradual decrease over time for all cell lines up to 21 days in cultivation, the extent to which was much stronger compared to static conditions. However, similar to static cultivation conditions, permeability of HT29 cells did not decreased further and stagnated around day 21 post reseeding. Both MTX and E12 cells continued to decline in their permeability indicating the formation of an epithelial barrier that showed no additional decrease in permeability after 28 days in culture.

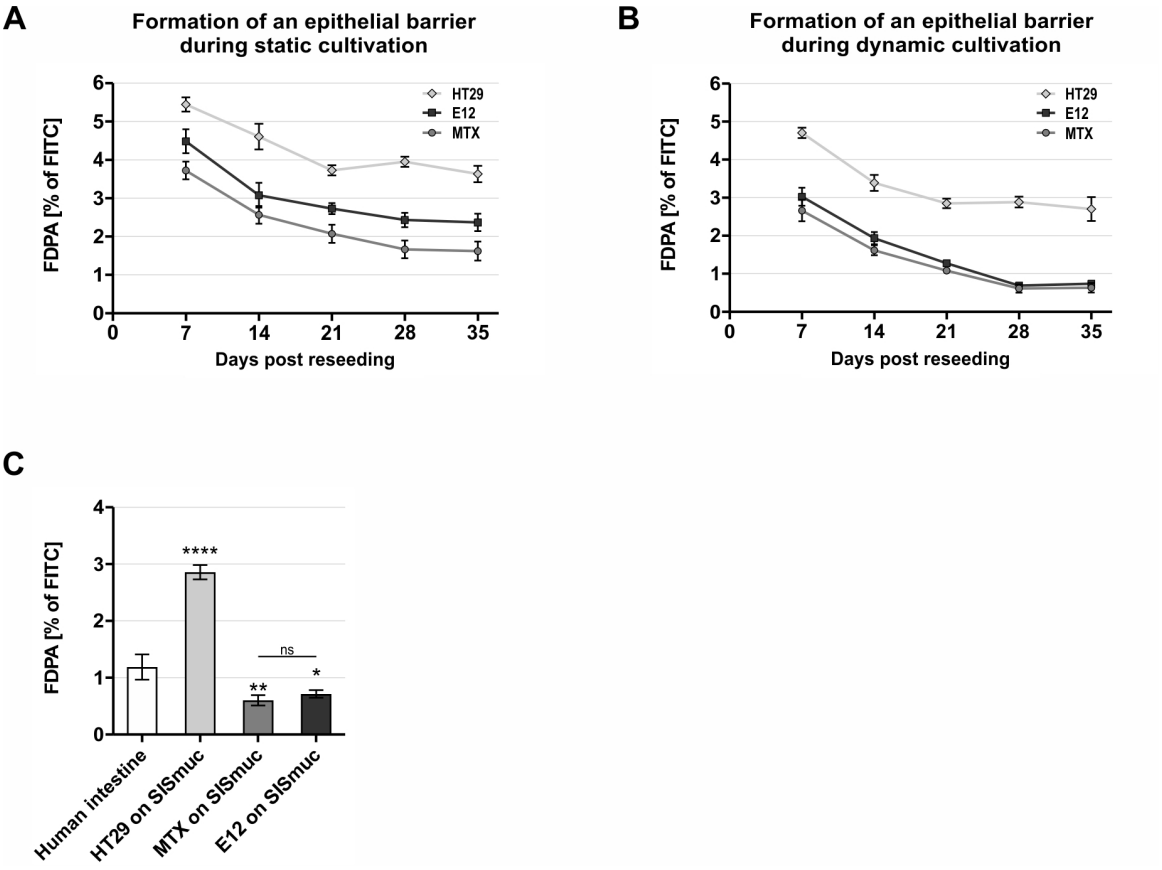

Figure 4.1: MTX and E12, but not HT29 cells, form a tight epithelial barrier on the SISmuc with dynamic cultivation comparable to native human small intestine. (A, B) The SISmuc was re-seeded with either HT29, MTX, or E12 cells and cultivated for up to 35 days under static **(A)** or dynamic **(B)** conditions caused by rotational movement of an orbital shaker at a speed of 65 rpm. Formation of an epithelial barrier is indicated by a decrease in permeability measured via FDPA. Data are depicted as mean values of three biological replicates with according SDs. **(C)** Permeability measurements of tissue models based on HT29, MTX, or E12 cells after dynamic cultivation for 28 days in comparison to measurements performed on native human mucosa from human small intestine that has been fixed into cell crowns. FDPA values are presented as the percentage of input FITC-dextran of four biological replicates. Asterisks above the columns indicate statistical analysis in comparison to the results for the native human intestine. ****: $p < 0.0001$, **: $p < 0.01$, *: $p < 0.05$, ns: not significant. Statistical data analysis was conducted using the Student's *t*-test.

In order to set these measurements in relation to permeability values from native human intestine, FDPA values obtained from HT29, MTX, and E12 cells on SISmuc after 28 days in dynamic culture were compared to human intestinal tissue. To this end, a piece of human small intestine derived from a stomach bypass surgery was separated from the underlying muscle tissue to isolate the mucosa. Subsequently, mucosal tissue was fixed into a cell crown and FITC-dextran measurements were performed just as described for the tissue models. Comparisons of permeability degrees between tissue models (SISmuc + HT29, MTX, or E12 cells) and human small intestine (mucosa only) showed that while MTX

and E12 cells formed similarly tight barriers on the SISmuc after 28 days under dynamic cultivation, both barriers were measurably tighter compared to native small intestine (Figure 4.1 C). However, permeability of these reconstructed epithelia came closer to human mucosal tissue than *e.g.* Caco-2 cells dynamically cultivated on SISmuc (0.14 % of FITC input) (Figure 2.2 B) potentially suggesting a more physiologically relevant barrier formed by MTX and E12 cells. HT29 cells were unable to establish a barrier comparable to native small intestinal mucosa and significantly differed in permeability values. These results support the idea that FDPA values of MTX or E12 cells on the SISmuc at 28 days post reseeding are likely reminiscent of the intestinal barrier exhibited in the human GIT.

Histological staining of the above-described tissue models with hematoxylin and eosin reinforced the results observed for barrier measurements (Figure 4.2 A). HT29 cells were unable to form a confluent epithelial monolayer on the SISmuc both under static and

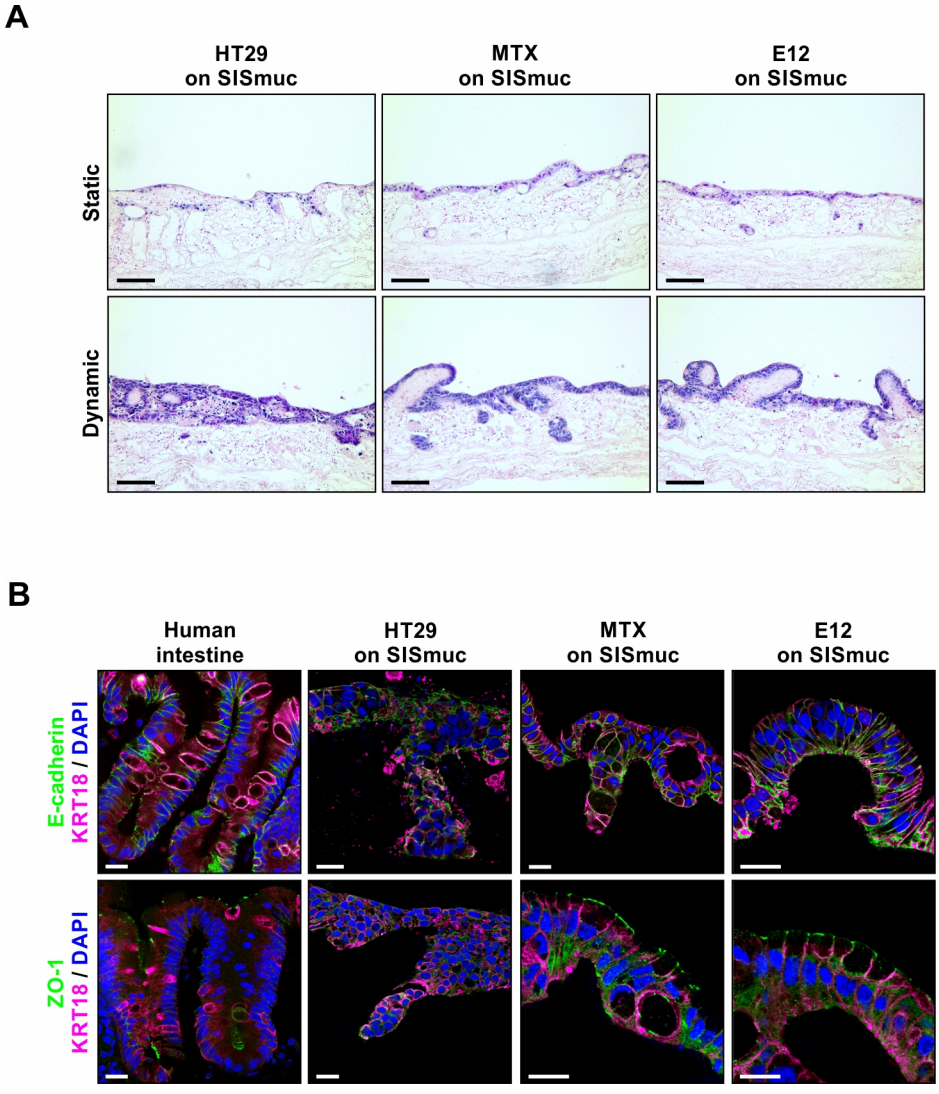

Figure legend on next page

Figure 4.2: Dynamic cultivation enhances tissue morphology and localization of cell-cell junction proteins in MTX- and E12-based tissue models. (A) H&E staining of 5 µm thick paraffin sections of HT29, MTX, and E12 cells cultivated on SISmuc for 28 days either under static (*upper panel*) or dynamic culture conditions (*lower panel*). Scale bar 100 µm. **(B)** Confocal cross sections of paraffinated human intestine and HT29-/MTX-/E12-based tissue models stained to visualize nuclei (DAPI, blue), cytokeratin-18 (KRT18, magenta) and either adherens junctions (E-cadherin, green) (*upper panel*) or tight junctions (ZO-1, green) (*lower panel*). Scale bar 25 µm.

dynamic cultivation conditions. Additionally, these cells were prone to multilayer formation when confronted with shear stress and thus did not reflect the morphology of a mucosal epithelium. Similar to what had been observed previously for Caco-2 cells, static cultivation of MTX and E12 cells resulted in flat tissue and cell morphology (Figure 4.2 A, *upper panel*). Shear stress resulting from the dynamic environment stimulated the cells to grow into more columnar-like structures reminiscent of intestinal enterocytes. In addition, overall tissue morphology was also more complex compared to tissue models lacking the influence of fluidic shear stress (Figure 4.2 A, *lower panel*). Immunohistochemical staining for the adherence junction protein E-cadherin and the tight junction protein ZO-1 confirmed that MTX and E12 cells form highly differentiated and polarized epithelial barriers on the SISmuc under dynamic conditions (Figure 4.2 B). Other than their parental HT29 cells, both cell lines show highly distinctive staining for adherence junctions as well as apically localized tight junctions reminiscent of human small intestine.

As the aim was to engineer an intestinal *in-vitro* tissue model able to recapitulate key aspects of *in-vivo* tissue, the above-presented data eliminated HT29 cells as well as the static cultivation process from further experimental characterization, as they proved unsuitable for the desired goal. Hence, all following tissue models are based on SISmuc reseeded with either MTX or E12 cells cultivated for 28 days under dynamic conditions, as they most closely resembled the intestinal epithelial barrier observed for human small intestine.

4.2. The E12 cell line produces a thick adherent mucus layer in the context of the intestinal 3D tissue model

The mucosal surfaces of the GIT are lined with mucus layers that constitute the first line of defense against invading microorganisms. Thus, an *in-vitro* infection model for pathogens of the GIT should include a mucus barrier in order to be able to investigate the interaction of the pathogens with this viscoelastic host barrier. Consequently, the tissue models based on SISmuc reseeded with MTX or E12 cells (dynamically cultivated for 28 days) were investigated for their mucus production. To avoid false positive results, the Caco-2 based tissue model underwent the same staining processes, as it had previously been shown that

these cells are incapable to produce mucins (Navabi *et al.*, 2013). Histological PAS (Periodic acid-Schiff)/Alcian blue staining was performed on all tissue models and human small intestine to detect potential mucus production by the different cell lines on the extracellular matrix scaffold. Alcian blue is a cationic dye that binds via electrostatic forces to the anionic carboxylated or sulfated polysaccharide chains of mucin molecules staining all acidic mucins a deep blue. The PAS reaction is based on the reactivity of free aldehyde groups within the monosaccharide units of the mucins with the Schiff reagent to form a bright red magenta coloring. Hence, neutral mucins show a bright magenta staining and together with the acidic blue mucins, tissue that contains both mucin types might show a dark blue or purple coloration. Generally, neutral mucins are predominantly found in the surface epithelia of the stomach, while acidic mucins are widely distributed along the GIT. The tissue processing in preparation for the staining procedure requires extensive washing and careful fixation, embedding in paraffin, as well as de- and re-hydration. As mucus is mostly composed of water, fixation and dehydration of tissue sections will extensively shrink the layer. In addition, mucus in the small intestine is not firmly attached to the epithelial surface and can thus be easily removed by washing.

Imaging of the mucus present in paraffin sections of human small intestine showed a purple layer firmly attached to the surface of the enterocytes most likely representing in part the membrane-bound glycocalyx formed by transmembrane mucins (Figure 4.3 A). In addition, mucus can be observed in large accumulations in the intestinal goblet cells and as blue threads rising from the crypts and in between villi representing the loose mucus typically covering the small intestine (Figure 4.3 A, inlet). Neither Caco-2 nor MTX cells showed magenta or blue coloring along their epithelial surface. Some small spots of blue could be detected for the MTX cells (Figure 4.3 A, inlet), suggesting that a small percentage of these cells seem to be able to produce mucus even though it is not sufficient to cover the whole surface. Matrices reseeded with the E12 subclonal lineage displayed extensive blue and purple staining on the epithelial surface as well as deep inside crypts (Figure 4.3 A, inlet). Moreover, the staining on the cell surface spanned entire cell crowns exemplified for two different E12-based tissue models (Figure 4.3 B) resulting in a confluent mucus layer albeit to varying degrees of thickness. Quantification of mucus thickness above the cell surface supported these microscopic observations (Figure 4.3 C). No width could be measured for Caco-2 cells. The MTX cell line produced an average mucus thickness of 1.27 ± 0.04 µm potentially representing for the most part the glycocalyx, which generally extends approx. 0.5 – 1.0 µm from the brush border (Gao & Lipowsky, 2010). An almost 10-fold increase in mucus thickness could be measured for both the native small intestine (12.94 ± 0.63 µm) as well as the E12 cells (11.28 ± 0.27 µm). As the average mucus thickness in the

small intestine is generally stated to be 200 – 300 µm (Pelaseyed *et al.*, 2013), the here determined thickness for the mucus layer represents only a fraction of what is normally observed under *in-vivo* conditions owing most likely to the tissue preparation and its repercussions. Consequently, it is perceivable that the amount of mucus present in the E12-based tissue model is also most likely an underestimation.

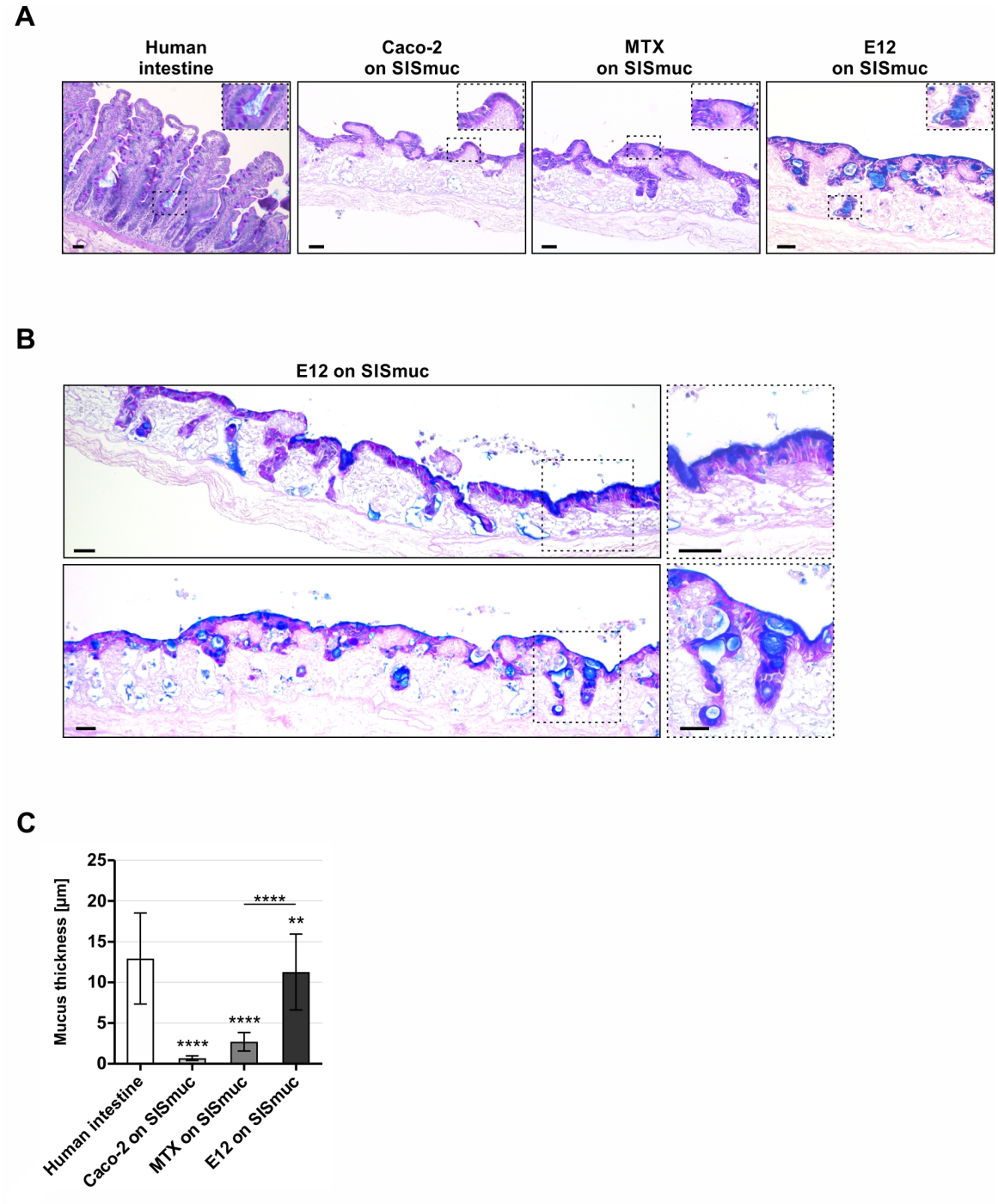

Figure legend on next page

Figure 4.3: E12 cells form a thick adherent mucus layer on their epithelial surface upon dynamic cultivation on the SISmuc scaffold. (A, B) PAS/Alcian blue staining of tissue samples that were fixed prior to sectioning (5 µm) with 2 % PFA and processed for paraffin embedding. **(A)** Light microscopic images of human intestine and Caco-2/MTX/E12 cells on SISmuc. Boxed regions are magnified as inlets. Scale bar 50 µm. **(B)** Overview images of two E12 based tissue models in order to depict the whole surface area (*left panel*) with magnifications of selected areas from each tissue model (*right panel*). Scale bar 50 µm. **(C)** Quantification of mucus thickness based on PAS/Alcian blue stainings. Ten microscopy images of five tissue models each or five human tissue samples were measured for their mucus thickness overlaying the epithelial cells in six regions spanning the entire image. Thus, 300 regions were measures in total for each condition and are depicted as the mean with respective SD. ****: $p < 0.0001$, **: $p < 0.01$. Statistical data analysis was performed using the Student's *t*-test.

Since it could be confirmed by PAS/Alcian blue staining that there is an abundant mucus layer overlaying the epithelial surface of E12 cells reseeded on the SISmuc, the mucin composition of this mucus is of particular interest. Mucin 2 (MUC2) is the most prominent gel-forming mucin of the gut, which along with other mucins is secreted into the lumen of the intestine (Johansson *et al.*, 2013; Naughton *et al.*, 2014). As it is not anchored to the epithelial surface, it needs to be continuously secreted from the goblet cells – in particular from the crypt openings – due to its constant removal by the peristaltic movements of the intestinal tract. Unsurprisingly, immunohistochemical staining against the MUC2 antigen in PFA-fixed paraffin sections of human small intestine revealed primarily a signal in goblet cells (Figure 4.4 A, *upper panel*). In addition, thin threadlike mucus could be observed between villi as had been described previously in a similar fashion (Ermund *et al.*, 2013). The MUC2 staining does not completely fill the space between the villi or the entire volume of the crypts, which is likely a shrinking artifact of the mucus gel during fixation and processing. As it has previously been proposed that mucus can be better preserved using Methacarn (a Carnoy fixative-based on dry methanol, chloroform, and glacial acetic acid) (Puchtler *et al.*, 1970; Pelaseyed *et al.*, 2013), mucus conservation was sought to be enhanced on the tissue models and human small intestine using this fixation technique (Figure 4.4 A, *lower panel*). However, no improvement could be observed either for antibody staining against MUC2 as well as later against the membrane-bound mucin 1 (MUC1). Equivalent to the PAS/Alcian blue staining, no Caco-2 and only a minority of MTX cells were positive for MUC2 staining. E12-based tissue models revealed extensive staining for MUC2 in huge aggregates inside and above goblet cells. However, no continuous epithelial surface coating with MUC2 could be observed for native small intestinal tissue. Nevertheless, there were areas of E12-based tissue models that revealed extensive MUC2 staining in large vacuoles between the cells (Figure 4.4 B, *left panel*), similar to what could be observed

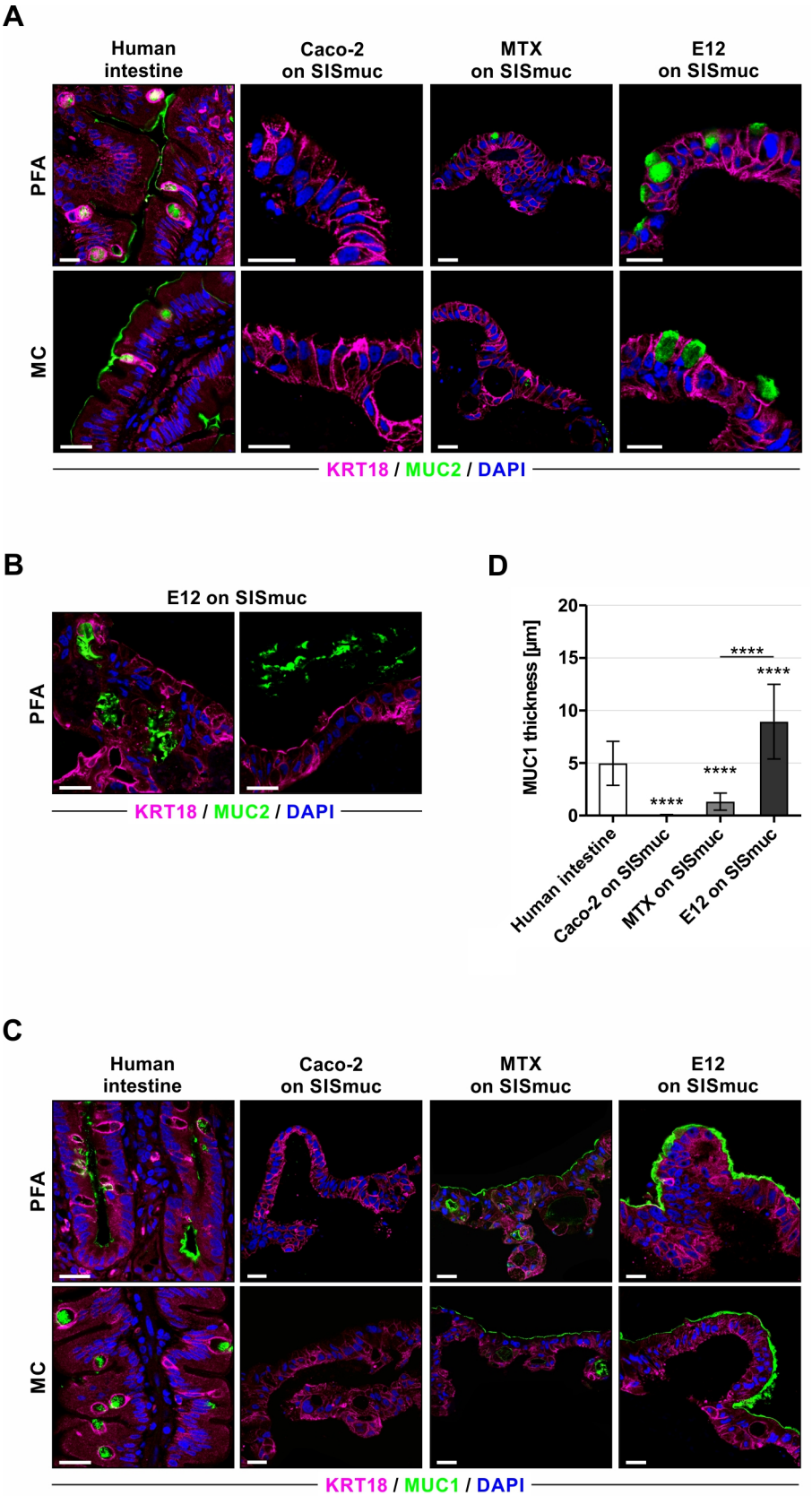

Figure 4.4: The mucus layer produced by E12 cells is mostly composed of the gastrointestinal mucins 1 and 2. (A – C) Cross sections of human intestine and tissue models based on Caco-2, MTX, or E12 cells. Nuclei are stained with DAPI (blue), epithelial cells are visualized with an antibody for

cytokeratin-18 (KRT18, magenta) and mucins are stained with anti-mucin 2 (MUC2, green) **(A, B)** or anti-mucin 1 (MUC1, green) **(C)**. Prior to antibody staining and confocal imaging, tissue models and human small intestinal samples were either fixed using 2 % PFA (*upper panels*) or Methacarn (MC, *lower panels*) with the exception of images in **(B)** where both left and right panel were fixed with 2 % PFA. Scale bar 25 µm. **(D)** Measurement of MUC1 thickness from ten confocal images of five different cell culture models/tissue samples. Eight areas in each image were measured resulting in quantification of MUC1 thickness of 400 regions per condition. Depicted is the mean of these measurements with respective SDs. ****: $p < 0.0001$. The Student's *t*-test was used to determine statistical significance.

in the histological mucus staining (Figure 4.3 A and B). This is likely due to entrapment of the loose mucus gel in these spaces, making it more difficult to remove by washing. Moreover, since there was also evidence for a layer-like structure within a greater distance from the epithelial surface, this suggests a MUC2 containing mucus layer produced by the E12 cells, which is most likely detached during the processing of the tissue (Figure 4.4 B, *right panel*).

Through PAS/Alcian blue staining of the tissue models it was revealed that there is an approximately 12 µm thick mucus layer on top of the E12 cells. While in the native intestine, this mucus layer is most likely composed of the MUC2 mucin, the lack of an equally thick MUC2 coating of E12 cells indicates the presence of a different mucin that is most likely membrane bound. One of the most common transmembrane mucins produced by carcinoma cells is the heavily glycosylated mucin 1 (MUC1), which is generally expressed on the apical surfaces of most secretory epithelia such as the mammary gland, respiratory, urinary, and gastrointestinal tracts (Gendler, 2001; Pelaseyed *et al.*, 2014). Thus, the tissue models and native small intestine were also investigated for the presence (Figure 4.4 C) and thickness (Figure 4.4 D) of MUC1. As expected, very little MUC1 could be observed in the human small intestine, where the glycocalyx is mostly composed of MUC3, MUC12, and MUC17. Furthermore, the Caco-2 cell-based tissue model showed no positive staining for MUC1. Both MTX and E12 cells produced this membrane-anchored mucin albeit in varying thickness. Whereas for MTX based tissue models, MUC1 staining seemed to barely extend above the confines of the glycocalyx (1.32 ± 0.04 µm), E12 cells were covered with an 8.93 ± 0.18 µm thick MUC1 layer (Figure 4.4 D). Together, immunohistochemical staining for the gel forming MUC2 and the membrane bound MUC1 support the data obtained for the histological detection of all mucins by the PAS/Alcian blue technique.

Overall, FDPA measurements from the previous chapter in addition to mucus-detecting staining methods showed that reseeding of the SISmuc with mucus-producing E12 cells under dynamic conditions allows the formation of a tight epithelial barrier with an adherent mucus layer. Permeability values are highly similar to native human small

intestine and the presence of the gastrointestinal mucins MUC1 and MUC2 add another layer of *in-vivo* relevance to the tissue model in order to study infection processes with pathogenic bacteria.

4.3. The mucus layer provides protection against *C. jejuni* colonization, transmigration, and barrier disruption

The mucus layer covering the epithelial lining of the gastrointestinal tract provides direct protection against invading microorganism by separating them from epithelial cells as well as by promoting their clearance from the GIT. In particular in the small intestine, bacteria have to avoid being trapped in the mucus in order to reach the surface of the epithelium or disseminate through deeper tissue regions.

To investigate the role of an adherent mucus layer on the pathogenesis and virulence of *C. jejuni*, infection experiments were conducted with either the rod-shaped wild-type strain NCTC11168 (Figure 4.5) or the spiral-shaped 81-176 (Figure 4.6). In order to most directly compare the influence of a thicker mucus layer, bacterial transmigration, colonization, and epithelial barrier integrity were determined on both the MTX-based tissue model with only a very thin layer of MUC1, and on the E12-based tissue model harboring a thick mucus layer consisting of both MUC1 and the intestinal MUC2 (Figures 4.5 A and 4.6 A). Whether the substantial mucus produced by E12 cells poses a barrier for the transmigration of *C. jejuni* strain NCTC11168 was determined by the number of CFUs in the basolateral compartment of tissue models seeded with MTX or E12 cells during the early time points post infection (1 – 6 hrs p. i.) (Figure 4.5 B). Transmigration of the rod-shaped isolate took up to three hours and reached only low percentages of the input CFUs with respect to the MTX-based model. Transmigration trough the E12-based tissue model was not only strongly delayed but was almost indistinguishable for this particular wild-type strain from a non-motile Δ*flaA* mutant (Figure 4.5 B). This suggests that while NCTC11168 is able to cross the epithelial barrier composed of MTX cells, which display a similar permeability as E12 cells (Figure 4.1 B), the presence of a thick mucus layer almost abolishes the transmigration potential of this same strain. In addition, observations stemming from the isolation of colonizing bacteria support the protective effect of the mucus layer. CFUs isolated for this rod-shaped strain were significantly lower at all time points p. i. in the E12-based tissue model compared to the MTX-based tissue model (Figure 4.5 C). While in the latter, the number of colonizing bacteria recovered to above input percentages at later time points (72 – 120 hrs p. i.), bacterial numbers in the E12-based model did not significantly increase over time. And while bacterial CFUs did not drop to

zero, they remained an almost constant 8.0 % of the initial input. This indicates that the mucus layer prevents the rod-shaped NCTC11168 from firmly taking hold of the epithelial niche and/or from sufficiently replicating to establish colonies on the surface. This might either be due to the fact that they cannot penetrate this viscoelastic barrier to begin with, or that they are stuck in this mucin-spun web and are consequently shed off with continuous mucus production before they can safely establish residence on the epithelial cell surface.

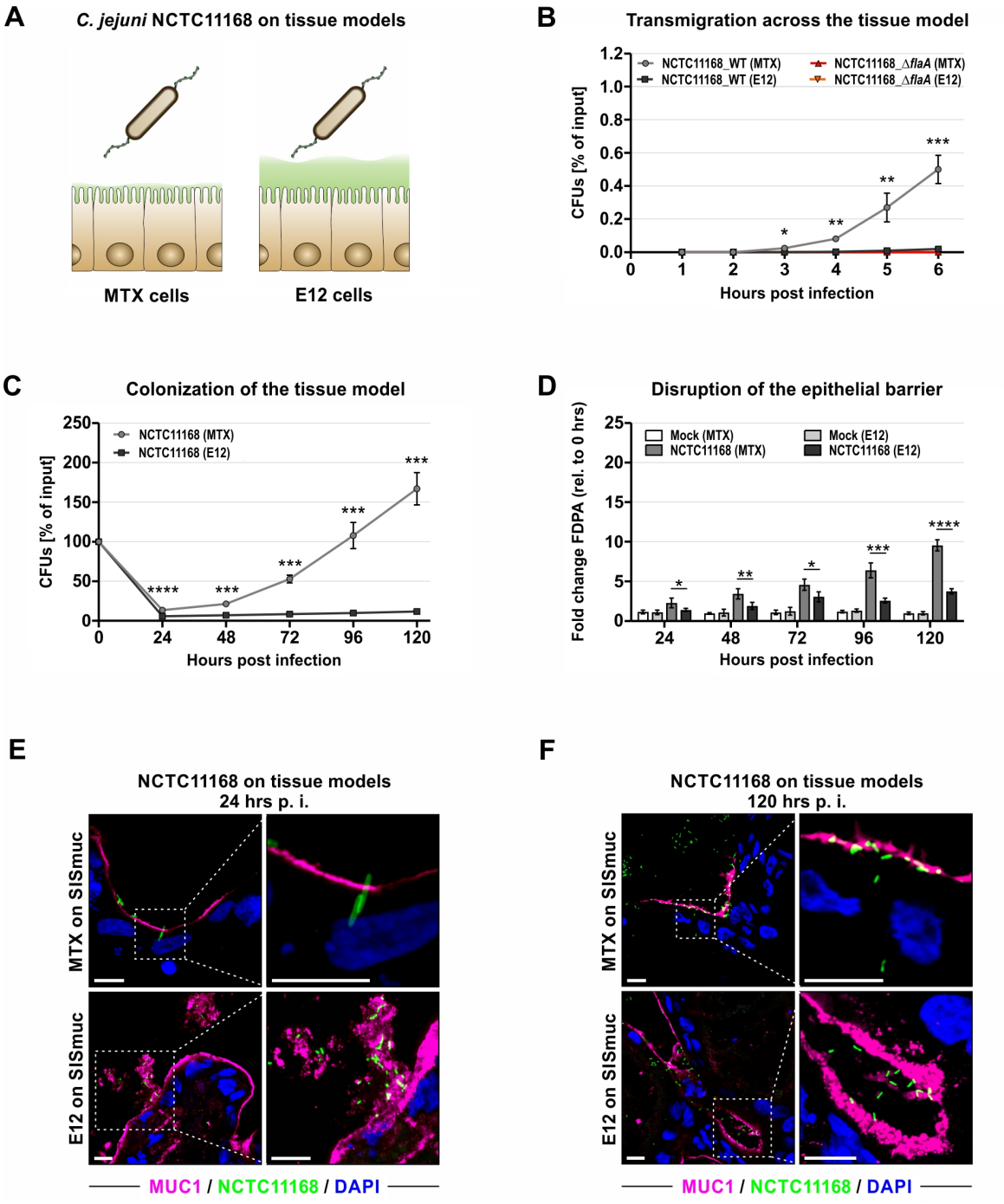

Figure legend on next page

Figure 4.5: The rod-shaped *C. jejuni* NCTC11168 is greatly hindered in transmigrating, colonizing, and disrupting a mucus-protected epithelial barrier. (A) 3D tissue models based on MTX (little mucus) and E12 cells (strong mucus production) were infected with the rod-shaped *C. jejuni* wild-type strain NCTC11168. **(B)** Transmigration across tissue models reseeded with MTX or E12 cells was determined by isolation of CFUs from the basolateral compartment from 0 – 6 hrs p. i. for strain NCTC11168 and its isogenic Δ*flaA* mutant. CFUs are depicted as a percentage of input and as the mean of four replicates with corresponding SDs. **(C)** Colonization of the MTX-/E12-based tissue model by strain NCTC11168 from 24 – 120 hrs post infection. CFUs are represented as the mean value of four independent experiments with corresponding SDs and are depicted as the percentage of input CFUs. **(D)** FDPA measurements were conducted to determine disruption of epithelial barrier function of the MTX- and the E12-based tissue models. Cell culture models were either left untreated (mock MTX/E12) or infected for up to 120 hrs with strain NCTC11168. FDPA values are depicted as fold changes relative to time point zero. ****: $p < 0.0001$, ***: $p < 0.001$, **: $p < 0.01$, *: $p < 0.05$, ns: not significant. Statistical analysis was conducted using the Student's *t*-test. **(E, F)** Paraffinated cross sections (5 µm thickness) of tissue models based on MTX/E12 cells infected with the rod-shaped NCTC11168 were stained with DAPI (nuclei, blue) and antibodies for mucin 1 (MUC1, magenta) as well as *Campylobacter* (NCTC11168, green). Images for tissue models infected for 24 hrs **(E)** or 120 hrs **(F)** were obtained with a confocal Leica SP5 microscope using z-stack scanning mode. Right panels are magnifications of the areas indicated by dashed frames in the left panel images. Scale bar 10 µm.

Regarding disruption of the epithelial barrier, in the MTX-based tissue model, *C. jejuni* strain NCTC11168 induced a significant increase in permeability over time compared to non-infected controls (Figure 4.5 D). FDPA measurements at all time points tested revealed a significantly lower disruption of the epithelial barrier when the mucus layer was more pronounced as is the case in E12 tissue models. The permeability of infected E12 tissue models was significantly higher at all time points p. i. compared to non-infected control models. At 72 hrs p. i., permeability in the tissue model with E12 cells reached a plateau of two- to three-fold increase, which did not significantly increase further over the remaining time course of infection (up to 120 hrs) (Figure 4.5 D). The observations made by determining the bacterial load (Figure 4.5 C) are supported by confocal microscopy images of infected tissue models at the earliest (Figure 4.5 E) and latest time point (Figure 4.5 F). As observed previously, only a thin layer of MUC1 is visible on MTX cells and thus, some bacterial cells can be detected close to the cell surface or even reaching through the thin mucus layer 24 hrs p. i. (Figure 4.5 E, *upper panel*). At the same time point, almost all bacteria in the tissue model with E12 cells are seemingly trapped in mucous clouds (Figure 4.5 E, *lower panel*). This might suggest that they could not reach the cell surface in order to firmly attach themselves to avoid being trapped and shed off during mucus production. At later time points, more and more bacteria can be seen attached to or traversing the MTX cell layer (Figure 4.5 F, *upper panel*). In addition, the MUC1 layer appears fuzzy in places of contact with *C. jejuni* or is absent entirely, potentially indicating an ongoing degradation

process. The presence of bacteria in the highly mucus-producing E12 model is also at this late time point scarce at best. Nevertheless, some bacterial cells can be observed deep inside intestinal crypts indicating the potential of the NCTC11168 wild-type strain to theoretically establish residence albeit the presence of the protective mucus layer (Figure 4.5 F, *lower panel*).

In addition to the rod-shaped *C. jejuni* strain described above, the spiral-shaped wildtype 81-176 was also tested in the mucus-producing tissue models for its ability to traverse, colonize, and disrupt the reconstructed epithelia based on MTX and E12 cells (Figure 4.6 A). This strain could transmigrate through the highly mucus-producing tissue model composed of E12 cells at equal speed compared to MTX-based tissue (Figure 4.6 B). Accordingly, CFUs in the basolateral compartment could be isolated as early as three hours p. i. for both infection models (MTX/E12) albeit to a much lower extent when a thick mucus layer was present. This trend continued also at later time points (up to 6 hrs p. i.), whereas no CFUs could be isolated for the isogenic *flaA* deletion strain at all time points tested. This indicates that *C. jejuni* strain 81-176 is generally able to transmigrate through the mucus layer in a more effective way than the rod-shaped NCTC11168 wildtype (Figure 4.5 B). Nevertheless, the viscoelastic barrier poses similarly a greater obstacle for the bacterium to overcome. Analogously, *C. jejuni* strain 81-176 also colonized the mucus-containing tissue model at all time points p. i. to a significantly lower degree compared to the MTX-based model (Figure 4.6 C). However, contrary to NCTC11168 (Figure 4.5 C), CFUs isolated for 81-176 steadily increased in the E12-based model, indicating the potential ability to more firmly establish a replicative niche to increase the bacterial load. A similar trend could also be observed for the disruption of epithelial barrier function during infection with the spiral-shaped wildtype (Figure 4.6 D). While in both tissue models, epithelial permeability increased continuously over time and was always significantly higher compared to non-infected tissue, colonization of the E12-based tissue model seemed to elicit a significantly lower disruption of epithelial permeability at all time points tested (up to 120 hrs p. i.). This suggests that also in the case of the spiral-shaped 81-176, the presence of a thick mucus layer conveys a certain degree of protection for the underlying epithelium. Similar observations can be made from confocal microscopy images stained for MUC1 and 81-176 at early (Figure 4.6 E) and late (Figure 4.6 F) time points during the infection process. The thin mucus layer above MTX cells is not sufficient to keep *C. jejuni* strain 81-176 from reaching epithelial cells and thus, many bacterial cells can be seen in contact with host cells or in the process of crossing the viscoelastic barrier provided by MUC1 after 24 hrs of infection (Figure 4.6 E, *upper panel*). In contrast, similar to what has been observed for

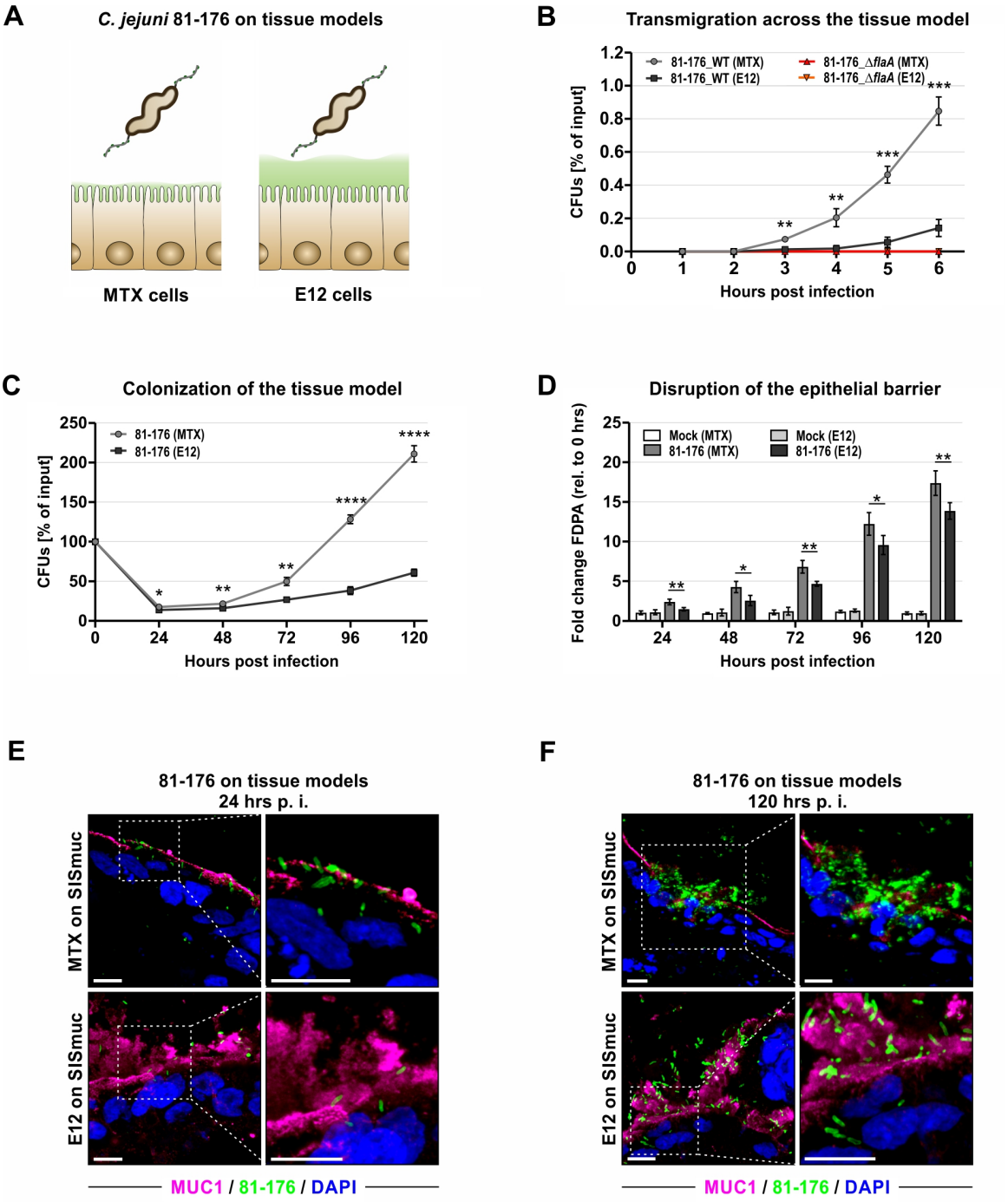

Figure 4.6: A thicker mucus layer exerts a protective effect against the transmigration, colonization, and barrier disruption of the spiral-shaped 81-176 *C. jejuni* strain. (A) The spiral wild-type strain 81-176 was used for infection experiments of MTX-/E12-based tissue models with a thin/thick mucus layer, respectively. **(B)** Traversing bacterial cells of *C. jejuni* strain 81-176 and its isogenic *flaA* deletion mutant were isolated by sampling from the basolateral compartment of cell crowns reseeded with MTX or E12 cells starting at 1 h up to 6 hrs p. i. in four independent experiments. Mean CFUs are displayed as a percentage of input with corresponding SDs. **(C)** Over a time course of 120 hrs, colonizing CFUs were isolated for strain 81-176 from tissue models reconstructed from MTX or E12 cells. The graph displays the mean CFUs of four biological replicates (incl. SDs) as a percentage of their respective input. **(D)** Changes in permeability of the epithelial barrier during infection experiments were measured using the FITC-dextran permeability assay.

Displayed are bar graphs for uninfected MTX-/E12-based tissue models (mock) and 81-176-infected cell crowns. The mean fold change of FDPA values relative to time point zero was determined in four independent experiments and is shown with according SDs for each respective time point. ****: $p < 0.0001$, ***: $p < 0.001$, **: $p < 0.01$, *: $p < 0.05$. The Student's *t*-test was employed for statistical analysis. **(E, F)** Infected tissue models were processed for paraffin embedding and subsequently sectioned to 5 µm slices. Afterwards, tissue sections were stained for the presence of nuclei (DAPI, blue), mucin 1 (MUC1, magenta), and *C. jejuni* strain 81-176 (81-176, green). Confocal microscopy was used for imaging tissue models reconstructed from MTX and E12 cells infected for either 24 hrs **(E)** or 120 hrs **(F)** with strain 81-176. Magnifications of areas in the left panel are depicted in their respective right panels. Scale bar 10 µm.

strain NCTC11168, most of the bacterial cells of strain 81-176 are equally trapped in great mucous clouds rising from the cell surface at the same time point (Figure 4.6 E, *lower panel*). The images however differ at later stages of the infection. The MTX-based tissue model is seemingly overrun with bacteria and *C. jejuni* can be found above, on top of, as well as inside the underlying epithelial cells (Figure 4.6 F, *upper panel*). Moreover, many bacteria can also be seen in deeper tissue regions having traversed the barrier but sticking to the extracellular matrix scaffold. In addition, the mucus layer seems to be greatly diminished in areas of elevated bacterial concentration. In the case of the highly mucus-producing E12 cells, *C. jejuni* strain 81-176 is less able to invade the reconstructed epithelium and can be seen trapped in the overlying mucus (Figure 4.6 F, *lower panel*). But contrary to the rod-shaped NCTC11168, this strain seems potentially better at crossing the mucus barrier and thus more efficient in establishing residence in/on its host cells.

In conclusion, the above-described results suggest an isolate-dependent protective effect of the mucus layer against transmigration, bacterial colonization, and disruption of epithelial permeability. However, the mucus layer on the epithelial surface does not seem to protect the cells from initial colonization by *C. jejuni* but rather prevents extensive replication and thus, a higher bacterial burden during later time points of infection. This protective effect seemed to be much stronger against the rod-shaped NCTC11168 wild-type strain.

4.4. Spiral morphology of *C. jejuni* leads to increased colonization and stronger barrier disruption in the mucus-producing 3D tissue model

The helical shape of *C. jejuni*, as for many other bacteria as well, has long been suggested to be critical for successful host colonization in particular for its ability to burrow through the mucosal layer of gastrointestinal epithelia. As shown in this thesis, the rod-shaped wildtype NCTC11168 is hampered in its capacity to colonize the epithelial surface of the 3D tissue

model whenever a thick mucus layer is protecting it. Contrary to that, the spiral shaped wildtype 81-176 is able to more efficiently colonize the same tissue. This goes in line with a stronger increase in permeability due to infection with strain 81-176 compared to NCTC11168. However, it would be remiss to allocate these different pathogenic attributes solely to their variance in shape. While both *C. jejuni* strains were originally isolated from a human source, genome sequences of both strains suggest that approx. 5 % of the NCTC11168 genome is missing in 81-176 (Parkhill *et al.*, 2000; Dorrell *et al.*, 2001; Gaynor *et al.*, 2004; Hofreuter *et al.*, 2006). In addition to many other discrepancies in their genomes, only NCTC11168 carries a type II-C CRISPR/Cas system (Dugar *et al.*, 2013, 2018). Nevertheless, it is the spiral-shaped 81-176 that is considered highly pathogenic not least due to the large two plasmids it is carrying (Bacon *et al.*, 2000, 2002; Batchelor *et al.*, 2004).

Deletion of the peptidoglycan-modifying enzyme Pgp1 (Δ*pgp1*) abrogates the characteristic spiral morphology of *C. jejuni* strain 81-176 and renders it rod-shaped (Figure 4.7 A) (Frirdich *et al.*, 2012). Complementation of the deletion mutant by expressing the gene from the unrelated *rdxA* locus effectively returns bacterial morphology to a helical shape (C *pgp1*). A previous study has shown that by deleting this metal-dependent

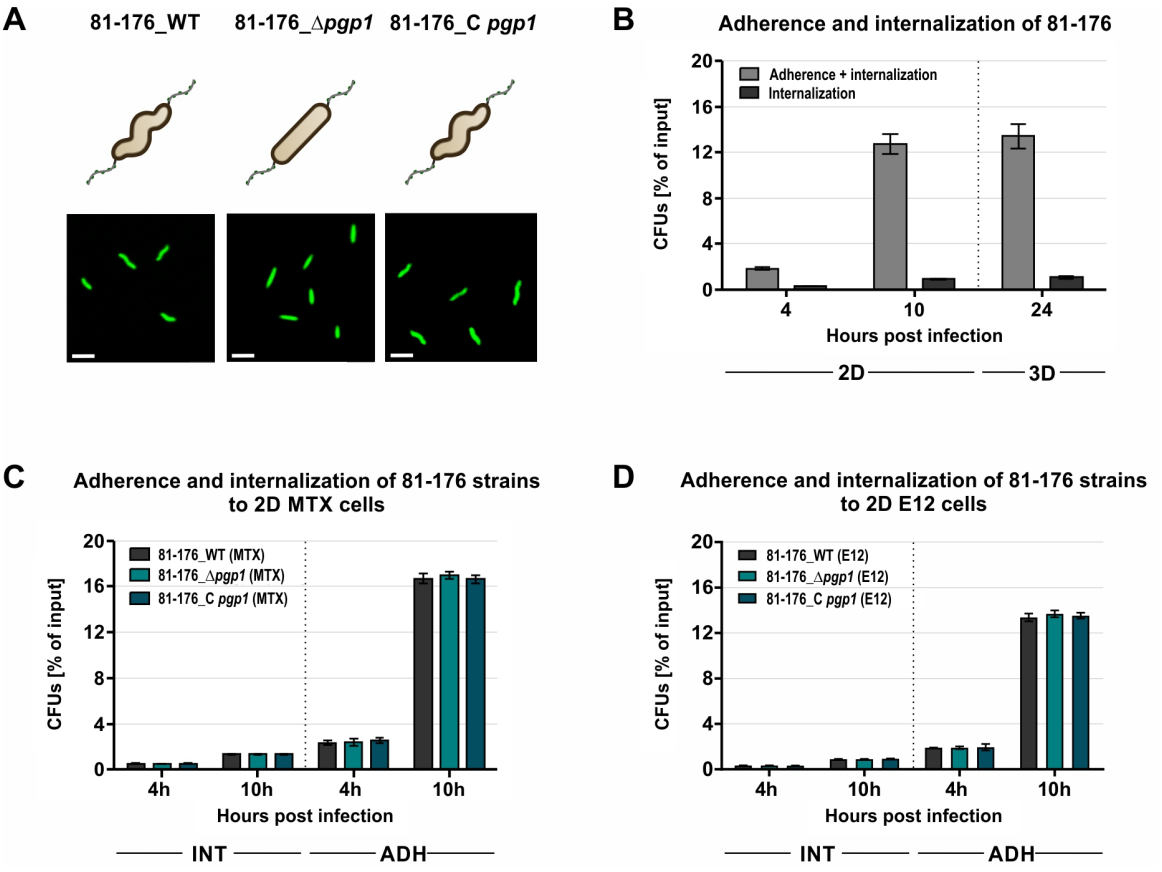

Figure legend on next page

Figure 4.7: Adherence and internalization of the rod-shaped 81-176 mutant does not differ during infection of 2D MTX and E12 cells. (A) Schematic representation and confocal images of FITC-labeled 81-176 wildtype (WT), deletion (Δ*pgp1*), and complementation of *pgp1* (C *pgp1*). Deletion of *pgp1* results in a straight morphology of the spiral-shaped wild-type strain. Complementation of this mutant restores the parental helical shape. Scale bar 2.5 µm. **(B)** Adherence and internalization of *C. jejuni* 81-176 wildtype was examined at 4 and 10 hrs p. i. in 2D E12 monolayers and 24 hrs p. i. in E12-based 3D tissue models. Bars represent the mean of four independent experiments with their respective SDs. **(C, D)** CFUs of adherent and internalized (ADH) bacteria as well as of internalized bacteria only (INT) were isolated for 81-176 WT, Δ*pgp1*, and C *pgp1* in 2D monolayer infections of MTX cells **(C)** and E12 cells **(D)** at 4 and 10 hrs p. i.. CFUs are depicted as a percentage of input and represent the mean of three biological replicates with corresponding SDs.

DL-carboxypeptidase the resulting rod-shaped mutant strain is slightly less motile and exhibits reduced biofilm formation compared to wildtype (Frirdich *et al.*, 2012). In their study, adherence and internalization of the rod-shaped mutant were not affected in conventional 2D monolayer infections (with Caco-2 cells). However, deletion of *pgp1* resulted in a colonization defect in chickens (Frirdich *et al.*, 2012). Thus, the *pgp1* deletion mutant was initially tested for its ability to colonize and transmigrate in the mucus-containing tissue model to pinpoint the influence of morphology on these *C. jejuni* pathogenesis-determining processes.

In order to compare 2D E12 monolayer infections with the E12-based 3D tissue model, first, a time point in 2D had to be determined that more closely resembles the bacterial load in the tissue model at 24 hrs p. i. (similar to Figure 2.7 for Caco-2 cells). Whereas this was already reached at 4 hrs p. i. for 2D Caco-2 cells, it was prolonged to 10 hrs p. i. for the E12 cell line (Figure 4.7 B). At this time point, the number of CFUs was comparable to those isolated after 24 hrs in 3D. To compare colonization efficiency of the helical wildtype and its straight mutant in 2D and 3D infection models, it was first determined whether adherence and internalization was equally independent of morphology for the intestinal MTX (Figure 4.7 C) and E12 (Figure 4.7 D) cells in a conventional 2D monolayer setting, where mucus production is sparse (Horstmann *et al.*, 2017). Indeed, determination of CFUs in these assays revealed for both cell lines similar adherence and internalization rates for Δ*pgp1* compared to wildtype and the complementation strain at four as well as 10 hrs p. i. (Figure 4.7 C and D). This supports the observation that spiral morphology seems to be dispensable for *C. jejuni* to effectively interact with non-polarized and non-mucus producing host cells.

Subsequently, MTX- and E12-based tissue models were infected with 81-176 WT, Δ*pgp1*, and C *pgp1* (Figure 4.8 A). On tissue models containing a thin mucus layer (MTX-based), colonization rates at earlier time points (24 – 72 hrs p. i.) were indistinguishable

between the helical wild-type, the complementation strain, and the straight *pgp1* deletion mutant (Figure 4.8 B). Only at later time points (96 and 120 hrs p. i.), a significant decrease in colonization for Δ*pgp1* became apparent, which could be fully complemented. However, in the E12-based tissue model containing a thick mucus layer, deletion of *pgp1* resulted in a significantly impaired colonization rate during the whole infection process (Figure 4.8 C). As this phenotype could be fully complemented, it suggests that indeed spiral morphology in strain 81-176 confers an advantage in colonizing the mucus-covered epithelial surface.

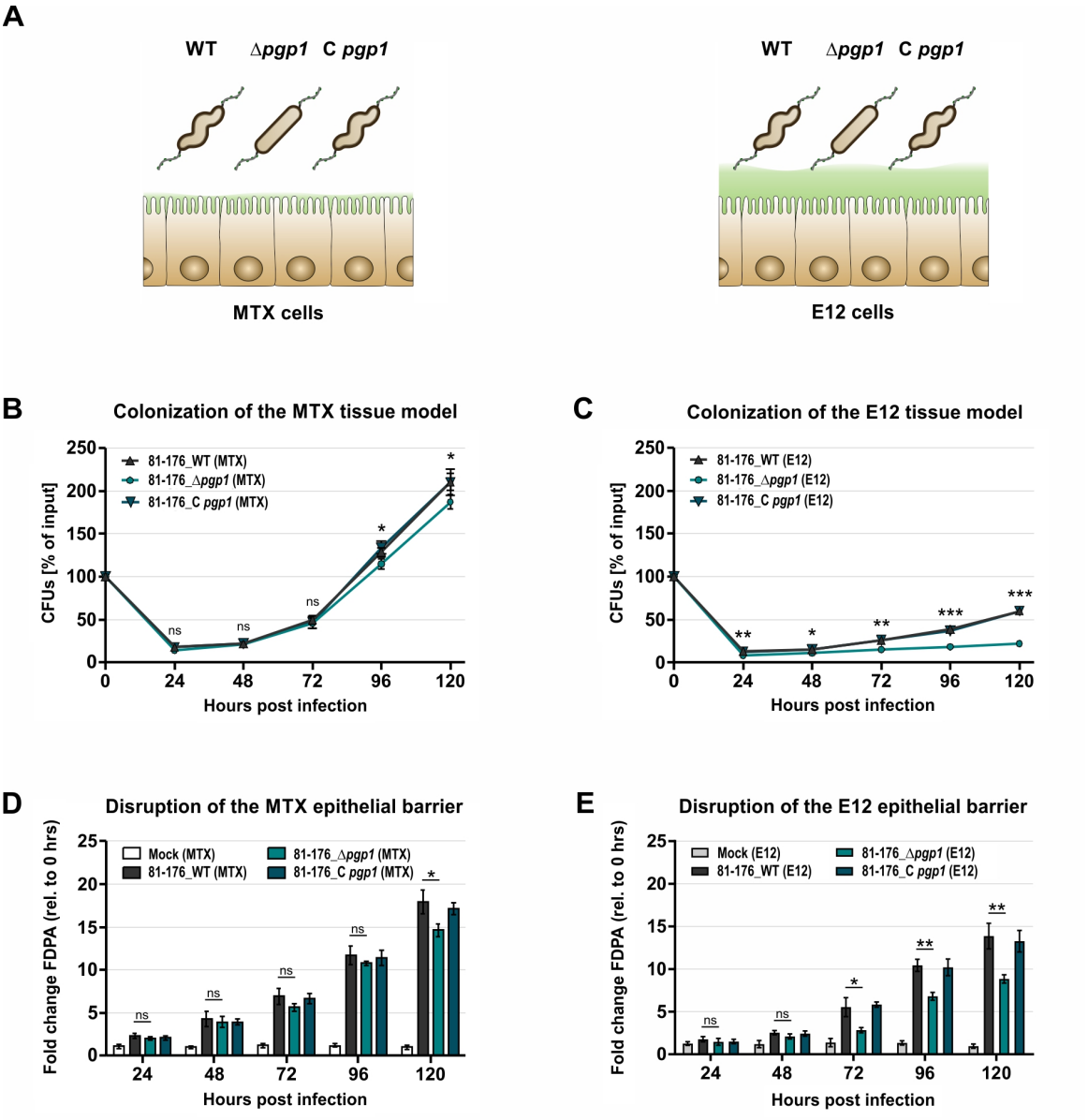

Figure 4.8: The helical shape of *C. jejuni* confers a greater colonization advantage on the mucus-producing tissue model leading to increased destruction of the epithelial barrier. (A) Schematic of the different infection experiments depicting 81-176 wildtype (WT), deletion of *pgp1* (Δ*pgp1*), and complementation of *pgp1* (C *pgp1*) on either the MTX-based tissue model containing very little mucus (*left panel*) or the strong mucus-producing E12 model (*right panel*). **(B, C)** CFUs of

81-176 WT, Δ*pgp1*, and C *pgp1* were isolated from tissue models based on MTX **(B)** and E12 **(C)** cells at the indicated time points and are depicted as mean values (as the percentage of input CFUs) of four independent experiments with corresponding SDs. **(D, E)** FDPA measurements of epithelial barrier function during infection with 81-176 WT, Δ*pgp1*, and C *pgp1* of MTX **(D)** or E12 **(E)** cell culture models. FDPA values are depicted as fold changes relative to 0 hrs. ***: $p < 0.001$, **: $p < 0.01$, *: $p < 0.05$, ns: not significant. Statistical analysis was performed with the Student's *t*-test.

Similar to the rod-shaped NCTC11168, the straight mutant of strain 81-176 might be less able to penetrate the mucus layer. Analogous observations could be made from barrier measurements during infection with these three strains. In tissue models reseeded with MTX cells, induction of permeability was similar between WT, C *pgp1*, and Δ*pgp1* and, except for the late 120 hrs time point, exhibited no significant difference in FDPA measurements (Figure 4.8 D). In contrast, deletion of *pgp1* elicited an overall decreased disruption of the epithelial barrier in the E12-based model for all time points (Figure 4.8 E). While WT and C *pgp1* induced permeability in an equal manner, epithelial barrier function was less disrupted when the tissue model was colonized by Δ*pgp1*. In line with these results, transmigration of the rod-shaped *pgp1* mutant was analogously affected. This mutant exhibited a decreased capability in reaching the basolateral compartment in both tissue models with an even lower percentage of bacteria transmigrating through the E12-based model (Figure 4.9 A and B).

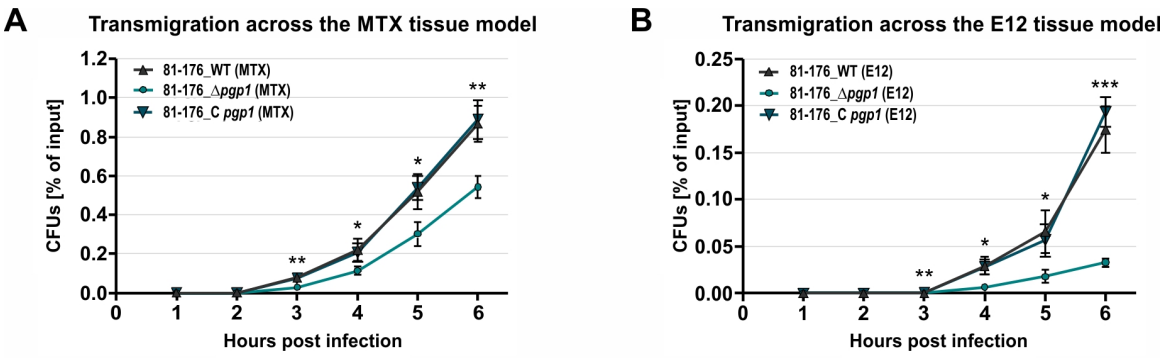

Figure 4.9: The rod-shaped 81-176 *pgp1* deletion mutant is obstructed in its ability to cross the mucus layer and epithelial barrier. (A, B) Transmigration of *C. jejuni* 81-176 WT, Δ*pgp1*, and C *pgp1* was determined by isolating CFUs up to 6 hrs p. i. from the basolateral compartment of MTX-based **(A)** and E12-based **(B)** tissue models. Experiments were conducted three times and graphs represent the mean value with SDs. ***: $p < 0.001$, **: $p < 0.01$, *: $p < 0.05$. The Student's *t*-test was used to determine statistical significance.

In summary, the newly developed tissue model based on E12 cells seeded on the extracellular matrix scaffold SISmuc proved to be a valuable reconstruction of human intestinal tissue regarding morphology, epithelial barrier function, and mucus production.

This allowed for the first time *in vitro* to demonstrate the contribution of bacterial morphology to *C. jejuni* interaction with intestinal host cells. Losing its spiral shape renders the bacterium unable to properly colonize or traverse the epithelium reconstructed in the 3D tissue model. This seems to be largely due to an inefficiency to penetrate to overlying mucus layer, which so far could only be shown *in vivo* (Frirdich *et al.*, 2012). Once more, this highlights the strength of the tissue models developed in this thesis in their ability to uncover *in-vivo* like phenotypes generally not observable during conventional cell culture experiments.

5. Conclusion and Outlook

Although infectious diseases have been documented throughout history, in many cases the underlying molecular mechanisms by which different bacterial pathogens cause disease(s) still remain unknown. Thus, it is vital to investigate the molecular interactions of pathogens with their respective hosts in order to prevent infections and design vaccines or treatment strategies. Studies of bacterial pathogenesis often employ (small) animal models or simplified 2D cell culture systems to monitor disease development or virulence phenotypes of certain mutant strains. While both infection models (animal and 2D) have greatly contributed, and continue to contribute, to our understanding of host-pathogen interactions, especially for human pathogens they can be limited in their ability to reflect their natural host environment (Masopust *et al.*, 2017). This drives the need to establish new model systems to study microbial virulence strategies.

In this thesis, tissue-engineered intestinal 3D models were employed for infectious disease studies and further advanced to combine the characteristic villi and crypt microarchitecture of the small intestine with a mucus-producing epithelial barrier fortified by cell-cell and cell-ECM interactions. These 3D tissue models allowed for the assessment of epithelial barrier function during infection with two *C. jejuni* wild-type strains as well as for the quantification of bacterial adherence, internalization, and transmigration. Moreover, investigation of *C. jejuni* mutant strains revealed *in-vivo* relevant infection outcomes that could so far not be observed in conventional *in-vitro* 2D cell culture settings. In addition, the Tn-seq screen performed in this thesis with a *C. jejuni* Tn5 mutant library in both 2D cell culture and 3D tissue model represents a comprehensive analysis of fitness genes essential or dispensable for host-pathogen interactions in these two environments. Overall, the results of this thesis support the utility of these novel intestinal tissue models for exploring host interactions with *C. jejuni* and other gastrointestinal pathogens.

5.1. The 3D intestinal tissue model combines crucial properties of native tissue relevant for infection research of gastrointestinal pathogens

In general, 2D *in-vitro* infection models offer a feasible approach to study host-pathogen interactions in high throughput. However, they are a very simplistic representation of *in-vivo* tissue architecture and complexity. Thus, the aim of this thesis was to develop and advance 3D *in-vitro* infection models that mimic key features of native human intestine in order to identify potential novel factors specifically required for host-pathogen interactions in this 3D environment. In terms of the small intestine, these architectural characteristics

entail the villi and crypt microarchitecture, a single-layered epithelium supported by ECM, and a protective mucus layer. The apical side of enterocytes faces the lumen of the intestine and is in constant contact with its environment; thus, it expresses receptors and transporters to mediate the exchange of *e.g.* nutrients from the lumen into deeper tissue regions (Bryant & Mostov, 2008). The basal side interacts through various receptors such as integrins with the underlying ECM and basement membrane. Growth of epithelial cells in a 3D environment supported by an ECM scaffold might alter the biological function of epithelial cells such cellular differentiation or expression/localization of cellular receptors (Pusch *et al.*, 2011; De Gregorio *et al.*, 2018).

The 3D tissue model presented in this thesis offers a chance to factor components of a native tissue-derived ECM into the interactions of the host mucosa with *C. jejuni* and also other enteric bacteria. The previously developed (Pusch *et al.*, 2011) and in this study advanced Caco-2 cell-based 3D tissue model represents a cell line-based epithelial barrier interconnected with a tissue-derived ECM scaffold expressing functional tight and adherence junctions. Consisting mainly of collagen-, laminin-, and elastin-fibers, this ECM scaffold provides tissue-distinctive stiffness and components such as fibronectin necessary for specific cell-matrix interactions (Simon-Assmann *et al.*, 2010) and altered expression/localization of cellular transporters and receptors (Pusch *et al.*, 2011). However, *in-vitro* ECM scaffolds can differ greatly in their composition depending on their origin and thus, impact cellular processes such as adhesion, interaction, or differentiation. In particular, while 3D collagen scaffolds did not mimic cellular properties observed *in vivo*, tissue-derived 3D matrices were highly effective in enhancing cellular function and adhesion (Cukierman *et al.*, 2001). However, using decellularized tissues or organs as natural scaffolds can lead to alterations in the downstream development of *in-vitro* human tissue depending on the source of the scaffolds. An alternative could be presented by a standardized artificial matrix merging human extracellular matrix proteins into a scaffold with *in-vivo* like properties such as texture and 3D architecture while providing biomechanical cues for the differentiation of the reseeded cells. Bioprinting tools might offer the required flexibility to generate a scaffold fitting these criteria. In fact, ECM-based or decellularized bioinks already demonstrate progress towards the development of functional tissues (Gopinathan & Noh, 2018).

In establishing an *in-vitro* 3D infection model, not only intestinal cell differentiation itself is influenced by the presence of such a tissue-derived ECM scaffold, but thereby also interactions between microbial pathogens and host cells. Specifically, contact of cells to ECM components leads to decreased expression of β1-integrin (Delcommenne & Streuli, 1995), which has been shown to contribute *e.g.* to the uptake of *C. jejuni* into host cells (Boehm *et*

al., 2011). Furthermore, the binding of bacterial surface adhesins to components of the ECM itself plays a crucial role in colonization of the digestive tract by several other gastrointestinal pathogens such as *Salmonella*, *H. pylori*, *Shigella* spp., and *Clostridium difficile* (*C. difficile*) (Singh *et al.*, 2012).

The advanced intestinal tissue model developed in this thesis unites previously reported crucial features of native tissue into an *in-vitro* cell culture model applicable for infection research. It has been demonstrated that cellular function and behavior can be substantially impacted by the simulation of physiological conditions *in vitro* such as the application of defined mechanical stimuli achieved by a bioreactor system (Chen & Hu, 2006; Minuth *et al.*, 2010; Pusch *et al.*, 2011; Zhou *et al.*, 2018). The RWV bioreactor is a masterful example to develop organotypic 3D cell culture models in relatively high throughput (Barrila *et al.*, 2010). It has been extensively used to study host-pathogen interactions for numerous different tissues including the lung (Carterson *et al.*, 2005), vaginal epithelium (Hjelm *et al.*, 2010), and the human GIT (Nickerson *et al.*, 2001; Carvalho *et al.*, 2005; Höner zu Bentrup *et al.*, 2006). The RWV utilizes fluid shear as a biomechanical force during growth of the tissue-like models, which has been shown multiple times to influence the differentiation potential of eukaryotic cells (Guo *et al.*, 2000; Ingber, 2006). Moreover, this particular approach of cultivation led to a differentiation status of host cells that was able to detect the SPI-1-independent invasion of a *Salmonella* strain previously only observed *in vivo* (Höner zu Bentrup *et al.*, 2006). While this technology allows the use of primary cells as well as immortalized cell lines and grants immense experimental and technological flexibility, it still cannot recapitulate architectural tissue features such as intestinal villi and crypts.

Incorporation of a tissue-derived ECM scaffold into a fluid shear bioreactor can overcome this restriction. In 2011, Push and colleagues impressively demonstrated that Caco-2 cells exposed to defined biophysical stimuli within a dynamic bioreactor system module exhibited more *in-vivo* like cellular characteristics compared to statically grown cell culture models (Pusch *et al.*, 2011). However, the cultivation in the current perfusion bioreactor system comes at the high cost of throughput. Only 3 – 4 tissue models can be grown in parallel, severely limiting infection studies in terms of experimental parameters and outputs. To incorporate tissue models developed during fluid shear with at least medium throughput, this thesis utilized cultivation of cell culture models on an orbital shaker. Through these easily achievable dynamic cultivation conditions, the polarization status of the differentiating cells in the tissue model could be significantly improved when compared to static cultivation or the same cells grown on Transwell inserts. This was demonstrated by an increasingly distinct localization of cell-cell junctions and a gain in cell

height comparable to native human enterocytes. Similar observations have been made for Caco-2 (Tan *et al.*, 2018) or tubule epithelial cells (Duan *et al.*, 2008). When grown in channel fluidic systems, these cells showed altered organization of their cell-cell junctional complexes demonstrated by increased apical localization of tight junction proteins. The orbital shaker culture does not necessarily provide the uniform shear stress of a laminar flow system (Thomas *et al.*, 2011). Nevertheless, this approach has been frequently used to apply shear stress to a variety of cell types and is easily scalable to a larger throughput of tissue models (Basson, 2003; Gayer & Basson, 2009; Navabi *et al.*, 2013). For example, shaker cultivation of renal tubular epithelial cells altered their differentiation phenotype towards improved functional cellular capacity (Jang *et al.*, 2011) as well as an increased expression of an apical brush border enzyme (Ferrell *et al.*, 2018). Morphological comparison to the same cells cultivated statically on porous Transwell inserts or in multi-well plates revealed a decrease in cellular complexity reflected for instance in a reduction of cell height. This is in agreement with results obtained in this thesis, where Caco-2 cells approached *in-vivo* enterocyte morphology with increasingly complex cultivation (static Transwell to static tissue model to dynamic tissue model).

The mechanisms by which cells sense and respond to physical forces have not been fully elucidated although it was suggested that the cytoskeleton likely plays an important role. Triggered by fluid-induced cellular distortion, cytoskeletal elements might activate intracellular signaling cascades ultimately altering the biological properties of the cell. In addition, as mucosal epithelial cells are dependent on the vascular circulation for sufficient oxygen supply (Sinaasappel *et al.*, 1999), increased oxygenation through shaker cultivation might contribute to epithelial cell development induced by shear stress (Sahai *et al.*, 1989). To comply with the cellular need for ample oxygen availability, air-liquid interface cultivation has been utilized to promote polarization and differentiation of cells (Nossol *et al.*, 2011; Navabi *et al.*, 2013; Boccellato *et al.*, 2018). Here, only a thin layer of medium covers the apical cell surface to facilitate easier oxygen diffusion leading for example to an elongated cell morphology reminiscent of native enterocytes in addition to apical localization of brush border markers (Nossol *et al.*, 2011).

Consequently, in order to preserve *in-vivo* like physiology in *in-vitro* cell culture systems, it is crucial to expose the cells to biophysical forces generally experienced in their native environment. In this thesis, implementing these vital developmental cues advanced the previously developed Caco-2 cell-based tissue model to include *in-vivo* like characteristics of native intestinal tissue.

5.2. The tissue-engineered 3D environment influences pathogenicity-determining processes of *C. jejuni*

Many cell line-based *in-vitro* infection models lack the unique villi and crypt structure of the small intestine. Thus, bacterial localization within the mucosal microarchitecture was so far restricted to animal models. Both in chicken (Beery *et al.*, 1988) and in mice (Lee *et al.*, 1986; Stahl *et al.*, 2014, 2016), *C. jejuni* was found in relatively high numbers deep inside intestinal crypts. For the first time *in vitro*, this localization phenotype could be observed in the human cell line-based tissue model presented in this thesis. The resulting complex morphology supported the formation of highly organized TJ and AJ complexes important for upholding the tight mucosal barrier characteristic for highly polarized tissues. This is seemingly reflected in the infection behavior of *C. jejuni*, whose initial adherence to, internalization into, and translocation across host cells within the tissue model is decreased/delayed compared to cells grown in conventional multi-wells or on Transwell inserts. It has previously been observed that one of the most effective invasion pathways for *C. jejuni* involves the subvasion entry pathway, *i.e.* bacterial migration underneath the host cell and entry from the basal cell side (van Alphen *et al.*, 2008; Pryjma *et al.*, 2012; Bouwman *et al.*, 2013). When compared to cells grown as conventional 2D monolayers in multi-well plates, *C. jejuni* requires almost six times as long in the tissue model to reach a similar intracellular bacterial load. In addition, traversing an intact epithelial barrier supported by an ECM scaffold takes eight times longer compared to polarized cells grown on the Transwell. If the basolateral site is indeed the preferential spot of entry for *C. jejuni*, paracellular transmigration of the intact mucosal barrier is a prerequisite to invade host cells. This is in line with previous work showing bacterial invasion of polarized cells only after EDTA- (ethylenediaminetetraacetic acid) induced disruption of cellular junction complexes thus providing access to the subcellular space (Monteville & Konkel, 2002; van Alphen *et al.*, 2008). This does not necessarily exclude entry from the apical side of host cells, which might play a subsidiary role in the case of *C. jejuni*. Data presented in this thesis supports this observation by denoting a 25-fold lower invasion rate of strain 81-176 into the highly polarized Caco-2 cell-based epithelial mucosa of the tissue model compared to undifferentiated Caco-2 cells given the same amount of time. For the less virulent NCTC11168 isolate, a striking 300-fold drop in intracellular bacterial load could be observed, which might even correlate with the reduced translocation potential of this strain compared to 81-176. A similar, yet by far less prominent trend was previously observed in comparative infection of Caco-2 cells grown in multi-well plates for 1 day, or up to 15 days on Transwell inserts (Hu *et al.*, 2008). However, depending on the applied MOI, invasion of

C. jejuni strain 81-176 into non-polarized Caco-2 cells decreased less than 2-fold. This suggests that the higher degree of differentiation observed in the tissue model potentially in addition to/as a result of the ECM scaffold has an additional impact on *C. jejuni* pathogenicity-determining factors such as transmigration or invasion that might be more reflective of the disease progression *in vivo*. Moreover, crossing the mucosal surface of the intestinal tract is a strategy evolved not just by *C. jejuni*, but by many gastrointestinal pathogens to reach their desired niche or to spread systemically. Thus, investigating transmigration to the submucosal space in the tissue model might reveal additional virulence and/or fitness factors specifically involved in this key pathogenicity-determining process for *C. jejuni* and other pathogenic microorganisms.

In the case of *C. jejuni*, the literature is highly controversial regarding its actual route to the submucosal space. While some studies have reported translocation exclusively via the paracellular space (Everest *et al.*, 1992; Monteville & Konkel, 2002; Beltinger *et al.*, 2008; Boehm *et al.*, 2012; Hoy *et al.*, 2012), others strongly advocate transcellular passage through host cells (Van Deun *et al.*, 2008b; Wine *et al.*, 2008; Kalischuk *et al.*, 2009; Louwen *et al.*, 2012), or a mixture of both (Konkel *et al.*, 1992; Brás & Ketley, 1999; Harvey *et al.*, 1999; Hu *et al.*, 2008). It is most commonly conceived that paracellular bacterial transmigration is accompanied by a disruption of cellular junction complexes resulting in increased epithelial permeability and/or a loss in TER. Many gastrointestinal pathogens such as *Salmonella*, *S. flexneri*, *Neisseria gonorrhoeae* (*N. gonorrhoeae*), and *Listeria monocytogenes (L. monocytogenes*) indeed induce a very rapid and severe loss of barrier integrity within the first few hours of infection (Boehm *et al.*, 2012). Intriguingly, most *C. jejuni* studies utilizing the Transwell system agree on the fact that while the bacterium reaches the basolateral host cell site extremely rapidly (within 10 – 30 min), the integrity of the epithelial barrier is maintained within the first 24 hrs of infection. Similar results have been obtained in this thesis. While both NCTC11168 and 81-176 were able to cross the highly differentiated mucosal epithelium in the dynamically cultivated tissue model within four hours, the first indication of barrier disruption was detected after 48 hrs. Together with the evidence presented by others (Grant *et al.*, 1993; Harvey *et al.*, 1999; Beltinger *et al.*, 2008; Boehm *et al.*, 2012), this indicates that *C. jejuni* does not induce a permanent opening of AJs and TJs in order to translocate to the submucosal space. Furthermore, this is supported by evidence that cellular TJs can temporarily allow passage of solutes and neutrophils or even reseal following bacteria passing through the paracellular space (Takeuchi, 1967; Madara, 1998). Both ways of cellular passage are thus conceivable for *C. jejuni* and future research will be required to uncover the causal chain of events allowing the bacterium to invade and travel across polarized intestinal epithelia. Other than the up to now utilized Transwell system, the

tissue models described in this thesis might be valuable tools to shed light onto the processes participating in the infection process of enteric pathogens such as *C. jejuni*.

In fact, the results presented here indicate that the Caco-2 cell-based tissue model cannot just perform equally to existing infection models, but is able to display characteristics of a *C. jejuni* infection so far only observable *in vivo*. This was very prominent when the infection outcome of bacterial mutant strains was compared in the tissue model and conventional 2D cell monolayers. The tested mutants affect various aspects of *C. jejuni* biology such as motility, surface structures (CPS), protein glycosylation, and different layers of gene regulation previously implicated to play a role during colonization and/or virulence. For example, a *C. jejuni* strain lacking its extracellular polysaccharide capsule (Δ*kpsMT*) exhibited increased adherence to and internalization into Caco-2 cells grown as a flat monolayer. Astonishingly, for the same deletion mutant, decreased CFUs were recovered for bacteria adhered to or inside the mucosal epithelium of the 3D tissue model. Regarding previous research with *C. jejuni* strains lacking CPS structures, contradicting observations have been made in 2D cell culture models. Inactivation of the capsule producing machinery in strain 81-176 resulted in decreased adherence to and invasion into INT-407 cells (Bacon *et al.*, 2001; Bachtiar *et al.*, 2007), but an increased number of bacterial CFUs when faced with Caco-2 cells (Wong *et al.*, 2015). Moreover, the absence of the capsule in strain 11168H also led to enhanced adhesion to Caco-2 cells (Karlyshev *et al.*, n.d.) and greater binding to immobilized analogues of host cell receptors (Rubinchik *et al.*, 2014). Thus, both the choice of strains and cell line greatly impact the involvement of the capsule in *C. jejuni* pathogenicity-determining processes. This could partially be influenced by the higher mass and abundance of capsular polysaccharides on strain 81-176 compared to NCTC11168 (Karlyshev *et al.*, 2000), possibly contributing to the in general higher internalization rates into intestinal epithelial cells of 81-176. Even though the cell lines utilized in these studies were all of human intestinal origin, it has already been demonstrated that INT-407 cells are less efficiently colonized by various *C. jejuni* strains compared to *e.g.* Caco-2 or T84 cells (Poly & Guerry, 2008; Wine *et al.*, 2008), which could theoretically result in altered interactions between host cell surface and bacterial CPS structures. However, all observations made *in vivo* agree on a vital role for the capsular polysaccharides in *C. jejuni* colonization (Bacon *et al.*, 2001; Jones *et al.*, 2004; Stahl *et al.*, 2014; Wong *et al.*, 2015) and other virulence-determining factors such as *e.g.* sensitivity to osmotic stress (Cameron *et al.*, 2012) or antimicrobial peptides (Keo *et al.*, 2011). Thus, in the absence of the capsular polysaccharides, the observed 2-fold reduction of adherence to and internalization into the 3D tissue model is in complete agreement with the colonization defects observed *in vivo*.

Astoundingly, similar observations could be made for another deletion mutant affecting *C. jejuni* flagellin glycosylation (Δ*ptmG*). In general, glycosylation of flagella in a number of gram-negative bacteria has been reported to play a role in the interaction with eukaryotic cells as well as host cell specificity (Arora *et al.*, 2005). Examination of a *C. jejuni* strain lacking the *ptmG* gene revealed a significant defect in the colonization of chicken but a dispensability for these *O*-linked flagellin glycosylations during host cell interactions *in vitro* (Howard *et al.*, 2009). While the results of this thesis confirmed that lack of *ptmG* had no influence on adhesion or invasion of 2D Caco-2 monolayers, remarkably in the 3D environment of the tissue model, the *ptmG*-deficient mutant displayed a significant decrease in adherence and internalization when compared to its parental strain. Moreover, regulatory effects on *ptmG* by the *C. jejuni* sRNA pair CJnc180/190 were correspondingly transferable to a visible increase in colonization by a mutant strain lacking these sRNAs. While the phenotypes observed for other tested deletion mutants (Δ*flaA*, Δ*kpsMT*, Δ*cas9*, Δ*csrA*) await confirmation by complementation, a similar bacterial load compared to the wild-type strain could be achieved by expression of *ptmG* and CJnc180/190 in *trans*. Consequently, all of the results presented in this thesis, highlight the tissue model as a promising tool to accurately mimic the *C. jejuni* infection process observed *in vivo*.

5.3. A genome-wide screen in the 3D tissue model uncovers *C. jejuni* fitness factors relevant for interaction with polarized epithelial cells

Colonization of the intestinal mucosa by *C. jejuni* or any other gastrointestinal pathogen is inarguably a multi-factorial process. The reconstructed epithelium of the intestinal tissue model was able to mimic *in-vivo* infection outcomes of *C. jejuni* strains lacking previously recognized virulence-determining factors. These observations opened up the possibility that a genome-wide screen of a *C. jejuni* mutant library in the 3D tissue model would expose bacterial factors specifically required for efficient adherence to/internalization into a human *in-vivo* like host environment. A similar screen was performed with non-polarized host cell monolayers in order to distinguish between general colonization-relevant genes and those particularly relevant during host-pathogen interactions in 3D.

Overall, 71 and 76 Tn insertion mutants showed decreased fitness in the screen of a Tn5-based *C. jejuni* mutant library on 2D Caco-2 cells or the Caco-2 cell-based tissue model, respectively. The Tn-seq experiment described here was able to identify many of the previously reported factors important for *C. jejuni* interactions with *in-vivo* animal models and/or *in-vitro* 2D host cells (Hendrixson & DiRita, 2004; Novik *et al.*, 2010; Gao *et al.*, 2014, 2017; Johnson *et al.*, 2014; de Vries *et al.*, 2017a, 2017b). In general, 50 % of all Tn insertion

mutants with decreased fitness identified here were also found in at least one of these other genome-wide screens. Compared to the datasets of other *in-vitro* 2D Tn-seq experiments, which identified 36 – 57 potential *C. jejuni* fitness factors with a number of different cell lines (Novik *et al.*, 2010; Gao *et al.*, 2014; de Vries *et al.*, 2017a), there was only a modest overlap to the list of genes determined in this thesis. The most recent *in-vivo* Tn-seq experiments of *C. jejuni* mutant libraries revealed that disruption of 140, 168, and 122 genes led to decreased colonization in mouse (Gao *et al.*, 2017), chicken (de Vries *et al.*, 2017a), and pig (de Vries *et al.*, 2017b), respectively. Approx. 40 % of those (30 genes) were equally required for ADH and/or INT of the 3D tissue model, whereas only 15 % of Tn insertion mutants (11 genes) overlapped with the dataset acquired during infection of a 2D Caco-2 monolayer. This suggests that bacterial factors accounting for efficient colonization of the 3D tissue model not only markedly differ from those involved during *in-vitro* 2D infection, but also that they are likewise necessary contributors *in vivo*. Nevertheless, more than half of the Tn insertion mutants identified here differ from those obtained in others screens. Discrepancies in detection of colonization-determining fitness factors between the different studies might be due to the different nature of the *C. jejuni* strains. While the screen performed in this thesis utilized the NCTC11168 isolate, most other studies were conducted with the more virulent 81-176 strain (Novik *et al.*, 2010; Gao *et al.*, 2014, 2017; Johnson *et al.*, 2014) or the M1 isolate (de Vries *et al.*, 2017a, 2017b), which is a documented case of direct transmission from chicken to human (Friis *et al.*, 2010). In addition to different approaches used to construct the Tn mutant libraries, variations in library preparation protocols, sequencing platforms, and bioinformatics processing pipelines can alter the outcome of each genome-wide screen significantly. Different tactics for the identification of colonization factors (genome-wide screen vs. pre-screened mutant pool) and varying complexity of the mutant libraries (*e.g.* ~ 8,000 – 50,000 mutants) might additionally contribute to the moderate overlap between datasets (Chao *et al.*, 2016).

Several genes previously described to play a role in *C. jejuni* interactions with host cells did not show significantly altered transposon insertion counts in this screen, neither in 2D nor in 3D. Among those not identified in the genome-wide analysis were genes reported to play a role in cell adherence and internalization such as *cadF* (Konkel *et al.*, 1997; Monteville *et al.*, 2003; Krause-Gruszczynska *et al.*, 2007) or *flpA* (Flanagan *et al.*, 2009; Konkel *et al.*, 2010; Larson *et al.*, 2013). In addition, the gene coding for the protease HtrA, which was shown to be involved in cleavage of cell-cell junctions enabling access to the basolateral entry into epithelial cells (Boehm *et al.*, 2012, 2015; Backert *et al.*, 2018; Harrer *et al.*, 2019) did not show a fitness defect here. Many studies searching for *C. jejuni* pathogenicity-related fitness factors were also unable to detect these putative virulence

factors (Novik *et al.*, 2010; Gao *et al.*, 2014, 2017; Johnson *et al.*, 2014; de Vries *et al.*, 2017a, 2017b).

Potential explanations for this could be either because their disruption did not result in a decreased phenotype or because the attenuation was much lower than, for example observed for flagellar genes and below the here applied cut-offs. In addition, fitness or colonization factors might have been missed simply by chance due to an undersaturated transposon library or an insufficient sequencing depth. Decreased insertion counts in the output libraries of Tn-seq experiments (*e.g.* ADH, INT, or cecal content) do not necessarily point towards a direct role for the respective gene in host-pathogen interactions. A simple growth defect of a transposon insertion mutant could account for its underrepresentation in the output pool. Moreover, infection with a transposon mutant library is essentially a massive competition experiment between tens of thousands of different deletion strains. Naturally, mutants with fitness advantages *e.g.* in nutrient utilization or growth rate, will simply outcompete less equipped bacteria. As non-motile *C. jejuni* mutants grow much faster compared to motile strains (Wösten *et al.*, 2004; Radomska *et al.*, 2016), they might surpass other mutants despite their known infection defect (Burnham & Hendrixson, 2018). In addition to these potential explanations, the lack of detection of previously appointed *C. jejuni* virulence factors in many genome-wide screens might be owed to general disparities in experimental procedures such as the cultivation of bacteria, the origin of host cells, the difference in animal models, or the infection protocol.

Nevertheless, the Tn-seq screen presented in this thesis was able to identify both previously reported and more importantly also novel host interaction factors. Moreover, the nature of this screen allowed for a direct comparison between genes specifically required for host-cell interactions in 2D and 3D. Intriguingly, only a limited overlap of 12 attenuating Tn insertion mutants common for both infection models could be observed. Not surprisingly, these were mostly representative of genes involved in flagella biogenesis or the flagella motor undermining the unequivocal importance of motility for effective *C. jejuni* colonization of its host (Yao *et al.*, 1994; Hendrixson & DiRita, 2004; Guerry, 2007; Young *et al.*, 2007; Gao *et al.*, 2014; de Vries *et al.*, 2017a, 2017b; Burnham & Hendrixson, 2018). To compensate for the effect of motility, many *in-vitro* studies enforce host cell contact by a centrifugation step of 5 min with 1,000 x *g* (Backert & Hofreuter, 2013). Altered adherence and internalization capabilities of *C. jejuni* mutants might then be attributed to genuine virulence-determining factors, rather than a weakened ability of the bacteria to reach the host cell surface. Adding such a centrifugation step to a genome-wide screen *in vitro* might help to avoid an overrepresentation of flagella- and motility-related genes and instead focus on putative adhesins and other pathogenicity/fitness factors. While this might not harm

conventional 2D monolayer cultures, high centrifugal forces might damage or otherwise compromise the microarchitecture of the 3D tissue model. As mechanical stress influences growth and differentiation of eukaryotic cells, preceding studies would need to assess potential harmful effects of variable *g* forces on cellular morphology, barrier function, and gene expression of the tissue model.

Surface structure-related processes seemed to be the only relevant category for colonization of the tissue model. However, genes compiled in this category are not solely restricted to bacterial motility. Many of them are for example directly responsible for modification of the *C. jejuni* flagellum with legionaminic acid (*e.g. ptmA*) or involved in pseudaminic acid biosynthesis (*e.g. pseA*, *pseI*), the major flagellin modification of *C. jejuni* (Thibault *et al.*, 2001; Goon *et al.*, 2003). Intriguingly, almost all genes annotated to be involved in flagella modifications were unique to the 3D dataset, suggesting a potential dispensability for flagella modifications during infection of a 2D monolayer. This is supported by observations made in this thesis, where a *ptmG*-deficient *C. jejuni* strain reveals a deficit in adherence and internalization only within the environment of the tissue model, but not on a 2D cell monolayer (Howard *et al.*, 2009). Moreover, many general biological aspects such as *e.g.* metabolism, iron uptake, or cell wall/envelope biogenesis seemed to be important either in 2D or in 3D. No discernible overlap in these categories suggests a very different host environment encountered by *C. jejuni* requiring distinct bacterial modulations in metabolism or envelope structure in order to adapt to its surroundings.

Experimental validation was performed on three so far uncharacterized genes, whose corresponding Tn insertion mutants revealed the highest decreased fold changes predominantly in the 3D tissue model (Cj0892c, Cj0978c, Cj01643). Deletion of these three candidates revealed them to be essential for *C. jejuni* motility. However, loss of motility was not due to loss of the flagella filament or hook structures, opening up the possibility for a role in flagellar motor function or biogenesis. Future research such as *e.g.* cryo-electron tomography of the isogenic deletion mutants or identification of potential interaction partners of these three candidates might help to uncover their precise role in the powerful *C. jejuni* motility apparatus. Validation of a fourth candidate, the putative transcriptional regulator Cj0883c, matched the phenotype suggested by the Tn-seq screen performed in this thesis. More precisely, while deletion of Cj0883c had no visible effect on infection of a 2D Caco-2 monolayer as well as on adherence to the 3D tissue model, a ΔCj0883c mutant exhibited significantly reduced fitness during internalization of polarized 3D host cells. This might indicate a significant role for Cj0883c and its putative regulon during internalization and/or intracellular survival in a 3D host environment. Preliminary data analysis of an RNA-

seq experiment performed with *C. jejuni* NCTC11168 WT, ΔCj0883c, and its complementation revealed about 17 potential targets of the transcriptional regulator (Alzheimer, Svensson, and Sharma, unpublished). Among those activated by Cj0883c were *e.g.* the methylmenaquinol:fumarate reductase *mfr* genes as well as the nitrite reductase NrfA. During infection, *C. jejuni* undergoes a respiratory reprogramming to adapt to the oxygen-limiting conditions in its intracellular host cell compartment (Watson & Galán, 2008; Liu *et al.*, 2012; Pryjma *et al.*, 2012; Hofreuter, 2014). For this, it requires among many others the *mfr* and *nrf* genes, as they support respiration systems that utilize alternative electron acceptors other than oxygen such as nitrite or fumarate (Sellars *et al.*, 2002). In the absence of Cj0883c, these genes are not activated, which might contribute to the observed fitness defect of ΔCj0883c during internalization and/or intracellular survival in the 3D tissue model.

Cj0883c is a potential homolog of the regulator IscR, which is present in many bacterial species (Rodionov *et al.*, 2006). Initially, IscR seemed to be dedicated to the regulation of genes involved in Fe-S cluster biogenesis, but is now regarded as a pleiotropic regulator of gene expression *e.g.* in *E. coli* (Giel *et al.*, 2006; Py & Barras, 2010). In its mature holo-form, IscR has been shown to repress the Fe-S cluster assembly operon *isc* including *iscS* (Schwartz *et al.*, 2001), which is analogously repressed by Cj0883c in *C. jejuni* strain NCTC11168 supporting the potential homology between Cj0883c and IscR. The RNA-seq analysis also indicated repression of Cj0025c, a putative sodium:dicarboxylate symporter by the transcriptional regulator. Likewise, *E. coli* IscR has been demonstrated to reduce the expression of the C4-dicarboxylate transporter *dctA* (Giel *et al.*, 2006) indicating a regulon of similar functions. Notably, disruption of Cj0025c in the Tn-seq screen performed in this thesis revealed a striking fitness advantage of this insertion mutant specifically during internalization or intracellular survival in the 3D tissue model. At least in part, this phenotype might be linked to the repression of Cj0025c by the transcriptional regulator. As carbohydrate catabolism is extremely limited in *C. jejuni*, the bacterium preferentially uses *e.g.* the dicarboxylate forms of the amino acids glutamine and asparagine (*i.e.* glutamate and aspartate) (Hofreuter, 2014; Burnham & Hendrixson, 2018). In particular glutamine seems ideal for *C. jejuni* survival *in vivo*, as it is one of the most abundant and most utilized amino acids in the human intestine (Ahlman *et al.*, 1993; Wu, 1998). Glutamine is vital in upholding intestinal barrier function and suppressing apoptosis of enterocytes (Carneiro *et al.*, 2006; Wang *et al.*, 2015). In fact, glutamine supplementation has been shown to protect intestinal epithelial barrier function from infection by *E. coli* (Ewaschuk *et al.*, 2011). However, the explicit reasons how this could potentially be linked to the putative sodium:dicarboxylate

symporter, why disruption of Cj0025c seems to be beneficial for *C. jejuni*, and how this relates to its transcriptional regulation by Cj0883c remains to be investigated.

In addition, the infection outcome of many more attenuating Tn insertion mutants identified in the 2D and 3D Tn-seq screens still awaits confirmation by infection experiments with their respective isogenic deletion strains and how these might be connected to *C. jejuni* host-pathogen interactions. Determining their particular contribution to *C. jejuni* adherence to or internalization into intestinal host cells might expose new angles of the bacterium's success in causing disease in humans.

Contrary to many other studies, the Tn-seq screen performed here also analyzed *C. jejuni* genes with enriched representation during infection of unpolarized Caco-2 cells and the 3D tissue model. Three other reports took Tn insertion mutants with an enriched phenotype into consideration (Johnson *et al.*, 2014; de Vries *et al.*, 2017a, 2017b). However, there was very little overlap between these genome-wide studies and the Tn-seq results obtained in this thesis. Potential explanations for these observations might be the different *C. jejuni* strains employed in all of these screens, or the nature of the varying transposons utilized to create the bacterial mutant library. In addition, particularly the *in-vivo* genome-wide screens have been performed in organisms such as chicken (Johnson *et al.*, 2014), mouse (Gao *et al.*, 2017), or piglets (de Vries *et al.*, 2017a, 2017b) and thus, can only partially reflect similar host environments encountered by *C. jejuni* when compared to the intestinal tissue model. However strikingly, many increased fitness genes identified in the Tn-seq screen of this thesis have previously been found to decrease *C. jejuni* colonization either *in vitro* or *in vivo* (Novik *et al.*, 2010; Gao *et al.*, 2014, 2017). This was especially true for the functional categories *Motility and chemotaxis*, *Broad regulatory function*, and *Cell wall, membrane, and envelope biogenesis*. Most often, opposite fitness effects were found in the here-performed 2D Tn-seq screen compared to those conducted *in vivo* (chicken, mice, piglets) or between insertion mutants detected in the new tissue model and those identified in genome wide screens *in vitro* with various epithelial cell lines. These results paint an intriguing picture as they suggest that genes potentially essential for colonization of animals might be redundant or even obstructive for (I) adherence and internalization *in vitro* or (II) interactions with artificial cell lines rather than primary cells. In addition, approximately 80 % of Tn insertion mutants with a beneficial fitness effect in the 3D tissue model were either not detected during *in-vivo* colonization screens in animals or showed a decreased phenotype during interaction with non-polarized cell lines. This could potentially support a specific gene contribution for *C. jejuni* pathogenesis in a human three-dimensional environment.

Overall, 97 Tn insertion mutants showed an enriched phenotype in 2D, while disruption of only 36 genes proofed to be beneficial during interactions with the highly polarized mucosal epithelium of the tissue model. Disruption of many CPS and LOS biosynthesis genes led to a specific increase in bacterial adherence and/or internalization to Caco-2 cells. Many CPS and LOS genes are highly susceptible to phase variation, which occurs frequently *in vitro* and *in vivo* to generate different surface structures to evade immune responses or alter colonization behavior (Guerry *et al.*, 2012; Sørensen *et al.*, 2012). Indeed, it has been shown that phase variation of an *N*-acetylgalactosaminyltransferase (*cgtA*) correlates with an increased bacterial attachment and invasion of human intestinal epithelial cells (Guerry *et al.*, 2002). Thus, other *N*-acetylgalactosaminyltransferases identified here such as *neuA1* might similarly affect adherence and internalization. Disruption of 30 genes resulted in a beneficial infection outcome uniquely in the 3D tissue model. Among those were genes encoding for transport binding proteins but also many with so far unknown function. It is therefore challenging to discern or speculate about their involvement during *C. jejuni* interaction with polarized host cells. Nonetheless, it is interesting that a few of those genes specifically identified in the tissue model were recently shown to be down-regulated in a *C. jejuni* infection study with human volunteers (Crofts *et al.*, 2018b). These included Cj1004 (periplasmic protein), *ctsT* (periplasmic protein), and Cj0559 (thioredoxin reductase). While Cj1004 and *ctsT* have not been identified in other genome-wide screens for *C. jejuni* fitness factors, disruption of the Cj0559 led to decreased presence in chicken caecal content (de Vries *et al.*, 2017a). However, protein levels of the thioredoxin reductase were also shown to be decreased during intracellular survival experiments *in vitro* (Liu *et al.*, 2012) indicating at least its potential dispensability for *C. jejuni* pathogenesis-determining processes. Together, the results of the Tn-seq approach in this thesis and the RNA-seq data from human fecal samples (Crofts *et al.*, 2018b), suggest that during *in-vivo* infection of the human host as well as during colonization of the tissue model, these genes might not be required or even detrimental for efficient bacterial colonization.

At first glance, it might seem contradictory that disruption of a bacterial factor would lead to an increase in colonization. However, several other studies have also reported beneficial outcomes for bacterial deletion mutants during infection. For example, deletion of the PPE38 protein of *Mycobacterium tuberculosis* (*M. tuberculosis*) completely blocks the secretion of various substrates leading in turn to an increased virulence phenotype (Ates *et al.*, 2018). Importantly, it has been shown that hypervirulent clinical isolates of the *M. tuberculosis* Beijing lineage carry this inactive version of PPE38 (McEvoy *et al.*, 2009). In *S. aureus*, stress-induced loss of function mutations in the transcriptional regulator *purR*

lead to a hypervirulent systemic infection, indicating that the increased purine biosynthesis in the absence of PurR might help the bacteria survive a stressful environment (Goncheva *et al.*, 2019). Another example is the regulation of cellulose biosynthesis in *Salmonella*. Inhibition of cellulose biosynthesis by inactivation of the cellulose synthase gene *bcsA* increases *Salmonella* virulence in mice (Pontes *et al.*, 2015). In addition, the virulence factor MgtC prevents excessive synthesis of cellulose, which would otherwise lead to attenuated virulence. This intricate regulatory system to control cellulose production seems to ensure optimal infection levels of *Salmonella*. While contributing to the short-term fitness and/or dissemination of a bacterial pathogen, an increase in virulence is most likely detrimental to the host in the long run. An evolutionary perspective would thus rather suggest the development of virulence levels that carefully balance the utilization of host resources necessary for short-term survival against long-term spread of the pathogen (Frank, 1996; Pontes *et al.*, 2015).

So far, the genome-wide screen to identify *C. jejuni* factors involved in host-pathogen interactions was performed with a 2D cell monolayer and the Caco-2 cell-based tissue model. The microarchitecture of the 3D model already provides a host environment approaching the intestinal morphology *C. jejuni* is faced with during human infection. But the bacterium is most often found in the mucus layer overlying the mucosal epithelium. Thus, screening the transposon mutant library during infection of the mucus producing tissue model developed in this thesis might reveal additional insights into the complex interrelationship between *C. jejuni* and its host. A direct comparison between these results with those obtained from the Tn-seq experiment performed in the Caco-2 tissue model could help to uncover bacterial factors specifically required for a life-style in the viscous environment of the intestinal mucus layer.

5.4. Advancement of the intestinal tissue model to include a mucus layer adds a major line of defense against the enteric pathogen *C. jejuni*

Enteric pathogens infecting gastrointestinal mucosal surfaces are not just faced with tightly linked epithelial cells, whose cellular junctions regulate and uphold barrier integrity. More than that, a vital component of the defense against infection is the viscoelastic mucus layer covering epithelial surfaces along the GIT. The organization of this protective barrier varies considerably from stomach to small intestine and generally owes its viscous properties to the high percentage of mucin glycoproteins (usually 50 – 80 %) (Naughton *et al.*, 2013). Secreted by goblet cells, gel-forming mucins such as MUC2 form a dense inner and/or a loose outer mucus layer, both of which are anchored to the glycocalyx, a structure composed

of transmembrane mucins, which covers the intestinal brush border. Together with a broad range of antimicrobial molecules, the mucus layer forges an impressive defensive line against invading microorganisms. To uphold this barrier, the heavily *O*-glycosylated proteins are continuously produced to shed unwelcome pathogens into the lumen of the GIT to be disposed with other waste products. Moreover, the constant secretion of mucus coupled with the specialized architecture along the GIT ensures the accumulation of mucus inside crypts or pits lending invaluable protection to stem cells localized at the base. Consequently, for most gastrointestinal pathogens, interaction with mucins constitutes an important first step in successfully colonizing mucosal surfaces and crypts. Despite the obvious implications for understanding these important host-pathogen interactions, this area of research has been hampered in no small part by the lack of suitable *in-vitro* tools facilitating such studies.

In particular, almost all cell line-based *in-vitro* models representing the human intestine lack the inevitably necessary combination of the unique villi and crypt architecture of the small intestine with a membrane-bound glycocalyx and secreted mucus layer. To fill this gap, the SISmuc scaffold was combined with the previously described mucus-producing cell line E12, a subclonal lineage of the methotrexate-adapted HT29 line (Behrens *et al.*, 2001; Alemka *et al.*, 2010a; Navabi *et al.*, 2013). Application of shear stress during cultivation of these advanced tissue models was necessary for the cells to form a polarized epithelial barrier with functional TJs and AJs similar to native human intestine. Moreover, the parental HT29 cell line was unable to establish a tight barrier as measured by the paracellular flux of FITC-dextran and was prone to form multilayer formation under dynamic culture conditions. Regardless, both MTX and E12 cells displayed a pronounced crypt and villi architecture upon application of shear stress in addition to a highly polarized cellular organization with distinct apical formation of TJ complexes. In addition, shear stress and connection to the ECM scaffold prompted the E12 cells in particular to produce both a secreted and a cell surface-bound mucus layer composed of the gel-forming MUC2 and the membrane-anchored MUC1. In total, its thickness was comparable to the mucus layer measured in human small intestinal biopsy samples.

Several other approaches have been documented to establish mucus-containing gastrointestinal models *in vitro* (Dosh *et al.*, 2017). The simplest idea but at the same time the hardest approach are *ex-vivo* human or animal gastrointestinal explants that can be mounted in horizontal perfusion chambers for further functional studies (Johansson *et al.*, 2011, 2015; Gustafsson *et al.*, 2012). This method has for example been used to determine mucus thickness *in vitro* or for the effect of dextran sodium sulfate on the penetrability of these mucus layers (Johansson *et al.*, 2010). While explant models offer the entire range of

host environmental properties, their maintenance is laborious, mucus preservation is difficult, and their lifetime is fairly limited. Nevertheless, they have been successfully used to study *e.g.* pathology elicited by *H. pylori* (Olfat *et al.*, 2002; Burkitt *et al.*, 2017), early stages of interaction with *Salmonella* (Haque *et al.*, 2004), or in the case of *C. jejuni* its propensity to preferentially adhere to the mucus layer (Grant *et al.*, 2006). Most commonly, human cells are cultured on Transwell inserts to induce polarization and/or mucus production. This includes cell lines such as the HT29-derived lineages (Pontier *et al.*, 2001; Gagnon *et al.*, 2013; Navabi *et al.*, 2013) as well as human gastrointestinal primary cells (Kauffman *et al.*, 2013; VanDussen *et al.*, 2015; Boccellato *et al.*, 2018). Recently, a combinatorial approach of Transwell inserts and bioprinting of human intestinal primary cells and myofibroblasts has generated a polarized epithelium with intestinal-specific cell lineages (Madden *et al.*, 2018). These models grant a similarly easy access to study host-pathogen interactions when compared to the tissue models presented in this thesis. However other than the tissue models, they lack an organotypic architecture because they rely on the potential of the cells to form 3D structures by themselves as the flat Transwell inserts do not offer a pre-structured architecture. Utilizing for example hydrogels, micromolding techniques have produced molds resembling the villus and crypt architecture of the small intestine. Subsequent reseeding with intestinal cell lines can approach the 3D structure of the organ, but so far have failed to produce its characteristic mucus layers (Costello *et al.*, 2014; Kim *et al.*, 2014). Alternatively, the use of two-channel microfluidic cell culture devices have been employed to construct gut-on-a-chip models (Kim & Ingber, 2013; Kasendra *et al.*, 2018). But again, the use of cell lines versus human primary cells comes at the price of either developing a tight intestinal barrier or an intact mucus layer but rarely both. Moreover, similar to the Transwell inserts, the microporous membranes separating the two-channels of a microfluidic chip do not provide a pre-patterned 3D structure for the cells to grow on.

Consequently and in comparison to these other approaches, the mucus-containing tissue model developed in this thesis combines numerous desired key characteristic intestinal features reconstructing the microenvironment an invading pathogen would face in its human host: a gut lumen-like apical compartment, continuously supplied with gel-forming mucins; an outer mucus layer composed of MUC2 loosely anchored to an inner MUC1 layer coupled to the brush border glycocalyx; a highly polarized mucosal epithelial barrier maintained by distinctly localized functional TJs and AJs and organized into a 3D villi and crypt architecture; a supportive extracellular matrix scaffold including a basement membrane, separating the luminal apical compartment from the submucosal basolateral space.

Undoubtedly, the mucus layer of the GIT is a vital frontline defense barrier against pathogenic microorganisms. Nevertheless, glycan epitopes are often exploited as binding receptors for bacterial adhesins (Borén *et al.*, 1993; Bouckaert *et al.*, 2005). The oligosaccharide structures present on mucins display a high degree of variability between species (Naughton *et al.*, 2013). In fact, work from the group of Marguerite Clyne showed that even though *C. jejuni* and *H. pylori* are closely related human pathogens, they interact with mucus in very different ways (Naughton *et al.*, 2013). Interaction studies with purified mucins showed a clear tropism of *C. jejuni* for chicken mucus with the strength of interaction even being dependent on the organ site of origin. The strongest binding was observed with mucins isolated from the chicken large intestine, with declining attraction towards the proximal small intestine and the cecum. While *C. jejuni* is able to reproduce in both chicken and human mucus (Van Deun *et al.*, 2008a; Alemka *et al.*, 2010a), purified intestinal chicken mucin inhibits its *in-vitro* pathogenicity (Alemka *et al.*, 2010b), whereas human mucus seemed to promote infection by *C. jejuni* (Naughton *et al.*, 2013). By contrast, *H. pylori* bound to a distinctly different subset of mucins, with the strongest interaction observed for porcine gastric mucus (Naughton *et al.*, 2013). In addition, both organisms were able to bind non-mucin based glycans expressed on cellular glycolipids, which have been shown to act as receptors for the bacteria (Lingwood, 1999; Styer *et al.*, 2010). These results highlight the multifaceted binding activities contributing to species- and organ-specific mucus tropism and colonization exhibited by *H. pylori* and *C. jejuni*. Consequently, interaction of gastrointestinal pathogens with the mucus present in various animal models could be significantly different and thus, potentially account for diverging disease progressions and/or outcomes in humans. Notably, the application of human colorectal cell lines in the tissue models presented in this thesis ensures that the heavily *O*-glycosylated mucin glycoproteins are not only of human origin but also tissue specific. The comparison between MTX- and E12-based tissue models aspired towards characterizing the direct influence of a thin versus a thick mucus layer in a three-dimensional organization. This eliminated the need for a non-mucus producing cell line, which in itself could already show altered interaction with bacterial cells and thus, observed differences in pathogenesis-determining processes might not solely be due to the missing mucus layer.

In this thesis, the presence of a thick mucus layer conferred a certain degree of protection to the underlying epithelial cells, as the bacterial load recovered for both *C. jejuni* wild-type strains was significantly lower at all time points post infection in the tissue model exhibiting a thicker mucus layer. These observations are contradictory to a previous *in-vitro* study, where the mucus layer of E12 cells grown on Transwell inserts enhanced adherence and invasion of the *C. jejuni* strain 81-176 to the underlying epithelial cells when compared

to similarly grown HT29 cells (Alemka *et al.*, 2010a). However, the results obtained in this thesis from the tissue model are in total agreement with what has been previously observed *in vivo* (McAuley *et al.*, 2007). Studies with MUC1-negative mice ($MUC1^{-/-}$) infected with three *C. jejuni* strains, including 81-176, revealed a strong protective effect of this membrane-anchored mucin against invading pathogens. Healthy, wild-type littermates ($MUC1^{+/+}$) suffered far less bacterial colonization throughout the GIT when compared to MUC1-lacking mice. The gastrointestinal mucosa of MUC1-positive animals was damaged to a lesser extent compared to animals lacking this particular mucin. In a very similar manner, permeability measurements in the 3D tissue models revealed a significantly reduced disruption of epithelial barrier function in the presence of the protective mucus layer in the E12-based tissue model. Moreover, *C. jejuni* readily crossed the gastrointestinal barrier of $MUC1^{-/-}$ mice leading to severe systemic spread of the pathogen to other organs such as liver, lung, or spleen. Whereas in healthy animals protected by the MUC1 layer other organs were eventually invaded by the pathogen at very late stages of the infection (14 days post inoculation), no systemic organ infection could be observed until then (McAuley *et al.*, 2007). Likewise, transmigration of both *C. jejuni* isolates occurred to a lesser extent and significantly slower in the mucus layer-protected E12 tissue model confirming the observations made *in vivo*. Once more, infection experiments conducted in the environment of the 3D intestinal tissue model contradict less sophisticated *in-vitro* cell culture models and instead mimic important *in-vivo* perceived pathogenesis-determining processes.

In the E12-based tissue model, bacterial cells seemed to be frequently trapped inside mucus clouds, rising from the cellular surface. In fact, up-regulation of the membrane-anchored MUC1 has been reported in mice upon infection with *C. jejuni* (McAuley *et al.*, 2007) as well as in human colonic biopsies following naturally occurring *C. jejuni* infection (Lindén *et al.*, 2008). In the case of the related Epsilonproteobacterium *H. pylori*, stimulated increase in MUC1 secretion into the lumen acts as a decoy for the bacteria to bind, effectively preventing them from reaching the mucosal cell surface (Lindén *et al.*, 2009). McAuley and colleagues observed the presence of MUC1 in the lumen along the GIT consistent with either a direct secretion or increased shedding from the cell surface (McAuley *et al.*, 2007). All of these observations could potentially support the hypothesis that in addition to bacterial removal, MUC1 might also act as a decoy ligand for *C. jejuni*. Consequently, the increased production and involved shedding of MUC1 can generally help eliminate bacterial burden by a combination of trapping bacteria inside mucus and shedding them into the lumen, where they will be removed along with other waste products.

In spite of this viscous safeguard on mucosal surfaces, enteric pathogens have evolved numerous specialized strategies to either circumvent or penetrate this physio-

chemical barrier. Some secrete mucin-degrading enzymes in order to break down the complex structure of the mucus barrier or to reduce its viscosity (Mantle & Rombough, 1993; Szabady *et al.*, 2011). Others such as *e.g. C. jejuni* rely on their remarkable motility or spiral body structure. In fact, corkscrew morphology of many bacterial pathogens has been suggested to play an important role in efficiently penetrating gel-like mucous layers in order to reach the underlying epithelium (Young *et al.*, 2007; Martínez *et al.*, 2016). In line with this, infection experiments in the advanced tissue models already implicated bacterial shape in successful colonization and in breaching the reconstructed epithelial barrier when comparing the rod-shaped NCTC11168 and the spiral 81-176 *C. jejuni* isolates. In particular, whereas the straight isolate is barely able to effectively colonize and replicate on the mucus-containing 3D tissue model, infection with the spiral-shaped strain leads to a higher bacterial burden and increased damage of the epithelium. Consequently, the corkscrew morphology of 81-176 seems to confer a certain advantage in colonizing viscous surfaces. The peptidoglycan hydrolase Pgp1 is necessary to determine the characteristic helical shape of *C. jejuni* (Frirdich *et al.*, 2012). While deletion of *pgp1* indeed renders strain 81-176 straight, the morphological difference has no impact on bacterial adhesion to or internalization into MTX or E12 cells, when grown as flat 2D monolayers without mucus production. This has previously been demonstrated for other gastrointestinal cell lines (T84, Caco-2, INT-407) as well as for human Thp-1 macrophages (Frirdich *et al.*, 2012). Attempts to mimic an overlying mucus layer by increasing the viscosity of the medium covering the host cells did not reveal impaired infection behavior of the *pgp1* deletion strain (Frirdich *et al.*, 2012). The very thin mucus layer in tissue models built from MTX cells seemed to grant a modicum of protection against the rod-shaped mutant, albeit only during later time points of the infection reflected in a reduced bacterial load (72 – 120 hrs) and epithelial barrier disruption (120 hrs). Yet, in the mucus producing E12-based tissue model, loss of spiral morphology is accompanied by a clear decrease in bacterial burden throughout the five days of infection. Moreover, the rod-shaped *pgp1* mutant elicited far less epithelial damage compared to its parental wildtype or a complementation strain expressing *pgp1* from the unrelated *rdxA* locus. Similar observations have been made *in vivo*, where a *pgp1* deletion strain was defective for colonization of chicks (Frirdich *et al.*, 2012), unable to colonize intestinal crypts of mice, and showed no significant pathology in the murine GIT (Stahl *et al.*, 2016). Thus, this thesis provides the first evidence *in vitro* that in the presence of a protective mucus layer, the corkscrew morphology of *C. jejuni* directly impacts bacterial colonization behavior and ensuing damage of the underlying epithelium.

The previous studies as well as the results obtained in this thesis highlight the different pathogenesis-related outcomes when a pathogenic bacterium is faced either with

an undifferentiated *in-vitro* monolayer, or the complex environment of intestinal tissue represented by the tissue model or actually *in vivo*. Moreover, the results obtained in this thesis emphasize the mucus layer as a major line of defense against invading enteric pathogens such as *C. jejuni*. In fact, the protective effect of the adherent mucus layer on the E12-based tissue model was recently demonstrated in a study investigating the interaction between the host and the commensal *E. coli* Nissle 1917 (EcN; Mutaflor®) (Reuter *et al.*, 2017). In the presence of mucus, the genotoxic effect of colibactin was attenuated by prevention of the generally observed induction of DNA doublestrand breaks. This supports the utility of the tissue models developed in this thesis in research with other bacteria as well as the protective impact of the gastrointestinal mucus layer. Indeed, the viscous barrier is increasingly recognized for its functionality against microbial infections of the gut (Ashida *et al.*, 2011; Zarepour *et al.*, 2013; Faderl *et al.*, 2015). Accordingly, the advanced mucus-producing tissue model developed in this thesis provides a suitable 3D *in-vitro* cell culture model encompassing key characteristics of the native human intestine to study virulence mechanisms of gastrointestinal pathogens. Knowledge of the exact interaction between pathogens and mucins and the protective effect exerted by mucus could lead to novel strategies to counteract infections.

In summary, these results strongly emphasize the effectiveness and usefulness of the novel 3D intestinal tissue models developed and advanced in this thesis to support infection research of gastrointestinal pathogens. The strength of these models lies in the combination of crucial aspects of the native tissue such as ECM, a highly polarized intestinal epithelium, the characteristic villi and crypt architecture of the small intestine, and a protective viscoelastic mucus layer into an *in-vitro* cell culture model that can be easily and cost-effectively set up in every lab. Investigating key pathogenicity-determining processes of enteric pathogens such as *C. jejuni* allowed the *in-vitro* visualization of phenotypic observations so far only made *in vivo*, without the high cost and sacrifice associated with laboratory animal models. Consequently, as demonstrated with the genome-wide screen of a *C. jejuni* mutant library, the 3D tissue models provide an opportunity to uncover and study virulence and/or fitness factors specifically involved in key pathogenicity-determining processes particular relevant for the interaction of *C. jejuni* and other pathogenic microorganisms with an intact three-dimensional human host environment.

5.5. Future directions and further advancements of the 3D tissue models

Profiling of bacterial fitness genes during infection of any kind of *in-vitro* or *in-vivo* model represents only half of the interaction partners involved in this process. Both pathogen and host undergo severe changes in their gene expression in order to effectively persist within the host environment or successfully clear the intruder, respectively. Thus, to obtain a deeper knowledge of the processes occurring at the interface of host and pathogen, it is necessary to understand the correlating gene expression changes in both interaction partners. Dual RNA-seq of host and pathogen promises a more comprehensive understanding of the events unfolding during the course of infection (Westermann *et al.*, 2012). In particular, *C. jejuni* lives commensally in birds, but elicits severe symptoms of gastroenteritis in humans. Simultaneously profiling the transcriptomic changes of the pathogen and the differing host environments might help to uncover both bacterial and avian/human factors involved in this variable disease progression. However, infected human tissue is not readily and sufficiently available. Hence, dual RNA-seq studies of *C. jejuni* in the tissue models present a genuine alternative to studies with patient volunteers. Moreover, the tissue models can be grown in necessary quantities to pose multiple specific questions. For example, host responses and adaptations by *C. jejuni* could be concurrently addressed during invasion and intracellular bacterial survival or at different time points of the infection. This could enlighten so far less well-understood pathogenesis-determining processes in addition to particular host defense mechanisms. Furthermore, comparative dual RNA-seq experiments between multiple infection models (*e.g.* 2D/3D, absence/presence of mucus), similar to the Tn-seq screen performed in this thesis, eliminate the multifactorial influence on host and pathogen gene expression during the progress of *in-vivo* infections. By reducing the participants to their essentials, precise questions could be more easily addressed enabling the decryption of pathogenesis-determining processes and the respective contributions by the pathogen and the host bit by bit. In addition, whereas genome-wide screens rely on easily-accessible readouts to reveal infection-relevant players, the nature of the dual RNA-seq approach permits the identification based on their "molecular phenotypes" (Barquist *et al.*, 2016; Westermann *et al.*, 2016). These transcriptional signatures can uncover the role of gene products during host-pathogen interactions, which might have been missed otherwise. For example, while deletion of the *Salmonella* sRNA PinT has no obvious phenotype during conventional cell culture infection studies, dual RNA-seq of infected human epithelial cells and porcine macrophages revealed the sRNA to be a posttranscriptional regulator of essential bacterial virulence genes (Westermann *et al.*, 2016, 2017). Simultaneously, transcriptomic changes of

the host can be addressed during these infection studies, aiding the discovery of strategic pathways involved in defense against pathogenic bacteria. Observations of these dual RNA-seq studies are mainly obtained on the population level of both pathogen and host. As these populations can be heterogenous in some of their properties, bulk analyses can lead to an averaged signal of all cells and might thus disguise strong cellular changes occurring in single cells (Saliba *et al.*, 2017). Profiling of gene expression patterns in individual cells, so-called single-cell RNA-seq, is able to attribute unique cellular responses to specific cells. For example, this technique has been applied to attribute transcriptomic signatures of macrophages to specific changes occurring upon infection with *Salmonella* (Avraham *et al.*, 2015; Saliba *et al.*, 2016). Currently, technical reasons limit single-cell RNA-seq to the analysis of the host transcriptome, but constant experimental and technological advancements will enable single-cell dual RNA-seq studies in the near future (Saliba *et al.*, 2017). This will permit to decipher RNA expression changes in single host and bacterial cells, exploring heterogeneity during pathogenesis.

Research on infectious diseases relies on the ability to comprehensively understand the interactions between host and pathogen. This in turn also requires a quantitative assessment of molecular events unfolding in a spatiotemporal manner. The development of advanced imaging modules and improved fluorescent probes coupled with new analytical computer tools can help to explore complex processes during infection of live tissues (Laketa, 2018). In the past limited by the Abbe diffraction limit, super-resolution microscopy imaging has sidestepped this restriction by allowing only a subset of molecules to emit a fluorescent signal at a certain time (Heilemann *et al.*, 2008; Wäldchen *et al.*, 2015). This way, host-pathogen interactions can be observed down to the nano-scale enabling for example the focal clustering of the viral envelope glycoprotein, which is important for efficient entry of the human immunodeficiency virus-1 (HIV-1) (Chojnacki *et al.*, 2012). As *in-vitro* systems grow more and more complex to study infectious diseases in a relevant 3D environment, conventional confocal and multi-photon microscopy reach their limits in visualization and/or quantification of pathogens in these more complex infection models not the least due to phototoxic damages of the tissues. Selective plane illumination microscopy (SPIM) or light sheet fluorescent microscopy (LSFM) facilitate fast, high-resolution imaging without photo-damage as only the actually observed section is illuminated at the time (Stelzer, 2015; Laketa, 2018). Together with the improvement of tissue clearing techniques, LSFM can provide single-cell level resolution in three dimensions (Brede *et al.*, 2012; Li *et al.*, 2017) and has for example been used to study the life cycle of *Trypanosoma brucei* (*T. brucei*) in the tse tse fly (Schuster *et al.*, 2017). An alternative approach couples efficient targeting of bacterial or viral components by light microscopy

with the high resolution of electron microscopy (Kukulski *et al.*, 2011; Howes *et al.*, 2018). Correlative light-electron microscopy (CLEM) has for example been successfully employed to visualize the rare process of macropinocytosis during *Shigella* infection (Weiner *et al.*, 2016).

Together, the power of advanced techniques such as dual RNA-seq, single-cell RNA-seq, and high-resolution microscopy combined with the strength of the tissue models in mimicking a human host environment can at the least support the unraveling of the complex mechanisms associated with the infection of gastrointestinal pathogens. This is turn could pave the way towards the discovery of new diagnostic/infective signatures and even the development of novel antimicrobial therapies.

So far, the intestinal tissue models incorporate cell line-based epithelial barriers maintained by functional tight and adherence junctions interconnected with an ECM scaffold and, in the case of the E12-based model, a protective mucus layer. While these properties are able to mimic native tissue characteristics and *in-vivo C. jejuni* infection outcomes, many advancements for the tissue models are conceivable to get closer still to *in-vitro* reconstructed human intestine. For example, a combination of a medium throughput bioreactor platform simulating intestinal peristalsis with cultivation under oxygen limitation approaches nearly identical *in-vivo* stimuli for differentiating enterocytes. Introducing bacterial pathogens into such a setting does on the one hand imitate the natural route of infection through *e.g.* contaminated water or food. On the other hand, the low oxygen conditions encountered in the human GIT have been shown to alter virulence behavior of pathogenic bacteria as well as the host response (Marteyn *et al.*, 2011; Crofts *et al.*, 2018a).

However, so far one of the major deficits of the current tissue models applied for infection studies is the use of immortalized cell lines as the source for human intestinal enterocytes. While these cells are fairly easy to handle, cost-efficient, and readily available, they do not provide the entire variety of cell types present in the human intestine. In light of the preferred interdependency of some enteric pathogens with a particular cellular subtype, using intestinal or colonic cell lines limits the study of host-pathogen interactions to enterocytes and/or goblet cells. In the last decade, 3D cell culture techniques have advanced greatly. In particular, organoid cultures expanded from human primary cells have been generated from many regions of the human body, such as lung, liver, kidney, stomach, or intestine (Fatehullah *et al.*, 2016). Pioneered by Sato and colleagues (Sato *et al.*, 2009), gastrointestinal organoid cultures have advanced our understanding of host-pathogen interactions *e.g.* with pathogenic *E. coli* strains (VanDussen *et al.*, 2015; Rajan *et al.*, 2018), *C. difficile* (Engevik *et al.*, 2015), *Salmonella* (Zhang *et al.*, 2014; Yin & Zhou, 2018), or

H. pylori (Bartfeld *et al.*, 2015; Sigal *et al.*, 2015; Schlaermann *et al.*, 2016; Boccellato *et al.*, 2018). But with organoids, it is challenging to study the interaction of gastrointestinal pathogens with the apical host cell surface, as it faces the lumen of the enclosed sphere. Delivery of the bacteria into the lumen by microinjection (Bartfeld & Clevers, 2015; Dutta & Clevers, 2017) as well as disruption of the organoids and subsequent cultivation as monolayers are two feasible techniques to enable the study of pathogenesis (Ettayebi *et al.*, 2016; Schlaermann *et al.*, 2016; Noel *et al.*, 2017; Boccellato *et al.*, 2018). However, a recent study has impressively demonstrated that polarity of conventional organoids can be reversed in a way that the apical cell surface now faces outwards (Co *et al.*, 2019). This enables easy access for microbial pathogens by bypassing the need for microinjections. These so-called "apical-out" enteroids quite remarkably recapitulate important infection parameter of *Salmonella* and *L. monocytogenes*, thus presenting a relevant and accessible model system to study host-pathogen interactions.

Combining organoid technology with ECM-based scaffolds would offer the chance to overcome cell line-based infection systems and develop human primary tissue models encompassing both key architectural features of native intestine and its multicellular complexity. Before advancing to cultivation on bioreactor platforms, these models could be dynamically cultivated in medium throughput as developed in this thesis for the cell line-based tissue. In this way, 3D primary human tissue models would be easily accessible for infection studies providing extensive, fairly cheap, and easily obtainable readouts for both pathogen and host. In fact, a recently developed human primary intestinal model based also on an extracellular matrix already demonstrates this possibility (Schweinlin *et al.*, 2016). However, while this model already combines human intestinal primary cells with a porcine ECM scaffold, it was not able to reflect the characteristic villi and crypt architecture found in the small intestine. Moreover, mucus production was sparse due to the limited presence of goblet cells, in spite of the application of DAPT (*N*-[*N*-(3,5-Difluorophenacetyl)-l-alanyl]-*S*-phenylglycine *t*-butyl ester), a γ-secretase inhibitor that drives differentiation toward secretory lineages (Navabi *et al.*, 2013; Ogaki *et al.*, 2013). Future research could focus on the integration of morphogen concentration gradients such as Wnt, as these signaling molecules are vital for intestinal homeostasis, growth, and differentiation (Leedham *et al.*, 2013; Miyoshi, 2017). Furthermore, co-culture models with endothelial or immune cells, which are not arising from the intestinal stem cell niche, might significantly improve this *in-vitro* reconstructed microenvironment. For example, fibroblasts have been shown to synthesize basic ECM components and to stimulate proliferation of intestinal epithelial cells (Göke *et al.*, 1998). In addition, the presence of sub-epithelial gut-derived fibroblasts seems to stabilize mucosal barrier integrity (Schweinlin *et al.*, 2016). Improving the balance

between a permeable absorptive epithelium and a tightly lined protective epithelium with an overlying sufficiently thick mucus layer is key in the development of fully functional intestinal tissue *in vitro*. By overcoming the described limitations and continuously improving upon the existing technologies, these tissue models could potentially circumvent the need for cell line based models altogether. This would consequently allow for a more authentic host response to infection with gastrointestinal pathogens such as *C. jejuni* predictive of disease progression in human patients. Together with continually improving technologies such as dual RNA-seq, single-cell RNA-seq, and advanced imaging modalities, these advanced human primary tissue models can help to better understand the complex interactions occurring at the level of host-pathogen interactions in the gut.

This thesis provides evidence for the importance of studying host-pathogen interactions in a 3D host environment. Moreover, the intestinal tissue models developed in this thesis prove their effectiveness and usefulness in investigating key pathogenicity-determining processes of enteric pathogens such as *C. jejuni* by visualizing *in-vivo* observed infection outcomes *in vitro*. The successful implementation of these reconstructed tissues in infection research opens up new avenues for investigating virulence mechanisms of other gastrointestinal pathogen, such as the related Epsilonproteobacterium *H. pylori*. This Gram-negative microbe uniquely thrives in the harsh acidic environment of the human stomach, where it can cause peptic ulcer disease. Long-term colonization by *H. pylori* has been associated with gastric adenocarcinoma and mucosa-associated lymphoid tissue (MALT) lymphoma (Suerbaum & Michetti, 2002; Cover & Blaser, 2009). As such, *H. pylori* was the first bacterium classified by the World's Health Organization (WHO) as a class I carcinogen in 1994 (International Agency for Research on Cancers, 1994). Many contributions have been made in understanding bacterial determinants and host predispositions leading to gastric cancer (Chang *et al.*, 2018; Waskito *et al.*, 2018). Yet, the precise mechanisms leading to *H. pylori*-induced precancerous lesions remain less well defined (Amieva & Peek, 2016). Similar to the case of *C. jejuni*, this is not the least due to the lack of suitable infection systems for the gastric pathogen. Thus, a complex human tissue model mimicking the *in-vivo* gastric environment would be beneficial to study the interplay between *H. pylori* and its unique niche in the human stomach. Latest efforts already allow the harnessing of human gastric primary cells and their sub-cultivation as spheroids or organoids (Bartfeld *et al.*, 2015; Schlaermann *et al.*, 2016). Organoids present suboptimal conditions for assessment of virulence-determining processes due to their spherical shape, luminal polarization, and the necessary cultivation in Matrigel. In a very recent study, so-called "mucosoid" cultures were established by seeding organoid-derived primary cells onto collagen-coated Transwell inserts allowing for long-term infection with *H. pylori* (Boccellato *et al.*, 2018). However,

there is evidence supporting a micro-niche for the gastric bacterium within gastric glands, which might be particularly susceptible to the oncogenic effects of *H. pylori* (Sigal *et al.*, 2015; Amieva & Peek, 2016). Consequently, combining the multicellular complexity of organoids/mucosoids with gastric ECM scaffolds could be beneficial in creating gastric tissue with a glandular architecture *in vitro*. The set-up of the intestinal SISmuc paved the way towards the development of such a gastric ECM scaffold supporting the pit-like environment of human corpus tissue. Maintained by native components of stomach-derived ECM, human primary cells could potentially develop and differentiate into a fully functional gastric mucosa supported by dynamic cultivation conditions to mimic fluidic shear stress. Enabling *H. pylori* not just to infect but to long-term colonize a 3D *in-vivo* like host environment will allow more comprehensive insights into the extent to which the bacterium engages mucosal homeostatis and/or differentiation. Furthermore, the inclusion of inflammatory or stromal cells to create a more complex gastric tissue model might enable a more detailed study of chronic *H. pylori*-induced inflammation and its potential contribution to the development of gastric cancer.

In summary, this thesis presents the development of novel intestinal 3D tissue models and their benefits in uncovering and investigating virulence- and/or fitness-factors of the enteric pathogen *C. jejuni*. The combination of *in-vivo* derived ECM with a highly prismatic mucosal epithelium in addition to a protective mucus layer and a three-dimensional villi and crypt architecture proved to be remarkably effective in studying the complex mechanisms associated with the infection of gastrointestinal pathogens. More than that, these tissue-engineered infection models have considerable potential for advanced development. Inclusion of human primary and inflammatory cells, cultivation in fluidic atmosphere-controlled bioreactor systems, or the development of other organ-specific tissue models is just the beginning. Ultimately, approaching the morphology and function of native human tissue *in vitro* can bridge the gap between 2D cell culture-based systems, animal models, and human patients, allowing for a more comprehensive understanding of microbial pathogenesis and reducing the need for animal sacrifices along the way.

6. Material and methods

6.1. Material

6.1.1. Instruments and devices

Table 6.1: Instruments and devices.

Instrument/device	Manufacturer
aspiration device for cell culture	Hartenstein
cell culture hood (eukaryotic cell lines), HERASafe KS	ThermoFisher Scientific
cell culture hood (*C. jejuni*), HERASafe	ThermoFisher Scientific
cell culture hood (*C. jejuni*), Safe 2020	ThermoFisher Scientific
centrifuge, 5415C	Eppendorf
centrifuge, 5424R	Eppendorf
centrifuge, 5418R	Eppendorf
centrifuge, 5810	Eppendorf
centrifuge, Heraeus Multifuge X3R	ThermoFisher Scientific
confocal laser scanning microscope TCS SP5 II	Leica Microsystems
electroporator MicroPulser	BioRad
embedding center, dispenser, and hot plate EG1160	Leica Biosystems
fluorimeter Qubit v 2.0	Invitrogen
gel documentation system Gel iX Imager	Intas
incubator for *C. jejuni* agar plates, HERAcell 240i	ThermoFisher Scientific
incubator for *C. jejuni* liquid cultures, HERAcell 150i	ThermoFisher Scientific
incubator for *E. coli*, HERAcell (Kendro)	ThermoFisher Scientific
incubator for eukaryotic cell lines, HERAcell (Heraeus)	ThermoFisher Scientific
microscope, Axiostar Plus	Zeiss
microscope, DM4000 B	Leica Biosystems
microscope, Eclipse TS100	Nikon
microwave	LG
NextSeq 500	Illumina
orbital shaker Celltron	Infors HT
paraffin oven, Heraeus	ThermoFisher Scientific
PCR engine, T3 thermocycler	Biometra
photometer Ultrospec 3100 pro Cell Density Meter	GE Healthcare
plate reader Infinite® 200 PRO	Tecan
power supplies for electrophoresis, peqPOWER E250, E300	Peqlab
rotary microtome, RM2255	Leica Biosystems
orbital shaker, SM-30	Bühler
sonication device Biorupter® Plus	Diagenode
spectrophotometer NanoDrop 2000	Peqlab
steamer FS 20	Braun
thermal mixing block MB-102	BIOER
tissue float bath 1052	GFL
tissue processor Asp200 S	Leica Biosystems
vortex mixer, Vortex-Genie 2	Scientific Industries
waterbath, GFL	Hartenstein
waterbath, WB 20	P-D Industriegesellschaft

6.1.2. Labware and consumables

Table 6.2: Glass/plastic ware and consumables.

Labware	Manufacturer
archiving container for paraffin blocks	R. Langenbrinck GmbH
biopsy punch (Ø 5 mm)	Medikbedarf
boxes (plastic), 20.5 x 20.5 cm or 9.5 x 20.5 cm	Hartenstein
boxes (metal), 10 x 21 cm	Hartenstein
brushes for microtome and cryostat	Pelikan
Canada balsam bottle	Hartenstein
cell crowns stainless steel	Fraunhofer IGB
cell culture flasks (*C. jejuni*) 25 cm^3	PAA, Corning
cell culture flasks (eukaryotic cell lines) 75 cm^3	Sarstedt
cotton swabs	DELTALAB, Stein Labortechnik
counting chamber, Neubauer-improved CE	Marienfeld
coverslips	Hartenstein
cryo freezer container	VWR
delimitting pen	DAKO
electroporation cuvettes	Hartenstein
embedding cassettes	Hartenstein
Eppendorf micropipettes 10 µl, 20 µl, 200 µl, 1000 µl	Eppendorf
Erlenmeyer glass flasks 250 ml, 1 l	DURAN, SIMAX
filter, Minisart (0.2 µm)	Sigma
filter paper for embedding cassettes	Medite
Gilson pipettes 10 µl, 20 µl, 200 µl, 1000 µl	Gilson
glass beads (2.85 – 3.35 mm)	Roth
glass bottles	Schott
glass test tubes and lids	Roth
lab timer	Hartenstein
microplates, 96-well FLUOTRAC™ 200	VWR
microscope slides, Polysine™	Hartenstein
microtome blades (stainless steel), Feather®	Hartenstein
microtube, 2ml, PP	Sarstedt
multi-well plates (24-well, 12-well, 6-well)	Corning Costar
pasteur pipettes (glass, 150 mm)	Hartenstein
pasteur pipettes (glass, 230 mm)	Hartenstein
PCR tubes 8 x 0.5 ml	ThermoFisher Scientific
petri dishes (94 x 16 mm)	Corning
petri dishes (145 x 20 mm)	Hartenstein
Pipetboy accu-jet pro	BRAND
micropipette tips 10 µl, 20 µl, 200 µl, 1000 µl	Sarstedt
racks for PCR tubes / reaction tubes	Hartenstein
reaction tubes 1.5 ml, 2.0 ml	Sarstedt
reagent and centrifuge tubes 15 ml, 50 ml	Sarstedt
safe-lock tubes 1.5 ml, 2.0 ml	Eppendorf
serological pipettes (plastic) 5 ml, 10 ml, 25 ml	Sarstedt
slide box	Hartenstein
spatula, Drigalski, L-shape	Hartenstein
spectrophotometer cuvettes	BRAND
SPRIselect beads	Beckman-Coulter
staining chamber	Semadeni Plastics Group
staining insert (stainless steel)	Hartenstein
staining jar with lid (glass)	Hartenstein
staining rack (glass)	Hartenstein

continued on next page

Labware	Manufacturer
sterile surgical blades	B. Braun
sterilizing container	Hartenstein
syringes, Inkjet® Solo Luer, 10 ml	B. Braun
tube holder 15 ml, 50 ml	Hartenstein
Transwell inserts (polycarbonate, Ø 12 mm, 0.4/3.0 µm pore size)	VWR
tweezers (stainless steel)	VWR

6.1.3. Chemicals and reagents

Table 6.3: Media, chemicals, reagents, and dyes.

Chemical/reagent	Manufacturer
acetic acid (100 %)	Roth
acetone	Roth
acrylamide	Roth
agarose	Roth
Alcian blue 8GX solution	Sigma
ammonium persulfate (APS)	Applichem
ampicillin sodium salt	Roth
antibody dilution solution	DCS Labline
BBL™ Brucella Broth (BB)	Becton, Dickinson and Company
boric acid (H_3BO_3)	Roth
bovine serum albumin, Fraction V (BSA)	Roth
bromophenol blue	Roth
calcium chloride ($CaCl_2$)	Roth
chloramphenicol	Roth
chlorine tablets	Roth
chloroform ($CHCl_3$)	Roth
citric acid monohydrate ($C_6H_8O_7 \bullet H_20$)	Roth
DAPI (4′,6-diamidine-2′-phenylindole dihydrochloride)	Sigma
Difco agar	BD
dimethyl sulfoxide (DMSO)	Roth
Dulbecco's Modified Eagle Medium (DMEM), high glucose + GlutaMAX™ + pyruvate	Gibco™
Dulbecco's Phosphate-Buffered Saline (DPBS)	Gibco™
Eosin G	Roth
ethanol, denatured (EtOH)	Roth
ethanol (absolute for analysis)	Merck
ethylenediaminetetraacetic acid disodium salt dehydrate (EDTA)	Roth
fetal calf serum (FCS)	Biochrom AG
fluorescein isothiocyanate (FITC)	Sigma
FITC-dextran (4 kDa)	Sigma
Gene Ruler 1 kb plus DNA ladder	ThermoFisher Scientific
Gene Ruler 100 bp DNA ladder	ThermoFisher Scientific
Genomic DNA buffer set	Qiagen
gentamicin sulfate	Roth
glycerol (99 %)	Sigma
hematoxylin solution, Meyer's	Roth
hydrochloric acid (HCl, 32 %)	Roth
immersion oil type F	Leica Microsystms
isopropanol	Roth
kanamycin sulfate	Roth
manganese(II) chloride ($MnCl_2$)	Sigma

continued on next page

Chemical/reagent	Manufacturer
Minimal Essential Medium (MEM) + GlutaMAX™ + Earle's Salts	Gibco™
MEM GlutaMAX™	Gibco™
MEM Non-Essential Amino Acids solution (NEAA), 100X	Gibco™
methanol (MeOH)	Roth
Midori Green	Nippon Genetics GmbH
monopotassium phosphate (KH_2PO_4)	Roth
mounting medium Entellan®	Merck Millipore
Mowiol® 40-88	Sigma
Mueller-Hinton (MH) broth	Becton, Dickinson and Company
paraformaldehyde (PFA)	Sigma
periodic acid (H_5IO_6)	Sigma
potassium acetate (CH_3CO_2K)	Roth
potassium chloride (KCl)	Applichem
potassium pyrosulfite ($K_2S_2O_5$)	Roth
saponin	Roth
Schiff's reagent	Sigma
sodium chloride (NaCl)	Roth
sodium phosphate dibasic dihydrate ($Na_2HPO_4 \bullet 2H_2O$)	Roth
Sodium Pyruvate (100 mM)	Gibco™
sodium hydroxide (NaOH)	Roth
sucrose	Roth
tetramethylethylendiamin (TEMED)	Roth
Triton X-100	Sigma
Trypsin 0.5 % EDTA	Gibco™
Tween^{20}	Roth
vancomycin sulfate	Roth
xylene cyanol	Roth
xylol	Roth

6.1.4. Commercial kits

Table 6.4: Commercial kits.

Kit	Manufacturer
DNA library Prep kit for Illumina®	New England Biolabs (NEB)
Genomic-tip 100/G	Qiagen
Illumina® NextSeq 500 (high output, 75 cycles)	Illumina
KAPA SYBR® FAST Library Quantification Kit	KAPA Biosystems
NEBNext® Ultra™ II DNA Library Prep Kit for Illumina®	New England Biolabs (NEB)
NucleoSpin Plasmid	Macherey-Nagel
NucleoSpin Gel and PCR Clean-up	Macherey-Nagel
Quant-iT™ PicoGreen® dsDNA Assay	Invitrogen
Qubit™ dsDNA HS Assay	ThermoFisher Scientific
Venor®GeM Mycoplasma Detection	Merck Millipore

6.1.5. Enzymes

Table 6.5: Enzymes.

Enzymes	Manufacturer
antarctic phosphatase	New England Biolabs

continued on next page

Enzymes	Manufacturer
Deoxyribonuclease I (DNase I, 1 u/µl)	ThermoFisher Scientific
DpnI (20 u /µl)	New England Biolabs
EZ-Tn5 transposase	Epicentre
Phusion High-Fidelity DNA polymerase (2 u/µl)	ThermoFisher Scientific
proteinase K	Dako
T4 DNA ligase (5 u/µl)	New England Biolabs
T4 DNA polymerase (3 u/µl)	New England Biolabs
Taq DNA polymerase (5 u/µl)	New England Biolabs
assorted restriction enzymes (*NheI*, *XhoI*, *XbaI*, *ClaI*, etc.)	New England Biolabs, ThermoFisher Scientific
diverse chemicals (buffers & solutions)	Merck, New England Biolabs, Roth, Sigma

6.1.6. Antibodies

Table 6.6: Antibodies and antisera.

Antibody/antiserum	Origin	Dilution	Manufacturer
monoclonal anti-*Campylobacter jejuni* (GTX42563)	mouse	1:100	GeneTex
monoclonal anti-cytokeratin-18 (KRT18) (M701029-2)	mouse	1:100	DakoCytomation
monoclonal anti-E-cadherin (610181)	mouse	1:100	BD Biosciences
monoclonal anti-mucin1 (MUC1) (GP1.4)	mouse	1:100	ThermoFisher Scientific
monoclonal anti-occludin (OC3F10)	mouse	1:100	ThermoFisher Scientific
monoclonal anti-ZO-1 (33-9100)	mouse	1:100	ThermoFisher Scientific
polyclonal anti-*Campylobacter jejuni* (GTX40882)	rabbit	1:100	GeneTex
polyclonal anti-cytokeratin-18 (KRT18) (1924-1)	rabbit	1:100	abcam
Polyclonal anti-mucin2 (MUC2) (PA1-23786)	rabbit	1:100	ThermoFisher Scientific
anti-mouse IgG, Alexa Fluor 555-conjugate (A21424)	goat	1:400	ThermoFisher Scientific
anti-mouse IgG, Alexa Fluor 647-conjugate (A21236)	goat	1:400	ThermoFisher Scientific
anti-rabbit IgG, Alexa Fluor 594-conjugate (A21207)	donkey	1:400	ThermoFisher Scientific
anti-rabbit IgG, Alexa Fluor 647-conjugate (A21246)	donkey	1:400	ThermoFisher Scientific

6.1.7. Oligonucleotides

Table 6.7: Synthetic DNA oligonucleotides.

Sequences are given in 5' → 3' direction; P~ denotes a 5'-monophosphate; *T denotes a phosphothiorate linkage; *aphA-3** describes a kanamycin resistance cassette containing the promoter and terminator from the *H. pylori* sRNA *repG*. All oligonucleotides were purchased from Sigma unless noted otherwise.

Name	Sequence 5' → 3'	Description
CSO-0023	CCACCAGCTTATATACCTTAGCA	Validation of C *ptmG*
CSO-0055	AATAAAGTAAATTTTGATAATCAAACTCGAGGTGAA GACGAAAG	Cloning of intermediary plasmid pGG5
CSO-0056	TAAGAATTTTATGCTAAAATCTTTTATGCATTGTGAG CGGATA	Cloning of intermediary plasmid pGG5
CSO-0073	CTAACAAGCTTTCATCTACGCA	Cloning of intermediary plasmid pSSv53.4
CSO-0075	TCCTTCACAAAGAAGGGG	Cloning of intermediary plasmid pSSv53.4

continued on next page

Name	Sequence 5' → 3'	Description
CSO-0103	ATATATGCATGTTAATAATTGGTTAGATTTTGCATTATA	Cloning of intermediary plasmid pGG9.1
CSO-0105	ATATGCTAGCGTTAGCCTGTTGTTGCTGTTG	Cloning of intermediary plasmid pGG9.1
CSO-0246	GAAAGGTAAACAATGAAAAGTGATT	Validation of deletion mutant strains
CSO-0247	GTGAATGAATTTAAAGCAAATCA	Cloning of ΔCJnc180/190
CSO-0248	ATTGCACTTATGGGGGTGTTTTTGCTTAAAGAGAACAAACGAT	Cloning of ΔCJnc180/190
CSO-0249	GATTTTAAAAATTATCCATAAAATGACATTTTATTCTAAAAACACTTAATCT	Cloning of ΔCJnc180/190
CSO-0250	GATTGATGGGTATTATGGGG	Cloning of ΔCJnc180/190
CSO-0345	GTTTTTTCTAGATGATAGGTGGCTTTGAAAAAG	Cloning of intermediary plasmid pGD7.1
CSO-0346	GTTTTTGAATTCCTATATGAGCTTGTTCTCTTGCA	Cloning of complementation plasmid pGD25.1 (C 180/190)
CSO-0347	GTTTTTATCGATCTCTAGCTAGCATACTTTACAGTGC	Sense primer for cloning of *C. jejuni rdxA* complementation vector; used for construction of complementation and *sfgfp*-fusion strains
CSO-0348	GTTTTTCTCGAGAGTAAAAGCCCTAAAAAAGCTG	Cloning of intermediary plasmid pGD7.1
CSO-0349	CTGCAAAAGAAGCATTGACA	Validation of C *ptmG* and C 180/190
CSO-0350	GTTTTTCATATGCTCGAATTCAGATCCACGTT	Antisense primer for cloning of *C. jejuni rdxA* complementation vector
CSO-0354	GTTTTTATCGATGCGAAACTATGGATAATGCTG	Cloning of complementation plasmid pGD25.1 (C 180/190)
CSO-0355	GTTTTTCATATGTTGCCGTGATTAATGGG	Cloning of complementation plasmid pGD25.1 (C 180/190)
CSO-0392	TACTCCTTAAGTCTTGATGATCAA	Validation of Δ*csrA*
CSO-0393	TCCTAGTTAGTCACCCGGGTACCTTGATAATATTAACATTTTTCAACCT	Cloning of Δ*csrA*
CSO-0394	TGCAAGGAATTATCTCCTATACAC	Cloning of Δ*csrA*
CSO-0395	ATCATAAACAGCTTTAGTTTGGC	Cloning of Δ*csrA*
CSO-0396	ATTGTTTTAGTACCTGGAGGGAATAGCAAAAAACTAATCAAATGAAAG	Cloning of Δ*csrA*
CSO-0493	GTTTTTCTGCAGCTCTAGCTAGCATACTTTACAGTGC	Cloning of complementation plasmid pSSv63.1 (C *ptmG*)
CSO-0573	TTTATTCAGCAAGTCTTGTAATTCA	Cloning of complementation plasmid pGD25.1 (C 180/190)
CSO-0613	AACAAATCGGAATTTACGGA	Sense primer for *C. coli cat*
CSO-0614	GGCACCAATAACTGCCTTAA	Antisense primer for *C. coli cat*
CSO-0616	TTTTAAGGCAGTTATTGGTGCCGCAAAAAACTAATCAAATGAAAG	Cloning of Δ*flaA* in NCTC11168
CSO-0643	TATTCCCTTATCAATTCAAGTGCATCATGCCG	Validation primer for all complementation strains
CSO-0644	ATGCACTTGAATTGATAAGGGAATATAGTATTTTCCGC	Validation of *sfgfp*-fusion strains
CSO-0748	P~TAACAAGTTCATGGATGAGCTT	Cloning of intermediary plasmid pGD69.1
CSO-0749	GTTTTTTCTAGAGTTTGCTTTTGCATTTAAAGCT	Cloning of intermediary plasmid pGD69.1
CSO-0752	TATGCAGGCAAAGGTGAAG	Cloning of Δ*flaA* in NCTC11168
CSO-0756	TATGCAGGCAAAGGTGAAG	Verification of Δ*flaA* in NCTC11168
CSO-0759	GTTTTTTCCCGGGAGTTGATTTTAACTAACTTTTGCTTAA	Validation of *sfgfp*-fusion strains
CSO-0760	GTTTTTTATGCATAAAAAGTCCTTTCATTTAAAATG	Cloning of complementation plasmids pSSv105.1, pSSv106.5, pSSv107.8 (C Cj0892c, C Cj0978c, C Cj1643)
CSO-0762	GTTTTTCCCGGGTCGATACTATGTTATACGCCAA	Cloning of complementation plasmid pSSv63.1 (C *ptmG*)

continued on next page

Name	Sequence 5' → 3'	Description
CSO-0801	CCAGCATAGCTAGAAATGACG	Verification of Δ*cas9* in NCTC11168
CSO-0802	TCCTAGTTAGTCACCCGGGTACTCCTATATCAAATGC CAAAATTC	Cloning of Δ*cas9*
CSO-0803	TTTTGCCGAAGCATTGATAT	Cloning of Δ*cas9*
CSO-0804	AGCAAAGCTCATCTCTTGAAA	Cloning of Δ*cas9*
CSO-0805	ATTGTTTTAGTACCTGGAGGGAATACAAAGGCTGAGT TTAGACAAAG	Cloning of Δ*cas9*
CSO-1138	GTTTTTTCATATGTATAAAATATTTTTTTGATTGCAC GATATAGC ATTTAACAAGTTCATGGATGAGCTT	Cloning of intermediary plasmid pGD98.12
CSO-1139	GTTTTTTATCGATAAGGCCCAGTCTTTCGACT	Cloning of intermediary plasmid pGD98.12
CSO-1402	GTTTTTTCTAGAGCTCTTAGTGGTATTACCAC	Cloning of intermediary plasmid pSSv53.4
CSO-1405	GTTTTTCTCGAGAAGTCCCATAGCAGAAGCAA	Cloning of intermediary plasmid pSSv53.4
CSO-1500	P~CTGTCTCTTATACACATCTCAACCCTGA	Construction of Tn mutant library
CSO-1501	P~CTGTCTCTTATACACATCTCAACCATCA	Construction of Tn mutant library
CSO-1503	ATAGGGAGACCGGCCTCAGGGTTGAGATGTGTATAAG	Cloning of intermediary plasmid pSSv8
CSO-1504	P~AGTGAGTCGTATTAAGCTCTTGTTGGCTAGTGC	Cloning of intermediary plasmid pSSv8
CSO-1531	AGCTTGACTATAGAAAGCTTAAATG	Verification of Δ*ptmG*
CSO-1532	GAAATCATGCAAATTCTTAGAGATAAT	Cloning of Δ*ptmG*
CSO-1535	GCTTTATCGATGAAATGTATAAAGC	Cloning of Δ*ptmG*
CSO-1536	TCCTAGTTAGTCACCCGGGTACTCCCCACCCCTTCAAT TTAATAA	Cloning of Δ*ptmG*
CSO-1537	TGTGTTTTAGTACCTGGAGGGAATAAAATATAAAGG AAAAAAATGCAAAACTCAT	Cloning of Δ*ptmG*
CSO-1548	TCCTAGTTAGTCACCCGGGTATTTAAATCCTTTTAAA AAAATTCAAGCT	Cloning of Δ*flaA* in NCTC11168
CSO-1549	ATTGTTTTAGTACCTGGAGGGAATATTTACAAAAGCT GCAATATATACAAAT	Cloning of Δ*flaA* in NCTC11168
CSO-1550	ATAGCTTGACCTAAAGTGGCT	Cloning of Δ*flaA* in NCTC11168
CSO-1551	AGTCGTGTTGTAAGAAATTTGCA	Cloning of Δ*flaA* in 81-176
CSO-1552	TCCTAGTTAGTCACCCGGGTATTTAAATCCTTTTAAA TAATTTCAAACTC	Cloning of Δ*flaA* in 81-176
CSO-1553	ATTGTTTTAGTACCTGGAGGGAATATTAAATCTTAAA ATCACTTTACATTCTTT	Cloning of Δ*flaA* in 81-176
CSO-1554	TTATAGCTTGACCTAAAGTTGCT	Cloning of Δ*flaA* in 81-176
CSO-1555	TATGCAGGCAAAGGTGAAG	Verification of Δ*flaA* in 81-176
CSO-1567	GTTTTGAATTCTTTTATGGATAATTTTTAAAATCATT TG	Cloning of plasmid pSSv9 for construction of Tn mutant library
CSO-1568	GTTTTAAGCTTTATTCCCTCCAGGTACTAAAACA	Cloning of plasmid pSSv9 for construction of Tn mutant library
CSO-1678	GTACCCGGGTGACTAACTAGGGTGACTAACTAGGAGG AATAAATG	Sense primer for *aph(7")*
CSO-1679	TATTCCCTCCAGGTACTAAAACAGTCATATTCCCTCC AGGTATCA	Antisense primer for *aph(7")*
CSO-2007	ACAATATGGATGAAAGAATTTTAGAA	Verification of Δ*kpsMT*
CSO-2008	TCCTAGTTAGTCACCCGGGTACTCTCTAAAAAATAAA GCATAAATTAC	Cloning of Δ*kpsMT*
CSO-2009	AGCAGCTTTTATCTTGGGCTA	Cloning of Δ*kpsMT*
CSO-2010	CCCTAAAAGCAGGATCTCCA	Cloning of Δ*kpsMT*
CSO-2011	ATTGTTTTAGTACCTGGAGGGAATAGTTAATTAATCT AACAAAATCTTATCC	Cloning of Δ*kpsMT*
CSO-2171	P~TCTCCTAAAAGAAGAAGTAAAAAAATCAAATCCC AAATGCTATATCGTGCAATCAAAA	Cloning of intermediary plasmid pGD117.1
CSO-2172	AGTACGTGAAAAATGTCATCATCATAGGAGCGGGTGG CTTTACTAGAGCAGAATTTGCCTGGCGGC	Cloning of intermediary plasmid pGD117.1
CSO-2276	CTTAATTTAACTTATCCTTTTGAAAC	Cloning of all *rdxA* complementation strains

continued on next page

Name	Sequence 5' → 3'	Description
CSO-2277	CAAGCATTTTATCGGCTAATGG	Cloning of all *rdxA* complementation strains
CSO-2620	AATTATCATGAATTGGCAAAACACT	Construction of *hupB-sfgfp* in NCTC11168
CSO-2621	GCAGCTTCTCCACCAGATCCTTTTTTCTTTTTGCCGCTTGCTT	Construction of *hupB-sfgfp* in NCTC11168
CSO-2622	GGATCTGGTGGAGAAGCTGCAGCTAAAGGAAGTAAAGGAGAAGAACTTTTCAC	Construction of *hupB-sfgfp* in NCTC11168
CSO-2624	TTTATCCTCCGTAAATTCCGATTTGTTTTATTTGTAGAGCTCATCCATG	Construction of *hupB-sfgfp* in NCTC11168
CSO-2625	AATTTTTTTAAGGCAGTTATTGGTGCCAACTTCGGCTAGATAAATTCTAG	Construction of *hupB-sfgfp* in NCTC11168
CSO-2626	TATTCTTACGATGCGCATTTTTATT	Construction of *hupB-sfgfp* in NCTC11168
CSO-2651	GCGAACCTGATGCCAAAGG	Validation of ΔCj0883c
CSO-2652	GCAAAAGCCCCGTAAAAAGG	Cloning of ΔCj0883c
CSO-2653	CCTAGTTAGTCACCCGGGTACGAAAGTAAAGCGTATTCGCTAG	Cloning of ΔCj0883c
CSO-2654	TGTTTTAGTACCTGGAGGGAATAGCAGTGGTGGCACTTGTC	Cloning of ΔCj0883c
CSO-2655	CTCACAGCTTCAGGGCCG	Cloning of ΔCj0883c
CSO-2657	ATCTTAGCTTGCTTTTTGAAAGC	Validation of *hupB*::*sfgfp* in NCTC11168
CSO-2658	TAATTTTTCTTTTAGTATTTCCCCAA	Validation of *hupB*::*sfgfp* in NCTC11168
CSO-2748	GTTTTTGAATTCCTGATGAAATAGGATTGGCTC	Cloning of intermediary plasmid pAI2.1
CSO-2818	GTTTTTGCGGCCGCGGATGTTTTTACCTGGTATAGC	Cloning of intermediary plasmid pAI2.1
CSO-2819	GTTTTTGAATTCAATTATCATGAATTGGCAAAACACT	Cloning of intermediary plasmid pAI2.1
CSO-2820	GTTTTTGCGGCCGCTATTCTTACGATGCGCATTTTTATT	Cloning of intermediary plasmid pAI2.1
CSO-2928	GTTTTTCCCGGGCCTTATAAAAAGGAATTTTAGGTAG	Cloning of complementation plasmid pSSv63.1 (C *ptmG*)
CSO-2929	GTTTTTCTGCAGCTGGAAAAAGTAATCCGTATCC	Cloning of complementation plasmid pSSv63.1 (C *ptmG*)
CSO-2963	AATGATACGGCGACCACCGAGATCTACACGGTTGAGATGTGTATAAGAGACAG	Construction of Tn-seq libraries
CSO-2964	ACCGAGATCTACACGGTTGAGATGTGTATAAGAGACAG	Construction of Tn-seq libraries
CSO-3040	CTATGGCAAATAAGCTTTTTGAG	Cloning of Δ*pgp1*
CSO-3041	TCCTAGTTAGTCACCCGGGTATGTTATAAAAAATAAAATT	Cloning of Δ*pgp1*
CSO-3042	ATTGTTTTAGTACCTGGAGGGAATAATGGCAAGATCAAAAGATAAATTCT	Cloning of Δ*pgp1*
CSO-3043	TTTATCAAAACTTTCTCCAAAGCTA	Cloning of Δ*pgp1*
CSO-3044	AAAAAAATATAGCAAAACTTTATATCACA	Validation of Δ*pgp1*
CSO-3270	AATATCAAGTGATAAATAAGAATCAAGC	Validation of C *pgp1*
CSO-3271	P~GATCCCACTAGTGTATTTTTTTTTTCAAAAAAA	Construction of Tn-seq libraries
CSO-3272	GACTGGAGTTCAGACGTGTCGCTCTTCCGATCTTACACTAGTGGGATC*T	Construction of Tn-seq libraries
CSO-3279	P~AGCAAAGGAGAAGAACTTTTCACT	Cloning of sfGFP-fusion plasmids pSSv113.1, pSSv114.1, pSSv115.1
CSO-3305	GATCGGAAGAGCACACGTCTGAACTCCAGTCAC	Construction of Tn-seq libraries
CSO-3339	ATAGAAACGATAAATGCAAAGACAA	Cloning of ΔCj0892c
CSO-3340	TCCTAGTTAGTCACCCGGGTATAATAAAATACTCAAAATGCTTATTGTAA	Cloning of ΔCj0892c
CSO-3341	ATTGTTTTAGTACCTGGAGGGAATAATCAAAGAATTAAAAAAATATAAAATAAATACA	Cloning of ΔCj0892c
CSO-3342	TATACGGATCATAGGCTAAAATTTT	Cloning of ΔCj0892c
CSO-3343	ATTGCAGATGTGGTTGAAGGA	Validation of ΔCj0892c
CSO-3344	AGAACTATATTGCCCAAAATTCTA	Cloning of ΔCj0978c
CSO-3345	TCCTAGTTAGTCACCCGGGTATAATAGCACCATTAAAGTATATTTTTT	Cloning of ΔCj0978c
		continued on next page

Name	Sequence 5' → 3'	Description
CSO-3346	ATTGTTTTAGTACCTGGAGGGAATAAAAAATTGGGT AGATATTAAAATGACT	Cloning of ΔCj0978c
CSO-3347	ACTCACTTGTCCTGAATTAAACA	Cloning of ΔCj0978c
CSO-3348	ATGATTAAAAAATGAGAATAAATTATAAAAAAA	Validation of ΔCj0978c
CSO-3359	AGTTTTAATGATAGAAGATAGAAAAGA	Cloning of ΔCj1643
CSO-3360	TCCTAGTTAGTCACCCGGGTATAAAAAGCATGCAAAT AATTAAAATTTTTTT	Cloning of ΔCj1643
CSO-3361	ATTGTTTTAGTACCTGGAGGGAATAAGGTGGCGATGG TAAATTTCA	Cloning of ΔCj1643
CSO-3362	AAGCTGCGGCGATCAATCT	Cloning of ΔCj1643
CSO-3363	AGAGATAAAACCAAACGCCCT	Validation of ΔCj1643
CSO-3477	GTTTTTCATATGGCAACTATTTCTGCTTTTTTGGC	Cloning of complementation plasmid pMA12.2 (C Cj0883c)
CSO-3478	GTTTTTATCGATACTAAAAAACCAACAATAGTCAAGC	Cloning of complementation plasmid pMA12.2 (C Cj0883c)
CSO-3607	GTTTTTATGCATAAAAAATATACTTTAATGGTGCTAT TA	Cloning of complementation plasmid pSSv105.1 (C Cj0978c)
CSO-3608	GTTTTTATCGATAGAAAATCAAGAACAAGGTGCC	Cloning of complementation plasmid pSSv105.1 (C Cj0978c)
CSO-3609	GTTTTTATGCATAAAAAAATTTTAATTATTTGCATGC TTTTTA	Cloning of complementation plasmid pSSv107.8 (C Cj1643)
CSO-3610	GTTTTTATCGATGCTTAAAAGCAATTGTGCGCG	Cloning of complementation plasmid pSSv107.8 (C Cj1643)
CSO-3611	GTTTTTATGCATAAAAAATACATTACAATAAGCATTT TGAG	Cloning of complementation plasmid pSSv106.5 (C Cj0892c)
CSO-3612	GTTTTTATCGATATAAGTTCATCTTTTGGAAATTTTG C	Cloning of complementation plasmid pSSv106.5 (C Cj0892c)
CSO-3641	GTTTTTCCCGGGCTCTAGCTAGCATACTTTACAGTGC	Cloning of complementation plasmid pMA16.1 (C *pgp1*)
CSO-3642	GTTTTTCATATGAAACAAGAAGATCTTGTGGCAAA	Cloning of complementation plasmid pMA16.1 (C *pgp1*)
CSO-3643	TTGTTTTAAAATCATACTCAAAAACCTCTTGCAGCAA ATTCTATCACATCAA	Cloning of complementation plasmid pMA16.1 (C *pgp1*)
CSO-3644	AAGAGGTTTTTGAGTATGATTTTAAAA	Cloning of complementation plasmid pMA16.1 (C *pgp1*)
CSO-3645	GTTTTTCCCGGGAGAAACGCTAAGCCCAGGT	Cloning of complementation plasmid pMA16.1 (C *pgp1*)
CSO-3646	GTTTTTCATATGTCACAGCAAGCGGCGGA	Cloning of complementation plasmid pMA16.1 (C *pgp1*)
CSO-3647	TTGTTTTAAAATCATACTCAAAAACCTCTTGGTTCTA TTAAAGCATCAATTTCTT	Cloning of complementation plasmid pMA16.1 (C *pgp1*)
CSO-3650	GTTTTTCATATGAGAAACGCTAAGCCCAGGT	Cloning of complementation plasmid pMA16.1 (C *pgp1*)
CSO-3717	GTTTTTATCGATTTATTTGTAGAGCTCATCCATGCCA	Cloning of sfGFP-fusion plasmids pSSv113.1, pSSv114.1, pSSv115.1
CSO-3718	AGGAGTCATTTTAATATCTACCC	Cloning of sfGFP-fusion plasmid pSSv113.1 (Cj0978c::*sfgfp*)
CSO-3719	CTTAGTAAGCCTTATGAAAAATTGAAAT	Cloning of sfGFP-fusion plasmid pSSv114.1 (Cj1643::*sfgfp*)
CSO-3720	AAATACAGAAGTAAAGGAAATTTGGTTA	Cloning of sfGFP-fusion plasmid pSSv115.1 (Cj0892c::*sfgfp*)
HPK1	GTACCCGGGTGACTAACTAGG	Sense primer for *aphA-3*
HPK2	TATTCCCTCCAGGTACTAAAACA	Antisense primer for *aphA-3*
HPK2-term	AAACACCCCCATAAGTGCAATTATGGGGATAAATATT CCCTCCAGGTACTAAAACA	Antisense primer for *aphA-3** cassette
JVO-0900	GGAGAAACAGTAGAGAGTTGC	Cloning of intermediary plasmid pGD69.1

continued on next page

Name	Sequence 5' → 3'	Description
JVO-0901	TTTTTTCTAGATTAAATCAGAACGCAGA	Cloning of intermediary plasmid pGD69.1
JVO-5068	TTTTATGGATAATTTTTAAAATCATTTG	Sense primer for *aphA-3** cassette
PCRFWD	ATTCAGGCTGCGCAACTGT	Construction of Tn mutant library (Epicentre)
PCRREV	GTCAGTGAGCGAGGAAGCGGAAG	Construction of Tn mutant library (Epicentre)

6.1.8. Plasmids

Plasmids constructed/used in this thesis are listed in Appendix Table 6.1. Detailed descriptions for the construction of selected plasmids are given in Chapter 6.2. (Microbiological methods).

6.1.9. Bacterial strains

Bacterial strains constructed/used in this thesis are listed in Appendix Table 6.2. Detailed descriptions for the generation of selected *C. jejuni* strains are given in Chapter 6.2. (Microbiological methods).

6.1.10. Media, buffer, and supplements

6.1.10.1. Media and agar

Brucella Broth (BB):	28 g	BBL™ Brucella Broth
	ad 1 l H_2O	
after autoclaving, supplement with		
	10 µg/ml	vancomycin
BB soft agar plates (0.4 %):	28 g	BBL™ Brucella Broth
	4 g	Difco-agar
	ad 1 l H_2O	
after autoclaving, supplement with		
	10 µg/ml	vancomycin
DMEM medium (HT29 cell lines):	500 ml	DMEM medium
	10 % (w/v)	FCS
	1 % (w/v)	NEAA
Lennox Broth (LB):	10 g	tryptone or peptone
	5 g	yeast extract
	5 g	NaCl
	ad 1 l H_2O	
LB agar plates:	LB medium (see above)	
	1.5 % (w/v)	Difco-agar

MEM medium (Caco-2 cell line):	500 ml	MEM medium
	20 % (w/v)	FCS
	1 % (w/v)	NEAA
	1 % (w/v)	Sodium Pyruvate
MH agar plates:	21 g	Mueller-Hinton Broth
	15 g	Difco Agar
	ad 1 l H_2O	
after autoclaving, supplement with		
	10 µg/ml	vancomycin
SOC broth (transformation of *E. coli*):	1 l	SOB medium
	5 ml	$MgCl_2$
	20 ml	1 M glucose
Superbroth (competent *E. coli*):	35 g	tryptone
	30 g	yeast extract
	5 g	NaCl
	ad 1 l H_2O	

6.1.10.2. Media supplements

Table 6.8: Antibiotics.

C. jejuni

Antibiotic	Solvent	Stock	Working concentration
chloramphenicol	100 % EtOH	20 mg/ml	20 µg/ml
hygromycin		250 mg/ml	250 µg/ml
kanamycin	H_2O	50 mg/ml	50 µg/ml
vancomycin	H_2O	10 mg/ml	10 µg/ml

E. coli

Antibiotic	Solvent	Stock	Working concentration
ampicillin	H_2O	100 mg/ml	100 µg/ml
chloramphenicol	100 % EtOH	20 mg/ml	20 µg/ml
kanamycin	H_2O	20 mg/ml	20 µg/ml

6.1.10.3. Buffers and solutions

10 x DNA loading dye:	1.66 ml	1 M Tris-HCl (pH 7.5)
	12 ml	0.5 M EDTA (pH 8.0)
	0.05 g	bromophenol blue
	0.05 g	xylene cyanol
	60 ml	glycerol
	ad 100 ml H_2O	
1 x Alcian blue solution:	40 ml	8GX Alcian blue
	350 ml	3 % (w/v) CH_3COOH

Agarose gel electrophoresis solution:	1 % (w/v)	agarose in 1 x TAE buffer
0.5 M EDTA, pH 8.0:	186.1 g	EDTA
	800 ml	H_2O
	adjust to pH 8.0 (using NaOH)	
	ad 1 l H_2O	
Eosin:	4 g	Eosin
	400 ml	H_2O
HCl-EtOH:	200 ml	50 % (w/v) EtOH
	27.4 ml	1 M HCl
	ad 400 ml with 50 % (w/v) EtOH	
Methacarn fixative:	60 ml	MeOH
	30 ml	$CHCl_3$
	10 ml	CH_3COOH
PAA gel (6 %, 70 ml):	10.5 ml	40 % PAA sol. (19:1)
	3.5 ml	10 x TBE
	56 ml	H_2O
	700 µl	10 % (w/v) APS
	70 µl	TEMED
Paraformaldehyde (4 %):	600 ml	H_2O
	40 g	PFA
	10 drops	1 M NaOH
	100 ml	10 x PBS
	40 g	sucrose
	ad 1 l H_2O	
PBS (10 x stock):	80 g	NaCl
	2 g	KCl
	18 g	$Na_2HPO_4 \cdot 2H_2O$
	2.4 g	KH_2PO_4
	ad 800 ml H_2O	
	adjust to pH 7.4	
	ad 1 l H_2O	
PBS-T:	995 ml	1 x PBS
	5 ml	Tween^{20}
Sulfite water:	40 ml	HCl
	40 ml	10 % $K_2S_2O_5$
	ad 800 ml H_2O	
TAE buffer (50 x stock):	242 g	Tris base
	51.7 ml	CH_3COOH
	100 ml	0.5 M EDTA (pH 8.0)
	ad 1 l H_2O	

TBE buffer (10 x stock):	108 g	Tris base
	55 g	H_3BO_3
	40 ml	0.5 M EDTA (pH 8.0)
	ad 1 l H_2O	
Tbf I buffer (competent *E. coli* TOP10):	1.47 g	CH_3CO_2K
	4.975 g	$MnCl_2$
	3.73 g	KCl
	400 ml	H_2O
	adjust pH to 5.8 (using CH_3COOH)	
	75 ml	glycerin
	ad 500 ml H_2O	
Tbf II buffer (competent *E. coli* TOP10):	2 ml	1 M MOPS
	150 ml	0.1 M $CaCl_2$
	8 ml	250 mM KCl
	30 ml	glycerin
	ad 200 ml H_2O	
TBS buffer (10 x stock):	24.11 g	Tris base
	87.66 g	NaCl
	adjust to pH 7.4 (using HCl)	
	ad 1 l H_2O	
TBS-T buffer (1 x):	100 ml	10 x stock solution
	1 ml	Tween[20]
	ad 1 l H_2O	

6.1.10.4. Sterilization

All media and solutions used in this study were sterilized prior to use by autoclaving at 120 °C and 1 bar atmospheric pressure for 20 minutes. Heat-sensitive solutions were sterile filtered. Glassware was sterilized by heating to 80 °C for a minimum of three hours.

6.2. Microbiological methods

6.2.1. Growth conditions and phenotypic characterization

6.2.1.1. *C. jejuni*

***C. jejuni* standard growth conditions**. All *C. jejuni* strains were routinely grown on Mueller-Hinton (MH; Becton Dickinson) agar plates supplemented with 10 µg/ml vancomycin for one or two passages. Agar plates were further supplemented with marker-selective antibiotics (20 µg/ml chloramphenicol, 250 µg/ml hygromycin, 50 µg/ml kanamycin) for selection of transformed clones. Bacteria were then transferred to Brucella

Broth (BB; Becton Dickinson) liquid cultures in T-25 flasks (Corning) by inoculation from plate to a final OD_{600} of 0.005 and grown under agitation at 140 rpm in a HERAcell 150i incubator (Thermo Fisher Scientific) in a microaerobic environment (10 % CO_2, 5 % O_2, 85 % N_2).

Motility assay. Liquid cultures of *C. jejuni* strains in BB media containing 10 µg/ml vancomycin were grown under agitation to mid-log phase (OD_{600} 0.4) at 37 °C in a microaerobic environment. For each strain, 0.5 µl of bacterial culture was inoculated into a motility soft-agar plate (BB broth + 0.4 % Difco agar) poured one day prior to the experiment. Plates were incubated right-side-up until halo formation could be observed (approx. 12 – 20 hrs post inoculation). For each inoculation, halo radius was measured three times and averaged to give the mean swimming distance for each strain on each plate. Each strain was inoculated in technical triplicate per experiment and motility assays were performed in three independent biological replicates. The average halo radius for each strain was used to compare motility between *C. jejuni* wild-type and mutant strains.

FITC labeling of bacterial cells. An FITC stock solution was prepared by dissolving 1 mg of FITC (Sigma) in 100 µl 100 % (w/v) EtOH. The final staining solution (1 ml staining solution per 1 ml *C. jejuni* liquid culture grown to mid-log phase) was prepared by mixing 10 µl FITC stock solution with 990 µl DPBS. *C. jejuni* strains were streaked out from cryostocks onto MH agar plates supplemented with 10 µg/ml vancomycin (+ antibiotics for mutant strains) and grown microaerobically with shaking at 140 rpm and 37 °C to OD_{600} 0.4. Bacteria (1 ml of liquid culture) were harvested by centrifugation at 6,500 x *g* for 5 minutes at room temperature (RT). After discarding the supernatant, the bacterial cell pellet was carefully resuspended in 1 ml of DPBS and again centrifuged (6,500 x *g*, 5 min, RT). For the staining process, the resulting cell pellet was resuspended in 1 ml of FITC staining solution and incubated for 30 minutes in the dark at 37 °C in a microaerobic environment while shaking at 140 rpm. FITC-labeled bacteria were washed twice with DPBS and fixed with 500 µl of 2 % PFA for at least 30 minutes at RT in the dark. After two additional washing steps, bacteria were resuspended in 500 µl DPBS and imaged for their morphology with a fluorescence confocal laser scanning microscope (Leica, TCS SP5 II).

Transmission electron microscopy (TEM). *C. jejuni* wild-type and mutant strains were grown on MH agar plates supplemented with 10 µg/ml vancomycin (+ additional antibiotics for deletion and complementation strains) for two passages. Bacterial strains were very gently resuspended in 1 ml DPBS and harvested by centrifugation at 5,000 x *g* for 5 minutes at RT. The cell pellet was subsequently resuspended in 2 % glutaraldehyde in 0.1 M

cacodylate buffer and incubated overnight at 4 °C. The following day, a 1:10 bacterial cell suspension was mounted onto TEM grids (already hydrophilized by Claudia Gehrig, Imaging Core Facility, Biocenter, University of Würzburg, Germany). After a washing step with H_2O for 1 minute, *C. jejuni* cells were stained with 2 % uranyl acetate and finally inspected using a Zeiss EM10 transmission electron microscope.

6.2.1.2. *E. coli*

***E. coli* growth conditions.** Bacteria were grown on Lennox broth (LB) agar plates and in LB liquid medium at 37 °C with normal aeration and shaking at 220 rpm. Cultures were inoculated from a single colony of strains grown overnight on plates at 37 °C, *e.g.* in 5 ml LB medium for plasmid preparation. When appropriate, media was supplemented with antibiotics (Table 7.8).

6.2.2. Genetic manipulation

6.2.2.1. *C. jejuni*

Construction of *C. jejuni* deletion mutant strains. Deletion mutants of *C. jejuni* used in this study were constructed by double-crossover homologous recombination with antibiotic resistance cassettes to remove most of the coding sequence into the genomic locus thereby disrupting the respective genes. Resistance cassettes used for cloning were either *aphA-3* (Kan^R) (Skouloubris *et al.*, 1998) amplified with HPK1/HPK2, *aph(7'')* (Hyg^R) (Cameron & Gaynor, 2014) amplified with CSO-1678 and CSO-1679, or *C. coli cat* (Cm^R) (Boneca *et al.*, 2008) amplified with CSO-0613 and CSO-0614. Non-polar resistance cassettes were amplified from pGG1 (Dugar *et al.*, 2016) for Kan^R, pAC1H (Cameron & Gaynor, 2014) for Hyg^R, and pGD107.1 (Dugar *et al.*, 2016) for Cm^R. Overlap PCR products carried these resistance cassettes flanked by ~ 500 bp of homologous sequence up- and downstream of the gene to be deleted.

As an example, deletion of *kpsMT* in *C. jejuni* strain NCTC11168 (CSS-0032) will be described in detail. First, ~ 500 bp upstream of the *kpsM* (Cj1448c) start codon using CSO-2009 and CSO-2008 and ~ 500 bp downstream of the *kpsM* stop codon using CSO-2011 and CSO-2010 were amplified from genomic DNA (gDNA) of NCTC11168 wild-type strain. As the start codon of the downstream gene *kpsT* (Cj1447c) overlaps with the stop codon of *kpsM*, the mutant created here likely resulted in the inactivation of *kpsT* as well. The kanamycin resistance cassette (*aphA-3*) was amplified from pGG1 using HPK1 and HKP2. To fuse the

up- and downstream region of *kpsM* with the *aphA-3* resistance cassette, the antisense oligonucleotide of the *kpsM* upstream region (CSO-2008) contained 22 bp of overlap with the sense oligonucleotide used to amplify the *aphA-3* resistance cassette (HPK1). Likewise, the sense oligonucleotide of the *kpsM* downstream region (CSO-2011) contained 26 bp overlap with the antisense oligonucleotide to amplify the *aphA-3* resistance cassette (HPK2). In a final 100 µl Phusion polymerase PCR reaction, the purified (Macherey-Nagel NucleoSpin PCR cleanup kit) up- and downstream regions of *kpsM* were added together with the *aphA-3* resistance cassette in a ratio of 50:50:90 ng and amplified using CSO-2009 and CSO-2011 (final concentration of 1 µM). The program for the overlap PCR was as follows: 1 cycle of [98 °C, 1 min; 61 °C, 1 min; 72 °C, 10 min; 98 °C, 1 min], 40 cycles of [98 °C, 15 s; 57 °C, 30 s; 72 °C, 1 min], followed by 72 °C for 10 min. Overlap PCR products were verified for their size by agarose gel electrophoresis and after purification subsequently transformed into the recipient *C. jejuni* strain by electroporation (see protocol described below). After verification of the resulting clones via colony PCR with CSO-2008 and HPK2, a positive clone was picked for the final *kpsMT* deletion strain (CSS-3805; NCTC11168 Δ*kpsMT*).

Deletion mutants in strain 81-176 (CSS-0063) were cloned in a similar manner and included *flaA*::*aphA-3* (CSS-2380) and *pgp1*::*aph(7'')* (CSS-3182). The following deletion mutants in *C. jejuni* strain NCTC11168 were cloned analogously: Dr. Sarah L. Svensson constructed deletion strains for *flaA*::*aphA-3* (CSS-1512) (Dugar *et al.*, 2016), *ptmG*::*aph(7'')* (CSS-2966), Cj0892c::*aphA-3* (CSS-4081), Cj0978c::*aphA-3* (CSS-4083), Cj1643::*aphA-3* (CSS-4087), and Cj0883c::*aphA-3* (CSS-4348). The deletion mutants for *cas9*::*aphA-3* (CSS-0936) (Dugar *et al.*, 2018), *csrA*::*cat.coli* (CSS-0643) (Dugar *et al.*, 2016), and *kpsMT*::*aphA-3* (CSS-3805) were cloned by Dr. Gaurav Dugar (formerly Sharma lab).

The sRNA locus CJnc180/190 was deleted in the same way as described above for non-polar deletion mutants with the exception of using a resistance cassette that included a promoter and a terminator. This resistance cassette was amplified using JVO-5068 and HPK2term from pGG1 and annealed together with the purified up- and downstream fragments of CJnc180/190. The up- and downstream regions of CJnc180/190 were amplified using CSO-0247/CSO-0248 and CSO-0249/CSO-0250, respectively, from wild-type genomic DNA of strain NCTC11168. CSO-0248 and CSO-0249 contained overlapping regions to the polar kanamycin resistance cassette with a promoter and terminator region from the *H. pylori* sRNA RepG (Pernitzsch *et al.*, 2014). The up, down, and cassette PCR amplicons were then annealed and the entire product was amplified with CSO-0247 and CSO-0250 and electroporated into the *C. jejuni* NCTC11168 wildtype strain. Kanamycin-resistant colonies were validated via colony PCR using CSO-0246 and HPK1 resulting in CJnc180/190::*aphA-3* (CSS-1157). Deletion of CJnc180/190 was carried out by Dr. Sarah L. Svensson (Sharma lab).

For a list of all bacterial deletion strains used in this study, including oligonucleotides for their construction, see Appendix Table 6.2.

Construction of *C. jejuni* complementation and overexpression strains. In order to complement the deletion of a gene, a wild-type copy of the respective gene was inserted into the *rdxA* (Cj1066) locus, which is frequently used for complementation in *C. jejuni* (Ribardo *et al.*, 2010). Complementation constructs were made in plasmids containing approx. 500 bp up- and downstream sequences of the *rdxA* gene, flanking Cm^R or Kan^R resistance cassettes with both a promoter and terminator. As an example, construction of the *pgp1* complementation in strain 81-176 is described in detail, where the gene itself (CJJ81-176_1344) including its ribosome binding site (RBS) and start codon was fused to the upstream promoter region and internal TSS of CJJ81-176_1345 ($iTSS_{1345}$). This complementation sequence was finally cloned into a *C. jejuni* complementation vector containing the *rdxA* region as well as a chloramphenicol resistance cassette.

The cloning of the *pgp1* complementation vector (pMA16.1) required a few intermediary plasmids, which were constructed as follows. First, the *rdxA* locus was amplified with CSO-0345 and CSO-348 from gDNA of *C. jejuni* strain NCTC11168, digested with *XbaI*/*XhoI*, and ligated to similarly digested pJV752.1 (Sharma *et al.*, 2007). This resulted in the *rdxA* complementation vector pGD7.1. A second intermediary plasmid was the complementation vector for ΔCJnc180/190 (pGD25.1). Specifically, the sRNA locus was amplified from gDNA of *C. jejuni* strain NCTC11168 with CSO-0354 and CSO-0355 and digested with *NdeI* and *ClaI*. This amplicon was ligated to a *ClaI*-digested PCR product of pGD7.1 amplified with CSO-0347 and CSO-0346, and an *NdeI*-digested PCR product amplified from pGD107.1 with CSO-0573 and CSO-0350 (Dugar *et al.*, 2016) to create pGD25.1. In a second branch of intermediary plasmids, pGD69.1 was constructed by ligation of PCR products from gDNA of NCTC11168 (CSO-0748 and CSO-0749) and on pKB8.35 (Papenfort *et al.*, 2006) using JVO-0900 and JVO-0901, both of which were digested with *XbaI* and *DpnI*. Next, pGD98.12 was constructed by PCR amplification of pGD69.2 with CSO-1138 and CSO-1139 and pGD25.1 with CSO-0347 and CSO-0350, followed by digestion of both products with *NdeI* and *ClaI*, and finally ligation. To construct the precursor vector pGD117.1, which was the source of the backbone for the *pgp1* complementation plasmid pMA16.1, pGD98.1 was amplified by inverse PCR with CSO-2171 and CSO-2172, digested with *DpnI*, and recircularized by ligation. Finally, the backbone for pMA16.1 was amplified from pGD117.1 with CSO-3647 and CSO-3650 and digested with *NdeI* and *XmaI*.

To construct the insert for pMA16.1, the coding region of *pgp1* including its own RBS was amplified from gDNA of *C. jejuni* strain 81-176 using CSO-3644 and CSO-3645. Similarly,

the internal TSS of CJJ81-176_1345 (Dugar *et al.*, 2013) including 200 bp upstream of the TSS, was amplified using CSO-3646 and CSO-3647. The PCR fragments were then fused via overlap PCR as described above using CSO-3646 and CSO-3645. The final PCR product was purified and, same as the backbone, digested with *XmaI* and *NdeI*. The plasmid backbone (containing the *rdxA* locus and the *C. coli cat* resistance cassette) and the insert (containing the fusion of P_{1345} and $iTSS_{1345}$ to *pgp1*) were ligated and transformed into *E. coli* Top10, resulting in pMA16.1. The clones were verified by colony PCR using CSO-0643 and CSO-3270 and sequenced using CSO-3646 and CSO-3270 (Macrogen). A purified PCR product, amplified from pMA16.1 with CSO-2276 and CSO-2277, was then transformed into *C. jejuni* strain 81-176 Δ*pgp1* (CSS-3182) via electroporation (see below). The final complementation clones were verified by colony PCR using CSO-0643 and CSO-3270 and sequencing using CSO-3646 and CSO-3270, resulting in the complementation strain 81-176_C *pgp1* (CSS-5643; *pgp1*::*aph(7'')*, *rdxA*::*cat.coli*::P_{1345}-$iTSS_{1345}$-*pgp1*). Complementation of Cj0883c (CSS-4167; Cj0883c::*aphA-3*, *rdxA*::*cat.coli*::Cj0883c) was cloned in a similar manner.

Analogues construction for all other complementation strains was carried out by Dr. Sarah L. Svensson (Sharma lab): C *ptmG* (CSS-2978; *ptmG*::*aph(7'')*, *rdxA*::*ptmG*::*aphA-3*), C CJnc180/190 (CSS-1158; CJnc180/190::*aphA-3*, *rdxA*::*cat.coli*::CJnc180/190), C Cj0892c (CSS-4327; Cj0892c::*aphA-3*, *rdxA*::*cat.coli*::Cj0892c), C Cj0978c (CSS-4325; Cj0978c::*aphA-3*, *rdxA*::*cat.coli*::Cj0978c), and C Cj1643 (CSS-4329; Cj1643::*aphA-3*, *rdxA*::*cat.coli*::Cj1643). Overexpression of *ptmG* (OE *ptmG*) was achieved by cloning the complementation construct into the NCTC11168 wild-type background, which resulted in strain *rdxA*::*ptmG*::*aphA-3* (CSS-2980).

For a list of all bacterial complementation strains used in this study, as well as oligonucleotides for their construction, see Appendix Table 6.2. All plasmids constructed and/or used in this thesis are listed in Appendix Table 6.1.

Cloning of translational reporter *sfgfp* fusions. For generation of *sfgfp* reporter fusions to Cj0892c, Cj0978c, and Cj1643, their respective coding sequences under the control of the strong *C. jejuni metK* (Cj1096c) promoter were amplified to the penultimate codon and fused to the second codon of *sfgfp* (Pédelacq *et al.*, 2006). The fusions were then introduced into the *rdxA* locus of their respective deletion strains. All *sfgfp* fusion strains were constructed by Dr. Sarah L. Svensson (Sharma lab).

As an example, construction of the *sfgfp* fusion construct to Cj0892c will be described in detail. The final Cj0892c-*sfgfp* sequence was encoded in the pSSv115.1 plasmid. First, the *sfgfp* gene was integrated into the *C. jejuni hupB* locus (Cj0913c) as a translational fusion of the *hupB* gene coupled to a domain-breaking linker sequence (as described in (Kjos

et al., 2015)) and the *sfgfp* coding region. For this, pGG5 was first constructed via blunt end ligation of inverse PCR products amplified from pXG10-SF (Corcoran *et al.*, 2012) with CSO-0055 and CSO-0056. Next, *NheI*/*NsiI*-digested pGG5 was ligated together with a similarly digested PCR product amplified with CSO-0103 and CSO-0105 on gDNA of *H. pylori* strain 26695 (CSS-0004) to result in pGG9.1. For a final 4-piece overlap PCR, the upstream and coding region of *hupB* to its penultimate codon were amplified with CSO-2620 and CSO-2621, and the downstream region of *hupB* with CSO-2625 and CSO-2626 on gDNA of *C. jejuni* strain NCTC11168. The *C. coli cat* resistance cassette was amplified from pGD107.1 with CSO-0613 and CSO-0614, and the *sfgfp* gene from pGG9.1 with CSO-2622 and CSO-2624. The resulting PCR sequence was electroporated into *C. jejuni* NTC11168 wildtype, and resistant clones were verified by colony PCR (CSO-2657 and CSO-2658) and Sanger sequencing with CSO-2620, CSO-2624, CSO-0613, and CSO-2626. This resulted in an NCTC11168 wild-type strain containing the translational fusion of *hupB* to *sfgfp* in the native *hupB* genomic locus (CSS-3357), which was constructed by Ann-Janine Imsiecke (Sharma lab).

In order to remove this fusion from the native *hupB* locus and instead place it into the *C. jejuni* pseudogene locus (Cj0046) (Rahman *et al.*, 2014), an appropriate complementation vector was constructed by ligation of *XbaI*/*XhoI*-digested PCR products amplified from pJV752.1 with CSO-0073 and CSO-0075, and on gDNA of *C. jejuni* NCTC11168 with CSO-1402 and CSO-1405, to result in pSSv53.4. The backbone of this pseudogene integration vector was then amplified with CSO-2748 and CSO-2818, digested with *NotI*/*NdeI*, and ligated to a similarly-digested PCR product amplified from gDNA extracted from the *C. jejuni* strain containing the translational *hupB-sfgfp* fusion (CSS-3357) with CSO-2819 and CSO-2820 to create plasmid pAI2.1. In order to translationally fuse *sfgfp* to Cj0892c, the complementation plasmid pSSv106.5 had to be constructed. This vector was cloned by first amplifying the backbone of pSE59.1 (Dugar *et al.*, 2018) with CSO-0347 and CSO-0760 and digesting with *NseI*/*ClaI*. The digested backbone was ligated together with a similarly-digested PCR product amplified with CSO-3611 and CSO-3612 from gDNA of *C. jejuni* strain NCTC11168 WT to give rise to pSSv106.5. Finally, the translational fusion of Cj0892c to *sfgfp* was constructed in pSSv115.1 by ligation of PCR amplicons digested with *ClaI* that had been amplified with CSO-3718 and CSO-3720 from pSSv106.5, and with CSO-3717 and CSO-3279 from pAI2.1. The final *sfgfp* fusion sequence was amplified with CSO-2276 and CSO-2277 from pSSv115.1 and electroporated (see below) into *C. jejuni* NCTC11168 ΔCj0892c (CSS-4081). Clones were verified via colony PCR and sequencing with CSO-0349 and CSO-0644. Colony PCR was also used to confirm retention of the original deletion with CSO-3343 and HPK2. This gave rise to the final *C. jejuni* strain containing the

translational fusion of *sfgfp* to the penultimate codon of Cj0892c (CSS-4666; Cj0892c::*aphA-3, rdxA*::*cat.coli*::Cj0892c-*sfgfp*). Fusion of *sfgfp* to Cj0978c (CSS-4626; Cj0978c::*aphA-3, rdxA*::*cat.coli*::Cj0978c-*sfgfp*) and Cj1643 (CSS-4668; Cj1643::*aphA-3, rdxA*::*cat.coli*::Cj1643-*sfgfp*) was cloned in a similar manner. For construction details of these *sfgfp* fusion strains see Appendix Table 6.1 and 6.2.

Transformation of *C. jejuni* by electroporation. For construction of deletion, complementation, or sfGFP-fusion strains, *C. jejuni* NCTC11168 wildtype or appropriate deletion mutants were streaked onto MH agar plates with the suitable antibiotics from cryostocks. After one passage, bacterial cells were harvested with a cotton swab and resuspended in cold Electroporation solution (272 mM sucrose, 15 % (w/v) glycerol). Bacteria were harvested by centrifugation at 4 °C and 6,500 x *g* for 5 minutes, and then resuspended in the same solution. After two additional washing steps, the final pellet was resuspended in an appropriate small volume of electroporation solution, depending on the size of the pellet. Next, 50 µl of this cell suspension was mixed with 200 – 400 ng of purified PCR product (not exceeding 4 µl volume in total)and electroporated (Biorad Genepulser) in a 1 mm gap cuvette (PEQLAB) at 2.5 kV, 200 Ω, and 25 µF. By adding 200 µl pre-warmed Brucella Broth, cells were then transferred onto a non-selective MH agar plate and recovered overnight at 37 °C in a microaerobic environment. The next day, bacterial cells were harvested with a cotton swab, streaked onto an appropriate selective MH agar plate, and incubated at 37 °C microaerobically until colonies were observed (typically 2 – 4 days). Clones were verified by colony PCR and sequencing, cryostocks were frozen in 25 % (w/v) glycerol in BB media, and stored at -80 °C.

Subcellular localization analysis of sfGFP-fusion proteins. In order to determine the subcellular localization of Cj0892c, Cj0978c, and Cj1643, their respective *sfgfp* fusion complementation strains were grown under agitation at 140 rpm in Brucella Broth liquid culture in a microaerobic environment until mid-log phase (OD_{600} of 0.4). Bacterial cells were then harvested by centrifugation (6,500 x *g*, 5 min, RT), washed once with DPBS, and fixed with 2 % PFA for 2 hrs at RT in the dark. After three washing steps with DPBS, ten confocal microscopy images per strain were taken. Bacterial cells depicting bipolar, unipolar, or non-polar fluorescence signal were then counted in randomized micrographs. In total, 218 bacteria were counted for Cj0892c::*sfgfp*, 202 for Cj0978c::*sfgfp*, and 289 for Cj1643::*sfgfp*.

Generation of a Tn5-based mutant pool in *C. jejuni* strain NCTC11168. A pool of transposon insertion mutants in *C. jejuni* strain NCTC11168 was generated by Dr. Sarah L.

Svensson (Sharma lab) as follows. First, a *Campylobacter* Tn5 transposon was constructed from the pMOD-2 plasmid (Epicentre) by replacing its native resistance cassette with the *aphA-3* kanamycin resistance cassette driven by the strong promoter of the *H. pylori* sRNA *repG* (Pernitzsch *et al.*, 2014), and adding a T7 promoter. In detail, pMOD-2 was amplified by inverse PCR using CSO-1503 and CSO-1504 to introduce an outward-facing T7 promoter. After ligation and transformation into *E. coli* TOP10, the resulting plasmid (pSSv8) was verified by colony PCR with CSO-1500 and CSO-1504 and Sanger sequencing with PCRFWD and PCRREV. Next, the *aphA-3* kanamycin resistance cassette with the *H. pylori repG* promoter was amplified from pST1.1 (Dugar *et al.*, 2018) using primers CSO-1567 and CSO-1568. Both pSSv8 and the resistance cassette insert were digested with *EcoRI* and *HindIII*, ligated, and transformed into *E. coli* to create plasmid pSSv9. Positive clones were verified by colony PCR with CSO-1500 and CSO-1501 and sequencing with PCRFWD and PCRREV. *In-vitro* transposition was then performed as follows. The *Campylobacter* Tn5 transposon, blunt-ended and 5'-phosphorylated, was amplified by PCR with Phusion polymerase with primers CSO-1500 and CSO-1501, each with 5' phosphates. Genomic DNA was then purified from *C. jejuni* NCTC11168 wildtype with the Qiagen genomic-tip 100/G kit. Subsequently, *in-vitro* transposition was performed using EZ-Tn5 transposase (Epicentre) according to the manufacturer's instructions with 0.25 pmol of transposon DNA and 1 µg of purified genomic DNA. The mutagenized DNA was purified by phenol:chloroform:isoamyl (25:24:1) alcohol extraction, and then insertion sites were repaired with T4 DNA polymerase (3 U), 10 mM dNTPs, and T4 DNA ligase (600 U) in T4 DNA ligase buffer (NEB). The repaired, mutagenized DNA was then used to transform *C. jejuni* NCTC11168 WT naturally as described previously (McLennan *et al.*, 2008), and mutant colonies were recovered on MH agar plates containing kanamycin. The pool was harvested from plates with BB + vancomycin + 25 % (w/v) glycerol and stored at -80 °C. Colony PCR using CSO-1500 and CSO-1501 on genomic DNA from the pool verified the presence of the Tn5 transposable element. Genomic DNA was extracted from the pool grown once on MH plates with kanamycin and then subjected to library preparation and sequencing (see below) to identify and quantify insertion sites. Detailed description on Tn-seq library construction and sequencing is given in Chapter 6.4. (Basic molecular biological methods).

6.2.2.2. *E. coli*

Generation of chemically competent *E. coli* cells using magnesium chloride ($MgCl_2$). *E. coli* TOP10 cells were streaked out as single colonies on LB agar plates from a cryostock stored at -80 °C and subsequently cultivated overnight in a liquid culture of 5 ml LB

medium. The following day, 350 µl of this overnight culture was used to inoculate 50 ml of Superbroth medium supplemented with 10 mM $MgCl_2$ and the culture was grown until early exponential growth phase (OD_{600} 0.3 – 0.4). To harvest *E. coli* cells from this culture, bacteria were centrifuged in pre-cooled tubes at 1,100 x *g* and 4 °C for 4 min. The cell pellet was resuspended in 15 ml cooled Tbf I buffer and incubated for 20 min on ice. Subsequently, bacteria were centrifuged for 8 min at 785 x *g* and 4 °C. Finally, bacteria were resuspended on ice in 900 µl TBf II buffer and 60 µl aliquots were snap-frozen in liquid nitrogen. Competent *E. coli* TOP10 aliquots were generated by Dr. Sandy R. Pernitzsch (formerly Sharma lab) and stored at -80 °C until use.

Transformation of chemically competent *E. coli* for plasmid construction. For each transformation, 5 µl of a ligation reaction, 10 – 50 ng of plasmid DNA or *DpnI*-digested inverse PCR product amplified from plasmid was mixed together with approx. 30 µl of chemically competent *E. coli* TOP10 cells (made as described above), and incubated on ice for 45 min. This mixture was subjected to heat shock for 90 sec at 42 °C and subsequently chilled on ice for 5 min. Next, 120 µl of warm SOC medium was added and bacteria were recovered for 60 min at 37 °C while shaking at 220 rpm. Finally, cells were plated on LB agar plates including appropriate antibiotics to select for positive transformants.

6.3. Eukaryotic cell line-based methods

6.3.1. Cultivation conditions and microscopy techniques

Culture of eukaryotic cell lines. The Caco-2 human epithelial colorectal adenocarcinoma cells were provided by the group of Prof. Dr. Heike Walles (formerly TERM, University Hospital Würzburg, Germany; now at Forschungszentrum Dynamische Systeme; Magdeburg, Germany) and were routinely passaged in MEM medium (Gibco) with GlutaMAX™ and Earle's salts, supplemented with 20 % (w/v) fetal calf serum (FCS; Biochrom), 1 % (w/v) Non-Essential Amino Acids (NEAA; Gibco), and 1 % (w/v) Sodium Pyruvate (Gibco) in a 5 % CO_2 humidified atmosphere at 37 °C. Dr. Tobias Ölschläger (Institute for Molecular Infection Biology, University Würzburg, Germany) kindly supplied the HT29 cell line, while both HT29-MTX (MTX) and HT29-MTX-E12 (E12) cells were a kind gift from Dr. Marguerite Clyne (UCD School of Medicine, University College Dublin, Ireland). All HT29-based cells were cultivated in a 5 % CO_2 humidified atmosphere at 37 °C in DMEM medium (Gibco) with GlutaMAX™, 4.5 g/l D-glucose, and pyruvate, supplemented with 10 % (w/v) FCS, and 1 % (w/v) NEAA. All cell lines were cultivated in T-75 (Sarstedt) flasks until

80 – 90 % confluence and passaged at a sub-cultivation ratio of 1/2 – 1/10. For passaging, cells were washed once with DPBS (without $CaCl_2$ and $MgCl_2$) to remove residual FCS and subsequently treated with 3 ml of 0.05 % Trypsin-EDTA (Gibco) for 5 min at 37 °C. The trypsination process was stopped by addition of fresh cell culture medium to the flask and gentle mixing of the cells to give a homogenous single-cell suspension. Depending on the passaging ratio, a certain volume of this suspension was transferred to a new flask containing 10 – 13 ml of freshly supplemented cell culture medium and cells were given appropriate time to grow to confluence again. An overview of cell lines used in this thesis is provided in Table 6.9.

Table 6.9: Characteristics of eukaryotic cell lines.

Name	Origin	Morphology	Culture properties	Reference
Caco-2	human colorectal adenocarcinoma	epithelial	adherent	(Hidalgo *et al.*, 1989)
HT29	human colorectal adenocarcinoma	epithelial	adherent	(von Kleist *et al.*, 1975)
HT29-MTX (MTX)	methotrexate-adapted HT29 cell line	epithelial mucin secreting	adherent	(Gouyer *et al.*, 2001)
HT29-MTX-E12 (E12)	subclone isolated from the MTX cell line	epithelial mucin secreting	adherent	(Behrens *et al.*, 2001)

Generation of 3D tissue models and simulation of fluid dynamics for cultivation under shear stress. For preparation of the decellularized intestinal scaffold (SISmuc), porcine jejunal segments were explanted from six week-old pigs (Niedermayer, Dettelbach, Germany). The jejunal segments were decellularized according to a standardized protocol published previously (Linke *et al.*, 2007; Schanz *et al.*, 2010). Briefly, after extensive washing with phosphate-buffered saline (PBS, Gibco), jejunal tissue was subjected to multiple rounds of decellularization with 4 % sodium deoxycholate (Sigma Aldrich), alternating with washing steps in PBS. Subsequently, the tissue was digested with a DNase I solution (Roche) and sterilized using Gamma-radiation (BBFS Sterilisationsservice GmbH, Rommelhausen, Germany). SISmuc scaffolds were kept in this state in PBS at 4 °C until usage. In order to generate 3D tissue models, the scaffolds were opened longitudinally, cut into 2 x 2 cm squares, and fixed between two metal rings (so-called cell crowns; Fraunhofer IGB, Stuttgart, Germany). This effectively created an apical and basolateral compartment with the native mucosal surface facing towards the apical side. The surface area of these scaffolds was previously estimated to be 3.1 cm^2 (Pusch *et al.*, 2011) and was seeded with 3 x 10^5 Caco-2 cells or 4 x 10^5 HT29/MTX/E12 cells in 500 µl of the appropriate cell culture

medium, while the basolateral compartment was filled with 1.5 ml of the same medium. Tissue models were then routinely cultivated either statically or dynamically on an orbital shaker (Celltron Infors HT) at 65 rpm in a 5 % CO_2 humidified atmosphere at 37 °C for 21 – 28 days. Fresh medium was supplied every two days. Transwell inserts (polycarbonate, Ø 12 mm, 0.4/3.0 µm pore size), were similarly seeded with 3 x 10^5 Caco-2 cells and cultivated statically with medium renewal every second day. Fluid dynamics to determine the rotary frequency of the shaker for dynamic cultivation conditions were simulated using COMSOL Multiphysics software (Comsol Multiphysics GmbH, Berlin, Germany) and were performed by Ivo Schwedholm (Tissue Engineering and Regenerative Medicine, University Hospital Würzburg, Germany) as previously described (Schweinlin *et al.*, 2016).

Determination of the final cell number on the Caco-2 based 3D tissue models. In order to assess the final number of epithelial cells present on a fully developed tissue model (21 days of cultivation for Caco-2 cells), two methods were employed. First, tissue models were subjected to 30 min treatment with 0.05 % Trypsin-EDTA at 37 °C, cells were detached by scratching with a pipette tip, and then finally counted using a Neubauer counting chamber. The numbers for 24 statically cultivated and 12 dynamically cultivated tissue models are depicted in Appendix Table 2.1 and 2.3, respectively. Second, the amount of DNA present in a tissue model was measured using the Quant-iT™ PicoGreen® dsDNA assay kit (ThermoFisher Scientific) according to the manufacturer's instructions. Briefly, DNA was isolated from 300,000 and 600,000 Caco-2 cells and quantified relative to a previously determined standard curve in order to correlate the DNA amount to a defined number of Caco-2 cells. DNA was also isolated from three statically grown Caco-2 cell-based tissue models and three unseeded SISmuc scaffolds and equally quantified. Based on these nucleic acid amounts, cell numbers in the tissue models (minus the residual DNA content of empty scaffolds), were calculated and are shown in Appendix Table 2.2.

Assessment of epithelial barrier integrity. Barrier integrity of the reconstructed mucosal tissue in cell crowns, as well as of confluent cell monolayers on Transwell inserts during either cultivation or infection with *C. jejuni* was assessed by determining the paracellular flux of FITC-dextran. Specifically, 0.25 mg/ml of FITC-dextran (4 kDa, Sigma Aldrich) was resuspended in 500 µl of the appropriate cell culture medium depending on the cell line used for the assay, and applied to the apical compartment of tissue models. Prior to that, 1.5 ml of the same culture medium without FITC-dextran was used to fill the basolateral compartment. From both the initial FITC-dextran solution as well as the fresh basolateral cell culture medium, three 100 µl samples were taken as a positive and negative control, respectively, and pipetted into separate wells of a black 96-well plate. Cell culture models

were incubated with the FITC-dextran solution in their apical compartments at 37 °C for 30 min. Afterwards, three 100 µl samples were taken from each basolateral compartment and measured for fluorescence intensity using the Infinite® 200 PRO plate reader (TECAN). Autofluorescence of the pure cell culture medium was subtracted from total fluorescence intensities, and FITC-dextran permeability values for each cell culture model were calculated relative to the fluorescence intensity of the initial FITC-dextran solution. Barrier integrity was assessed routinely every seven days during cultivation. During infection experiments, permeability was measured every 24 hours for the same infected crown as well as for non-infected control tissue models.

Histological and immunofluorescence staining and imaging. For histological staining, tissue models were fixed with 2 % PFA for at least one hour at RT or overnight at 4 °C, processed for paraffin embedding using a Leica ASP200S tissue processor (Leica Biosystems), and sectioned with a 5 µm thickness using a Leica RM2255 microtome (Leica Biosystems). After deparaffinization and rehydration, sections were either stained with hematoxylin and eosin (H&E; adapted from (Fischer *et al.*, 2008) or PAS/Alcian blue (adapted from (Yamabayashi, 1987). H&E staining shows cell nuclei in blue (hematoxylin) and eosinophilic structures in shades of red and pink (eosin). PAS/Alcian blue staining reveals acidic mucins as a deep blue color (Alcian blue), as well as neutral mucins as bright magenta-colored structures (PAS). After the staining process, light microscopy images were obtained with a Leica DM4000 B microscope (Leica Microsystems). The steps involved for both histological staining techniques are described below.

Hematoxylin and Eosin

Time	Reagent	Description
10 min each	Xylol I and II	
3 – 5 sec each	96 % EtOH I and II	Descending alcohol sequence for deparaffinization and
3 – 5 sec	70 % EtOH	rehydration of the tissue sections
3 – 5 sec	50 % EtOH	
	ddH_2O	Removal of residual alcohol
8 min	Hematoxylin	Staining of nuclei
	ddH_2O	Removal of residual Hematoxylin
3 – 5 sec	HCl-EtOH	Differentiation of Hematoxylin
	ddH_2O	Removal of residual alcohol
5 min	Tap water	Blueing of Hematoxylin
1 min	Eosin	Staining of cytosolic components
	ddH_2O	Removal of residual Eosin
3 – 5 sec	70 % EtOH	
2 min	96 % EtOH	Ascending alcohol sequence for dehydration of the tissue
5 min each	Isopropanol I and II	sections
5 min each	Xylol I and II	
	Entellan	Air tight sealing of the tissue sections between the microscope slide and cover slip

PAS/Alcian blue

Time	Reagent	Description
10 min each	Xylol I and II	
3 – 5 sec each	96 % EtOH I and II	Descending alcohol sequence for deparaffinization and
3 – 5 sec	70 % EtOH	rehydration of the tissue sections
3 – 5 sec	50 % EtOH	
	ddH_2O	Removal of residual alcohol
3 min	3 % Acetic acid	
30 min	1 % Alcian blue 8GX	Staining of acidic mucins
3 min	3 % Acetic acid	
5 min	ddH_2O	
10 min	0.5 % Periodic acid	
3 min	Tap water	Removal of residual periodic acid and dye
	ddH_2O	
15 min	Schiff's reagent	
2 min	Sulfite water	
2 min	Sulfite water	
2 min	Sulfite water	
3 min	Tap water	Removal of residual Schiff's reagent and sulfite water
	ddH_2O	
8 min	Hematoxylin	Staining of nuclei
	ddH_2O	Removal of residual Hematoxylin
3 – 5 sec	HCl-EtOH	Differentiation of Hematoxylin
	ddH_2O	Removal of residual alcohol
5 min	tab water	Blueing of Hematoxylin
3 – 5 sec	70 % EtOH	
2 min	96 % EtOH	Ascending alcohol sequence for dehydration of the tissue
5 min each	Isopropanol I and II	sections
5 min each	Xylol I and II	
	Entellan	Air tight sealing of the tissue sections between the microscope slide and cover slip

For immunofluorescence staining, tissue was processed as described above until the deparaffinization and rehydration of the tissue sections was completed. Subsequently, antigens were retrieved by incubation in 10 mM sodium citrate, pH 6 at 90 °C for 20 min. When staining for *C. jejuni*, an additional enzymatic antigen retrieval step was applied by incubation with Proteinase K (Dako) for 12 min at RT. Sections were then permeabilized in DPBS with 0.5 % Triton X-100 (Roth) for 30 min at RT and subsequently blocked with 1 % BSA (Roth) in PBS for 30 min at RT. Next, sections were incubated overnight at 4 °C in a humidity chamber with primary antibody solution (DCS labline), followed by washing 3 x 15 min with PBS + 0.05 % $Tween^{20}$ (Roth). Subsequently, tissue sections were incubated with the appropriate secondary antibody solution containing DAPI (Sigma Aldrich) for 4 hrs at RT in the dark. After three washing steps with PBS + 0.05 % $Tween^{20}$ for 15 min each at RT, samples were mounted in Mowiol (Sigma Aldrich) and imaged with a laser scanning Leica TCS SP5 II confocal microscope (Leica Microsystems). All primary and secondary antibodies used in this thesis including their origin and dilution factor are listed in Table 6.6.

Tissue fixation with Methacarn (methanol-Carnoy). For mucus preservation, tissue samples were also fixed with Methacarn for comparison to fixation with PFA solution. In a similar fashion, tissues were incubated either overnight at 4 °C or for at least one hour at RT with Methacarn solution (60 ml MeOH + 30 ml chloroform + 10 ml acetic acid). To remove the fixative, tissues were washed with 96 % EtOH until there was no more residual smell of acetic acid. Subsequently, tissue samples were processed for paraffin embedding, sectioning, and staining as described above.

Determination of cell height. For Caco-2 cells grown on Transwell inserts and SISmuc (static and dynamic cultivation), as well as for native human intestinal tissues, the mean height of cells was determined as follows. Tissues were fixed with 2 % PFA and processed according to the immunofluorescence staining procedure described above. Ten confocal microscopy images were taken for five different Caco-2 cell-based Transwell inserts and tissue models (static and dynamic cultivation), respectively. In addition, ten images of similarly processed small intestinal patient samples (n = 5) were used to measure the cell height of every second cell in native tissue. Measurements were made using the program ImageJ. Altogether, 269 cells were measured for Caco-2 cells cultivated on Transwell inserts, 271 cells for statically cultivated Caco-2 models, 277 cells for dynamic tissue models, and 199 cells for native human small intestine.

Determination of mucus/MUC1 layer thickness. Mucus or MUC1 layer thickness was determined for dynamically grown MTX and E12 tissue models. Following PAS/Alcian blue staining, the general thickness of the overlying mucus layer was measured in overview light microscopy images derived from five tissue models for both MTX- and E12-based systems. Each of these ten images was measured for their mucus layer thickness in six different regions representing the surface area of the tissue model. Human intestinal tissue samples were similarly processed, stained, imaged, and measured. Therefore, 300 regions in total were used to determine the mean mucus thickness in each condition (MTX- or E12-based tissue model, human intestine). Measurement of MUC1 layer thickness was performed in the same way as described above for general mucus layer thickness. Here, immunofluorescence confocal images were used, and instead of quantifying six regions from each image, eight measuring points were taken to such that 400 regions in total were measured for each condition.

6.3.2. Infection protocols

Infection of the 3D tissue model with *C. jejuni*. Caco-2 cell-based and MTX-/E12-based tissue models were cultivated for 21 days and 28 days, respectively, before they were used for infection experiments with *C. jejuni*. Bacteria were grown as described above, harvested from liquid culture in mid-log phase (OD_{600} 0.4), and resuspended in the appropriate cell culture medium to achieve an MOI of 20. From this bacterial cell suspension, serial dilutions were plated onto MH agar plates to determine the input amount of CFUs. Bacterial suspension were used to apically infect the tissue models and co-incubation was carried out in a 5 % CO_2 humidified atmosphere at 37 °C without further mechanical stimulation. For transmigration experiments, 100 µl samples from the basolateral compartment of infected tissue models were taken at indicated time points post infection (10 min – 8 hrs p. i.) and serial dilutions were plated on MH agar plates to determine the number of transmigrated bacteria. To isolate bacteria adherent to and internalized into the tissue models (ADH = adherence + internalization), infection was stopped at indicated time points post infection (4 – 120 hrs) and cell crowns were washed three times with DPBS to remove all non-adherent bacterial cells. Subsequently, two tissue pieces per crown were collected using a tissue punch (Ø 5 mm, Kai Medical) and transferred to an Eppendorf tube with 500 µl of 0.1 % saponin in DPBS. The tissue pieces were incubated for 10 min at 37 °C under agitation (1,500 rpm) to isolate bacteria from host cells. Serial dilutions were then plated on MH agar plates, colonies were counted, and CFU numbers were calculated as a percentage of input CFUs for each strain. In order to specifically isolate host cell-internalized *C. jejuni* (INT = internalization only), tissue models were additionally treated with 250 µg/ml gentamicin to kill extracellular bacteria for 2 hrs at 37 °C before CFUs were determined as described above for ADH samples.

Infection of 2D cell culture models (monolayer and Transwell) with *C. jejuni*. In general, infection experiments were carried out as described for 3D tissue models with a few modifications. For 2D monolayer infections, the respective epithelial cell lines were seeded into 6-well plates two days prior to the infection experiment in order to achieve a confluent cell monolayer. *C. jejuni* was grown in liquid culture to mid-log phase, resuspended in cell culture medium and used for infection of the epithelial monolayer at an MOI of 20. After infection, cells were washed three times with DPBS, lysed with 0.1 % saponin in 1 ml DPBS, and the resulting cell suspension was plated in serial dilutions on MH agar plates. For specific recovery of intracellular bacteria, cells were treated with 250 µg/ml gentamicin for 2 hrs at 37 °C and CFUs were determined as described. For 2D Transwell infections, Caco-2 cells were grown on polycarbonate Transwell inserts (Corning, 12 mm,

3.0 µm) for 21 days in a 5 % CO_2 humidified atmosphere at 37 °C. As for the tissue models, barrier integrity was routinely measured with the FITC-dextran permeability assay every seven days. Isolation and enumeration of transmigrated CFUs was carried out the same way as described above for the 3D tissue models.

Screen of the *C. jejuni* transposon mutant library in 3D ad 2D infection models. Similar to all *C. jejuni* strains used in this thesis, the transposon mutant library of strain NCTC11168 was stored at -80 °C in BB medium with 25 % (w/v) glycerol. In order to screen this pool of mutants for bacterial factors potentially required for the interaction with polarized (3D) and non-polarized (2D) host cells, bacteria in cryostocks were streaked onto MH agar plates containing vancomycin and kanamycin and grown overnight at 37 °C in a microaerobic environment. The mutant pool was subsequently cultivated in BB liquid medium (incl. vancomycin and kanamycin) to mid-log phase (OD_{600} 0.4). This liquid culture was used to infect 12 Caco-2 tissue models and 2 x 6-well plates (*i.e.* 12 wells in total) with a confluent Caco-2 monolayer as described above for both model systems. After 4 hrs of infection in 2D and 24 hrs in 3D, the supernatant above the epithelial cells in each crown/well was harvested, pooled either for all 12 cell crowns (3D SUP) or the 2 x 6-well plates (2D SUP). The bacteria in each supernatant pool were then plated on 12 x MH agar plates (145 x 20 mm) with vancomycin and kanamycin. The number of output CFUs recovered on each plate was approximated from a series of test infection experiments to result in approx. 4,000 colonies per plate. Next, bacterial CFUs both adherent to and internalized into the respective host cells (ADH) for half of the infected crowns and 6-well plates were isolated as described above for both 2D and 3D infection models. Bacterial cells harvested from these six tissue models or six wells were again pooled together and plated on 12 MH agar plates (145 x 20 mm) with vancomycin and kanamycin to recover 3D ADH and 2D ADH. The other half of the infected cell culture models were treated with fresh MEM medium supplemented with 250 µg/ml gentamicin for 2 hrs at 37 °C to kill extracellular bacteria and specifically isolate CFUs internalized into host cells (INT) as described for ADH samples (3D INT and 2D INT). All CFUs were recovered for 48 hrs at 37 °C in a microaerobic environment and subsequently harvested, together with colonies from all plates representing an infection condition (2D or 3D: SUP, ADH, or INT) as follows. 2 ml of fresh BB medium was pipetted onto each agar plate and colonies were carefully scraped off using an L-shaped Drigalski spatula (Hartenstein). Resulting bacterial suspensions for each condition were pooled in 50 ml Falcon tubes and well-mixed aliquots of approx. 10 OD_{600} were stored at -80 °C until subsequent extraction of gDNA and library preparation, detailed description of which can be found in the following Chapter 6.4. (Basic molecular biology methods).

6.4. Basic molecular biological methods

6.4.1. Determination of nucleic acid concentrations

The concentrations of all nucleic acid solutions were determined using a NanoDrop2000.

6.4.2. Preparation of plasmid DNA (*E. coli*) and genomic DNA (*C. jejuni*)

Using the NucleoSpin Plasmid kit, plasmid DNA from *E. coli* and genomic DNA from *C. jejuni* was extracted from bacterial cells according to the manufacturer's instructions.

6.4.3. Polymerase chain reaction

For construction of *C. jejuni* mutant strains, DNA fragments of interest were amplified by PCR. Recipes and amplification programs for either Phusion or *Taq* DNA polymerase reaction are listed below, and all synthetic DNA oligonucleotides used in this thesis are listed in Table 6.7. In general, due to its enhanced proof-reading characteristics, amplification of PCR fragments used for cloning were carried out using Phusion DNA polymerase, whereas colony PCR reactions and/or reactions for sequencing of plasmids/mutants were performed with *Taq* DNA polymerase.

	Phusion DNA polymerase	**_Taq_ DNA polymerase**
Reagents for 50 µl		
DNA template (plasmid, gDNA)	~ 50 – 100 ng	~ 100 ng
reaction buffer	10 µl (5 x HF buffer)	5 µl (10 x Thermopol buffer)
dNTPs (100 µM)	1 µl	1 µl
sense primer (100 µM)	0.3 µl	0.25 µl
antisense primer (100 µM)	0.3 µl	0.25 µl
polymerase	0.3 µl (2 u/µl)	0.25 µl (5 u/µl)
water	ad 50 µl	ad 50 µl

	Phusion DNA polymerase			**_Taq_ DNA polymerase**		
Program						
Step	**Time**	**Temperature**	**Cycles**	**Time**	**Temperature**	**Cycles**
initialization	30 sec	98 °C	1	5 min	95 °C	1
denaturation	10 sec	98 °C		30 sec	95 °C	
annealing	30 sec	T_m – 0.5 to 1 °C	40	30 sec	T_m – 0.5 to 1 °C	35
elongation	30 sec/kbp	72 °C		1 min/kbp	72 °C	
final elongation	10 min	72 °C	1	10 min	72 °C	1

E. coli transformants were screened by picking colonies directly from plates and inoculating them into PCR reactions to serve as templates for colony PCR. *C. jejuni* mutants

were validated by picking cell material of clones from selective plates, resuspending them in approx. 50 µl of ddH_2O, and using 1 µl of this suspension as template for subsequent PCR analysis.

6.4.4. Agarose gel electrophoresis

To check quality and size of PCR products, agarose gel electrophoresis (1 % agarose in 1 x TAE buffer) was used. Midori Green DNA stain (4 µl/100 ml) was included to allow UV visualization of nucleic acids. Gels were run in 1 x TAE buffer at 100 to 150 V for about 30 – 60 min (depending on the expected fragment size).

6.4.5. Restriction digestion and DNA ligation

Whenever plasmids served as template for PCR amplification, the resulting reactions were subsequently incubated with *DpnI* for 3 hrs at 37 °C to remove remnants of the template plasmid. Digestion with all other restriction enzymes was performed in the recommended/supplied buffers from New England Biolabs and Fermentas according to the conditions suggested by the manufacturers. T4 DNA ligase was used to ligate digested DNA inserts and linearized vectors (blunt or sticky-end) either for 1 h at RT or overnight at 16 °C prior to transformation.

6.4.6. Sanger sequencing of DNA fragments

In order to verify cloned DNA sequences (plasmid construction and/or *C. jejuni* mutant construction), fragments were amplified with appropriate primers and Phusion DNA polymerase. PCR products were purified with the NucleoSpin Gel and PCR Clean-up kit (Macherey-Nagel) and the concentration of nucleic acid was determined (NanoDrop2000). Approx. 250 ng of the PCR product in 5 µl of ddH_2O was mixed with 5 µl of an appropriate sequencing primer (5 µM) and sent for Sanger sequencing (Macrogen).

6.4.7. Tn-seq library construction and sequencing

For Tn-seq library preparation, genomic DNA was extracted from approximately 10 OD_{600} of thawed bacterial cells from each experimental output mutant pool (see description above) using the Qiagen Genomic-tip 100/G kit according to the manufacturer's instructions. Purified DNA was resuspended in 1 x TE buffer and checked for quality by agarose gel

electrophoresis. Next, 3 µg of purified DNA in 1 x TE was sheared by sonication in an ice bath to approx. 200 – 400 bp using a Bioruptor® Plus sonication device (Diagenode, Belgium) with low settings for 20 cycles of 30 sec on and 30 sec off. Following validation of shearing by electrophoresis on 6 % PAA gels, the DNA was end-repaired and A-tailed using the NEBNext Ultra II DNA library Prep kit for Illumina® (New England Biolabs, E7645S) according to the manufacturer's instructions. A Y-shaped splinkerette (Devon *et al.*, 1995) DNA adaptor, made by annealing CSO-3271 and CSO-3272 oligonucleotides (final concentration 15 µM), was then ligated to the sheared, repaired gDNA. Fragments of approximately 250 – 400 bp were then selected using SPRIselect beads (Beckman-Coulter, cat #B23317) according to the NEBNext Ultra II instructions (ratio of 0.4 x for the first selection and 0.2 x for the second selection) using a magnetic rack (Invitrogen). Transposon-chromosome junctions in size-selected, adaptor-ligated DNA (approx. 100 ng) were then amplified by PCR (19 – 22 cycles) with Phusion polymerase. Primers used for this enrichment PCR included a transposon-specific primer that adds the Illumina P7 sequence (CSO-2963), and a barcoding primer specific for the splinkerette adaptor (NEBNext Multiplex Oligos for Illumina®, Index Primer Sets 1 & 2) that adds a 6-nt long index and the Illumina P5 sequence. Following size selection from 6 % PAA gels (250 – 500 bp), libraries were quantified using a Qubit v 2.0 fluorimeter and the HS dsDNA Assay Kit (ThermoFisher), as well as qPCR with the KAPA SYBR FAST Library Quantification Kit (KAPA Biosystems). Libraries were then sequenced on an Illumina® NextSeq 500 (high output, 75 cycles) at the Core Unit SysMed (University of Würzburg) with HPLC-purified custom primers (Sigma) for Read1 and Index sequencing (CSO-2964 and CSO-3305, respectively). Tn-seq library construction and sequencing were performed by Dr. Sarah L. Svensson (Sharma lab).

6.5. Bioinformatic and computational analyses

6.5.1. Processing of Tn-seq sequence reads and mapping

In order to guarantee a high sequence quality and to retain genomic read sequences only, raw sequencing reads were processed as follows. The Illumina reads in FASTQ format were trimmed from the 3' end with cutadapt (Martin, 2011) version 1.9.1/1.12 using a cut-off phred score of 20 (-q 20) to remove a combination of the splinkerette and Illumina adapter sequences (-a AGATCCCACTAGTGTAAGATCGGAAGAGCACACGTCTGAACTCCAGTCAC). After trimming, the READemption pipeline (Förstner *et al.*, 2014) version 0.3.9/0.4.3 was applied to align all reads with a minimum length of 12 nt (-l 12) to the *C. jejuni* NCTC11168 genome

(RefSeq Acc.-No: NC_002163.1) using the segemehl software version 0.2.0 (Hoffmann *et al.*, 2009) with an accuracy cut-off of 95 % (-a 95). Subsequently, READemption was utilized to generate coverage plots representing the numbers of mapped reads per nucleotide, thereby considering only the 5' position of uniquely aligned reads (-u -b first_base_only). Detailed information for read mapping statistics is given in Appendix Table 6.3.

6.5.2. Definition of transposon insertion sites

Construction of a Tn5-based mutant library in *C. jejuni* strain NCTC11168 was accomplished using the EZ-Tn5 transposase, which inserts the transposon in between a 9-bp staggered double-stranded cut. This results in a 9-bp target site duplication on both sides of the inserted transposon. As the custom primer used for sequencing can bind to each 3' end of the palindromic transposon mosaic ends, read sequences of each insertion site should start with either 5' end of the 9-bp direct repeat. This in turn causes a distance of 8 bp between read starts that map to different strands of the *Campylobacter* reference genome. *Bona fide* transposon insertion sites based on the genomic coverage plots were therefore defined as follows. For all positions n with coverage X_n on the forward strand, it was computationally checked if coverage Y_{n+8} on the reverse strand is > 0. If this was the case, an insertion site was annotated at the center position (n + 4) with a score of $I_{n+4} = X_n + Y_{n+8}$. To normalize for sequencing depth, these scores were divided by the number of uniquely aligned reads for the respective library and multiplied by one million.

6.5.3. Gene fitness evaluation based on Tn-seq-measured transposon insertions

The raw positional transposon insertion scores were converted to plot files using Artemis (http://www.sanger.ac.uk/resources/software/artemis/). This was necessary to achieve a compatible format for downstream analysis using the Bio-TraDIS package (Barquist *et al.*, 2016). To map insertion sites to genes, NCBI and additional sRNA (Dugar *et al.*, 2013) annotations were included in a Genbank file and, together with the insertion plot files, used as input for the tradis_gene_insert_sites analysis script, thereby omitting the last 10 % of mRNA coding regions (-trim3 0.1). Afterwards, the tradis_comparison.R script was used to compare gene fitness between pairs of growth conditions based on two biological replicates, requiring at least 10 read counts per gene and condition (-f -t 10).

6.5.4. Functional enrichment analysis

For the list of candidate genes determined in the genome-wide screen performed in this thesis, two approaches were used to assess a potential overrepresentation of genes associated with distinct functional classes. First, the comparison of bacterial genes specifically required for ADH or INT in either 2D or 3D was evaluated manually. Specifically, genes were assigned to self-appointed functional categories ascertained by detailed literature search. Subsequently, the number of genes for 2D/3D adherence only (ADH), internalization only (INT), or shared between 2D/3D adherence and internalization (ADH & INT) was counted. Then, the percentage of genes belonging to these self-appointed functional categories was calculated relative to the total number of genes with decreased and increased insertion counts, respectively.

Second, in order to identify a potential overrepresentation of functional classes of genes required specifically for host pathogen interactions in 2D versus 3D, a functional enrichment analysis was performed. To that end, an existing functional classification of genes from *C. jejuni* strain NCTC11168 (Gundogdu *et al.*, 2007) was applied and their statistical enrichment was evaluated. Therefore, each class was analyzed for a potential functional overrepresentation using a one-side Fisher's exact test (scipy.stats.fisher_exact with alternative='greater') followed by multiple-testing correction using the Benjamini-Hochberg method (Benjamini & Hochberg, 1995). Functional categories with a p-value ≤ 0.1 were considered significantly enriched.

6.5.5. Protein sequence alignment and genomic context analysis

To study the protein sequence conservation of the four candidate genes (Cj0892c, Cj0978c, Cj1643, Cj0883c) selected from the Tn-seq screen, their respective amino acid sequences in other *C. jejuni* (NCTC11168, 81-176, 81116, RM1221, M1), *C. coli* (RM1875, RM5611, FB1), and *C. lari* (RM2100, CCUG22395, RM16701) strains were recovered from KEGG (Kyoto Encyclopedia of Genes and Genomes; https://www.genome.jp/kegg/) via the ortholog search. Sequences were aligned using MultAlin (http://multalin.toulouse.inra.fr/multalin/). The number of identical amino acids in reference to the sequence of strain NCTC11168 divided by the total number of amino acids in the respective protein sequence was multiplied by 100 to calculate the percentage of conservation between *Campylobacter* isolates. Similarly, the genomic context of each gene candidate in the above-mentioned *Campylobacter* strains was manually assessed in KEGG and orthologous genes were marked with the same color, whereas unrelated genes were illustrated in white.

6.5.6. Melting temperature of oligonucleotides

Melting temperatures of oligonucleotides were calculated according to Kibbe, 2007 using 'Oligo Calc' (http://biotools.nubic.northwestern.edu/OligoCalc.html).

6.5.7. Software

Table 6.10: Software used in this thesis.

Software	Manufacturer
4Peaks	A. Griekspoor and T. Groothuis
Adobe Acrobate Pro	Adobe Systems
Artemis	(Carver *et al.*, 2012)
Bio-TraDIS	(Barquist *et al.*, 2016)
Circos	(Krzywinski *et al.*, 2009)
COMSOL Multiphysics	Comsol Multiphysics GmbH
CoralDraw X6 – X8	Corel
F1000 Workspace	Faculty of 1000 Limited
Fiji	Image J (Schindelin *et al.*, 2012)
Graphic Converter 8.8.3	Lemke Software GmbH
GraphPad Prism 6.0	GraphPad Software
Integrated genome browser	Affymetrix
LAS X Life Science	Leica Microsystems
Microsoft Windows and Office	Windows
READemption	(Förstner *et al.*, 2014)
Segemehl 0.2.0	(Hoffmann *et al.*, 2009)

7. References

Abbott, A. (2003) Cell culture: biology's new dimension. *Nature*, **424**, 870–872.

Abuoun, M., Manning, G., Cawthraw, S.A., Ridley, A., Ahmed, I.H., Wassenaar, T.M., *et al.* (2005) Cytolethal distending toxin (CDT)-negative Campylobacter jejuni strains and anti-CDT neutralizing antibodies are induced during human infection but not during colonization in chickens. *Infection and Immunity*, **73**, 3053–3062.

Ahlman, B., Leijonmarck, C.E., Lind, C., Vinnars, E. & Wernerman, J. (1993a) Free amino acids in biopsy specimens from the human colonic mucosa. *The Journal of Surgical Research*, **55**, 647–653.

Ahlman, B., Leijonmarck, C.E. & Wernerman, J. (1993b) The content of free amino acids in the human duodenal mucosa. *Clinical Nutrition*, **12**, 266–271.

Albanese, C.T., Cardona, M., Smith, S.D., Watkins, S., Kurkchubasche, A.G., Ulman, I., *et al.* (1994) Role of intestinal mucus in transepithelial passage of bacteria across the intact ileum in vitro. *Surgery*, **116**, 76–82.

Alemka, A., Clyne, M., Shanahan, F., Tompkins, T., Corcionivoschi, N. & Bourke, B. (2010a) Probiotic colonization of the adherent mucus layer of HT29MTXE12 cells attenuates Campylobacter jejuni virulence properties. *Infection and Immunity*, **78**, 2812–2822.

Alemka, A., Whelan, S., Gough, R., Clyne, M., Gallagher, M.E., Carrington, S.D., *et al.* (2010b) Purified chicken intestinal mucin attenuates Campylobacter jejuni pathogenicity in vitro. *Journal of Medical Microbiology*, **59**, 898–903.

Alphen, L.B. van, Bleumink-Pluym, N.M.C., Rochat, K.D., Balkom, B.W.M. van, Wösten, M.M.S.M. & Putten, J.P.M. van. (2008) Active migration into the subcellular space precedes Campylobacter jejuni invasion of epithelial cells. *Cellular Microbiology*, **10**, 53–66.

Alphen, L.B. van, Wenzel, C.Q., Richards, M.R., Fodor, C., Ashmus, R.A., Stahl, M., *et al.* (2014) Biological Roles of the O-Methyl Phosphoramidate Capsule Modification in Campylobacter jejuni. *Plos One*, **9**, e87051.

Alvarez, L.A.J., Bourke, B., Pircalabioru, G., Georgiev, A.Y., Knaus, U.G., Daff, S., *et al.* (2013) Cj1411c encodes for a cytochrome P450 involved in Campylobacter jejuni 81-176 pathogenicity. *Plos One*, **8**, e75534.

Amieva, M.R., Vogelmann, R., Covacci, A., Tompkins, L.S., Nelson, W.J. & Falkow, S. (2003) Disruption of the epithelial apical-junctional complex by Helicobacter pylori CagA. *Science*, **300**, 1430–1434.

Amieva, M. & Peek, R.M. (2016) Pathobiology of Helicobacter pylori-Induced Gastric Cancer. *Gastroenterology*, **150**, 64–78.

Andersen-Nissen, E., Smith, K.D., Strobe, K.L., Barrett, S.L.R., Cookson, B.T., Logan, S.M., *et al.* (2005) Evasion of Toll-like receptor 5 by flagellated bacteria. *Proceedings of the National Academy of Sciences of the United States of America*, **102**, 9247–9252.

Ang, C.W., Laman, J.D., Willison, H.J., Wagner, E.R., Endtz, H.P., De Klerk, M.A., *et al.* (2002) Structure of Campylobacter jejuni lipopolysaccharides determines antiganglioside specificity and clinical features of Guillain-Barré and Miller Fisher patients. *Infection and Immunity*, **70**, 1202–1208.

Apel, D., Ellermeier, J., Pryjma, M., Dirita, V.J. & Gaynor, E.C. (2012) Characterization of Campylobacter jejuni RacRS reveals roles in the heat shock response, motility, and maintenance of cell length homogeneity. *Journal of Bacteriology*, **194**, 2342–2354.

Arora, S.K., Bangera, M., Lory, S. & Ramphal, R. (2001) A genomic island in Pseudomonas aeruginosa carries the determinants of flagellin glycosylation. *Proceedings of the National*

Academy of Sciences of the United States of America, **98**, 9342–9347.

Arora, S.K., Neely, A.N., Blair, B., Lory, S. & Ramphal, R. (2005) Role of motility and flagellin glycosylation in the pathogenesis of Pseudomonas aeruginosa burn wound infections. *Infection and Immunity*, **73**, 4395–4398.

Artursson, P., Palm, K. & Luthman, K. (2001) Caco-2 monolayers in experimental and theoretical predictions of drug transport. *Advanced Drug Delivery Reviews*, **46**, 27–43.

Ashida, H., Ogawa, M., Kim, M., Mimuro, H. & Sasakawa, C. (2011) Bacteria and host interactions in the gut epithelial barrier. *Nature Chemical Biology*, **8**, 36–45.

Ates, L.S., Dippenaar, A., Ummels, R., Piersma, S.R., Woude, A.D. van der, Kuij, K. van der, *et al.* (2018) Mutations in ppe38 block PE_PGRS secretion and increase virulence of Mycobacterium tuberculosis. *Nature microbiology*, **3**, 181–188.

Atuma, C., Strugala, V., Allen, A. & Holm, L. (2001) The adherent gastrointestinal mucus gel layer: thickness and physical state in vivo. *American Journal of Physiology. Gastrointestinal and Liver Physiology*, **280**, G922-9.

Audie, J.P., Janin, A., Porchet, N., Copin, M.C., Gosselin, B. & Aubert, J.P. (1993) Expression of human mucin genes in respiratory, digestive, and reproductive tracts ascertained by in situ hybridization. *The Journal of Histochemistry and Cytochemistry*, **41**, 1479–1485.

Avraham, R., Haseley, N., Brown, D., Penaranda, C., Jijon, H.B., Trombetta, J.J., *et al.* (2015) Pathogen Cell-to-Cell Variability Drives Heterogeneity in Host Immune Responses. *Cell*, **162**, 1309–1321.

Baba, T., Ara, T., Hasegawa, M., Takai, Y., Okumura, Y., Baba, M., *et al.* (2006) Construction of Escherichia coli K-12 in-frame, single-gene knockout mutants: the Keio collection. *Molecular Systems Biology*, **2**, 2006.0008.

Bachtiar, B.M., Coloe, P.J. & Fry, B.N. (2007) Knockout mutagenesis of the kpsE gene of Campylobacter jejuni 81116 and its involvement in bacterium-host interactions. *FEMS Immunology and Medical Microbiology*, **49**, 149–154.

Backert, S., Boehm, M., Wessler, S. & Tegtmeyer, N. (2013) Transmigration route of Campylobacter jejuni across polarized intestinal epithelial cells: paracellular, transcellular or both? *Cell Communication and Signaling*, **11**, 72.

Backert, S. & Hofreuter, D. (2013) Molecular methods to investigate adhesion, transmigration, invasion and intracellular survival of the foodborne pathogen Campylobacter jejuni. *Journal of Microbiological Methods*, **95**, 8–23.

Backert, S., Bernegger, S., Skórko-Glonek, J. & Wessler, S. (2018) Extracellular HtrA serine proteases: an emerging new strategy in bacterial pathogenesis. *Cellular Microbiology*, **20**, e12845.

Bacon, D.J., Alm, R.A., Burr, D.H., Hu, L., Kopecko, D.J., Ewing, C.P., *et al.* (2000) Involvement of a plasmid in virulence of Campylobacter jejuni 81-176. *Infection and Immunity*, **68**, 4384–4390.

Bacon, D.J., Szymanski, C.M., Burr, D.H., Silver, R.P., Alm, R.A. & Guerry, P. (2001) A phase-variable capsule is involved in virulence of Campylobacter jejuni 81-176. *Molecular Microbiology*, **40**, 769–777.

Bacon, D.J., Alm, R.A., Hu, L., Hickey, T.E., Ewing, C.P., Batchelor, R.A., *et al.* (2002) DNA sequence and mutational analyses of the pVir plasmid of Campylobacter jejuni 81-176. *Infection and Immunity*, **70**, 6242–6250.

Barker, N. (2014) Adult intestinal stem cells: critical drivers of epithelial homeostasis and regeneration. *Nature Reviews. Molecular Cell Biology*, **15**, 19–33.

Barquist, L., Boinett, C.J. & Cain, A.K. (2013) Approaches to querying bacterial genomes with

transposon-insertion sequencing. *RNA Biology*, **10**, 1161–1169.

Barquist, L., Mayho, M., Cummins, C., Cain, A.K., Boinett, C.J., Page, A.J., *et al.* (2016a) The TraDIS toolkit: sequencing and analysis for dense transposon mutant libraries. *Bioinformatics*, **32**, 1109–1111.

Barquist, L., Westermann, A.J. & Vogel, J. (2016b) Molecular phenotyping of infection-associated small non-coding RNAs. *Philosophical Transactions of the Royal Society of London. Series B, Biological Sciences*, **371**.

Barrero-Tobon, A.M. & Hendrixson, D.R. (2012) Identification and analysis of flagellar coexpressed determinants (Feds) of Campylobacter jejuni involved in colonization. *Molecular Microbiology*, **84**, 352–369.

Barrero-Tobon, A.M. & Hendrixson, D.R. (2014) Flagellar biosynthesis exerts temporal regulation of secretion of specific Campylobacter jejuni colonization and virulence determinants. *Molecular Microbiology*, **93**, 957–974.

Barrila, J., Radtke, A.L., Crabbé, A., Sarker, S.F., Herbst-Kralovetz, M.M., Ott, C.M., *et al.* (2010) Organotypic 3D cell culture models: using the rotating wall vessel to study host-pathogen interactions. *Nature Reviews. Microbiology*, **8**, 791–801.

Barrila, J., Yang, J., Crabbé, A., Sarker, S.F., Liu, Y., Ott, C.M., *et al.* (2017) Three-dimensional organotypic co-culture model of intestinal epithelial cells and macrophages to study Salmonella enterica colonization patterns. *NPJ microgravity*, **3**, 10.

Barrila, J., Crabbé, A., Yang, J., Franco, K., Nydam, S.D., Forsyth, R.J., *et al.* (2018) Modeling Host-Pathogen Interactions in the Context of the Microenvironment: 3-D Cell Culture Comes of Age. *Infection and Immunity*.

Bartfeld, S., Bayram, T., Wetering, M. van de, Huch, M., Begthel, H., Kujala, P., *et al.* (2015) In vitro expansion of human gastric epithelial stem cells and their responses to bacterial infection. *Gastroenterology*, **148**, 126–136.e6.

Bartfeld, S. & Clevers, H. (2015) Organoids as model for infectious diseases: culture of human and murine stomach organoids and microinjection of helicobacter pylori. *Journal of Visualized Experiments*.

Basson, M.D. (2003) Paradigms for mechanical signal transduction in the intestinal epithelium. Category: molecular, cell, and developmental biology. *Digestion*, **68**, 217–225.

Batchelor, R.A., Pearson, B.M., Friis, L.M., Guerry, P. & Wells, J.M. (2004) Nucleotide sequences and comparison of two large conjugative plasmids from different Campylobacter species. *Microbiology*, **150**, 3507–3517.

Bayliss, C.D., Bidmos, F.A., Anjum, A., Manchev, V.T., Richards, R.L., Grossier, J.-P., *et al.* (2012) Phase variable genes of Campylobacter jejuni exhibit high mutation rates and specific mutational patterns but mutability is not the major determinant of population structure during host colonization. *Nucleic Acids Research*, **40**, 5876–5889.

Beeby, M., Ribardo, D.A., Brennan, C.A., Ruby, E.G., Jensen, G.J. & Hendrixson, D.R. (2016) Diverse high-torque bacterial flagellar motors assemble wider stator rings using a conserved protein scaffold. *Proceedings of the National Academy of Sciences of the United States of America*, **113**.

Beery, J.T., Hugdahl, M.B. & Doyle, M.P. (1988) Colonization of gastrointestinal tracts of chicks by Campylobacter jejuni. *Applied and Environmental Microbiology*, **54**, 2365–2370.

Behrens, I., Stenberg, P., Artursson, P. & Kissel, T. (2001) Transport of lipophilic drug molecules in a new mucus-secreting cell culture model based on HT29-MTX cells. *Pharmaceutical Research*, **18**, 1138–1145.

Beltinger, J., Buono, J. del, Skelly, M.M., Thornley, J., Spiller, R.C., Stack, W.A., *et al.* (2008)

Disruption of colonic barrier function and induction of mediator release by strains of Campylobacter jejuni that invade epithelial cells. *World Journal of Gastroenterology*, **14**, 7345–7352.

Benjamini, Y. & Hochberg, Y. (1995) Controlling the false discovery rate: a practical and powerful approach to multiple testing. *Journal of the royal statistical society. Series B …*.

Bereswill, S., Fischer, A., Plickert, R., Haag, L.-M., Otto, B., Kühl, A.A., *et al.* (2011) Novel murine infection models provide deep insights into the "ménage à trois" of Campylobacter jejuni, microbiota and host innate immunity. *Plos One*, **6**, e20953.

Bergmann, S. & Steinert, M. (2015) From Single Cells to Engineered and Explanted Tissues: New Perspectives in Bacterial Infection Biology. *International review of cell and molecular biology*, **319**, 1–44.

Birkness, K.A., Swisher, B.L., White, E.H., Long, E.G., Ewing, E.P. & Quinn, F.D. (1995) A tissue culture bilayer model to study the passage of Neisseria meningitidis. *Infection and Immunity*, **63**, 402–409.

Bischoff, S.C., Barbara, G., Buurman, W., Ockhuizen, T., Schulzke, J.-D., Serino, M., *et al.* (2014) Intestinal permeability--a new target for disease prevention and therapy. *BMC Gastroenterology*, **14**, 189.

Biswas, D., Itoh, K. & Sasakawa, C. (2003) Role of microfilaments and microtubules in the invasion of INT-407 cells by Campylobacter jejuni. *Microbiology and Immunology*, **47**, 469–473.

Boccellato, F., Woelffling, S., Imai-Matsushima, A., Sanchez, G., Goosmann, C., Schmid, M., *et al.* (2018) Polarised epithelial monolayers of the gastric mucosa reveal insights into mucosal homeostasis and defence against infection. *Gut*.

Boehm, M., Krause-Gruszczynska, M., Rohde, M., Tegtmeyer, N., Takahashi, S., Oyarzabal, O.A., *et al.* (2011) Major host factors involved in epithelial cell invasion of Campylobacter jejuni: role of fibronectin, integrin beta1, FAK, Tiam-1, and DOCK180 in activating Rho GTPase Rac1. *Frontiers in cellular and infection microbiology*, **1**, 17.

Boehm, M., Hoy, B., Rohde, M., Tegtmeyer, N., Bæk, K.T., Oyarzabal, O.A., *et al.* (2012) Rapid paracellular transmigration of Campylobacter jejuni across polarized epithelial cells without affecting TER: role of proteolytic-active HtrA cleaving E-cadherin but not fibronectin. *Gut Pathogens*, **4**, 3.

Boehm, M., Lind, J., Backert, S. & Tegtmeyer, N. (2015) Campylobacter jejuni serine protease HtrA plays an important role in heat tolerance, oxygen resistance, host cell adhesion, invasion, and transmigration. *European journal of microbiology & immunology*, **5**, 68–80.

Boll, J.M. & Hendrixson, D.R. (2013) A regulatory checkpoint during flagellar biogenesis in Campylobacter jejuni initiates signal transduction to activate transcription of flagellar genes. *mBio*, **4**, e00432-13.

Boneca, I.G., Ecobichon, C., Chaput, C., Mathieu, A., Guadagnini, S., Prévost, M.-C., *et al.* (2008) Development of inducible systems to engineer conditional mutants of essential genes of Helicobacter pylori. *Applied and Environmental Microbiology*, **74**, 2095–2102.

Bonsor, D.A., Pham, K.T., Beadenkopf, R., Diederichs, K., Haas, R., Beckett, D., *et al.* (2015) Integrin engagement by the helical RGD motif of the Helicobacter pylori CagL protein is regulated by pH-induced displacement of a neighboring helix. *The Journal of Biological Chemistry*, **290**, 12929–12940.

Borén, T., Falk, P., Roth, K.A., Larson, G. & Normark, S. (1993) Attachment of Helicobacter pylori to human gastric epithelium mediated by blood group antigens. *Science*, **262**, 1892–1895.

Bouckaert, J., Berglund, J., Schembri, M., De Genst, E., Cools, L., Wuhrer, M., *et al.* (2005)

Receptor binding studies disclose a novel class of high-affinity inhibitors of the Escherichia coli FimH adhesin. *Molecular Microbiology*, **55**, 441–455.

Bouwman, L.I., Niewold, P. & Putten, J.P.M. van. (2013) Basolateral invasion and trafficking of Campylobacter jejuni in polarized epithelial cells. *Plos One*, **8**, e54759.

Brás, A.M., Chatterjee, S., Wren, B.W., Newell, D.G. & Ketley, J.M. (1999) A novel Campylobacter jejuni two-component regulatory system important for temperature-dependent growth and colonization. *Journal of Bacteriology*, **181**, 3298–3302.

Brás, A.M. & Ketley, J.M. (1999) Transcellular translocation of Campylobacter jejuni across human polarised epithelial monolayers. *FEMS Microbiology Letters*, **179**, 209–215.

Brede, C., Friedrich, M., Jordán-Garrote, A.-L., Riedel, S.S., Bäuerlein, C.A., Heinze, K.G., *et al.* (2012) Mapping immune processes in intact tissues at cellular resolution. *The Journal of Clinical Investigation*, **122**, 4439–4446.

Breemen, R.B. van & Li, Y. (2005) Caco-2 cell permeability assays to measure drug absorption. *Expert Opinion on Drug Metabolism & Toxicology*, **1**, 175–185.

Brøndsted, L., Andersen, M.T., Parker, M., Jørgensen, K. & Ingmer, H. (2005) The HtrA protease of Campylobacter jejuni is required for heat and oxygen tolerance and for optimal interaction with human epithelial cells. *Applied and Environmental Microbiology*, **71**, 3205–3212.

Browning, T.H. & Trier, J.S. (1969) Organ culture of mucosal biopsies of human small intestine. *The Journal of Clinical Investigation*, **48**, 1423–1432.

Bryant, D.M. & Mostov, K.E. (2008) From cells to organs: building polarized tissue. *Nature Reviews. Molecular Cell Biology*, **9**, 887–901.

Buelow, D.R., Christensen, J.E., Neal-McKinney, J.M. & Konkel, M.E. (2011) Campylobacter jejuni survival within human epithelial cells is enhanced by the secreted protein CiaI. *Molecular Microbiology*, **80**, 1296–1312.

Bullen, T.F., Forrest, S., Campbell, F., Dodson, A.R., Hershman, M.J., Pritchard, D.M., *et al.* (2006) Characterization of epithelial cell shedding from human small intestine. *Laboratory Investigation*, **86**, 1052–1063.

Burkitt, M.D., Duckworth, C.A., Williams, J.M. & Pritchard, D.M. (2017) Helicobacter pylori-induced gastric pathology: insights from in vivo and ex vivo models. *Disease Models & Mechanisms*, **10**, 89–104.

Burnham, P.M. & Hendrixson, D.R. (2018) Campylobacter jejuni: collective components promoting a successful enteric lifestyle. *Nature Reviews. Microbiology*, **16**, 551–565.

Butcher, J. & Stintzi, A. (2017) Campylobacter jejuni.

Cameron, A., Frirdich, E., Huynh, S., Parker, C.T. & Gaynor, E.C. (2012) Hyperosmotic stress response of Campylobacter jejuni. *Journal of Bacteriology*, **194**, 6116–6130.

Cameron, A. & Gaynor, E.C. (2014) Hygromycin B and apramycin antibiotic resistance cassettes for use in Campylobacter jejuni. *Plos One*, **9**, e95084.

Carneiro, B.A., Fujii, J., Brito, G.A.C., Alcantara, C., Oriá, R.B., Lima, A.A.M., *et al.* (2006) Caspase and bid involvement in Clostridium difficile toxin A-induced apoptosis and modulation of toxin A effects by glutamine and alanyl-glutamine in vivo and in vitro. *Infection and Immunity*, **74**, 81–87.

Carterson, A.J., Höner zu Bentrup, K., Ott, C.M., Clarke, M.S., Pierson, D.L., Vanderburg, C.R., *et al.* (2005) A549 lung epithelial cells grown as three-dimensional aggregates: alternative tissue culture model for Pseudomonas aeruginosa pathogenesis. *Infection and Immunity*, **73**, 1129–1140.

Carvalho, H.M., Teel, L.D., Goping, G. & O'Brien, A.D. (2005) A three-dimensional tissue

culture model for the study of attach and efface lesion formation by enteropathogenic and enterohaemorrhagic Escherichia coli. *Cellular Microbiology*, **7**, 1771–1781.

Carver, T., Harris, S.R., Berriman, M., Parkhill, J. & McQuillan, J.A. (2012) Artemis: an integrated platform for visualization and analysis of high-throughput sequence-based experimental data. *Bioinformatics*, **28**, 464–469.

Chandrashekhar, K., Kassem, I.I. & Rajashekara, G. (2017) Campylobacter jejuni transducer like proteins: Chemotaxis and Beyond. *Gut microbes*, **8**, 0.

Chang, C. & Miller, J.F. (2006) Campylobacter jejuni colonization of mice with limited enteric flora. *Infection and Immunity*, **74**, 5261–5271.

Chang, W.-L., Yeh, Y.-C. & Sheu, B.-S. (2018) The impacts of H. pylori virulence factors on the development of gastroduodenal diseases. *Journal of Biomedical Science*, **25**, 68.

Chao, M.C., Abel, S., Davis, B.M. & Waldor, M.K. (2016) The design and analysis of transposon insertion sequencing experiments. *Nature Reviews. Microbiology*, **14**, 119–128.

Chen, H.-C. & Hu, Y.-C. (2006) Bioreactors for tissue engineering. *Biotechnology Letters*, **28**, 1415–1423.

Chen, M.L., Ge, Z., Fox, J.G. & Schauer, D.B. (2006) Disruption of tight junctions and induction of proinflammatory cytokine responses in colonic epithelial cells by Campylobacter jejuni. *Infection and Immunity*, **74**, 6581–6589.

Chen, Y., Lin, Y., Davis, K.M., Wang, Q., Rnjak-Kovacina, J., Li, C., *et al.* (2015) Robust bioengineered 3D functional human intestinal epithelium. *Scientific reports*, **5**, 13708.

Chen, Y., Zhou, W., Roh, T., Estes, M.K. & Kaplan, D.L. (2017) In vitro enteroid-derived three-dimensional tissue model of human small intestinal epithelium with innate immune responses. *Plos One*, **12**, e0187880.

Chojnacki, J., Staudt, T., Glass, B., Bingen, P., Engelhardt, J., Anders, M., *et al.* (2012) Maturation-dependent HIV-1 surface protein redistribution revealed by fluorescence nanoscopy. *Science*, **338**, 524–528.

Christensen, J.E., Pacheco, S.A. & Konkel, M.E. (2009) Identification of a Campylobacter jejuni-secreted protein required for maximal invasion of host cells. *Molecular Microbiology*, **73**, 650–662.

Clark, C.G., Price, L., Ahmed, R., Woodward, D.L., Melito, P.L., Rodgers, F.G., *et al.* (2003) Characterization of waterborne outbreak-associated Campylobacter jejuni, Walkerton, Ontario. *Emerging Infectious Diseases*, **9**, 1232–1241.

Clark, M.A., Jepson, M.A., Simmons, N.L. & Hirst, B.H. (1994) Preferential interaction of Salmonella typhimurium with mouse Peyer's patch M cells. *Research in Microbiology*, **145**, 543–552.

Clark, M.A., Hirst, B.H. & Jepson, M.A. (1998) M-cell surface beta1 integrin expression and invasin-mediated targeting of Yersinia pseudotuberculosis to mouse Peyer's patch M cells. *Infection and Immunity*, **66**, 1237–1243.

Clevers, H. (2016) Modeling Development and Disease with Organoids. *Cell*, **165**, 1586–1597.

Co, J.Y., Margalef-Català, M., Li, X., Mah, A.T., Kuo, C.J., Monack, D.M., *et al.* (2019) Controlling Epithelial Polarity: A Human Enteroid Model for Host-Pathogen Interactions. *Cell reports*, **26**, 2509–2520.e4.

Cohn, M.T., Ingmer, H., Mulholland, F., Jørgensen, K., Wells, J.M. & Brøndsted, L. (2007) Contribution of conserved ATP-dependent proteases of Campylobacter jejuni to stress tolerance and virulence. *Applied and Environmental Microbiology*, **73**, 7803–7813.

Corcionivoschi, N., Clyne, M., Lyons, A., Elmi, A., Gundogdu, O., Wren, B.W., *et al.* (2009)

Campylobacter jejuni cocultured with epithelial cells reduces surface capsular polysaccharide expression. *Infection and Immunity*, **77**, 1959–1967.

Corcoran, C.P., Podkaminski, D., Papenfort, K., Urban, J.H., Hinton, J.C.D. & Vogel, J. (2012) Superfolder GFP reporters validate diverse new mRNA targets of the classic porin regulator, MicF RNA. *Molecular Microbiology*, **84**, 428–445.

Costello, C.M., Hongpeng, J., Shaffiey, S., Yu, J., Jain, N.K., Hackam, D., *et al.* (2014) Synthetic small intestinal scaffolds for improved studies of intestinal differentiation. *Biotechnology and Bioengineering*, **111**, 1222–1232.

Cover, T.L. & Blaser, M.J. (2009) Helicobacter pylori in health and disease. *Gastroenterology*, **136**, 1863–1873.

Crabbé, A., Ledesma, M.A. & Nickerson, C.A. (2014) Mimicking the host and its microenvironment in vitro for studying mucosal infections by Pseudomonas aeruginosa. *Pathogens and disease*, **71**, 1–19.

Crofts, A.A., Giovanetti, S.M., Rubin, E.J., Poly, F.M., Gutiérrez, R.L., Talaat, K.R., *et al.* (2018a) Enterotoxigenic E. coli virulence gene regulation in human infections. *Proceedings of the National Academy of Sciences of the United States of America*.

Crofts, A.A., Poly, F.M., Ewing, C.P., Kuroiwa, J.M., Rimmer, J.E., Harro, C., *et al.* (2018b) Campylobacter jejuni transcriptional and genetic adaptation during human infection. *Nature microbiology*, **3**, 494–502.

Cukierman, E., Pankov, R., Stevens, D.R. & Yamada, K.M. (2001) Taking cell-matrix adhesions to the third dimension. *Science*, **294**, 1708–1712.

D'Amour, K.A., Agulnick, A.D., Eliazer, S., Kelly, O.G., Kroon, E. & Baetge, E.E. (2005) Efficient differentiation of human embryonic stem cells to definitive endoderm. *Nature Biotechnology*, **23**, 1534–1541.

Dandekar, A.A., Chugani, S. & Greenberg, E.P. (2012) Bacterial quorum sensing and metabolic incentives to cooperate. *Science*, **338**, 264–266.

Darwich, A.S., Aslam, U., Ashcroft, D.M. & Rostami-Hodjegan, A. (2014) Assessing the Turnover of Intestinal Epithelia in Pre-clinical Animal Species and Human. *Drug Metabolism and Disposition: the Biological Fate of Chemicals*.

Dasti, J.I., Tareen, A.M., Lugert, R., Zautner, A.E. & Gross, U. (2010) Campylobacter jejuni: a brief overview on pathogenicity-associated factors and disease-mediating mechanisms. *International Journal of Medical Microbiology*, **300**, 205–211.

Day, C.J., King, R.M., Shewell, L.K., Tram, G., Najnin, T., Hartley-Tassell, L.E., *et al.* (2016) A direct-sensing galactose chemoreceptor recently evolved in invasive strains of Campylobacter jejuni. *Nature Communications*, **7**, 13206.

De Bolós, C., Garrido, M. & Real, F.X. (1995) MUC6 apomucin shows a distinct normal tissue distribution that correlates with Lewis antigen expression in the human stomach. *Gastroenterology*, **109**, 723–734.

De Gregorio, V., Imparato, G., Urciuolo, F. & Netti, P.A. (2018) 3D stromal tissue equivalent affects intestinal epithelium morphogenesis in vitro. *Biotechnology and Bioengineering*, **115**, 1062–1075.

DeCicco RePass, M.A., Chen, Y., Lin, Y., Zhou, W., Kaplan, D.L. & Ward, H.D. (2017) Novel Bioengineered Three-Dimensional Human Intestinal Model for Long-Term Infection of Cryptosporidium parvum. *Infection and Immunity*, **85**.

Delcommenne, M. & Streuli, C.H. (1995) Control of integrin expression by extracellular matrix. *The Journal of Biological Chemistry*, **270**, 26794–26801.

Delie, F. & Rubas, W. (1997) A human colonic cell line sharing similarities with enterocytes

as a model to examine oral absorption: advantages and limitations of the Caco-2 model. *Critical reviews in therapeutic drug carrier systems*, **14**, 221–286.

Devon, R.S., Porteous, D.J. & Brookes, A.J. (1995) Splinkerettes--improved vectorettes for greater efficiency in PCR walking. *Nucleic Acids Research*, **23**, 1644–1645.

Dorrell, N., Mangan, J.A., Laing, K.G., Hinds, J., Linton, D., Al-Ghusein, H., *et al.* (2001) Whole genome comparison of Campylobacter jejuni human isolates using a low-cost microarray reveals extensive genetic diversity. *Genome Research*, **11**, 1706–1715.

Dosh, R.H., Jordan-Mahy, N., Sammon, C. & Le Maitre, C. (2017) Tissue engineering laboratory models of the small intestine. *Tissue Engineering. Part B, Reviews*.

Drummond, C.G., Bolock, A.M., Ma, C., Luke, C.J., Good, M. & Coyne, C.B. (2017) Enteroviruses infect human enteroids and induce antiviral signaling in a cell lineage-specific manner. *Proceedings of the National Academy of Sciences of the United States of America*, **114**, 1672–1677.

Duan, Y., Gotoh, N., Yan, Q., Du, Z., Weinstein, A.M., Wang, T., *et al.* (2008) Shear-induced reorganization of renal proximal tubule cell actin cytoskeleton and apical junctional complexes. *Proceedings of the National Academy of Sciences of the United States of America*, **105**, 11418–11423.

Dugar, G., Herbig, A., Förstner, K.U., Heidrich, N., Reinhardt, R., Nieselt, K., *et al.* (2013) High-resolution transcriptome maps reveal strain-specific regulatory features of multiple Campylobacter jejuni isolates. *PLoS Genetics*, **9**, e1003495.

Dugar, G., Svensson, S.L., Bischler, T., Wäldchen, S., Reinhardt, R., Sauer, M., *et al.* (2016) The CsrA-FliW network controls polar localization of the dual-function flagellin mRNA in Campylobacter jejuni. *Nature Communications*, **7**, 11667.

Dugar, G., Leenay, R.T., Eisenbart, S.K., Bischler, T., Aul, B.U., Beisel, C.L., *et al.* (2018) CRISPR RNA-Dependent Binding and Cleavage of Endogenous RNAs by the Campylobacter jejuni Cas9. *Molecular Cell*, **69**, 893–905.e7.

Dutta, D. & Clevers, H. (2017) Organoid culture systems to study host-pathogen interactions. *Current Opinion in Immunology*, **48**, 15–22.

Dwivedi, R., Nothaft, H., Garber, J., Xin Kin, L., Stahl, M., Flint, A., *et al.* (2016) L-fucose influences chemotaxis and biofilm formation in Campylobacter jejuni. *Molecular Microbiology*, **101**, 575–589.

Elliott, K.T. & Dirita, V.J. (2008) Characterization of CetA and CetB, a bipartite energy taxis system in Campylobacter jejuni. *Molecular Microbiology*, **69**, 1091–1103.

Engevik, M.A., Yacyshyn, M.B., Engevik, K.A., Wang, J., Darien, B., Hassett, D.J., *et al.* (2015) Human Clostridium difficile infection: altered mucus production and composition. *American Journal of Physiology. Gastrointestinal and Liver Physiology*, **308**, G510-24.

Ermund, A., Schütte, A., Johansson, M.E.V., Gustafsson, J.K. & Hansson, G.C. (2013) Studies of mucus in mouse stomach, small intestine, and colon. I. Gastrointestinal mucus layers have different properties depending on location as well as over the Peyer's patches. *American Journal of Physiology. Gastrointestinal and Liver Physiology*, **305**, G341-7.

Ettayebi, K., Crawford, S.E., Murakami, K., Broughman, J.R., Karandikar, U., Tenge, V.R., *et al.* (2016) Replication of human noroviruses in stem cell-derived human enteroids. *Science*, **353**, 1387–1393.

Everest, P.H., Goossens, H., Butzler, J.P., Lloyd, D., Knutton, S., Ketley, J.M., *et al.* (1992) Differentiated Caco-2 cells as a model for enteric invasion by Campylobacter jejuni and C. coli. *Journal of Medical Microbiology*, **37**, 319–325.

Ewaschuk, J.B., Murdoch, G.K., Johnson, I.R., Madsen, K.L. & Field, C.J. (2011) Glutamine

supplementation improves intestinal barrier function in a weaned piglet model of Escherichia coli infection. *The British Journal of Nutrition*, **106**, 870–877.

Faderl, M., Noti, M., Corazza, N. & Mueller, C. (2015) Keeping bugs in check: The mucus layer as a critical component in maintaining intestinal homeostasis. *IUBMB Life*, **67**, 275–285.

Fakruddin, M., Rahaman, M., Ahmed, M. & Hoque, M. (2014) Stress tolerant virulent strains of Cronobacter sakazakii from food. *Biological research*, **47**, 63.

Fasano, A., Baudry, B., Pumplin, D.W., Wasserman, S.S., Tall, B.D., Ketley, J.M., *et al.* (1991) Vibrio cholerae produces a second enterotoxin, which affects intestinal tight junctions. *Proceedings of the National Academy of Sciences of the United States of America*, **88**, 5242–5246.

Fatehullah, A., Tan, S.H. & Barker, N. (2016) Organoids as an in vitro model of human development and disease. *Nature Cell Biology*, **18**, 246–254.

Ferrell, N., Cheng, J., Miao, S., Roy, S. & Fissell, W.H. (2018) Orbital shear stress regulates differentiation and barrier function of primary renal tubular epithelial cells. *ASAIO Journal*, **64**, 766–772.

Ferrero, R.L. & Lee, A. (1988) Motility of Campylobacter jejuni in a viscous environment: comparison with conventional rod-shaped bacteria. *Journal of general microbiology*, **134**, 53–59.

Fields, J.A. & Thompson, S.A. (2008) Campylobacter jejuni CsrA mediates oxidative stress responses, biofilm formation, and host cell invasion. *Journal of Bacteriology*, **190**, 3411–3416.

Fields, J.A., Li, J., Gulbronson, C.J., Hendrixson, D.R. & Thompson, S.A. (2016) Campylobacter jejuni CsrA Regulates Metabolic and Virulence Associated Proteins and Is Necessary for Mouse Colonization. *Plos One*, **11**, e0156932.

Finkbeiner, S.R., Freeman, J.J., Wieck, M.M., El-Nachef, W., Altheim, C.H., Tsai, Y.-H., *et al.* (2015) Generation of tissue-engineered small intestine using embryonic stem cell-derived human intestinal organoids. *Biology open*, **4**, 1462–1472.

Finn, R.D., Attwood, T.K., Babbitt, P.C., Bateman, A., Bork, P., Bridge, A.J., *et al.* (2017) InterPro in 2017-beyond protein family and domain annotations. *Nucleic Acids Research*, **45**, D190–D199.

Fischer, A.H., Jacobson, K.A., Rose, J. & Zeller, R. (2008) Hematoxylin and eosin staining of tissue and cell sections. *CSH protocols*, **2008**, pdb.prot4986.

Flanagan, R.C., Neal-McKinney, J.M., Dhillon, A.S., Miller, W.G. & Konkel, M.E. (2009) Examination of Campylobacter jejuni putative adhesins leads to the identification of a new protein, designated FlpA, required for chicken colonization. *Infection and Immunity*, **77**, 2399–2407.

Floren, M., Bonani, W., Dharmarajan, A., Motta, A., Migliaresi, C. & Tan, W. (2015) Human mesenchymal stem cells cultured on silk hydrogels with variable stiffness and growth factor differentiate into mature smooth muscle cell phenotype. *Acta Biomaterialia*, **31**, 156–166.

Förstner, K.U., Vogel, J. & Sharma, C.M. (2014) READemption-a tool for the computational analysis of deep-sequencing-based transcriptome data. *Bioinformatics*, **30**, 3421–3423.

Forbester, J.L., Goulding, D., Vallier, L., Hannan, N., Hale, C., Pickard, D., *et al.* (2015) Interaction of Salmonella enterica Serovar Typhimurium with Intestinal Organoids Derived from Human Induced Pluripotent Stem Cells. *Infection and Immunity*, **83**, 2926–2934.

Fox, J.G., Rogers, A.B., Whary, M.T., Ge, Z., Taylor, N.S., Xu, S., *et al.* (2004) Gastroenteritis in NF-kappaB-deficient mice is produced with wild-type Camplyobacter jejuni but not with C. jejuni lacking cytolethal distending toxin despite persistent colonization with both strains.

Infection and Immunity, **72**, 1116–1125.

Frank, S.A. (1996) Models of parasite virulence. *The Quarterly Review of Biology*, **71**, 37–78.

Friis, C., Wassenaar, T.M., Javed, M.A., Snipen, L., Lagesen, K., Hallin, P.F., *et al.* (2010) Genomic characterization of Campylobacter jejuni strain M1. *Plos One*, **5**, e12253.

Frirdich, E., Biboy, J., Adams, C., Lee, J., Ellermeier, J., Gielda, L.D., *et al.* (2012) Peptidoglycan-modifying enzyme Pgp1 is required for helical cell shape and pathogenicity traits in Campylobacter jejuni. *PLoS Pathogens*, **8**, e1002602.

Frirdich, E., Vermeulen, J., Biboy, J., Soares, F., Taveirne, M.E., Johnson, J.G., *et al.* (2014) Peptidoglycan LD-carboxypeptidase Pgp2 influences Campylobacter jejuni helical cell shape and pathogenic properties and provides the substrate for the DL-carboxypeptidase Pgp1. *The Journal of Biological Chemistry*, **289**, 8007–8018.

Frost, A.J., Bland, A.P. & Wallis, T.S. (1997) The early dynamic response of the calf ileal epithelium to Salmonella typhimurium. *Veterinary Pathology*, **34**, 369–386.

Fuchs, T.M., Eisenreich, W., Heesemann, J. & Goebel, W. (2012) Metabolic adaptation of human pathogenic and related nonpathogenic bacteria to extra- and intracellular habitats. *FEMS Microbiology Reviews*, **36**, 435–462.

Gagnon, M., Zihler Berner, A., Chervet, N., Chassard, C. & Lacroix, C. (2013) Comparison of the Caco-2, HT-29 and the mucus-secreting HT29-MTX intestinal cell models to investigate Salmonella adhesion and invasion. *Journal of Microbiological Methods*, **94**, 274–279.

Gao, B., Lara-Tejero, M., Lefebre, M., Goodman, A.L. & Galán, J.E. (2014) Novel components of the flagellar system in epsilonproteobacteria. *mBio*, **5**, e01349-14.

Gao, B., Vorwerk, H., Huber, C., Lara-Tejero, M., Mohr, J., Goodman, A.L., *et al.* (2017) Metabolic and fitness determinants for in vitro growth and intestinal colonization of the bacterial pathogen Campylobacter jejuni. *PLoS Biology*, **15**, e2001390.

Gao, L. & Lipowsky, H.H. (2010) Composition of the endothelial glycocalyx and its relation to its thickness and diffusion of small solutes. *Microvascular Research*, **80**, 394–401.

García Rodríguez, L.A., Ruigómez, A. & Panés, J. (2006) Acute gastroenteritis is followed by an increased risk of inflammatory bowel disease. *Gastroenterology*, **130**, 1588–1594.

Garrity, G.M. (2005) Bergey's Manual of Systematic Bacteriology: Vol. 2-The Proteobacteria. Part C-The Alpha-, Beta-, Delta-, and Epsilonproteobacteria.

Gayer, C.P. & Basson, M.D. (2009) The effects of mechanical forces on intestinal physiology and pathology. *Cellular Signalling*, **21**, 1237–1244.

Gaynor, E.C., Ghori, N. & Falkow, S. (2001) Bile-induced "pili" in Campylobacter jejuni are bacteria-independent artifacts of the culture medium. *Molecular Microbiology*, **39**, 1546–1549.

Gaynor, E.C., Cawthraw, S., Manning, G., MacKichan, J.K., Falkow, S. & Newell, D.G. (2004) The genome-sequenced variant of Campylobacter jejuni NCTC 11168 and the original clonal clinical isolate differ markedly in colonization, gene expression, and virulence-associated phenotypes. *Journal of Bacteriology*, **186**, 503–517.

Gendler, S.J. (2001) MUC1, the renaissance molecule. *Journal of mammary gland biology and neoplasia*, **6**, 339–353.

Gerbe, F., Legraverend, C. & Jay, P. (2012) The intestinal epithelium tuft cells: specification and function. *Cellular and Molecular Life Sciences*, **69**, 2907–2917.

Gerdes, S.Y., Scholle, M.D., Campbell, J.W., Balázsi, G., Ravasz, E., Daugherty, M.D., *et al.* (2003) Experimental determination and system level analysis of essential genes in Escherichia coli MG1655. *Journal of Bacteriology*, **185**, 5673–5684.

Giel, J.L., Rodionov, D., Liu, M., Blattner, F.R. & Kiley, P.J. (2006) IscR-dependent gene expression links iron-sulphur cluster assembly to the control of O2-regulated genes in Escherichia coli. *Molecular Microbiology*, **60**, 1058–1075.

Gilbreath, J.J., Cody, W.L., Merrell, D.S. & Hendrixson, D.R. (2011) Change is good: variations in common biological mechanisms in the epsilonproteobacterial genera Campylobacter and Helicobacter. *Microbiology and Molecular Biology Reviews*, **75**, 84–132.

Göke, M., Kanai, M. & Podolsky, D.K. (1998) Intestinal fibroblasts regulate intestinal epithelial cell proliferation via hepatocyte growth factor. *The American Journal of Physiology*, **274**, G809-18.

Golden, N.J. & Acheson, D.W.K. (2002) Identification of motility and autoagglutination Campylobacter jejuni mutants by random transposon mutagenesis. *Infection and Immunity*, **70**, 1761–1771.

Goncheva, M.I., Flannagan, R.S., Sterling, B.E., Laakso, H.A., Friedrich, N.C., Kaiser, J.C., *et al.* (2019) Stress-induced inactivation of the Staphylococcus aureus purine biosynthesis repressor leads to hypervirulence. *Nature Communications*, **10**, 775.

Goon, S., Kelly, J.F., Logan, S.M., Ewing, C.P. & Guerry, P. (2003) Pseudaminic acid, the major modification on Campylobacter flagellin, is synthesized via the Cj1293 gene. *Molecular Microbiology*, **50**, 659–671.

Goon, S., Ewing, C.P., Lorenzo, M., Pattarini, D., Majam, G. & Guerry, P. (2006) A sigma28-regulated nonflagella gene contributes to virulence of Campylobacter jejuni 81-176. *Infection and Immunity*, **74**, 769–772.

Gopinathan, J. & Noh, I. (2018) Recent trends in bioinks for 3D printing. *Biomaterials research*, **22**, 11.

Gouyer, V., Wiede, A., Buisine, M.P., Dekeyser, S., Moreau, O., Lesuffleur, T., *et al.* (2001) Specific secretion of gel-forming mucins and TFF peptides in HT-29 cells of mucin-secreting phenotype. *Biochimica et Biophysica Acta*, **1539**, 71–84.

Grant, A.J., Woodward, J. & Maskell, D.J. (2006) Development of an ex vivo organ culture model using human gastro-intestinal tissue and Campylobacter jejuni. *FEMS Microbiology Letters*, **263**, 240–243.

Grant, C.C., Konkel, M.E., Cieplak, W. & Tompkins, L.S. (1993) Role of flagella in adherence, internalization, and translocation of Campylobacter jejuni in nonpolarized and polarized epithelial cell cultures. *Infection and Immunity*, **61**, 1764–1771.

Griffith, L.G. & Swartz, M.A. (2006) Capturing complex 3D tissue physiology in vitro. *Nature Reviews. Molecular Cell Biology*, **7**, 211–224.

Gripenland, J., Netterling, S., Loh, E., Tiensuu, T., Toledo-Arana, A. & Johansson, J. (2010) RNAs: regulators of bacterial virulence. *Nature Reviews. Microbiology*, **8**, 857–866.

Grotz, M.R., Deitch, E.A., Ding, J., Xu, D., Huang, Q. & Regel, G. (1999) Intestinal cytokine response after gut ischemia: role of gut barrier failure. *Annals of Surgery*, **229**, 478–486.

Guerry, P., Alm, R.A., Power, M.E., Logan, S.M. & Trust, T.J. (1991) Role of two flagellin genes in Campylobacter motility. *Journal of Bacteriology*, **173**, 4757–4764.

Guerry, P., Ewing, C.P., Hickey, T.E., Prendergast, M.M. & Moran, A.P. (2000) Sialylation of lipooligosaccharide cores affects immunogenicity and serum resistance of Campylobacter jejuni. *Infection and Immunity*, **68**, 6656–6662.

Guerry, P., Szymanski, C.M., Prendergast, M.M., Hickey, T.E., Ewing, C.P., Pattarini, D.L., *et al.* (2002) Phase variation of Campylobacter jejuni 81-176 lipooligosaccharide affects ganglioside mimicry and invasiveness in vitro. *Infection and Immunity*, **70**, 787–793.

Guerry, P. (2007) Campylobacter flagella: not just for motility. *Trends in Microbiology*, **15**,

456–461.

Guerry, P., Poly, F., Riddle, M., Maue, A.C., Chen, Y.-H. & Monteiro, M.A. (2012) Campylobacter polysaccharide capsules: virulence and vaccines. *Frontiers in cellular and infection microbiology*, **2**, 7.

Gundogdu, O., Bentley, S.D., Holden, M.T., Parkhill, J., Dorrell, N. & Wren, B.W. (2007) Re-annotation and re-analysis of the Campylobacter jejuni NCTC11168 genome sequence. *BMC Genomics*, **8**, 162.

Gundogdu, O., Silva, D.T. da, Mohammad, B., Elmi, A., Wren, B.W., Vliet, A.H.M. van, *et al.* (2016) The Campylobacter jejuni Oxidative Stress Regulator RrpB Is Associated with a Genomic Hypervariable Region and Altered Oxidative Stress Resistance. *Frontiers in microbiology*, **7**, 2117.

Guo, P., Weinstein, A.M. & Weinbaum, S. (2000) A hydrodynamic mechanosensory hypothesis for brush border microvilli. *American Journal of Physiology. Renal Physiology*, **279**, F698-712.

Guo, B., Wang, Y., Shi, F., Barton, Y.-W., Plummer, P., Reynolds, D.L., *et al.* (2008) CmeR functions as a pleiotropic regulator and is required for optimal colonization of Campylobacter jejuni in vivo. *Journal of Bacteriology*, **190**, 1879–1890.

Gustafsson, J.K., Sjövall, H. & Hansson, G.C. (2012) Ex vivo measurements of mucus secretion by colon explants. *Methods in Molecular Biology*, **842**, 237–243.

Haag, L.M., Fischer, A., Otto, B., Grundmann, U., Kühl, A.A., Göbel, U.B., *et al.* (2012a) Campylobacter jejuni infection of infant mice: acute enterocolitis is followed by asymptomatic intestinal and extra-intestinal immune responses. *European journal of microbiology & immunology*, **2**, 2–11.

Haag, L.-M., Fischer, A., Otto, B., Plickert, R., Kühl, A.A., Göbel, U.B., *et al.* (2012b) Campylobacter jejuni induces acute enterocolitis in gnotobiotic IL-10-/- mice via Toll-like-receptor-2 and -4 signaling. *Plos One*, **7**, e40761.

Haines, S., Arnaud-Barbe, N., Poncet, D., Reverchon, S., Wawrzyniak, J., Nasser, W., *et al.* (2015) IscR regulates synthesis of CFA/I fimbriae in response to iron starvation in Enterotoxigenic Escherichia coli. *Journal of Bacteriology*.

Hall, S.J., Hitchcock, A., Butler, C.S. & Kelly, D.J. (2008) A Multicopper oxidase (Cj1516) and a CopA homologue (Cj1161) are major components of the copper homeostasis system of Campylobacter jejuni. *Journal of Bacteriology*, **190**, 8075–8085.

Haque, A., Bowe, F., Fitzhenry, R.J., Frankel, G., Thomson, M., Heuschkel, R., *et al.* (2004) Early interactions of Salmonella enterica serovar typhimurium with human small intestinal epithelial explants. *Gut*, **53**, 1424–1430.

Harrer, A., Bücker, R., Boehm, M., Zarzecka, U., Tegtmeyer, N., Sticht, H., *et al.* (2019) Campylobacter jejuni enters gut epithelial cells and impairs intestinal barrier function through cleavage of occludin by serine protease HtrA. *Gut Pathogens*, **11**, 4.

Harris, T.J.C. & Tepass, U. (2010) Adherens junctions: from molecules to morphogenesis. *Nature Reviews. Molecular Cell Biology*, **11**, 502–514.

Hartley-Tassell, L.E., Shewell, L.K., Day, C.J., Wilson, J.C., Sandhu, R., Ketley, J.M., *et al.* (2010) Identification and characterization of the aspartate chemosensory receptor of Campylobacter jejuni. *Molecular Microbiology*, **75**, 710–730.

Harvey, P., Battle, T. & Leach, S. (1999) Different invasion phenotypes of Campylobacter isolates in Caco-2 cell monolayers. *Journal of Medical Microbiology*, **48**, 461–469.

Havelaar, A.H., Kirk, M.D., Torgerson, P.R., Gibb, H.J., Hald, T., Lake, R.J., *et al.* (2015) World health organization global estimates and regional comparisons of the burden of foodborne

disease in 2010. *PLoS Medicine*, **12**, e1001923.

He, Z., Gharaibeh, R.Z., Newsome, R.C., Pope, J.L., Dougherty, M.W., Tomkovich, S., *et al.* (2019) Campylobacter jejuni promotes colorectal tumorigenesis through the action of cytolethal distending toxin. *Gut*, **68**, 289–300.

Heilemann, M., Linde, S. van de, Schüttpelz, M., Kasper, R., Seefeldt, B., Mukherjee, A., *et al.* (2008) Subdiffraction-resolution fluorescence imaging with conventional fluorescent probes. *Angewandte Chemie*, **47**, 6172–6176.

Heimesaat, M.M., Haag, L.-M., Fischer, A., Otto, B., Kühl, A.A., Göbel, U.B., *et al.* (2013) Survey of extra-intestinal immune responses in asymptomatic long-term Campylobacter jejuni-infected mice. *European journal of microbiology & immunology*, **3**, 174–182.

Heimesaat, M.M., Alutis, M., Grundmann, U., Fischer, A., Tegtmeyer, N., Böhm, M., *et al.* (2014) The role of serine protease HtrA in acute ulcerative enterocolitis and extra-intestinal immune responses during Campylobacter jejuni infection of gnotobiotic IL-10 deficient mice. *Frontiers in cellular and infection microbiology*, **4**, 77.

Heimesaat, M.M., Lugert, R., Fischer, A., Alutis, M., Kühl, A.A., Zautner, A.E., *et al.* (2014) Impact of Campylobacter jejuni cj0268c knockout mutation on intestinal colonization, translocation, and induction of immunopathology in gnotobiotic IL-10 deficient mice. *Plos One*, **9**, e90148.

Helander, H.F. & Fändriks, L. (2014) Surface area of the digestive tract - revisited. *Scandinavian Journal of Gastroenterology*, **49**, 681–689.

Hendrixson, D.R., Akerley, B.J. & DiRita, V.J. (2001) Transposon mutagenesis of Campylobacter jejuni identifies a bipartite energy taxis system required for motility. *Molecular Microbiology*, **40**, 214–224.

Hendrixson, D.R. & DiRita, V.J. (2003) Transcription of sigma54-dependent but not sigma28-dependent flagellar genes in Campylobacter jejuni is associated with formation of the flagellar secretory apparatus. *Molecular Microbiology*, **50**, 687–702.

Hendrixson, D.R. & DiRita, V.J. (2004) Identification of Campylobacter jejuni genes involved in commensal colonization of the chick gastrointestinal tract. *Molecular Microbiology*, **52**, 471–484.

Heroven, A.K., Nuss, A.M. & Dersch, P. (2017) RNA-based mechanisms of virulence control in Enterobacteriaceae. *RNA Biology*, **14**, 471–487.

Hicks, S., Candy, D.C. & Phillips, A.D. (1996) Adhesion of enteroaggregative Escherichia coli to pediatric intestinal mucosa in vitro. *Infection and Immunity*, **64**, 4751–4760.

Hidalgo, I.J., Raub, T.J. & Borchardt, R.T. (1989) Characterization of the human colon carcinoma cell line (Caco-2) as a model system for intestinal epithelial permeability. *Gastroenterology*, **96**, 736–749.

Hitchen, P., Brzostek, J., Panico, M., Butler, J.A., Morris, H.R., Dell, A., *et al.* (2010) Modification of the Campylobacter jejuni flagellin glycan by the product of the Cj1295 homopolymeric-tract-containing gene. *Microbiology*, **156**, 1953–1962.

Hjelm, B.E., Berta, A.N., Nickerson, C.A., Arntzen, C.J. & Herbst-Kralovetz, M.M. (2010) Development and characterization of a three-dimensional organotypic human vaginal epithelial cell model. *Biology of Reproduction*, **82**, 617–627.

Hoffmann, S., Otto, C., Kurtz, S., Sharma, C.M., Khaitovich, P., Vogel, J., *et al.* (2009) Fast mapping of short sequences with mismatches, insertions and deletions using index structures. *PLoS Computational Biology*, **5**, e1000502.

Hofreuter, D., Tsai, J., Watson, R.O., Novik, V., Altman, B., Benitez, M., *et al.* (2006) Unique features of a highly pathogenic Campylobacter jejuni strain. *Infection and Immunity*, **74**,

4694–4707.

Hofreuter, D., Novik, V. & Galán, J.E. (2008) Metabolic diversity in Campylobacter jejuni enhances specific tissue colonization. *Cell Host & Microbe*, **4**, 425–433.

Hofreuter, D. (2014) Defining the metabolic requirements for the growth and colonization capacity of Campylobacter jejuni. *Frontiers in cellular and infection microbiology*, **4**, 137.

Holst Sørensen, M.C., Alphen, L.B. van, Fodor, C., Crowley, S.M., Christensen, B.B., Szymanski, C.M., *et al.* (2012) Phase variable expression of capsular polysaccharide modifications allows Campylobacter jejuni to avoid bacteriophage infection in chickens. *Frontiers in cellular and infection microbiology*, **2**, 11.

Höner zu Bentrup, K., Ramamurthy, R., Ott, C.M., Emami, K., Nelman-Gonzalez, M., Wilson, J.W., *et al.* (2006) Three-dimensional organotypic models of human colonic epithelium to study the early stages of enteric salmonellosis. *Microbes and Infection*, **8**, 1813–1825.

Horstmann, J.A., Zschieschang, E., Truschel, T., Diego, J. de, Lunelli, M., Rohde, M., *et al.* (2017) Flagellin phase-dependent swimming on epithelial cell surfaces contributes to productive Salmonella gut colonisation. *Cellular Microbiology*, **19**.

Howard, S.L., Jagannathan, A., Soo, E.C., Hui, J.P.M., Aubry, A.J., Ahmed, I., *et al.* (2009) Campylobacter jejuni glycosylation island important in cell charge, legionaminic acid biosynthesis, and colonization of chickens. *Infection and Immunity*, **77**, 2544–2556.

Howes, S.C., Koning, R.I. & Koster, A.J. (2018) Correlative microscopy for structural microbiology. *Current Opinion in Microbiology*, **43**, 132–138.

Hoy, B., Löwer, M., Weydig, C., Carra, G., Tegtmeyer, N., Geppert, T., *et al.* (2010) Helicobacter pylori HtrA is a new secreted virulence factor that cleaves E-cadherin to disrupt intercellular adhesion. *EMBO Reports*, **11**, 798–804.

Hoy, B., Geppert, T., Boehm, M., Reisen, F., Plattner, P., Gadermaier, G., *et al.* (2012) Distinct roles of secreted HtrA proteases from gram-negative pathogens in cleaving the junctional protein and tumor suppressor E-cadherin. *The Journal of Biological Chemistry*, **287**, 10115–10120.

Hu, L. & Kopecko, D.J. (1999) Campylobacter jejuni 81-176 associates with microtubules and dynein during invasion of human intestinal cells. *Infection and Immunity*, **67**, 4171–4182.

Hu, L., Tall, B.D., Curtis, S.K. & Kopecko, D.J. (2008a) Enhanced microscopic definition of Campylobacter jejuni 81-176 adherence to, invasion of, translocation across, and exocytosis from polarized human intestinal Caco-2 cells. *Infection and Immunity*, **76**, 5294–5304.

Hu, Q., Coburn, B., Deng, W., Li, Y., Shi, X., Lan, Q., *et al.* (2008b) Salmonella enterica serovar Senftenberg human clinical isolates lacking SPI-1. *Journal of Clinical Microbiology*, **46**, 1330–1336.

Hubatsch, I., Ragnarsson, E.G.E. & Artursson, P. (2007) Determination of drug permeability and prediction of drug absorption in Caco-2 monolayers. *Nature Protocols*, **2**, 2111–2119.

Hugdahl, M.B., Beery, J.T. & Doyle, M.P. (1988) Chemotactic behavior of Campylobacter jejuni. *Infection and Immunity*, **56**, 1560–1566.

Hurley, B.P. & McCormick, B.A. (2003) Translating tissue culture results into animal models: the case of Salmonella typhimurium. *Trends in Microbiology*, **11**, 562–569.

In, J., Foulke-Abel, J., Zachos, N.C., Hansen, A.-M., Kaper, J.B., Bernstein, H.D., *et al.* (2016) Enterohemorrhagic Escherichia coli reduce mucus and intermicrovillar bridges in human stem cell-derived colonoids. *Cellular and molecular gastroenterology and hepatology*, **2**, 48–62.e3.

Ingber, D.E. (2006) Mechanical control of tissue morphogenesis during embryological development. *The International Journal of Developmental Biology*, **50**, 255–266.

Jakus, A.E., Rutz, A.L. & Shah, R.N. (2016) Advancing the field of 3D biomaterial printing. *Biomedical Materials*, **11**, 014102.

Jang, K.-J., Cho, H.S., Kang, D.H., Bae, W.G., Kwon, T.-H. & Suh, K.-Y. (2011) Fluid-shear-stress-induced translocation of aquaporin-2 and reorganization of actin cytoskeleton in renal tubular epithelial cells. *Integrative Biology: Quantitative Biosciences from Nano to Macro*, **3**, 134–141.

Javed, M.A., Grant, A.J., Bagnall, M.C., Maskell, D.J., Newell, D.G. & Manning, G. (2010) Transposon mutagenesis in a hyper-invasive clinical isolate of Campylobacter jejuni reveals a number of genes with potential roles in invasion. *Microbiology*, **156**, 1134–1143.

Jerome, J.P., Bell, J.A., Plovanich-Jones, A.E., Barrick, J.E., Brown, C.T. & Mansfield, L.S. (2011) Standing genetic variation in contingency loci drives the rapid adaptation of Campylobacter jejuni to a novel host. *Plos One*, **6**, e16399.

Jin, S., Joe, A., Lynett, J., Hani, E.K., Sherman, P. & Chan, V.L. (2001) JlpA, a novel surface-exposed lipoprotein specific to Campylobacter jejuni, mediates adherence to host epithelial cells. *Molecular Microbiology*, **39**, 1225–1236.

Johansson, M.E.V., Phillipson, M., Petersson, J., Velcich, A., Holm, L. & Hansson, G.C. (2008) The inner of the two Muc2 mucin-dependent mucus layers in colon is devoid of bacteria. *Proceedings of the National Academy of Sciences of the United States of America*, **105**, 15064–15069.

Johansson, M.E.V., Gustafsson, J.K., Sjöberg, K.E., Petersson, J., Holm, L., Sjövall, H., *et al.* (2010) Bacteria penetrate the inner mucus layer before inflammation in the dextran sulfate colitis model. *Plos One*, **5**, e12238.

Johansson, M.E.V., Ambort, D., Pelaseyed, T., Schütte, A., Gustafsson, J.K., Ermund, A., *et al.* (2011) Composition and functional role of the mucus layers in the intestine. *Cellular and Molecular Life Sciences*, **68**, 3635–3641.

Johansson, M.E.V., Sjövall, H. & Hansson, G.C. (2013) The gastrointestinal mucus system in health and disease. *Nature Reviews. Gastroenterology & Hepatology*, **10**, 352–361.

Johansson, M.E.V., Jakobsson, H.E., Holmén-Larsson, J., Schütte, A., Ermund, A., Rodríguez-Piñeiro, A.M., *et al.* (2015) Normalization of Host Intestinal Mucus Layers Requires Long-Term Microbial Colonization. *Cell Host & Microbe*, **18**, 582–592.

Johansson, M.E.V. & Hansson, G.C. (2016) Immunological aspects of intestinal mucus and mucins. *Nature Reviews. Immunology*, **16**, 639–649.

Johnson, J.G., Livny, J. & Dirita, V.J. (2014) High-throughput sequencing of Campylobacter jejuni insertion mutant libraries reveals mapA as a fitness factor for chicken colonization. *Journal of Bacteriology*, **196**, 1958–1967.

Jones, K. (2001) Campylobacters in water, sewage and the environment. *Symposium series (Society for Applied Microbiology)*, 68S–79S.

Jones, M.A., Marston, K.L., Woodall, C.A., Maskell, D.J., Linton, D., Karlyshev, A.V., *et al.* (2004) Adaptation of Campylobacter jejuni NCTC11168 to high-level colonization of the avian gastrointestinal tract. *Infection and Immunity*, **72**, 3769–3776.

Josenhans, C., Vossebein, L., Friedrich, S. & Suerbaum, S. (2002) The neuA/flmD gene cluster of Helicobacter pylori is involved in flagellar biosynthesis and flagellin glycosylation. *FEMS Microbiology Letters*, **210**, 165–172.

Juge, N. (2012) Microbial adhesins to gastrointestinal mucus. *Trends in Microbiology*, **20**, 30–39.

Kaakoush, N.O., Castaño-Rodríguez, N., Mitchell, H.M. & Man, S.M. (2015) Global Epidemiology of Campylobacter Infection. *Clinical Microbiology Reviews*, **28**, 687–720.

Kalischuk, L.D., Inglis, G.D. & Buret, A.G. (2009) Campylobacter jejuni induces transcellular translocation of commensal bacteria via lipid rafts. *Gut Pathogens*, **1**, 2.

Kampmann, C., Dicksved, J., Engstrand, L. & Rautelin, H. (2016) Composition of human faecal microbiota in resistance to Campylobacter infection. *Clinical Microbiology and Infection*, **22**, 61.e1-8.

Kang, E., Crouse, A., Chevallier, L., Pontier, S.M., Alzahrani, A., Silué, N., *et al.* (2018) Enterobacteria and host resistance to infection. *Mammalian Genome*, 1–19.

Kaplan-Türköz, B., Jiménez-Soto, L.F., Dian, C., Ertl, C., Remaut, H., Louche, A., *et al.* (2012) Structural insights into Helicobacter pylori oncoprotein CagA interaction with β1 integrin. *Proceedings of the National Academy of Sciences of the United States of America*, **109**, 14640–14645.

Kanipes, M.I., Holder, L.C., Corcoran, A.T., Moran, A.P. & Guerry, P. (2004) A deep-rough mutant of Campylobacter jejuni 81-176 is noninvasive for intestinal epithelial cells. *Infection and Immunity*, **72**, 2452–2455.

Kanungpean, D., Kakuda, T. & Takai, S. (2011) Participation of CheR and CheB in the chemosensory response of Campylobacter jejuni. *Microbiology*, **157**, 1279–1289.

Karim, Q.N., Logan, R.P., Puels, J., Karnholz, A. & Worku, M.L. (1998) Measurement of motility of Helicobacter pylori, Campylobacter jejuni, and Escherichia coli by real time computer tracking using the Hobson BacTracker. *Journal of Clinical Pathology*, **51**, 623–628.

Karlsson, N.G., Johansson, M.E., Asker, N., Karlsson, H., Gendler, S.J., Carlstedt, I., *et al.* (1996) Molecular characterization of the large heavily glycosylated domain glycopeptide from the rat small intestinal Muc2 mucin. *Glycoconjugate journal*, **13**, 823–831.

Karlyshev, A.V., Linton, D., Gregson, N.A., Lastovica, A.J. & Wren, B.W. (2000) Genetic and biochemical evidence of a Campylobacter jejuni capsular polysaccharide that accounts for Penner serotype specificity. *Molecular Microbiology*, **35**, 529–541.

Karlyshev, A.V., McCrossan, M.V. & Wren, B.W. (2001) Demonstration of polysaccharide capsule in Campylobacter jejuni using electron microscopy. *Infection and Immunity*, **69**, 5921–5924.

Karlyshev, A.V., Linton, D., Gregson, N.A. & Wren, B.W. (2002) A novel paralogous gene family involved in phase-variable flagella-mediated motility in Campylobacter jejuni. *Microbiology*, **148**, 473–480.

Karlyshev, A.V., Ketley, J.M. & Wren, B.W. (2005) The Campylobacter jejuni glycome. *FEMS Microbiology Reviews*, **29**, 377–390.

Karlyshev, A.V., Wren, B.W. & Moran, A.P. (n.d.) Campylobacter jejuni capsular polysaccharide. *Campylobacter*.

Kasendra, M., Tovaglieri, A., Sontheimer-Phelps, A., Jalili-Firoozinezhad, S., Bein, A., Chalkiadaki, A., *et al.* (2018) Development of a primary human Small Intestine-on-a-Chip using biopsy-derived organoids. *Scientific reports*, **8**, 2871.

Kauffman, A.L., Gyurdieva, A.V., Mabus, J.R., Ferguson, C., Yan, Z. & Hornby, P.J. (2013) Alternative functional in vitro models of human intestinal epithelia. *Frontiers in pharmacology*, **4**, 79.

Kazmierczak, B.I., Mostov, K. & Engel, J.N. (2001) Interaction of bacterial pathogens with polarized epithelium. *Annual Review of Microbiology*, **55**, 407–435.

Keo, T., Collins, J., Kunwar, P., Blaser, M.J. & Iovine, N.M. (2011) Campylobacter capsule and lipooligosaccharide confer resistance to serum and cationic antimicrobials. *Virulence*, **2**, 30–40.

Kim, H.J., Huh, D., Hamilton, G. & Ingber, D.E. (2012a) Human gut-on-a-chip inhabited by

microbial flora that experiences intestinal peristalsis-like motions and flow. *Lab on A Chip*, **12**, 2165–2174.

Kim, H.J. & Ingber, D.E. (2013) Gut-on-a-Chip microenvironment induces human intestinal cells to undergo villus differentiation. *Integrative Biology: Quantitative Biosciences from Nano to Macro*, **5**, 1130–1140.

Kim, H.J., Li, H., Collins, J.J. & Ingber, D.E. (2016) Contributions of microbiome and mechanical deformation to intestinal bacterial overgrowth and inflammation in a human gut-on-a-chip. *Proceedings of the National Academy of Sciences of the United States of America*, **113**, E7-15.

Kim, J.-S., Artymovich, K.A., Hall, D.F., Smith, E.J., Fulton, R., Bell, J., *et al.* (2012b) Passage of Campylobacter jejuni through the chicken reservoir or mice promotes phase variation in contingency genes Cj0045 and Cj0170 that strongly associates with colonization and disease in a mouse model. *Microbiology*, **158**, 1304–1316.

Kim, S.-H., Lee, B.-Y., Lau, G.W. & Cho, Y.-H. (2009) IscR modulates catalase A (KatA) activity, peroxide resistance and full virulence of Pseudomonas aeruginosa PA14. *Journal of Microbiology and Biotechnology*, **19**, 1520–1526.

Kim, S.H., Chi, M., Yi, B., Kim, S.H., Oh, S., Kim, Y., *et al.* (2014) Three-dimensional intestinal villi epithelium enhances protection of human intestinal cells from bacterial infection by inducing mucin expression. *Integrative Biology: Quantitative Biosciences from Nano to Macro*, **6**, 1122–1131.

Kjos, M., Aprianto, R., Fernandes, V.E., Andrew, P.W., Strijp, J.A.G. van, Nijland, R., *et al.* (2015) Bright fluorescent Streptococcus pneumoniae for live-cell imaging of host-pathogen interactions. *Journal of Bacteriology*, **197**, 807–818.

Kleist, S. von, Chany, E., Burtin, P., King, M. & Fogh, J. (1975) Immunohistology of the antigenic pattern of a continuous cell line from a human colon tumor. *Journal of the National Cancer Institute*, **55**, 555–560.

König, J., Wells, J., Cani, P.D., García-Ródenas, C.L., MacDonald, T., Mercenier, A., *et al.* (2016) Human intestinal barrier function in health and disease. *Clinical and translational gastroenterology*, **7**, e196.

Konkel, M.E. & Joens, L.A. (1989) Adhesion to and invasion of HEp-2 cells by Campylobacter spp. *Infection and Immunity*, **57**, 2984–2990.

Konkel, M.E., Mead, D.J., Hayes, S.F. & Cieplak, W. (1992) Translocation of Campylobacter jejuni across human polarized epithelial cell monolayer cultures. *The Journal of Infectious Diseases*, **166**, 308–315.

Konkel, M.E., Garvis, S.G., Tipton, S.L., Anderson, D.E. & Cieplak, W. (1997) Identification and molecular cloning of a gene encoding a fibronectin-binding protein (CadF) from Campylobacter jejuni. *Molecular Microbiology*, **24**, 953–963.

Konkel, M.E., Kim, B.J., Rivera-Amill, V. & Garvis, S.G. (1999) Identification of proteins required for the internalization of Campylobacter jejuni into cultured mammalian cells. *Advances in Experimental Medicine and Biology*, **473**, 215–224.

Konkel, M.E., Klena, J.D., Rivera-Amill, V., Monteville, M.R., Biswas, D., Raphael, B., *et al.* (2004) Secretion of virulence proteins from Campylobacter jejuni is dependent on a functional flagellar export apparatus. *Journal of Bacteriology*, **186**, 3296–3303.

Konkel, M.E., Larson, C.L. & Flanagan, R.C. (2010) Campylobacter jejuni FlpA binds fibronectin and is required for maximal host cell adherence. *Journal of Bacteriology*, **192**, 68–76.

Koonin, E.V., Makarova, K.S. & Zhang, F. (2017) Diversity, classification and evolution of CRISPR-Cas systems. *Current Opinion in Microbiology*, **37**, 67–78.

Korlath, J.A., Osterholm, M.T., Judy, L.A., Forfang, J.C. & Robinson, R.A. (1985) A point-source outbreak of campylobacteriosis associated with consumption of raw milk. *The Journal of Infectious Diseases*, **152**, 592–596.

Krause-Gruszczynska, M., Alphen, L.B. van, Oyarzabal, O.A., Alter, T., Hänel, I., Schliephake, A., *et al.* (2007) Expression patterns and role of the CadF protein in Campylobacter jejuni and Campylobacter coli. *FEMS Microbiology Letters*, **274**, 9–16.

Kreuder, A.J., Schleining, J.A., Yaeger, M., Zhang, Q. & Plummer, P.J. (2017) RNAseq Reveals Complex Response of Campylobacter jejuni to Ovine Bile and In vivo Gallbladder Environment. *Frontiers in microbiology*, **8**, 940.

Krieg, N.R. & Hoffman, P.S. (1986) Microaerophily and oxygen toxicity. *Annual Review of Microbiology*, **40**, 107–130.

Krute, C.N., Carroll, R.K., Rivera, F.E., Weiss, A., Young, R.M., Shilling, A., *et al.* (2014) The Disruption of Prenylation Leads to Pleiotropic Rearrangements in Cellular Behavior in Staphylococcus aureus. *Molecular Microbiology*.

Krzywinski, M., Schein, J., Birol, I., Connors, J., Gascoyne, R., Horsman, D., *et al.* (2009) Circos: an information aesthetic for comparative genomics. *Genome Research*, **19**, 1639–1645.

Kukulski, W., Schorb, M., Welsch, S., Picco, A., Kaksonen, M. & Briggs, J.A.G. (2011) Correlated fluorescence and 3D electron microscopy with high sensitivity and spatial precision. *The Journal of Cell Biology*, **192**, 111–119.

Kundu, B., Rajkhowa, R., Kundu, S.C. & Wang, X. (2013) Silk fibroin biomaterials for tissue regenerations. *Advanced Drug Delivery Reviews*, **65**, 457–470.

Kurkchubasche, A.G., Cardona, M., Watkins, S.C., Smith, S.D., Albanese, C.T., Simmons, R.L., *et al.* (1998) Transmucosal passage of bacteria across rat intestinal epithelium in the Ussing chamber: effect of nutritional factors and bacterial virulence. *Shock*, **9**, 121–127.

Kwok, T., Zabler, D., Urman, S., Rohde, M., Hartig, R., Wessler, S., *et al.* (2007) Helicobacter exploits integrin for type IV secretion and kinase activation. *Nature*, **449**, 862–866.

Laketa, V. (2018) Microscopy in Infectious Disease Research-Imaging Across Scales. *Journal of Molecular Biology*, **430**, 2612–2625.

Langridge, G.C., Phan, M.-D., Turner, D.J., Perkins, T.T., Parts, L., Haase, J., *et al.* (2009) Simultaneous assay of every Salmonella Typhi gene using one million transposon mutants. *Genome Research*, **19**, 2308–2316.

Lara-Tejero, M. & Galán, J.E. (2000) A bacterial toxin that controls cell cycle progression as a deoxyribonuclease I-like protein. *Science*, **290**, 354–357.

Lara-Tejero, M. & Galán, J.E. (2001) CdtA, CdtB, and CdtC form a tripartite complex that is required for cytolethal distending toxin activity. *Infection and Immunity*, **69**, 4358–4365.

Larson, C.L., Samuelson, D.R., Eucker, T.P., O'Loughlin, J.L. & Konkel, M.E. (2013) The fibronectin-binding motif within FlpA facilitates Campylobacter jejuni adherence to host cell and activation of host cell signaling. *Emerging microbes & infections*, **2**, e65.

Le, M.T., Veldhuizen, M. van, Porcelli, I., Bongaerts, R.J., Gaskin, D.J.H., Pearson, B.M., *et al.* (2015) Conservation of σ28-Dependent Non-Coding RNA Paralogs and Predicted σ54-Dependent Targets in Thermophilic Campylobacter Species. *Plos One*, **10**, e0141627.

Lee, A., O'Rourke, J.L., Barrington, P.J. & Trust, T.J. (1986) Mucus colonization as a determinant of pathogenicity in intestinal infection by Campylobacter jejuni: a mouse cecal model. *Infection and Immunity*, **51**, 536–546.

Leedham, S.J., Rodenas-Cuadrado, P., Howarth, K., Lewis, A., Mallappa, S., Segditsas, S., *et al.* (2013) A basal gradient of Wnt and stem-cell number influences regional tumour distribution in human and mouse intestinal tracts. *Gut*, **62**, 83–93.

Lertsethtakarn, P., Ottemann, K.M. & Hendrixson, D.R. (2011) Motility and chemotaxis in Campylobacter and Helicobacter . *Annual Review of Microbiology*, **65**, 389–410.

Lesuffleur, T., Barbat, A., Dussaulx, E. & Zweibaum, A. (1990) Growth adaptation to methotrexate of HT-29 human colon carcinoma cells is associated with their ability to differentiate into columnar absorptive and mucus-secreting cells. *Cancer Research*, **50**, 6334–6343.

Lesuffleur, T., Porchet, N., Aubert, J.P., Swallow, D., Gum, J.R., Kim, Y.S., *et al.* (1993) Differential expression of the human mucin genes MUC1 to MUC5 in relation to growth and differentiation of different mucus-secreting HT-29 cell subpopulations. *Journal of Cell Science*, **106 (Pt 3)**, 771–783.

Li, R., Fang, L., Tan, S., Yu, M., Li, X., He, S., *et al.* (2016) Type I CRISPR-Cas targets endogenous genes and regulates virulence to evade mammalian host immunity. *Cell Research*, **26**, 1273–1287.

Li, W., Germain, R.N. & Gerner, M.Y. (2017) Multiplex, quantitative cellular analysis in large tissue volumes with clearing-enhanced 3D microscopy (Ce3D). *Proceedings of the National Academy of Sciences of the United States of America*, **114**, E7321–E7330.

Li, X., Bleumink-Pluym, N.M.C., Luijkx, Y.M.C.A., Wubbolts, R.W., Putten, J.P.M. van & Strijbis, K. (2019) MUC1 is a receptor for the Salmonella SiiE adhesin that enables apical invasion into enterocytes. *PLoS Pathogens*, **15**, e1007566.

Li, Z., Lou, H., Ojcius, D.M., Sun, A., Sun, D., Zhao, J., *et al.* (2014) Methyl-accepting chemotaxis protein-3 and -4 are responsible for Campylobacter jejuni chemotaxis and jejuna colonization in mice in response to sodium deoxycholate. *Journal of Medical Microbiology*.

Lin, R.-Z., Lin, R.-Z. & Chang, H.-Y. (2008) Recent advances in three-dimensional multicellular spheroid culture for biomedical research. *Biotechnology Journal*, **3**, 1172–1184.

Lindén, S.K., Driessen, K.M. & McGuckin, M.A. (2007) Improved in vitro model systems for gastrointestinal infection by choice of cell line, pH, microaerobic conditions, and optimization of culture conditions. *Helicobacter*, **12**, 341–353.

Lindén, S.K., Florin, T.H.J. & McGuckin, M.A. (2008) Mucin dynamics in intestinal bacterial infection. *Plos One*, **3**, e3952.

Linden, S.K., Sutton, P., Karlsson, N.G., Korolik, V. & McGuckin, M.A. (2008) Mucins in the mucosal barrier to infection. *Mucosal Immunology*, **1**, 183–197.

Lindén, S.K., Sheng, Y.H., Every, A.L., Miles, K.M., Skoog, E.C., Florin, T.H.J., *et al.* (2009) MUC1 limits Helicobacter pylori infection both by steric hindrance and by acting as a releasable decoy. *PLoS Pathogens*, **5**, e1000617.

Lingwood, C.A. (1999) Glycolipid receptors for verotoxin and Helicobacter pylori: role in pathology. *Biochimica et Biophysica Acta*, **1455**, 375–386.

Linke, S., Niedrig, M., Kaiser, A., Ellerbrok, H., Müller, K., Müller, T., *et al.* (2007) Serologic evidence of West Nile virus infections in wild birds captured in Germany. *The American Journal of Tropical Medicine and Hygiene*, **77**, 358–364.

Liu, X., Gao, B., Novik, V. & Galán, J.E. (2012) Quantitative Proteomics of Intracellular Campylobacter jejuni Reveals Metabolic Reprogramming. *PLoS Pathogens*, **8**, e1002562.

Logan, S.M. (2006) Flagellar glycosylation - a new component of the motility repertoire? *Microbiology*, **152**, 1249–1262.

Logan, S.M., Hui, J.P.M., Vinogradov, E., Aubry, A.J., Melanson, J.E., Kelly, J.F., *et al.* (2009) Identification of novel carbohydrate modifications on Campylobacter jejuni 11168 flagellin using metabolomics-based approaches. *The FEBS Journal*, **276**, 1014–1023.

Longley, D.B., Harkin, D.P. & Johnston, P.G. (2003) 5-fluorouracil: mechanisms of action and

clinical strategies. *Nature Reviews. Cancer*, **3**, 330–338.

Louwen, R., Heikema, A., Belkum, A. van, Ott, A., Gilbert, M., Ang, W., *et al.* (2008) The sialylated lipooligosaccharide outer core in Campylobacter jejuni is an important determinant for epithelial cell invasion. *Infection and Immunity*, **76**, 4431–4438.

Louwen, R., Nieuwenhuis, E.E.S., Marrewijk, L. van, Horst-Kreft, D., Ruiter, L. de, Heikema, A.P., *et al.* (2012) Campylobacter jejuni translocation across intestinal epithelial cells is facilitated by ganglioside-like lipooligosaccharide structures. *Infection and Immunity*, **80**, 3307–3318.

Louwen, R., Horst-Kreft, D., Boer, A.G. de, Graaf, L. van der, Knegt, G. de, Hamersma, M., *et al.* (2013) A novel link between Campylobacter jejuni bacteriophage defence, virulence and Guillain-Barré syndrome. *European Journal of Clinical Microbiology & Infectious Diseases*, **32**, 207–226.

Louwen, R., Staals, R.H.J., Endtz, H.P., Baarlen, P. van & Oost, J. van der. (2014) The role of CRISPR-Cas systems in virulence of pathogenic bacteria. *Microbiology and Molecular Biology Reviews*, **78**, 74–88.

Lucchetti-Miganeh, C., Burrowes, E., Baysse, C. & Ermel, G. (2008) The post-transcriptional regulator CsrA plays a central role in the adaptation of bacterial pathogens to different stages of infection in animal hosts. *Microbiology*, **154**, 16–29.

Luethy, P.M., Huynh, S., Ribardo, D.A., Winter, S.E., Parker, C.T. & Hendrixson, D.R. (2017) Microbiota-Derived Short-Chain Fatty Acids Modulate Expression of Campylobacter jejuni Determinants Required for Commensalism and Virulence. *mBio*, **8**.

MacCallum, A., Hardy, S.P. & Everest, P.H. (2005) Campylobacter jejuni inhibits the absorptive transport functions of Caco-2 cells and disrupts cellular tight junctions. *Microbiology*, **151**, 2451–2458.

Madara, J.L. (1998) Regulation of the movement of solutes across tight junctions. *Annual Review of Physiology*, **60**, 143–159.

Madden, L.R., Nguyen, T.V., Garcia-Mojica, S., Shah, V., Le, A.V., Peier, A., *et al.* (2018) Bioprinted 3D primary human intestinal tissues model aspects of native physiology and adme/tox functions. *iScience*, **2**, 156–167.

Makarova, K.S., Haft, D.H., Barrangou, R., Brouns, S.J.J., Charpentier, E., Horvath, P., *et al.* (2011) Evolution and classification of the CRISPR-Cas systems. *Nature Reviews. Microbiology*, **9**, 467–477.

Makarova, K.S., Wolf, Y.I., Alkhnbashi, O.S., Costa, F., Shah, S.A., Saunders, S.J., *et al.* (2015) An updated evolutionary classification of CRISPR-Cas systems. *Nature Reviews. Microbiology*, **13**, 722–736.

Malik-Kale, P., Parker, C.T. & Konkel, M.E. (2008) Culture of Campylobacter jejuni with sodium deoxycholate induces virulence gene expression. *Journal of Bacteriology*, **190**, 2286–2297.

Mandal, R.K., Jiang, T. & Kwon, Y.M. (2017) Essential genome of Campylobacter jejuni. *BMC Genomics*, **18**, 616.

Mansfield, L.S., Bell, J.A., Wilson, D.L., Murphy, A.J., Elsheikha, H.M., Rathinam, V.A.K., *et al.* (2007) C57BL/6 and congenic interleukin-10-deficient mice can serve as models of Campylobacter jejuni colonization and enteritis. *Infection and Immunity*, **75**, 1099–1115.

Mantle, M. & Rombough, C. (1993) Growth in and breakdown of purified rabbit small intestinal mucin by Yersinia enterocolitica. *Infection and Immunity*, **61**, 4131–4138.

Martens, E.C., Neumann, M. & Desai, M.S. (2018) Interactions of commensal and pathogenic microorganisms with the intestinal mucosal barrier. *Nature Reviews. Microbiology*, **16**, 457–

470.

Marteyn, B., Scorza, F.B., Sansonetti, P.J. & Tang, C. (2011) Breathing life into pathogens: the influence of oxygen on bacterial virulence and host responses in the gastrointestinal tract. *Cellular Microbiology*, **13**, 171–176.

Martin, M. (2011) Cutadapt removes adapter sequences from high-throughput sequencing reads. *EMBnet.journal*, **17**, 10.

Martínez, L.E., Hardcastle, J.M., Wang, J., Pincus, Z., Tsang, J., Hoover, T.R., *et al.* (2016) Helicobacter pylori strains vary cell shape and flagellum number to maintain robust motility in viscous environments. *Molecular Microbiology*, **99**, 88–110.

Masopust, D., Sivula, C.P. & Jameson, S.C. (2017) Of mice, dirty mice, and men: using mice to understand human immunology. *Journal of Immunology*, **199**, 383–388.

Matter, K. & Balda, M.S. (2003) Functional analysis of tight junctions. *Methods*, **30**, 228–234.

Maue, A.C., Mohawk, K.L., Giles, D.K., Poly, F., Ewing, C.P., Jiao, Y., *et al.* (2013) The polysaccharide capsule of Campylobacter jejuni modulates the host immune response. *Infection and Immunity*, **81**, 665–672.

McAuley, J.L., Linden, S.K., Png, C.W., King, R.M., Pennington, H.L., Gendler, S.J., *et al.* (2007) MUC1 cell surface mucin is a critical element of the mucosal barrier to infection. *The Journal of Clinical Investigation*, **117**, 2313–2324.

McClelland, M., Sanderson, K.E., Clifton, S.W., Latreille, P., Porwollik, S., Sabo, A., *et al.* (2004) Comparison of genome degradation in Paratyphi A and Typhi, human-restricted serovars of Salmonella enterica that cause typhoid. *Nature Genetics*, **36**, 1268–1274.

McCracken, K.W., Catá, E.M., Crawford, C.M., Sinagoga, K.L., Schumacher, M., Rockich, B.E., *et al.* (2014) Modelling human development and disease in pluripotent stem-cell-derived gastric organoids. *Nature*, **516**, 400–404.

McEvoy, C.R.E., Helden, P.D. van, Warren, R.M. & Gey van Pittius, N.C. (2009) Evidence for a rapid rate of molecular evolution at the hypervariable and immunogenic Mycobacterium tuberculosis PPE38 gene region. *BMC Evolutionary Biology*, **9**, 237.

McGuckin, M.A., Lindén, S.K., Sutton, P. & Florin, T.H. (2011) Mucin dynamics and enteric pathogens. *Nature Reviews. Microbiology*, **9**, 265–278.

McLennan, M.K., Ringoir, D.D., Frirdich, E., Svensson, S.L., Wells, D.H., Jarrell, H., *et al.* (2008) Campylobacter jejuni biofilms up-regulated in the absence of the stringent response utilize a calcofluor white-reactive polysaccharide. *Journal of Bacteriology*, **190**, 1097–1107.

McNally, D.J., Hui, J.P.M., Aubry, A.J., Mui, K.K.K., Guerry, P., Brisson, J.-R., *et al.* (2006) Functional characterization of the flagellar glycosylation locus in Campylobacter jejuni 81-176 using a focused metabolomics approach. *The Journal of Biological Chemistry*, **281**, 18489–18498.

McNally, D.J., Lamoureux, M.P., Karlyshev, A.V., Fiori, L.M., Li, J., Thacker, G., *et al.* (2007) Commonality and biosynthesis of the O-methyl phosphoramidate capsule modification in Campylobacter jejuni. *The Journal of Biological Chemistry*, **282**, 28566–28576.

Mertins, S., Allan, B.J., Townsend, H.G., Köster, W. & Potter, A.A. (2013) Role of motAB in adherence and internalization in polarized Caco-2 cells and in cecal colonization of Campylobacter jejuni. *Avian Diseases*, **57**, 116–122.

Mertsching, H., Walles, T., Hofmann, M., Schanz, J. & Knapp, W.H. (2005) Engineering of a vascularized scaffold for artificial tissue and organ generation. *Biomaterials*, **26**, 6610–6617.

Messmann, H. (2011) Klinische Gastroenterologie: Das Buch für Fort-und Weiterbildung plus DVD mit über 1.000 Befunden.

Metris, A., Reuter, M., Gaskin, D.J.H., Baranyi, J. & Vliet, A.H.M. van. (2011) In vivo and in

silico determination of essential genes of Campylobacter jejuni. *BMC Genomics*, **12**, 535.

Miller, H.K., Kwuan, L., Schwiesow, L., Bernick, D.L., Mettert, E., Ramirez, H.A., *et al.* (2014) IscR Is Essential for Yersinia pseudotuberculosis Type III Secretion and Virulence. *PLoS Pathogens*, **10**, e1004194.

Mills, J.C. & Shivdasani, R.A. (2011) Gastric epithelial stem cells. *Gastroenterology*, **140**, 412–424.

Minuth, W.W., Denk, L. & Glashauser, A. (2010) A modular culture system for the generation of multiple specialized tissues. *Biomaterials*, **31**, 2945–2954.

Miyoshi, H. (2017) Wnt-expressing cells in the intestines: guides for tissue remodeling. *Journal of Biochemistry*, **161**, 19–25.

Mohanraju, P., Makarova, K.S., Zetsche, B., Zhang, F., Koonin, E.V. & Oost, J. van der. (2016) Diverse evolutionary roots and mechanistic variations of the CRISPR-Cas systems. *Science*, **353**, aad5147.

Mohawk, K.L., Poly, F., Sahl, J.W., Rasko, D.A. & Guerry, P. (2014) High frequency, spontaneous motA mutations in Campylobacter jejuni strain 81-176. *Plos One*, **9**, e88043.

Molina-Henares, A.J., Krell, T., Eugenia Guazzaroni, M., Segura, A. & Ramos, J.L. (2006) Members of the IclR family of bacterial transcriptional regulators function as activators and/or repressors. *FEMS Microbiology Reviews*, **30**, 157–186.

Monteville, M.R. & Konkel, M.E. (2002) Fibronectin-facilitated invasion of T84 eukaryotic cells by Campylobacter jejuni occurs preferentially at the basolateral cell surface. *Infection and Immunity*, **70**, 6665–6671.

Monteville, M.R., Yoon, J.E. & Konkel, M.E. (2003) Maximal adherence and invasion of INT 407 cells by Campylobacter jejuni requires the CadF outer-membrane protein and microfilament reorganization. *Microbiology*, **149**, 153–165.

Moore, J.E., Corcoran, D., Dooley, J.S.G., Fanning, S., Lucey, B., Matsuda, M., *et al.* (2005) Campylobacter. *Veterinary Research*, **36**, 351–382.

Moran, A.P. (1997) Structure and conserved characteristics of Campylobacter jejuni lipopolysaccharides. *The Journal of Infectious Diseases*, **176 Suppl 2**, S115-21.

Mortensen, N.P., Schiellerup, P., Boisen, N., Klein, B.M., Locht, H., Abuoun, M., *et al.* (2011) The role of Campylobacter jejuni cytolethal distending toxin in gastroenteritis: toxin detection, antibody production, and clinical outcome. *Acta Pathologica, Microbiologica, et Immunologica Scandinavica*, **119**, 626–634.

Moxon, R., Bayliss, C. & Hood, D. (2006) Bacterial contingency loci: the role of simple sequence DNA repeats in bacterial adaptation. *Annual Review of Genetics*, **40**, 307–333.

Müller-Esparza, H. & Randau, L. (2017) Commentary: Type I CRISPR-Cas targets endogenous genes and regulates virulence to evade mammalian host immunity. *Frontiers in microbiology*, **8**, 319.

Murray, R.A. & Lee, C.A. (2000) Invasion genes are not required for Salmonella enterica serovar typhimurium to breach the intestinal epithelium: evidence that salmonella pathogenicity island 1 has alternative functions during infection. *Infection and Immunity*, **68**, 5050–5055.

Naikare, H., Butcher, J., Flint, A., Xu, J., Raymond, K.N. & Stintzi, A. (2013) Campylobacter jejuni ferric-enterobactin receptor CfrA is TonB3 dependent and mediates iron acquisition from structurally different catechol siderophores. *Metallomics: Integrated Biometal Science*, **5**, 988–996.

Naughton, J.A., Mariño, K., Dolan, B., Reid, C., Gough, R., Gallagher, M.E., *et al.* (2013) Divergent mechanisms of interaction of Helicobacter pylori and Campylobacter jejuni with

mucus and mucins. *Infection and Immunity*, **81**, 2838–2850.

Naughton, J., Duggan, G., Bourke, B. & Clyne, M. (2014) Interaction of microbes with mucus and mucins: recent developments. *Gut microbes*, **5**, 48–52.

Navabi, N., McGuckin, M.A. & Lindén, S.K. (2013) Gastrointestinal cell lines form polarized epithelia with an adherent mucus layer when cultured in semi-wet interfaces with mechanical stimulation. *Plos One*, **8**, e68761.

Neunlist, M., Van Landeghem, L., Mahé, M.M., Derkinderen, P., Varannes, S.B. des & Rolli-Derkinderen, M. (2013) The digestive neuronal-glial-epithelial unit: a new actor in gut health and disease. *Nature Reviews. Gastroenterology & Hepatology*, **10**, 90–100.

Neutra, M.R., Mantis, N.J., Frey, A. & Giannasca, P.J. (1999) The composition and function of M cell apical membranes: implications for microbial pathogenesis. *Seminars in Immunology*, **11**, 171–181.

Nickerson, C.A., Goodwin, T.J., Terlonge, J., Ott, C.M., Buchanan, K.L., Uicker, W.C., *et al.* (2001) Three-dimensional tissue assemblies: novel models for the study of Salmonella enterica serovar Typhimurium pathogenesis. *Infection and Immunity*, **69**, 7106–7120.

Nickerson, C.A., Ott, C.M., Wilson, J.W., Ramamurthy, R. & Pierson, D.L. (2004) Microbial responses to microgravity and other low-shear environments. *Microbiology and Molecular Biology Reviews*, **68**, 345–361.

Nickerson, C.A., Richter, E.G. & Ott, C.M. (2007) Studying host-pathogen interactions in 3-D: organotypic models for infectious disease and drug development. *Journal of Neuroimmune Pharmacology*, **2**, 26–31.

Nickerson, K.P., Senger, S., Zhang, Y., Lima, R., Patel, S., Ingano, L., *et al.* (2018) Salmonella typhi colonization provokes extensive transcriptional changes aimed at evading host mucosal immune defense during early infection of human intestinal tissue. *EBioMedicine*, **31**, 92–109.

Niessen, C.M. (2007) Tight junctions/adherens junctions: basic structure and function. *The Journal of Investigative Dermatology*, **127**, 2525–2532.

Noel, G., Baetz, N.W., Staab, J.F., Donowitz, M., Kovbasnjuk, O., Pasetti, M.F., *et al.* (2017) A primary human macrophage-enteroid co-culture model to investigate mucosal gut physiology and host-pathogen interactions. *Scientific reports*, **7**, 45270.

Nossol, C., Diesing, A.K., Walk, N., Faber-Zuschratter, H., Hartig, R., Post, A., *et al.* (2011) Air-liquid interface cultures enhance the oxygen supply and trigger the structural and functional differentiation of intestinal porcine epithelial cells (IPEC). *Histochemistry and Cell Biology*, **136**, 103–115.

Nourry, C., Grant, S.G.N. & Borg, J.-P. (2003) PDZ domain proteins: plug and play! *Science's STKE: Signal Transduction Knowledge Environment*, **2003**, RE7.

Novik, V., Hofreuter, D. & Galán, J.E. (2010) Identification of Campylobacter jejuni genes involved in its interaction with epithelial cells. *Infection and Immunity*, **78**, 3540–3553.

Oelschlaeger, T.A., Guerry, P. & Kopecko, D.J. (1993) Unusual microtubule-dependent endocytosis mechanisms triggered by Campylobacter jejuni and Citrobacter freundii. *Proceedings of the National Academy of Sciences of the United States of America*, **90**, 6884–6888.

Ogaki, S., Shiraki, N., Kume, K. & Kume, S. (2013) Wnt and Notch signals guide embryonic stem cell differentiation into the intestinal lineages. *Stem Cells*, **31**, 1086–1096.

Ogden, I.D., Dallas, J.F., MacRae, M., Rotariu, O., Reay, K.W., Leitch, M., *et al.* (2009) Campylobacter excreted into the environment by animal sources: prevalence, concentration shed, and host association. *Foodborne Pathogens and Disease*, **6**, 1161–1170.

Olfat, F.O., Näslund, E., Freedman, J., Borén, T. & Engstrand, L. (2002) Cultured human gastric explants: a model for studies of bacteria-host interaction during conditions of experimental Helicobacter pylori infection. *The Journal of Infectious Diseases*, **186**, 423–427.

O'Rourke, J.L. & Lee, A. (2003) Animal models of Helicobacter pylori infection and disease. *Microbes and Infection*, **5**, 741–748.

Palyada, K., Threadgill, D. & Stintzi, A. (2004) Iron acquisition and regulation in Campylobacter jejuni. *Journal of Bacteriology*, **186**, 4714–4729.

Papenfort, K., Pfeiffer, V., Mika, F., Lucchini, S., Hinton, J.C.D. & Vogel, J. (2006) SigmaE-dependent small RNAs of Salmonella respond to membrane stress by accelerating global omp mRNA decay. *Molecular Microbiology*, **62**, 1674–1688.

Papenfort, K. & Vogel, J. (2010) Regulatory RNA in bacterial pathogens. *Cell Host & Microbe*, **8**, 116–127.

Parkhill, J., Wren, B.W., Mungall, K., Ketley, J.M., Churcher, C., Basham, D., *et al.* (2000) The genome sequence of the food-borne pathogen Campylobacter jejuni reveals hypervariable sequences. *Nature*, **403**, 665–668.

Pédelacq, J.-D., Cabantous, S., Tran, T., Terwilliger, T.C. & Waldo, G.S. (2006) Engineering and characterization of a superfolder green fluorescent protein. *Nature Biotechnology*, **24**, 79–88.

Pelaseyed, T., Gustafsson, J.K., Gustafsson, I.J., Ermund, A. & Hansson, G.C. (2013) Carbachol-induced MUC17 endocytosis is concomitant with NHE3 internalization and CFTR membrane recruitment in enterocytes. *American Journal of Physiology. Cell Physiology*, **305**, C457-67.

Pelaseyed, T., Bergström, J.H., Gustafsson, J.K., Ermund, A., Birchenough, G.M.H., Schütte, A., *et al.* (2014) The mucus and mucins of the goblet cells and enterocytes provide the first defense line of the gastrointestinal tract and interact with the immune system. *Immunological Reviews*, **260**, 8–20.

Pequegnat, B., Laird, R.M., Ewing, C.P., Hill, C.L., Omari, E., Poly, F., *et al.* (2017) Phase variable changes in the position of O-methyl phosphoramidate modifications on the polysaccharide capsule of Campylobacter jejuni modulate serum resistance. *Journal of Bacteriology*.

Perera, V.N., Nachamkin, I., Ung, H., Patterson, J.H., McConville, M.J., Coloe, P.J., *et al.* (2007) Molecular mimicry in Campylobacter jejuni: role of the lipo-oligosaccharide core oligosaccharide in inducing anti-ganglioside antibodies. *FEMS Immunology and Medical Microbiology*, **50**, 27–36.

Pernitzsch, S.R., Tirier, S.M., Beier, D. & Sharma, C.M. (2014) A variable homopolymeric G-repeat defines small RNA-mediated posttranscriptional regulation of a chemotaxis receptor in Helicobacter pylori. *Proceedings of the National Academy of Sciences of the United States of America*, **111**, E501-10.

Phillipson, M., Johansson, M.E.V., Henriksnäs, J., Petersson, J., Gendler, S.J., Sandler, S., *et al.* (2008) The gastric mucus layers: constituents and regulation of accumulation. *American Journal of Physiology. Gastrointestinal and Liver Physiology*, **295**, G806-12.

Poly, F. & Guerry, P. (2008) Pathogenesis of Campylobacter. *Current Opinion in Gastroenterology*, **24**, 27–31.

Pontes, M.H., Lee, E.-J., Choi, J. & Groisman, E.A. (2015) Salmonella promotes virulence by repressing cellulose production. *Proceedings of the National Academy of Sciences of the United States of America*, **112**, 5183–5188.

Pontier, C., Pachot, J., Botham, R., Lenfant, B. & Arnaud, P. (2001) HT29-MTX and Caco-2/TC7 monolayers as predictive models for human intestinal absorption: role of the mucus layer. *Journal of Pharmaceutical Sciences*, **90**, 1608–1619.

Ponting, C.P., Phillips, C., Davies, K.E. & Blake, D.J. (1997) PDZ domains: targeting signalling molecules to sub-membranous sites. *Bioessays: News and Reviews in Molecular, Cellular and Developmental Biology*, **19**, 469–479.

Porcelli, I., Reuter, M., Pearson, B.M., Wilhelm, T. & Vliet, A.H. van. (2013) Parallel evolution of genome structure and transcriptional landscape in the Epsilonproteobacteria. *BMC Genomics*, **14**, 616.

Pryjma, M., Apel, D., Huynh, S., Parker, C.T. & Gaynor, E.C. (2012) FdhTU-modulated formate dehydrogenase expression and electron donor availability enhance recovery of Campylobacter jejuni following host cell infection. *Journal of Bacteriology*, **194**, 3803–3813.

Puchtler, H., Waldrop, F.S., Meloan, S.N., Terry, M.S. & Conner, H.M. (1970) Methacarn (methanol-Carnoy) fixation. Practical and theoretical considerations. *Histochemie. Histochemistry. Histochimie*, **21**, 97–116.

Purdy, D., Buswell, C.M., Hodgson, A.E., McAlpine, K., Henderson, I. & Leach, S.A. (2000) Characterisation of cytolethal distending toxin (CDT) mutants of Campylobacter jejuni. *Journal of Medical Microbiology*, **49**, 473–479.

Pusch, J., Votteler, M., Göhler, S., Engl, J., Hampel, M., Walles, H., *et al.* (2011) The physiological performance of a three-dimensional model that mimics the microenvironment of the small intestine. *Biomaterials*, **32**, 7469–7478.

Py, B. & Barras, F. (2010) Building Fe-S proteins: bacterial strategies. *Nature Reviews. Microbiology*, **8**, 436–446.

Quereda, J.J. & Cossart, P. (2017) Regulating Bacterial Virulence with RNA. *Annual Review of Microbiology*, **71**, 263–280.

Radomska, K.A., Ordoñez, S.R., Wösten, M.M.S.M., Wagenaar, J.A. & Putten, J.P.M. van. (2016) Feedback control of Campylobacter jejuni flagellin levels through reciprocal binding of FliW to flagellin and the global regulator CsrA. *Molecular Microbiology*, **102**, 207–220.

Rahman, H., King, R.M., Shewell, L.K., Semchenko, E.A., Hartley-Tassell, L.E., Wilson, J.C., *et al.* (2014) Characterisation of a multi-ligand binding chemoreceptor CcmL (Tlp3) of Campylobacter jejuni. *PLoS Pathogens*, **10**, e1003822.

Rajan, A., Vela, L., Zeng, X.-L., Yu, X., Shroyer, N., Blutt, S.E., *et al.* (2018) Novel Segment- and Host-Specific Patterns of Enteroaggregative Escherichia coli Adherence to Human Intestinal Enteroids. *mBio*, **9**.

Raphael, B.H., Pereira, S., Flom, G.A., Zhang, Q., Ketley, J.M. & Konkel, M.E. (2005) The Campylobacter jejuni response regulator, CbrR, modulates sodium deoxycholate resistance and chicken colonization. *Journal of Bacteriology*, **187**, 3662–3670.

Reid, A.N., Pandey, R., Palyada, K., Naikare, H. & Stintzi, A. (2008) Identification of Campylobacter jejuni genes involved in the response to acidic pH and stomach transit. *Applied and Environmental Microbiology*, **74**, 1583–1597.

Reuter, C., Alzheimer, M., Walles, H. & Oelschlaeger, T.A. (2017) An adherent mucus layer attenuates the genotoxic effect of colibactin. *Cellular Microbiology*, **20**.

Reuter, M. & Vliet, A.H.M. van. (2013) Signal balancing by the CetABC and CetZ chemoreceptors controls energy taxis in Campylobacter jejuni. *Plos One*, **8**, e54390.

Revez, J., Schott, T., Rossi, M. & Hänninen, M.-L. (2012) Complete genome sequence of a variant of Campylobacter jejuni NCTC 11168. *Journal of Bacteriology*, **194**, 6298–6299.

Ribardo, D.A., Bingham-Ramos, L.K. & Hendrixson, D.R. (2010) Functional analysis of the RdxA and RdxB nitroreductases of Campylobacter jejuni reveals that mutations in rdxA confer metronidazole resistance. *Journal of Bacteriology*, **192**, 1890–1901.

Rodionov, D.A., Gelfand, M.S., Todd, J.D., Curson, A.R.J. & Johnston, A.W.B. (2006)

Computational reconstruction of iron- and manganese-responsive transcriptional networks in alpha-proteobacteria. *PLoS Computational Biology*, **2**, e163.

Rubinchik, S., Seddon, A.M. & Karlyshev, A.V. (2014) A negative effect of Campylobacter capsule on bacterial interaction with an analogue of a host cell receptor. *BMC Microbiology*, **14**, 141.

Sahai, A., Cole, L.A., Clarke, D.L. & Tannen, R.L. (1989) Rocking promotes differentiated properties in LLC-PK cells by improved oxygenation. *The American Journal of Physiology*, **256**, C1064-9.

Saitoh, Y., Suzuki, H., Tani, K., Nishikawa, K., Irie, K., Ogura, Y., *et al.* (2015) Tight junctions. Structural insight into tight junction disassembly by Clostridium perfringens enterotoxin. *Science*, **347**, 775–778.

Salama, N.R., Shepherd, B. & Falkow, S. (2004) Global transposon mutagenesis and essential gene analysis of Helicobacter pylori. *Journal of Bacteriology*, **186**, 7926–7935.

Salama, N.R., Hartung, M.L. & Müller, A. (2013) Life in the human stomach: persistence strategies of the bacterial pathogen Helicobacter pylori. *Nature Reviews. Microbiology*, **11**, 385–399.

Sałamaszyńska-Guz, A. & Klimuszko, D. (2008) Functional analysis of the Campylobacter jejuni cj0183 and cj0588 genes. *Current Microbiology*, **56**, 592–596.

Salamasznska-Guz, A., Grodzik, M. & Klimuszko, D. (2013) Mutational analysis of cj0183 Campylobacter jejuni promoter. *Current Microbiology*, **67**, 696–702.

Saliba, A.-E., Li, L., Westermann, A.J., Appenzeller, S., Stapels, D.A.C., Schulte, L.N., *et al.* (2016) Single-cell RNA-seq ties macrophage polarization to growth rate of intracellular Salmonella. *Nature microbiology*, **2**, 16206.

Saliba, A.-E., C Santos, S. & Vogel, J. (2017) New RNA-seq approaches for the study of bacterial pathogens. *Current Opinion in Microbiology*, **35**, 78–87.

Sampson, T.R. & Weiss, D.S. (2013) Cas9-dependent endogenous gene regulation is required for bacterial virulence. *Biochemical Society Transactions*, **41**, 1407–1411.

Sampson, T.R., Napier, B.A., Schroeder, M.R., Louwen, R., Zhao, J., Chin, C.-Y., *et al.* (2014) A CRISPR-Cas system enhances envelope integrity mediating antibiotic resistance and inflammasome evasion. *Proceedings of the National Academy of Sciences of the United States of America*, **111**, 11163–11168.

Samuelson, D.R., Eucker, T.P., Bell, J.A., Dybas, L., Mansfield, L.S. & Konkel, M.E. (2013) The Campylobacter jejuni CiaD effector protein activates MAP kinase signaling pathways and is required for the development of disease. *Cell Communication and Signaling*, **11**, 79.

Sarmento, B., Andrade, F., Silva, S.B. da, Rodrigues, F., Neves, J. das & Ferreira, D. (2012) Cell-based in vitro models for predicting drug permeability. *Expert Opinion on Drug Metabolism & Toxicology*, **8**, 607–621.

Sato, T., Vries, R.G., Snippert, H.J., Wetering, M. van de, Barker, N., Stange, D.E., *et al.* (2009) Single Lgr5 stem cells build crypt-villus structures in vitro without a mesenchymal niche. *Nature*, **459**, 262–265.

Sato, T., Stange, D.E., Ferrante, M., Vries, R.G.J., Van Es, J.H., Van den Brink, S., *et al.* (2011) Long-term expansion of epithelial organoids from human colon, adenoma, adenocarcinoma, and Barrett's epithelium. *Gastroenterology*, **141**, 1762–1772.

Schacht, K., Jüngst, T., Schweinlin, M., Ewald, A., Groll, J. & Scheibel, T. (2015) Biofabrication of cell-loaded 3D spider silk constructs. *Angewandte Chemie*, **54**, 2816–2820.

Schanz, J., Pusch, J., Hansmann, J. & Walles, H. (2010) Vascularised human tissue models: a new approach for the refinement of biomedical research. *Journal of Biotechnology*, **148**, 56–

63.

Schielke, A., Rosner, B.M. & Stark, K. (2014) Epidemiology of campylobacteriosis in Germany - insights from 10 years of surveillance. *BMC Infectious Diseases*, **14**, 30.

Schindelin, J., Arganda-Carreras, I., Frise, E., Kaynig, V., Longair, M., Pietzsch, T., *et al.* (2012) Fiji: an open-source platform for biological-image analysis. *Nature Methods*, **9**, 676–682.

Schlaermann, P., Toelle, B., Berger, H., Schmidt, S.C., Glanemann, M., Ordemann, J., *et al.* (2016) A novel human gastric primary cell culture system for modelling Helicobacter pylori infection in vitro. *Gut*, **65**, 202–213.

Schmeichel, K.L. & Bissell, M.J. (2003) Modeling tissue-specific signaling and organ function in three dimensions. *Journal of Cell Science*, **116**, 2377–2388.

Schmidt, T.P., Perna, A.M., Fugmann, T., Böhm, M., Jan Hiss, Haller, S., *et al.* (2016) Identification of E-cadherin signature motifs functioning as cleavage sites for Helicobacter pylori HtrA. *Scientific reports*, **6**, 23264.

Schuster, S., Krüger, T., Subota, I., Thusek, S., Rotureau, B., Beilhack, A., *et al.* (2017) Developmental adaptations of trypanosome motility to the tsetse fly host environments unravel a multifaceted in vivo microswimmer system. *eLife*, **6**.

Schwartz, C.J., Giel, J.L., Patschkowski, T., Luther, C., Ruzicka, F.J., Beinert, H., *et al.* (2001) IscR, an Fe-S cluster-containing transcription factor, represses expression of Escherichia coli genes encoding Fe-S cluster assembly proteins. *Proceedings of the National Academy of Sciences of the United States of America*, **98**, 14895–14900.

Schweinlin, M., Wilhelm, S., Schwedhelm, I., Hansmann, J., Rietscher, R., Jurowich, C., *et al.* (2016) Development of an advanced primary human in vitro model of the small intestine. *Tissue Engineering. Part C, Methods*, **22**, 873–883.

Secott, T.E., Lin, T.L. & Wu, C.C. (2004) Mycobacterium avium subsp. paratuberculosis fibronectin attachment protein facilitates M-cell targeting and invasion through a fibronectin bridge with host integrins. *Infection and Immunity*, **72**, 3724–3732.

Sellars, M.J., Hall, S.J. & Kelly, D.J. (2002) Growth of Campylobacter jejuni supported by respiration of fumarate, nitrate, nitrite, trimethylamine-N-oxide, or dimethyl sulfoxide requires oxygen. *Journal of Bacteriology*, **184**, 4187–4196.

Sharma, C.M., Darfeuille, F., Plantinga, T.H. & Vogel, J. (2007) A small RNA regulates multiple ABC transporter mRNAs by targeting C/A-rich elements inside and upstream of ribosome-binding sites. *Genes & Development*, **21**, 2804–2817.

Shigematsu, M., Umeda, A., Fujimoto, S. & Amako, K. (1998) Spirochaete-like swimming mode of Campylobacter jejuni in a viscous environment. *Journal of Medical Microbiology*, **47**, 521–526.

Siebers, A. & Finlay, B.B. (1996) M cells and the pathogenesis of mucosal and systemic infections. *Trends in Microbiology*, **4**, 22–29.

Sigal, M., Rothenberg, M.E., Logan, C.Y., Lee, J.Y., Honaker, R.W., Cooper, R.L., *et al.* (2015) Helicobacter pylori Activates and Expands Lgr5(+) Stem Cells Through Direct Colonization of the Gastric Glands. *Gastroenterology*, **148**, 1392–404.e21.

Silva, A.J., Pham, K. & Benitez, J.A. (2003) Haemagglutinin/protease expression and mucin gel penetration in El Tor biotype Vibrio cholerae. *Microbiology*, **149**, 1883–1891.

Simon-Assmann, P., Spenle, C., Lefebvre, O. & Kedinger, M. (2010) The role of the basement membrane as a modulator of intestinal epithelial-mesenchymal interactions. *Progress in molecular biology and translational science*, **96**, 175–206.

Sinaasappel, M., Donkersloot, C., Bommel, J. van & Ince, C. (1999) PO2 measurements in the rat intestinal microcirculation. *The American Journal of Physiology*, **276**, G1515-20.

Singh, B., Fleury, C., Jalalvand, F. & Riesbeck, K. (2012) Human pathogens utilize host extracellular matrix proteins laminin and collagen for adhesion and invasion of the host. *FEMS Microbiology Reviews*, **36**, 1122–1180.

Sjöberg, Å., Lutz, M., Tannergren, C., Wingolf, C., Borde, A. & Ungell, A.-L. (2013) Comprehensive study on regional human intestinal permeability and prediction of fraction absorbed of drugs using the Ussing chamber technique. *European Journal of Pharmaceutical Sciences*, **48**, 166–180.

Skouloubris, S., Thiberge, J.M., Labigne, A. & De Reuse, H. (1998) The Helicobacter pylori UreI protein is not involved in urease activity but is essential for bacterial survival in vivo. *Infection and Immunity*, **66**, 4517–4521.

Smith, H.K., Shepherd, M., Monk, C., Green, J. & Poole, R.K. (2011) The NO-responsive hemoglobins of Campylobacter jejuni: concerted responses of two globins to NO and evidence in vitro for globin regulation by the transcription factor NssR. *Nitric Oxide: Biology and Chemistry*, **25**, 234–241.

Smith, Y.C., Grande, K.K., Rasmussen, S.B. & O'Brien, A.D. (2006) Novel three-dimensional organoid model for evaluation of the interaction of uropathogenic Escherichia coli with terminally differentiated human urothelial cells. *Infection and Immunity*, **74**, 750–757.

Solnick, J.V., Eaton, K.A. & Peek, R.M. (2016a) Animal models of Helicobacter pylori infection. *Helicobacter pylori Research*.

Solnick, J.V., Eaton, K.A. & Peek, R.M. (2016b) Animal Models of Helicobacter pylori Infection. In *Helicobacter pylori Research* (ed. Backert, S. & Yamaoka, Y.). Springer Japan, Tokyo, pp. 273–297.

Sommerlad, S.M. & Hendrixson, D.R. (2007) Analysis of the roles of FlgP and FlgQ in flagellar motility of Campylobacter jejuni. *Journal of Bacteriology*, **189**, 179–186.

Sørensen, M.C.H., Van Alphen, L.B. & Frodor…, C. (2012) Phase variable expression of capsular polysaccharide modifications allows Campylobacter jejuni to avoid bacteriophage infection in chickens. *Frontiers in cellular …*.

Song, Y.C., Jin, S., Louie, H., Ng, D., Lau, R., Zhang, Y., *et al.* (2004) FlaC, a protein of Campylobacter jejuni TGH9011 (ATCC43431) secreted through the flagellar apparatus, binds epithelial cells and influences cell invasion. *Molecular Microbiology*, **53**, 541–553.

Sperandio, B., Fischer, N., Joncquel Chevalier-Curt, M., Rossez, Y., Roux, P., Robbe Masselot, C., *et al.* (2013) Virulent Shigella flexneri affects the secretion, expression, and glycosylation of gel-forming mucins in mucus-producing cells. *Infection and Immunity*.

Spreeuwel, J.P. van, Duursma, G.C., Meijer, C.J., Bax, R., Rosekrans, P.C. & Lindeman, J. (1985) Campylobacter colitis: histological immunohistochemical and ultrastructural findings. *Gut*, **26**, 945–951.

Stahl, M., Friis, L.M., Nothaft, H., Liu, X., Li, J., Szymanski, C.M., *et al.* (2011) L-fucose utilization provides Campylobacter jejuni with a competitive advantage. *Proceedings of the National Academy of Sciences of the United States of America*, **108**, 7194–7199.

Stahl, M. & Stintzi, A. (2011) Identification of essential genes in C. jejuni genome highlights hyper-variable plasticity regions. *Functional & Integrative Genomics*, **11**, 241–257.

Stahl, M., Ries, J., Vermeulen, J., Yang, H., Sham, H.P., Crowley, S.M., *et al.* (2014) A novel mouse model of Campylobacter jejuni gastroenteritis reveals key pro-inflammatory and tissue protective roles for Toll-like receptor signaling during infection. *PLoS Pathogens*, **10**, e1004264.

Stahl, M. & Vallance, B.A. (2015) Insights into Campylobacter jejuni colonization of the mammalian intestinal tract using a novel mouse model of infection. *Gut microbes*, **6**, 143–148.

Stahl, M., Frirdich, E., Vermeulen, J., Badayeva, Y., Li, X., Vallance, B.A., *et al.* (2016) The Helical Shape of Campylobacter jejuni Promotes In Vivo Pathogenesis by Aiding Transit through Intestinal Mucus and Colonization of Crypts. *Infection and Immunity*, **84**, 3399–3407.

Stahl, M., Graef, F.A. & Vallance, B.A. (2017) Mouse Models for Campylobacter jejuni Colonization and Infection. *Methods in Molecular Biology*, **1512**, 171–188.

Stel, A.-X. van der, Mourik, A. van, Dijk, L.H. van, Parker, C.T., Kelly, D.J., Lest, C.H.A. van de, *et al.* (2014) The Campylobacter jejuni RacRS system regulates fumarate utilization in a low oxygen environment. *Environmental Microbiology*.

Stelzer, E.H.K. (2015) Light-sheet fluorescence microscopy for quantitative biology. *Nature Methods*, **12**, 23–26.

Storz, G., Wolf, Y.I. & Ramamurthi, K.S. (2014) Small proteins can no longer be ignored. *Annual Review of Biochemistry*, **83**, 753–777.

Straub, T.M., Höner zu Bentrup, K., Orosz-Coghlan, P., Dohnalkova, A., Mayer, B.K., Bartholomew, R.A., *et al.* (2007) In vitro cell culture infectivity assay for human noroviruses. *Emerging Infectious Diseases*, **13**, 396–403.

Styer, C.M., Hansen, L.M., Cooke, C.L., Gundersen, A.M., Choi, S.S., Berg, D.E., *et al.* (2010) Expression of the BabA adhesin during experimental infection with Helicobacter pylori. *Infection and Immunity*, **78**, 1593–1600.

Suerbaum, S. & Michetti, P. (2002) Helicobacter pylori infection. *The New England Journal of Medicine*, **347**, 1175–1186.

Svensson, S.L., Davis, L.M., MacKichan, J.K., Allan, B.J., Pajaniappan, M., Thompson, S.A., *et al.* (2009) The CprS sensor kinase of the zoonotic pathogen Campylobacter jejuni influences biofilm formation and is required for optimal chick colonization. *Molecular Microbiology*, **71**, 253–272.

Svensson, S.L. & Sharma, C.M. (2016) Small rnas in bacterial virulence and communication. *Microbiology spectrum*, **4**.

Szabady, R.L., Yanta, J.H., Halladin, D.K., Schofield, M.J. & Welch, R.A. (2011) TagA is a secreted protease of Vibrio cholerae that specifically cleaves mucin glycoproteins. *Microbiology*, **157**, 516–525.

Szymanski, C.M., King, M., Haardt, M. & Armstrong, G.D. (1995) Campylobacter jejuni motility and invasion of Caco-2 cells. *Infection and Immunity*, **63**, 4295–4300.

Szymanski, C.M., Michael, F.S., Jarrell, H.C., Li, J., Gilbert, M., Larocque, S., *et al.* (2003) Detection of conserved N-linked glycans and phase-variable lipooligosaccharides and capsules from campylobacter cells by mass spectrometry and high resolution magic angle spinning NMR spectroscopy. *The Journal of Biological Chemistry*, **278**, 24509–24520.

Takeichi, M. (1991) Cadherin cell adhesion receptors as a morphogenetic regulator. *Science*, **251**, 1451–1455.

Takeuchi, A. (1967) Electron microscope studies of experimental Salmonella infection. I. Penetration into the intestinal epithelium by Salmonella typhimurium. *The American Journal of Pathology*, **50**, 109–136.

Tan, H.-Y., Trier, S., Rahbek, U.L., Dufva, M., Kutter, J.P. & Andresen, T.L. (2018) A multi-chamber microfluidic intestinal barrier model using Caco-2 cells for drug transport studies. *Plos One*, **13**, e0197101.

Tan, S., Tompkins, L.S. & Amieva, M.R. (2009) Helicobacter pylori usurps cell polarity to turn the cell surface into a replicative niche. *PLoS Pathogens*, **5**, e1000407.

Tan, S., Noto, J.M., Romero-Gallo, J., Peek, R.M. & Amieva, M.R. (2011) Helicobacter pylori

perturbs iron trafficking in the epithelium to grow on the cell surface. *PLoS Pathogens*, **7**, e1002050.

Tao, L., Zhang, J., Meraner, P., Tovaglieri, A., Wu, X., Gerhard, R., *et al.* (2016) Frizzled proteins are colonic epithelial receptors for C. difficile toxin B. *Nature*, **538**, 350–355.

Tareen, A.M., Dasti, J.I., Zautner, A.E., Gross, U. & Lugert, R. (2010) Campylobacter jejuni proteins Cj0952c and Cj0951c affect chemotactic behaviour towards formic acid and are important for invasion of host cells. *Microbiology*, **156**, 3123–3135.

Tareen, A.M., Lüder, C.G.K., Zautner, A.E., Groβ, U., Heimesaat, M.M., Bereswill, S., *et al.* (2013) The Campylobacter jejuni Cj0268c protein is required for adhesion and invasion in vitro. *Plos One*, **8**, e81069.

Taveirne, M.E., Theriot, C.M., Livny, J. & DiRita, V.J. (2013) The complete Campylobacter jejuni transcriptome during colonization of a natural host determined by RNAseq. *Plos One*, **8**, e73586.

Tegtmeyer, N., Wessler, S., Necchi, V., Rohde, M., Harrer, A., Rau, T.T., *et al.* (2017) Helicobacter pylori Employs a Unique Basolateral Type IV Secretion Mechanism for CagA Delivery. *Cell Host & Microbe*, **22**, 552–560.e5.

Teunis, P., Van den Brandhof, W., Nauta, M., Wagenaar, J., Van den Kerkhof, H. & Van Pelt, W. (2005) A reconsideration of the Campylobacter dose-response relation. *Epidemiology and Infection*, **133**, 583–592.

Tezera, L.B., Bielecka, M.K., Chancellor, A., Reichmann, M.T., Shammari, B.A., Brace, P., *et al.* (2017) Dissection of the host-pathogen interaction in human tuberculosis using a bioengineered 3-dimensional model. *eLife*, **6**.

Thibault, P., Logan, S.M., Kelly, J.F., Brisson, J.R., Ewing, C.P., Trust, T.J., *et al.* (2001) Identification of the carbohydrate moieties and glycosylation motifs in Campylobacter jejuni flagellin. *The Journal of Biological Chemistry*, **276**, 34862–34870.

Thomas, J.M.D., Chakraborty, A., Sharp, M.K. & Berson, R.E. (2011) Spatial and temporal resolution of shear in an orbiting petri dish. *Biotechnology Progress*, **27**, 460–465.

Torras, N., García-Díaz, M., Fernández-Majada, V. & Martínez, E. (2018) Mimicking Epithelial Tissues in Three-Dimensional Cell Culture Models. *Frontiers in bioengineering and biotechnology*, **6**, 197.

Tsilingiri, K., Barbosa, T., Penna, G., Caprioli, F., Sonzogni, A., Viale, G., *et al.* (2012) Probiotic and postbiotic activity in health and disease: comparison on a novel polarised ex-vivo organ culture model. *Gut*, **61**, 1007–1015.

Turner, J.R. (2009) Intestinal mucosal barrier function in health and disease. *Nature Reviews. Immunology*, **9**, 799–809.

Ulasi, G.N., Creese, A.J., Hui, S.X., Penn, C.W. & Cooper, H.J. (2015) Comprehensive mapping of O-glycosylation in flagellin from Campylobacter jejuni 11168: A multienzyme differential ion mobility mass spectrometry approach. *Proteomics*, **15**, 2733–2745.

Unsworth, B.R. & Lelkes, P.I. (1998) Growing tissues in microgravity. *Nature Medicine*, **4**, 901–907.

Ussing, H.H. (1949) The active ion transport through the isolated frog skin in the light of tracer studies. *Acta Physiologica Scandinavica*, **17**, 1–37.

Van Deun, K., Haesebrouck, F., Van Immerseel, F., Ducatelle, R. & Pasmans, F. (2008a) Short-chain fatty acids and L-lactate as feed additives to control Campylobacter jejuni infections in broilers. *Avian Pathology*, **37**, 379–383.

Van Deun, K., Pasmans, F., Ducatelle, R., Flahou, B., Vissenberg, K., Martel, A., *et al.* (2008b) Colonization strategy of Campylobacter jejuni results in persistent infection of the chicken

gut. *Veterinary Microbiology*, **130**, 285–297.

Van Deun, K., Pasmans, F., Van Immerseel, F., Ducatelle, R. & Haesebrouck, F. (2008c) Butyrate protects Caco-2 cells from Campylobacter jejuni invasion and translocation. *The British Journal of Nutrition*, **100**, 480–484.

VanDussen, K.L., Marinshaw, J.M., Shaikh, N., Miyoshi, H., Moon, C., Tarr, P.I., *et al.* (2015) Development of an enhanced human gastrointestinal epithelial culture system to facilitate patient-based assays. *Gut*, **64**, 911–920.

Vegge, C.S., Brøndsted, L., Li, Y.-P., Bang, D.D. & Ingmer, H. (2009) Energy taxis drives Campylobacter jejuni toward the most favorable conditions for growth. *Applied and Environmental Microbiology*, **75**, 5308–5314.

Velayudhan, J., Jones, M.A., Barrow, P.A. & Kelly, D.J. (2004) L-serine catabolism via an oxygen-labile L-serine dehydratase is essential for colonization of the avian gut by Campylobacter jejuni. *Infection and Immunity*, **72**, 260–268.

Vries, S.P. de, Gupta, S., Baig, A., Wright, E., Wedley, A., Jensen, A.N., *et al.* (2017a) Genome-wide fitness analyses of the foodborne pathogen Campylobacter jejuni in in vitro and in vivo models. *Scientific reports*, **7**, 1251.

Vries, S.P.W. de, Linn, A., Macleod, K., MacCallum, A., Hardy, S.P., Douce, G., *et al.* (2017b) Analysis of Campylobacter jejuni infection in the gnotobiotic piglet and genome-wide identification of bacterial factors required for infection. *Scientific reports*, **7**, 44283.

Wäldchen, S., Lehmann, J., Klein, T., Linde, S. van de & Sauer, M. (2015) Light-induced cell damage in live-cell super-resolution microscopy. *Scientific reports*, **5**, 15348.

Wang, B., Wu, G., Zhou, Z., Dai, Z., Sun, Y., Ji, Y., *et al.* (2015) Glutamine and intestinal barrier function. *Amino Acids*, **47**, 2143–2154.

Wang, L., Jeon, B., Sahin, O. & Zhang, Q. (2009) Identification of an arsenic resistance and arsenic-sensing system in Campylobacter jejuni. *Applied and Environmental Microbiology*, **75**, 5064–5073.

Wang, Y., Gunasekara, D.B., Reed, M.I., DiSalvo, M., Bultman, S.J., Sims, C.E., *et al.* (2017) A microengineered collagen scaffold for generating a polarized crypt-villus architecture of human small intestinal epithelium. *Biomaterials*, **128**, 44–55.

Waskito, L.A., Salama, N.R. & Yamaoka, Y. (2018) Pathogenesis of Helicobacter pylori infection. *Helicobacter*, **23 Suppl 1**, e12516.

Wassenaar, T.M., Bleumink-Pluym, N.M. & Zeijst, B.A. van der. (1991) Inactivation of Campylobacter jejuni flagellin genes by homologous recombination demonstrates that flaA but not flaB is required for invasion. *The EMBO Journal*, **10**, 2055–2061.

Wassenaar, T.M., Zeijst, B.A. van der, Ayling, R. & Newell, D.G. (1993) Colonization of chicks by motility mutants of Campylobacter jejuni demonstrates the importance of flagellin A expression. *Journal of general microbiology*, **139 Pt 6**, 1171–1175.

Watson, A.J.M. & Hughes, K.R. (2012) TNF-α-induced intestinal epithelial cell shedding: implications for intestinal barrier function. *Annals of the New York Academy of Sciences*, **1258**, 1–8.

Watson, R.O. & Galán, J.E. (2008) Campylobacter jejuni survives within epithelial cells by avoiding delivery to lysosomes. *PLoS Pathogens*, **4**, e14.

Weiner, A., Mellouk, N., Lopez-Montero, N., Chang, Y.-Y., Souque, C., Schmitt, C., *et al.* (2016) Macropinosomes are key players in early shigella invasion and vacuolar escape in epithelial cells. *PLoS Pathogens*, **12**, e1005602.

Westermann, A.J., Gorski, S.A. & Vogel, J. (2012) Dual RNA-seq of pathogen and host. *Nature Reviews. Microbiology*, **10**, 618–630.

Westermann, A.J., Förstner, K.U., Amman, F., Barquist, L., Chao, Y., Schulte, L.N., *et al.* (2016) Dual RNA-seq unveils noncoding RNA functions in host-pathogen interactions. *Nature*, **529**, 496–501.

Westermann, A.J., Barquist, L. & Vogel, J. (2017) Resolving host-pathogen interactions by dual RNA-seq. *PLoS Pathogens*, **13**, e1006033.

Westermann, A.J. (2018) Regulatory RNAs in Virulence and Host-Microbe Interactions. *Microbiology spectrum*, **6**.

Westra, E.R., Buckling, A. & Fineran, P.C. (2014) CRISPR-Cas systems: beyond adaptive immunity. *Nature Reviews. Microbiology*, **12**, 317–326.

Whitehouse, C.A., Balbo, P.B., Pesci, E.C., Cottle, D.L., Mirabito, P.M. & Pickett, C.L. (1998) Campylobacter jejuni cytolethal distending toxin causes a G2-phase cell cycle block. *Infection and Immunity*, **66**, 1934–1940.

Wilson, S.S., Tocchi, A., Holly, M.K., Parks, W.C. & Smith, J.G. (2015) A small intestinal organoid model of non-invasive enteric pathogen-epithelial cell interactions. *Mucosal Immunology*, **8**, 352–361.

Wine, E., Chan, V.L. & Sherman, P.M. (2008) Campylobacter jejuni mediated disruption of polarized epithelial monolayers is cell-type specific, time dependent, and correlates with bacterial invasion. *Pediatric Research*, **64**, 599–604.

Wong, A., Lange, D., Houle, S., Arbatsky, N.P., Valvano, M.A., Knirel, Y.A., *et al.* (2015) Role of capsular modified heptose in the virulence of Campylobacter jejuni. *Molecular Microbiology*, **96**, 1136–1158.

Worton, K.J., Candy, D.C., Wallis, T.S., Clarke, G.J., Osborne, M.P., Haddon, S.J., *et al.* (1989) Studies on early association of Salmonella typhimurium with intestinal mucosa in vivo and in vitro: relationship to virulence. *Journal of Medical Microbiology*, **29**, 283–294.

Wösten, M.M.S.M., Wagenaar, J.A. & Putten, J.P.M. van. (2004) The FlgS/FlgR two-component signal transduction system regulates the fla regulon in Campylobacter jejuni. *The Journal of Biological Chemistry*, **279**, 16214–16222.

Woude, M.W. van der. (2011) Phase variation: how to create and coordinate population diversity. *Current Opinion in Microbiology*, **14**, 205–211.

Wright, J.A., Grant, A.J., Hurd, D., Harrison, M., Guccione, E.J., Kelly, D.J., *et al.* (2009) Metabolite and transcriptome analysis of Campylobacter jejuni in vitro growth reveals a stationary-phase physiological switch. *Microbiology*, **155**, 80–94.

Wroblewski, L.E., Peek, R.M. & Wilson, K.T. (2010) Helicobacter pylori and gastric cancer: factors that modulate disease risk. *Clinical Microbiology Reviews*, **23**, 713–739.

Wu, G. (1998) Intestinal mucosal amino acid catabolism. *The Journal of Nutrition*, **128**, 1249–1252.

Wu, Z., Nybom, P. & Magnusson, K.E. (2000) Distinct effects of Vibrio cholerae haemagglutinin/protease on the structure and localization of the tight junction-associated proteins occludin and ZO-1. *Cellular Microbiology*, **2**, 11–17.

Xu, F., Wu, C., Guo, F., Cui, G., Zeng, X., Yang, B., *et al.* (2015) Transcriptomic analysis of Campylobacter jejuni NCTC 11168 in response to epinephrine and norepinephrine. *Frontiers in microbiology*, **6**, 452.

Yamabayashi, S. (1987) Periodic acid-Schiff-alcian blue: a method for the differential staining of glycoproteins. *The Histochemical journal*, **19**, 565–571.

Yao, R., Burr, D.H., Doig, P., Trust, T.J., Niu, H. & Guerry, P. (1994) Isolation of motile and non-motile insertional mutants of Campylobacter jejuni: the role of motility in adherence and invasion of eukaryotic cells. *Molecular Microbiology*, **14**, 883–893.

Yao, R., Burr, D.H. & Guerry, P. (1997) CheY-mediated modulation of Campylobacter jejuni virulence. *Molecular Microbiology*, **23**, 1021–1031.

Yin, Y. & Zhou, D. (2018) Organoid and enteroid modeling of salmonella infection. *Frontiers in cellular and infection microbiology*, **8**, 102.

Yokoyama, T., Paek, S., Ewing, C.P., Guerry, P. & Yeo, H.-J. (2008) Structure of a sigma28-regulated nonflagellar virulence protein from Campylobacter jejuni. *Journal of Molecular Biology*, **384**, 364–376.

Young, K.T., Davis, L.M. & Dirita, V.J. (2007) Campylobacter jejuni: molecular biology and pathogenesis. *Nature Reviews. Microbiology*, **5**, 665–679.

Yuki, N. (1997) Molecular mimicry between gangliosides and lipopolysaccharides of Campylobacter jejuni isolated from patients with Guillain-Barré syndrome and Miller Fisher syndrome. *The Journal of Infectious Diseases*, **176 Suppl 2**, S150-3.

Yuki, N. & Miyatake, T. (1998) Guillain-Barré syndrome and Fisher's syndrome following Campylobacter jejuni infection. *Annals of the New York Academy of Sciences*, **845**, 330–340.

Yuki, N., Susuki, K., Koga, M., Nishimoto, Y., Odaka, M., Hirata, K., *et al.* (2004) Carbohydrate mimicry between human ganglioside GM1 and Campylobacter jejuni lipooligosaccharide causes Guillain-Barre syndrome. *Proceedings of the National Academy of Sciences of the United States of America*, **101**, 11404–11409.

Zarepour, M., Bhullar, K., Montero, M., Ma, C., Huang, T., Xia, L., *et al.* (2013) The mucin Muc2 limits pathogen burdens and epithelial barrier dysfunction during Salmonella Typhimurium colitis. *Infection and Immunity*.

Zebian, N., Merkx-Jacques, A., Pittock, P.P., Houle, S., Dozois, C.M., Lajoie, G.A., *et al.* (2016) Comprehensive analysis of flagellin glycosylation in Campylobacter jejuni NCTC 11168 reveals incorporation of legionaminic acid and its importance for host colonization. *Glycobiology*, **26**, 386–397.

Zhang, B., Korolj, A., Lai, B.F.L. & Radisic, M. (2018) Advances in organ-on-a-chip engineering. *Nature reviews. Materials*, **3**, 257–278.

Zhang, D., Tan, M., Zhong, W., Xia, M., Huang, P. & Jiang, X. (2017) Human intestinal organoids express histo-blood group antigens, bind norovirus VLPs, and support limited norovirus replication. *Scientific reports*, **7**, 12621.

Zhang, S. (2004) Beyond the Petri dish. *Nature Biotechnology*, **22**, 151–152.

Zhang, Y.-G., Wu, S., Xia, Y. & Sun, J. (2014) Salmonella-infected crypt-derived intestinal organoid culture system for host-bacterial interactions. *Physiological reports*, **2**.

Zhou, D. & Galán, J. (2001) Salmonella entry into host cells: the work in concert of type III secreted effector proteins. *Microbes and Infection*, **3**, 1293–1298.

Zhou, K., Aertsen, A. & Michiels, C.W. (2014) The role of variable DNA tandem repeats in bacterial adaptation. *FEMS Microbiology Reviews*, **38**, 119–141.

Zhou, W., Chen, Y., Roh, T., Lin, Y., Ling, S., Zhao, S., *et al.* (2018) Multifunctional bioreactor system for human intestine tissues. *ACS biomaterials science & engineering*, **4**, 231–239.

8. List of Figures

9. List of Tables

10. Curriculum vitae

Mona Alzheimer

11. List of Publications

Publications associated to the present work:

Reuter C, **Alzheimer M**, Walles H, Ölschläger TA (2018). An adherent mucus layer attenuates the genotoxic effect of colibactin. *Cellular Microbiology*, 20(2): e 12812.
(Research article)

Manuscripts related to this PhD thesis, which are in preparation and/or submitted:

Alzheimer M, Svensson SL, Schweinlin M, Metzger M, Walles H, Sharma CM (2019). A three-dimensional intestinal tissue model reveals bacterial factors important for colonization with *Campylobacter jejuni*.
(Research article)

Alzheimer M, Schweinlin M, Metzger M, Walles H, Sharma CM (2019). Development of a mucus containing intestinal tissue model and the impact of a protective mucus layer on *Campylobacter jejuni* pathogenesis.
(Research article)

Alzheimer M, Svensson SL, Bischler T, Sharma CM (2019). A genome-wide screen in engineered human tissue identifies new motility and host interaction factors in the food-borne pathogen *Campylobacter jejuni*.
(Research article)

Previous studies that were published prior to the beginning of and/or are unrelated to this PhD thesis:

Springer J, Morton CO, Perry M, Heinz W, Paholcsek M, **Alzheimer M**, Rogers TR, Barnes RA, Einsele H, Loeffler J, White PL (2013). Multicenter comparison of serum and whole-blood specimens for detection of *Aspergillus* DNA in high-risk hematological patients. *J Clin Microbiol*, 51(5): 1445-1450.

Guenther UP, Handoko L, Laggerbauer B, Jablonka S, Chari A, **Alzheimer M**, Ohmer J, Plöttner O, Gehring N, Sickmann A, von Au K, Schuelke M, Fischer U (2009). IGHMBP2 is a ribosome-associated helicase inactive in the neuromuscular disorder distal SMA type 1 (DSMA1). *Hum Mol Genet*, 18(7): 1288-1300.

12. Acknowledgments

In the end, I would like to thank all the people, who contributed with their expertise, time, and energy to the completion of this thesis.

My deepest gratitude is to my mentor Prof. Dr. Cynthia M. Sharma, who never stopped believing in me, even when I lost faith in myself. In an inspiring academic environment, she gave me the opportunity to perform this work in her group and to advance my scientific thinking and experimental skills. She encouraged me from the very beginning to be passionate about my work and present it as such at national and international conferences. Her guidance and continuous support provided me with the chance to learn and to teach, to work and to rest, to progress and to grow. For all that, I am exceedingly grateful.

I am very thankful to Prof. Dr. Heike Walles and Prof. Dr. Jörg Vogel for being part of my PhD thesis committee. Their respective passions for tissue engineering and all things RNA provided invaluable expertise for this work. Also, I thank Prof. Dr. Thomas Dandekar for chairing the doctoral committee and the defense of this thesis.

Much of my gratitude is owed to Dr. Sandy Pernitzsch. She has managed to markedly influence both my professional and personal life in a relatively short time. The unique combination of her scientific mind and artistic creativity has contributed significantly to this work and will have a lasting effect on my path. For me, Sandy's loving and brilliant life force is a beacon in the dark that brightens my life.

I would like to express my immense gratitude to all present and former coworkers of the Sharma lab. Especially, I want to thank Anjie Imsiecke for her strength and positivity, Beli Bremer for the most infectious smile, grazie mille a Eli Fiore per aver reso la mia vita un po' piú italiana, thanks to Dr. Gaurav Dugar for teaching me balance, Dr. Patrick Tan for his inspired food compositions, Sara Eisenbart for always sharing her pastry accomplishments, Dr. Sarah Svensson for her seemingly endless supply of comfort food and Campy knowledge, and Dr. Thorsten Bischler for showing me "the matrix" on my very first day. I am grateful to my former master students Anjie Imsiecke and Stephan Tirier for their excellent work and for indulging my passion for teaching. Thanks to Sarah Zehnter and Mela Schott for their excellent technical assistance over the last years. Also, I want to thank Christine Hambrecht-Schleyer, Fabian König, Kathrin Froschauer, Dr. Lydia Hadjeras, Philipp Kible, and Dr. Sahil Sharma for creating a friendly working atmosphere. Continuous help, intellectual input, and shared laughs constitute the supportive foundation of this group.

I am exceptionally thankful to Dr. Carmen Aguilar and Hilde Merkert. The quiet and emotional but at the same time fun and educational time I shared with them during my sabbatical on the second floor helped me find my way back.

Thanks to PD Dr. Marco Metzger and Dr. Matthias Schweinlin for being my faithful liaison to the TERM, for a fruitful collaboration, and for always having enough pig intestine.

I am particularly grateful to Dr. Sandy Pernitzsch and Dr. Sarah Svensson for proofreading this thesis, their critical comments, and helpful suggestions. Also thanks to Eli Fiore for the final cut.

I thank the Graduate School of Life Sciences (GSLS) of the University of Würzburg for providing such an outstanding and interdisciplinary PhD program. In particular, I am extremely thankful to Dr. Gabi Blum-Oehler for her kind and supportive nature and for always having an open door.

Finally, I want to take this opportunity to express my profound gratitude to the people who have shaped me. First and foremost, I am deeply thankful to my parents, who are caring, inspirational, and unbelievably generous people. They are the pillars, without whom I could not stand. I am eternally grateful to my kind and compassionate parents-in-law for their infinite love and support. My utmost gratitude goes to my aunt. She is my counsel, my lifeline, and the ace up my sleeve. I thank my grandpas for having been the unfaltering foundation of this family and my grandmas for building on this basis with love, food, and laughter. Thanks to my sister and brother, my sister- and brother-in-law, my niece and nephew for making my live exciting, weird, and never boring.

But I owe the greatest support to my husband. Dominik never gave me the feeling that I could not accomplish whatever I wanted to. He is my biggest fan, my most constructive advisor, my rational thinking, my conscience, my safe haven, and my love. Thank you for everything.

13. Appendices

13.1. Appendix to Chapter 2

Appendix Table 2.1: Cell counting of statically cultivated tissue models. Caco-2 cells were reseeded on 24 cell crowns spanned with SISmuc. After 21 days of static cultivation, cells were harvested by trypsin treatment coupled with extensive mechanical dissolution. Subsequently, cells were counted in a Neubauer counting chamber using the trypan blue exclusion method.

Tissue model	No. of cells	Tissue model	No. of cells	Tissue model	No. of cells
crown #01	620,000	crown #09	650,000	crown #17	590,000
crown #02	680,000	crown #10	680,000	crown #18	675,000
crown #03	600,000	crown #11	690,000	crown #19	650,000
crown #04	675,000	crown #12	550,000	crown #20	700,000
crown #05	590,000	crown #13	635,000	crown #21	660,000
crown #06	620,000	crown #14	675,000	crown #22	660,000
crown #07	675,000	crown #15	640,000	crown #23	650,000
crown #08	710,000	crown #16	600,000	crown #24	630,000
Average number of Caco-2 cells					**650,000**

Appendix Table 2.2: PicoGreen assay of statically cultivated tissue models. Using the Quant-iT™ PicoGreen® dsDNA assay kit (ThermoFisher Scientific), DNA was isolated from 300,000 and 600,000 Caco-2 cells routinely cultivated in cell culture flasks. DNA content was determined relative to a prior standard curve. In addition, after 21 days of cultivation, three tissue models were also subjected to determination of DNA content and the number of Caco-2 cells on the respective tissue models was calculated in retrospect. The relative fluorescence intensities designated with an asterisk (*) indicate the final intensity after subtraction of background fluorescence of unseeded SISmuc.

	Relative fluorescence intensity	**DNA content λ [ng/ml]**	**Calculated No. of Caco-2 cells**
300,000 Caco-2 cells	124333.176	219	–
600,000 Caco-2 cells	23811.072	423	–
crown #01	33515.748*	597	830,000
crown #02	20855.050*	370	520,000
crown #03	28551.862*	508	710,000
	Average number of Caco-2 cells		**690,000**

Appendix Table 2.3: Cell counting of dynamically cultivated tissue models. Same as for the static tissue models, Caco-2 cells were seeded on SISmuc (12 cell crowns in total) and statically cultivated for two days before resettling them on an orbital shaker. After additional 19 days in dynamic culture, Caco-2 cells were harvested as described previously and counted in a Neubauer counting chamber after selectively staining for live cells using the dye trypan blue.

Tissue model	No. of cells	Tissue model	No. of cells	Tissue model	No. of cells
crown #01	675,000	crown #05	685,000	crown #09	630,000
crown #02	630,000	crown #06	640,000	crown #10	680,000
crown #03	640,000	crown #07	670,000	crown #11	690,000
crown #04	690,000	crown #08	690,000	crown #12	720,000
Average number of Caco-2 cells					**670,000**

13.2. Appendix to Chapter 3

Appendix Table 3.1: Operon structures of genes identified in this Tn-seq study with attenuating transposon insertions. According to primary TSS annotations obtained from dRNA-seq data of (Dugar *et al.*, 2013), genes identified in this genome-wide screen with decreased transposon insertion counts in the output libraries (ADH/INT) compared to the input libraries (SUP) (see also Chapter 3.2.1, Table 3.1) were allocated to operonic transcripts. The first column (Operon) shows the first and last gene spanning the operon structure. Genes within the respective operon that showed significant (p-value ≤ 0.05) $\log_2$ fold changes ≤ 1 are shown in bold (values in bold represent those fold changes). Those in the same operon that did not pass the set cut-offs, *i.e.* with $\log_2$ fold changes < |1| and/or p-values > 0.05, are depicted in grey. Genes with less than 10 read counts per condition were excluded from the analysis and their values are not shown (–). Those not identified in previous *in-vitro* or *in-vivo* genome-wide screens are highlighted in grey.

Operon	Genes in the operon	2D Tn-seq ADH/INT	3D Tn-seq ADH/INT
Motility and Chemotaxis			
Cj0040-Cj0041	**Cj0040**	+1.77/–	-1.74/**-9.32**
	Cj0041 (*fliK*)	+0.35/-0.90	-0.66/**-3.92**
Cj0042-Cj0043	**Cj0042 (*flgD*)**	+0.72/+1.35	+0.06/**-1.56**
	Cj0043 (*flgE*)	**-1.40**/-0.70	+0.02/+0.51
Cj0062c-Cj0060c	**Cj0062c**	+2.00/+2.10	**-1.47/-3.20**
	Cj0061c (*fliA*)	-0.91/**-1.15**	**-2.44/-5.15**
	Cj0060c (*fliM*)	+0.07/-1.06	**-2.22/-5.20**
Cj0164c-Cj0160c	Cj0164c (*ubiA*)	–/–	–/–
	Cj0163c	+0.21/-0.94	**-1.88/-7.26**
	Cj0162c (*flgW*)	**+1.76**/+1.04	-0.14/**-1.95**
	Cj0161c (*moaA*)	+0.75/-0.91	+0.22/+0.99
	Cj0160c	-2.12/+0.50	-0.41/+0.31
Cj0318-Cj0321	**Cj0318 (*fliF*)**	-0.19/-0.45	**-1.08/-3.94**
	Cj0319 (*fliG*)	-0.29/**-1.44**	**-1.07/-3.24**
	Cj0320 (*fliH*)	+1.92/+0.81	-0.93/**-3.10**
	Cj0321 (*dxs*)	–/–	–/–
Cj0337c-Cj0336c	**Cj0337c (*motA*)**	+0.45/**-1.22**	**-2.61/-5.42**
	Cj0336c (*motB*)	+0.25/-0.76	**-2.85/-5.85**
Cj0350-Cj0352	**Cj0350**	**-2.31/-2.21**	+0.20/**-1.06**
	Cj0351 (*fliN*)	+3.00/+3.33	-1.59/**-3.82**
	Cj0352	-0.44/**-1.30**	-0.18/-0.54
Cj0456c-Cj0454c	**Cj0456c**	+0.52/+0.45	**-2.11/-3.96**
	Cj0455c	+0.19/-0.79	**-2.80/-5.81**
	Cj0454c	+0.18/-0.67	**-2.83/-5.88**
Cj0547-Cj0550	**Cj0547 (*flaG*)**	**+6.49**/–	-0.84/-0.98
	Cj0548 (*fliD*)	-0.48/-2.14	-0.84/**-2.75**
	Cj0549 (*fliS*)	**-11.63/-11.79**	-0.77/**-3.34**
	Cj0550	–/–	-2.11/-1.23
Cj0883c-Cj0882c	**Cj0883c**	-0.35/-0.11	+0.28/**-2.49**
	Cj0882c (*flhA*)	-0.69/**-1.36**	-0.96/**-3.99**
Cj1026c-Cj1025c	**Cj1026c (*flgP*)**	+0.82/-0.94	**-2.88/-6.08**
	Cj1025c (*flgQ*)	-0.14/-0.45	**-2.50/-5.47**

continued on next page

Operon	Genes in the operon	2D Tn-seq ADH/INT	3D Tn-seq ADH/INT
Cj1345c-Cj1340c	Cj1345c	-0.59/+0.29	+0.19/+1.53
	Cj1344c	–/–	–/–
	Cj1343c	**-1.26**/-0.74	-0.39/-0.72
	Cj1342c	-0.52/-0.11	-0.29/-0.60
	Cj1341c	+0.29/+0.24	-0.48/-1.05
	Cj1340c	-0.38/-0.07	-0.92/**-1.94**
Flagella modifications			
Cj1331-Cj1333	**Cj1331 (*ptmB*)**	**-1.61**/-0.07	+0.08/-0.47
	Cj1332 (*ptmA*)	-0.33/-0.71	-0.75/**-1.48**
	Cj1333 (*pseD*)	-0.77/-0.56	**-1.67/-3.17**
Unknown function			
Cj1077-Cj1079	**Cj1077 (*ctsT*)**	-0.21/+0.29	+0.19/**+1.53**
	Cj1078	-0.69/**-1.06**	+0.02/+0.40
	Cj1079	-0.89/**-11.25**	-0.74/+0.63
Cj0809c-Cj0808c	**Cj0809c**	**-1.43/-1.72**	**-1.07/-2.46**
	Cj0808c	–/–	-1.54/**-3.27**

Appendix Table 3.2: Operon structures of genes identified in this Tn-seq study with beneficial transposon insertions. According to primary TSS annotations obtained from dRNA-seq data of (Dugar *et al.*, 2013), genes identified in this genome-wide screen with decreased transposon insertion counts in the output libraries (ADH/INT) compared to the input libraries (SUP) (see also Chapter 3.2.2, Table 3.2) were allocated to operonic transcripts. The first column (Operon) shows the first and last gene spanning the operon structure. Genes within the respective operon that showed significant (p-value ≤ 0.05) $\log_2$ fold changes ≥ 1 are shown in bold (values in bold represent those fold changes). Those in the same operon that did not pass the set cut-offs, *i.e.* with $\log_2$ fold changes < |1| and/or p-values > 0.05, are depicted in grey. Genes with less than 10 read counts per condition were excluded from the analysis and their values are not shown (–). Those not identified in previous *in-vitro* or *in-vivo* genome-wide screens are highlighted in grey.

Operon	Genes in the operon	2D Tn-seq ADH/INT	3D Tn-seq ADH/INT
Motility and chemotaxis			
Cj0285c-Cj0281c	**Cj0285c (*cheV*)**	+0.86/**+1.52**	+0.46/+0.74
	Cj0284c (*cheA*)	**+3.18/+3.65**	+0.70/**+1.49**
	Cj0283c (*cheW*)	-1.40/+0.08	+0.01/+0.23
	Cj0282c (*serB*)	–/–	–/–
	Cj0281c (*tal*)	+1.27/+2.02	-0.11/+0.17
Broad regulatory function			
Cj1261-Cj1262	**Cj1261 (*racR*)**	–/+3.80	**+9.02**/–
	Cj1262 (*racS*)	**+2.13/+2.58**	+0.52/+0.73
	Cj1263 (*recR*)	+0.89/+0.10	+0.20/+0.84
Ion transporters			
Cj1164c-Cj1161c	**Cj1164c**	**+1.97/+2.68**	-0.99/+0.56
	Cj1163c	+0.26/**+1.53**	+1.18/**+1.40**
	Cj1162c	–/–	–/+0.79
	Cj1161c	+0.33/-0.23	+0.37/+0.40
Cell wall, membrane, and envelope biogenesis			
Cj1448c-Cj1447c	**Cj1448c (*kpsM*)**	**–/+13.15**	**–/–**
	Cj1447c (*kpsT*)	**+7.30/+7.77**	+1.80/+2.58
Cj1445c-Cj1441c	**Cj1445c (*kpsE*)**	+3.49/**+3.90**	+1.19/+0.55
	Cj1444c (*kpsD*)	**+13.65/+13.23**	+2.19/+2.20
	Cj1443c (*kpsF*)	–/–	–/–
	Cj1442c	–/–	–/–
	Cj1441c (*kfiD*)	**+13.14/+13.59**	**–/–**
Cj1439c-Cj1434c	**Cj1439c (*glf*)**	**+5.2/+6.31**	+2.01/**+2.88**
	Cj1438c	**+12.40/+15.35**	**–/–**
	Cj1437c	+2.25/+2.57	+0.35/-0.05
	Cj1436c	**+1.21**/+0.92	+0.25/-0.17
	Cj1435c	–/–	–/–
	Cj1434c	**+11.60/–**	**–/–**
Cj1133-Cj1136	Cj1133 (*waaC*)	–/–	–/–
	Cj1134 (*htrB*)	–/–	–/–
	Cj1135	**+3.33/+3.89**	+0.13/+0.03
	Cj1136	**+2.20/+2.36**	+0.14/-0.15

continued on next page

Operon	Genes in the operon	2D Tn-seq ADH/INT	3D Tn-seq ADH/INT
Cj1140-Cj1143	**Cj1140 (*cstIII*)**	**+2.19/+2.13**	-0.24/-0.11
	Cj1141 (*neuB1*)	**+2.02/+2.14**	-0.23/-0.59
	Cj1142 (*neuC1*)	**+2.29/+2.06**	-0.17/+0.13
	Cj1143 (*neuA1*)	**+1.92/+1.92**	-0.02/+0.70
Energy production and respiration			
Cj1411c-Cj1410c	**Cj1411c**	**+3.22/+5.28**	-0.01/+0.64
	Cj1410c	+3.61/**+5.18**	+0.68/+0.50
Function unknown			
Cj0248-0249	**Cj0248**	**+1.09/+1.75**	+0.48/+0.25
	Cj0249	**+1.46/+2.35**	+0.86/**+1.27**

13.3. Appendix to Chapter 6

Appendix Table 6.1: Plasmids. Please note that detailed descriptions for the construction of selected plasmids are given in Chapter 6.2. (Microbiological method).

Name	Description/Generation	Origin/ Marker	Reference
pAC1H	**Plasmid carrying hygromycin resistance cassette (*aph(7'')*)**	ColE1/ pBR 332/ Hyg^R	(Cameron & Gaynor, 2014)
pAI2.1	**Intermediary plasmid for translational fusions to *sfgfp* in *C. jejuni* strain NCTC11168.** Ligation of *NotI/EcoRI*-digested PCR product amplified with CSO-2819/2820 on gDNA of a *C. jejuni* NCTC11168 strain carrying a translational fusion of *hupB* (Cj0913c) to *sfGFP* (CSS-3357) with CSO-2748/2818 on pSSv53 (*DpnI*-digested).	p15Amod/ Amp^R, Cm^R	A. Imsiecke, Sharma lab
pGD7.1	**Intermediary plasmid for construction of pGD25.1, complementation of CJnc180/190 deletion with CJnc180/190 in *C. jejuni* strain NCTC11168.** Insertion of the *rdxA* (Cj1066) locus of *C. jejuni* strain NCTC11168 into pJV752.1 cloning vector. Ligation of *XbaI/XhoI*-digested PCR product amplified with CSO-0345/0348 on gDNA of *C. jejuni* NCTC11168 and pJV752.1 (*DpnI/XbaI/Xho1*-digested).	p15Amod/ Amp^R	G. Dugar, Sharma lab
pGD25.1	**Plasmid for complementation of CJnc180/190 deletion with CJnc180/190 in *C. jejuni* strain NCTC11168 using *C. coli cat* cassette.** Ligation of *NdeI/ClaI*-digested PCR product amplified with CSO-0354/0355 on gDNA of *C. jejuni* NCTC11168, *NdeI*-digested PCR product amplified with CSO-0573/0350 on pGD107.1 (*DpnI*-digested), and *ClaI*-digested PCR product amplified with CSO-0347/0346 on pGD7.1 (*DpnI*-digested).	p15Amod/ Amp^R, Cm^R	G. Dugar, Sharma lab
pGD69.1	**Intermediary plasmid for construction of pMA16.1, complementation of *pgp1* deletion with *pgp1* in *C. jejuni* strain 81-176.** Ligation of *XbaI/DpnI*-digested PCR product amplified with CSO-0748/0749 on gDNA of *C. jejuni* NCTC11168 and *XbaI/DpnI*-digested PCR product amplified with JVO-0900/0901 on pKP8.35.	pBR322/ Amp^R	G. Dugar, Sharma lab
pGD98.12	**Intermediary plasmid for construction of pMA16.1, complementation of *pgp1* deletion with *pgp1* in *C. jejuni* strain 81-176.** Ligation of *NdeI/ClaI/DpnI*-digested PCR product amplified with CSO-0347/0350 on pGD25.1 and *NdeI/ClaI*-digested PCR product amplified with CSO-1138/1139 on pGD69.1.	p15Amod/ Amp^R, Cm^R	G. Dugar, Sharma lab
pGD107.1	**Plasmid carrying chloramphenicol resistance cassette (*C. coli cat*)**	p15Amod/ Amp^R, Cm^R	(Dugar *et al.*, 2016)
pGD117.1	**Intermediary plasmid for construction of pMA16.1, complementation of *pgp1* deletion with *pgp1* in *C. jejuni* strain 81-176.** Ligation of inverse PCR product amplified with CSO-2171/2172 on pGD98.12 (*Dpn1*-digested).	p15Amod/ Amp^R, Cm^R	G. Dugar, Sharma lab
pGG1	**Plasmid carrying kanamycin resistance cassette (*aphA-3*)**	ColE1/ Kan^R	(Dugar *et al.*, 2016)
pGG5	**Intermediary plasmid for translational fusions to *sfgfp* in *C. jejuni* strain NCTC11168.** Blunt end ligation of inverted PCR product amplified with CSO-0055/0056 on pXG10-SF.	pSC101*/ Cm^R	G. Golfieri, Sharma lab
pGG9.1	**Intermediary plasmid for translational fusions to *sfgfp* in *C. jejuni* strain NCTC11168.** Ligation of *NheI/NsI*-digested PCR product amplified with CSO-0103/0105 on gDNA of *H. pylori* strain 26695 and *NheI/NsI*-digested pGG5.	pSC101*/ Cm^R	G. Golfieri, Sharma lab

continued on next page

Name	Description/Generation	Origin/ Marker	Reference
pJV752.1	**Cloning vector, pZE12-*luc* with modified p15A origin**	p15Amod/ Amp^R	(Sharma *et al.*, 2007)
pKP8.35	pBAD control plasmid, expresses 50 nt nonsense RNA derived from *rrnB* terminator	pBR322/ Amp^R	(Papenfort *et al.*, 2006)
pMA16.1	**Plasmid for complementation of *pgp1* deletion with *pgp1* in *C. jejuni* strain 81-176 using *C. coli cat* cassette.** Insert was constructed via overlap PCR (CSO-3646/3645) of PCR products amplified with CSO-3646/3647 and CSO-3644/3645 on gDNA of *C. jejuni* strain 81-176. Insert was *NdeI/XmaI*-digested and ligated to product amplified with CSO-3641/3650 on pGD117.1 (*Dpn/NdeI/XmaI-I* digested).	p15Amod/ Amp^R, Cm^R	This study
pMA12.2	**Plasmid for complementation of Cj0883c deletion with Cj0883c in *C. jejuni* strain NCTC11168 using *C. coli cat* cassette.** Ligation of *NdeI/ClaI*-digested PCR product amplified with CSO-3477/3478 on gDNA of *C. jejuni* NCTC11168 and *NdeI/ClaI*-digested PCR product amplified with CSO-0347/0350 on pGD98.12 (*DpnI*-digested).	p15Amod/ Amp^R, Cm^R	This study
pMOD-2	**EZ-Tn5™ pMOD™ transposon construction vector**	p15A/ Amp^R	Epicentre
pSE59.1	***Campylobacter* complementation plasmid carrying chloramphenicol resistance cassette (*C. coli cat*)**	p15Amod/ Amp^R, Cm^R	(Dugar *et al.*, 2018)
pSSv8	**Intermediary plasmid for construction of a Tn5 based mutant library in *C. jejuni* NCTC11168.** Ligation of PCR product amplified with CSO-1503/1504 on pMOD-2 to introduce an outwards-facing T7 promoter.	p15A/ Amp^R	S. Svensson, Sharma lab
pSSv9	**Plasmid for construction of a Tn5 based mutant library in *C. jejuni* NCTC11168.** Ligation of *EcoRI/HindIII*-digested PCR product amplified with CSO-1567/1568 on pST1.1 and *EcoRI/HindIII*-digested pSSv8.	p15A/ Amp^R, Kan^R	S. Svensson, Sharma lab
pSSv53.4	**Intermediary plasmid for translational fusions to *sfgfp* in *C. jejuni* strain NCTC11168.** Insertion of a pseudogene (Cj0046) locus of *C. jejuni* strain NCTC11168 into pJV752.1 cloning vector. Ligation of *XbaI/XhoI*-digested PCR product amplified with CSO-1402/1405 on gDNA of *C. jejuni* NCTC11168 and CSO-0073/0075 on pJV752.1 (*DpnI/XbaI/Xho1*-digested).	p15Amod/ Amp^R	S. Svensson, Sharma lab
pSSv63.1	**Plasmid for complementation of *ptmG* deletion with *ptmG* in *C. jejuni* strain NCTC11168 using *aphA-3* cassette.** Ligation of *PstI/XmaI*-digested PCR product amplified with CSO-2928/2929 on gDNA of *C. jejuni* NCTC11168 and *PstI/XmaI*-digested PCR product amplified with CSO-0762/0493 on pST1.1 (*DpnI*-digested).	p15Amod/ Amp^R, Kan^R	S. Svensson, Sharma lab
pSSv105.1	**Plasmid for complementation of Cj0978c deletion with Cj0978c in *C. jejuni* strain NCTC11168 using *C. coli cat* cassette.** Ligation of *NseI/ClaI*-digested PCR product amplified with CSO-3607/3608 on gDNA of *C. jejuni* NCTC11168 and *NseI/ClaI*-digested PCR product amplified with CSO-0347/0760 on pSE59.1 (*DpnI*-digested).	p15Amod/ Amp^R, Cm^R	S. Svensson, Sharma lab
pSSv106.5	**Plasmid for complementation of Cj0892c deletion with Cj0892c in *C. jejuni* strain NCTC11168 using *C. coli cat* cassette.** Ligation of *NseI/ClaI*-digested PCR product amplified with CSO-3611/3612 on gDNA of *C. jejuni* NCTC11168 and *NseI/ClaI*-digested PCR product amplified with CSO-0347/0760 on pSE59.1 (*DpnI*-digested).	p15Amod/ Amp^R, Cm^R	S. Svensson, Sharma lab

continued on next page

Name	Description/Generation	Origin/ Marker	Reference
pSSv107.8	**Plasmid for complementation of Cj1643 deletion with Cj1643 in *C. jejuni* strain NCTC11168 using *C. coli cat* cassette.** Ligation of *NseI/ClaI*-digested PCR product amplified with CSO-3609/3610 on gDNA of *C. jejuni* NCTC11168 and *NseI/ClaI*-digested PCR product amplified with CSO-0347/0760 on pSE59.1 (*DpnI*-digested).	p15Amod/ Amp^R, Cm^R	S. Svensson, Sharma lab
pSSv113.1	**Plasmid for translational fusion of Cj0978c to *sfgfp* in *C. jejuni* strain NCTC11168.** Ligation of *ClaI*-digested PCR product amplified with CSO-0347/3718 on pSSv105.1 (*DpnI*-digested) and *ClaI*-digested PCR product amplified with CSO-3717/3279 on pAI2.1.	p15Amod/ Amp^R, Cm^R	S. Svensson, Sharma lab
pSSv114.1	**Plasmid for translational fusion of Cj1643 to *sfgfp* in *C. jejuni* strain NCTC11168.** Ligation of *ClaI*-digested PCR product amplified with CSO-0347/3719 on pSSv107.8 (*DpnI*-digested) and *ClaI*-digested PCR product amplified with CSO-3717/3279 on pAI2.1.	p15Amod/ Amp^R, Cm^R	S. Svensson, Sharma lab
pSSv115.1	**Plasmid for translational fusion of Cj0892c to *sfgfp* in *C. jejuni* strain NCTC11168.** Ligation of *ClaI*-digested PCR product amplified with CSO-0347/3720 on pSSv106.5 (*DpnI*-digested) and *ClaI*-digested PCR product amplified with CSO-3717/3279 on pAI2.1.	p15Amod/ Amp^R, Cm^R	S. Svensson, Sharma lab
pST1.1	***Campylobacter* complementation plasmid carrying kanamycin resistance cassette (*aphA-3*)**	p15Amod/ Amp^R, Kan^R	(Dugar *et al.*, 2018)
pXG10-SF	Plasmid for construction of translational *sfgfp* fusion; contains 5'UTR of lacZ plus 185 amino acids.	pSC101*/ Cm^R	(Corcoran *et al.*, 2012)

Amp^R: ampicillin resistance; Cm^R: chloramphenicol resistance; Hyg^R: hygromycin resistance; Kan^R: kanamycin resistance

Appendix Table 6.2: Bacterial strains. Please note that detailed descriptions for the construction of selected *C jejuni* mutants are given in Chapter 6.2. (Microbiologiocal methods).

Trivial name used in this thesis	*C jejuni* strain	Mutation	Description	Strain number	Marker	Oligos for upstream region	Oligos for cassette	Oligos for downstream region
WT/NCTC11168	NCTC111168		Wildtype, kindly provided by Arnoud van Vliet (Institute of Food Research, Norwich, UK) (Parkhill *et al.*, 2000)	CSS-0032				
NCTC111168_Δ*flaA*	NCTC111168	*flaA*::*aphA-3*	Deletion of *flaA* in CSS-0032 (NCTC11168); verification by colony-PCR using CSO-0756/HPK2	CSS-1512	Kan^R	CSO-1548/0752	HPK1/HPK2	CSO-1549/1550
Δ*kpsMT*	NCTC111168	*kpsMT*::*aphA-3*	Deletion of *kpsMT* in CSS-0032 (NCTC11168); verification by colony-PCR using CSO-2007/HPK2	CSS-3805	Kan^R	CSO-2008/2009	HPK1/HPK2	CSO-2010/2011
Δ*cas9*	NCTC111168	*cas9*::*aphA-3*	Deletion of *cas9* in CSS-0032 (NCTC11168); verification by colony-PCR using CSO-0801/HPK2	CSS-0936	Kan^R	CSO-0802/0803	HPK1/HPK2	CSO-0804/0805
Δ*csrA*	NCTC111168	*csrA*::*cat.coli*	Deletion of *csrA* in CSS-0032 (NCTC11168); verification by colony-PCR using CSO-0392/0614	CSS-0643	Cm^R	CSO-0393/0394	HPK1/HPK2	CSO-0395/0396
Δ*ptmG*	NCTC111168	*ptmG*::*aph(7'')*	Deletion of *ptmG* in CSS-0032 (NCTC11168); verification by colony-PCR using CSO-1531/2857	CSS-2966	Hyg^R	CSO-1532/1536	CSO-1678/1679	CSO-1537/1535
ΔCJnc180/190	NCTC111168	CJnc180/190::*aphA-3*	Deletion of CJnc180/190 in CSS-0032 (NCTC11168); verification by colony-PCR using CSO-0246/HPK1	CSS-1157	Kan^R	CSO-0247/0248	JVO-5068/ HPK2-term	CSO-0249/0250
C *ptmG*	NCTC111168	*ptmG*::*aph(7'')*, *rdxA*::*ptmG*::*aphA-3*	Complementation of Δ*ptmG* (CSS-2966) with wild-type *ptmG*; verification by colony-PCR using CSO-0023/0349 and sequencing with CSO-0023	CSS-2978	Hyg^R Kan^R	Transformation of PCR product amplified with CSO-2276/2277 on pSSv63.1 in CSS-2966		
OE *ptmG*	NCTC111168	*rdxA*::*ptmG*::*aphA-3*	Overexpression of *ptmG* in CSS-0032 (NCTC11168); verification by colony-PCR using CSO-0023/0349 and sequencing with CSO-0023	CSS-2980	Kan^R	Transformation of PCR product amplified with CSO-2276/2277 on pSSv63.1 in CSS-0032		
C CJnc180/190	NCTC111168	CJnc180/190::*aphA-3*, *rdxA*::*cat.coli*:: CJnc180/190	Complementation of ΔCJnc180/190 (CSS-1157) with wild-type CJnc180/190; verification by colony-PCR using CSO-0643/0349 and sequencing with CSO-0643	CSS-1158	Kan^R Cm^R	Transformation of PCR product amplified with CSO-2276/2277 on pGD25.1 in CSS-1157		
ΔCj0892c	NCTC111168	Cj0892c::*aphA-3*	Deletion of Cj0892c in CSS-0032 (NCTC11168); verification by colony-PCR using CSO-3343/HPK2	CSS-4081	Kan^R	CSO-3339/3340	HPK1/HPK2	CSO-3341/3342
ΔCj0978c	NCTC111168	Cj0978c::*aphA-3*	Deletion of Cj0978c in CSS-0032 (NCTC11168); verification by colony-PCR using CSO-3348/HPK2	CSS-4083	Kan^R	CSO-3344/3345	HPK1/HPK2	CSO-3346/3347
ΔCj1643	NCTC111168	Cj1643::*aphA-3*	Deletion of Cj1643 in CSS-0032 (NCTC11168); verification by colony-PCR using CSO-3363/HPK2	CSS-4087	Kan^R	CSO-3359/3360	HPK1/HPK2	CSO-3361/3362
ΔCj0883c	NCTC111168	Cj0883c::*aphA-3*	Deletion of Cj0883c in CSS-0032 (NCTC11168); verification by colony-PCR using CSO-2651/HPK2	CSS-4348	Kan^R	CSO-2652/2653	HPK1/HPK2	CSO-2654/2655
C Cj0892c	NCTC111168	Cj0892c::*aphA-3*, *rdxA*::*cat.coli*::Cj0892c	Complementation of ΔCj0892c (CSS-4081) with wild-type Cj0892c; verification by colony-PCR using CSO-0644/0349 and sequencing with CSO-0644	CSS-4327	Kan^R Cm^R	Transformation of PCR product amplified with CSO-2276/2277 on pSSv106.5 in CSS-4081		
C Cj0978c	NCTC111168	Cj0978c::*aphA-3*, *rdxA*::*cat.coli*::Cj0978c	Complementation of ΔCj0978c (CSS-4083) with wild-type Cj0892c; verification by colony-PCR using CSO-0644/0349 and sequencing with CSO-0644	CSS-4325	Kan^R Cm^R	Transformation of PCR product amplified with CSO-2276/2277 on pSSv105.1 in CSS-4083		

continued on next page

Trivial name used in this thesis	*C jejuni* strain	Mutation	Description	Strain number	Marker	Oligos for upstream region	Oligos for cassette	Oligos for downstream region
C Cj1643	NCTC111168	Cj1643::*aphA-3, rdxA*::*cat.coli*::Cj1643	Complementation of ΔCj1643 (CSS-4087) with wild-type Cj1643; verification by colony-PCR using CSO-0644/0349 and sequencing with CSO-0644	CSS-4329	Kan^R Cm^R	Transformation of PCR product amplified with CSO-2276/2277 on pSSv107.8 in CSS-4087		
C Cj883c	NCTC111168	Cj0883c::*aphA-3, rdxA*::*cat.coli*::Cj0883c	Complementation of ΔCj0883c (CSS-4348) with wild-type Cj0883c; verification by colony-PCR using CSO-0574/3478 and sequencing with CSO-0643	CSS-4167	Kan^R Cm^R	Transformation of PCR product amplified with CSO-2276/2277 on pMA12.2 in CSS-4348		
Cj0892c::sfGFP	NCTC111168	Cj0892c::*aphA-3, rdxA*::*cat.coli*::Cj0892c-*sfgfp*	Complementation of ΔCj0892c (CSS-4081) with translational fusion of Cj0892c to *sfgfp*; verification by colony-PCR using CSO-0644/0349 and sequencing with CSO-0644	CSS-4666	Kan^R Cm^R	Transformation of PCR product amplified with CSO-2276/2277 on pSSv115.1 in CSS-4081		
Cj0978c::sfGFP	NCTC111168	Cj0978c::*aphA-3, rdxA*::*cat.coli*::Cj0978c-*sfgfp*	Complementation of ΔCj0978c (CSS-4083) with translational fusion of Cj0978c to *sfgfp*; verification by colony-PCR using CSO-0644/0349 and sequencing with CSO-0644	CSS-4626	Kan^R Cm^R	Transformation of PCR product amplified with CSO-2276/2277 on pSSv113.1 in CSS-4083		
Cj1643::sfGFP	NCTC111168	Cj1643::*aphA-3, rdxA*::*cat.coli*::Cj1643-sfgfp	Complementation of ΔCj1643 (CSS-4087) with translational fusion of Cj1643 to *sfgfp*; verification by colony-PCR using CSO-0644/0349 and sequencing with CSO-0644	CSS-4668	Kan^R Cm^R	Transformation of PCR product amplified with CSO-2276/2277 on pSSv114.1 in CSS-4087		
hupB*::*sfgfp	NCTC111168	P_{hupB}-*hupB*-linker-*sfgfp*-*cat.coli*-*hup*	Integration of a translational *hupB*::*sfgfp* fusion into the *hupB* (Cj0913c) locus; verification by colony-PCR using CSO-2657/2658 and sequencing with CSO-2620, CSO-2624, CSO-0613, and CSO-2626	CSS-3357	Cm^R	Transformation of overlap PCR product amplified with CSO-2620/2626 in CSS-0032		
81-176_WT	81-176		Wildtype, kindly provided by Patricia Guerry (Naval Medical Research Center, Silver Spring, MD, USA); (Korlath *et al.*, 1985)	CSS-0063				
81-176_Δ*flaA*	81-176	*flaA*::*aphA-3*	Deletion of *flaA* in CSS-0063 (81-176); verification by colony-PCR using CSO-1555/HPK2	CSS-2380	Kan^R	CSO-1551/1552	HPK1/HPK2	CSO-1553/1554
81-176_Δ*pgp1*	81-176	*pgp1*:: *aph(7'')*	Deletion of *pgp1* in CSS-0063 (81-176); verification by colony-PCR using CSO-3044/HPK2	CSS-3182	Hyg^R	CSO-3040/3041	HPK1/HPK2	CSO-3042/3043
81-176_C *pgp1*	81-176	*pgp1*:: *aph(7'')*, *rdxA*::*cat.coli*::P_{1345}-$iTSS_{1345}$-*pgp1*	Complementation of Δ*pgp1* (CSS-3182) with wild-type *pgp1* under control of the internal TSS of Cjj1345; verification by colony-PCR using CSO-0643/3270 and sequencing with CSO-3270	CSS-5643	Hyg^R Cm^R	Transformation of PCR product amplified with CSO-2276/2277 on pMA16.1 in CSS-3182		

Trivial name used in this thesis	*H. pylori* strain	Mutation	Description	Strain number	Marker	Oligos used for upstream region	Oligos for cassette	Oligos used for downstream region
26695	26695		Wildtype (NCBI Acc-no. NC_000915), kindly provided by T. F. Meyer (MPI-IB, Berlin, Germany); (Tomb *et al.*, 1997)	CSS-0004				

Appendix Table 6.3: Tn-seq read mapping statistics. Please note that detailed descriptions for the processing and mapping of sequencing reads is given in Chapter 6.5. (Bioinformatics and computational analyses).

Libraries	2D SUP R1	2D ADH R1	2D INT R1	2D SUP R2	2D ADH R2	2D INT R2
Input reads	33,795,397	41,856,946	56,230,936	23,873,725	24,751,743	29,148,389
Long enough reads	33,595,146	41,649,154	56,012,546	23,651,625	24,469,393	28,949,587
Too short reads	200,251	162,792	218,39	222,1	282,35	198,802
Aligned reads	31,209,079	39,193,938	52,560,065	22,085,655	22,904,995	27,102,426
% of aligned reads	92.9	94.0	93.8	93.4	93.6	93.6
Uniquely aligned reads	29,918,070	37,663,332	50,372,187	21,163,340	21,983,196	25,968,805
% of uniquely aligned reads	89.1	90.3	89.9	89.5	89.9	89.7

Libraries	3D SUP R1	3D ADH R1	3D INT R1	3D SUP R2	3D ADH R2	3D INT R2
Input reads	8,075,715	8,757,581	3,824,716	17,578,872	20,449,173	21,224,779
Long enough reads	7,542,781	7,823,266	3,470,860	17,207,924	20,030,315	20,627,788
Too short reads	532,934	934,315	353,856	370,948	418,858	596,991
Aligned reads	6,779,403	7,200,667	3,255,356	15,246,740	17,958,328	19,135,154
% of aligned reads	89.9	92.0	93.8	88.6	89.7	92.8
Uniquely aligned reads	6,491,668	6,873,704	3,076,147	14,859,392	17,430,283	18,310,140
% of uniquely aligned reads	86.1	87.9	88.6	86.4	87.0	88.8

R1: replicate 1; R2: replicate 2; 2D: screen of unpolarized Caco-2 monolayer; 2D: screen of intestinal tissue model; SUP: supernatant; ADH: adherence (+internalization); INT: internalization only